UNIVERSITÀ DEGLI STUDI DI ROMA TRE

SCUOLA DOTTORALE IN

GEOLOGIA DELL'AMBIENTE E DELLE RISORSE

(SDIGAR)

Ciclo XXII

REOLOGIA MULTIFASE DEI MAGMI ALCALINI ITALIANI

(MULTIPHASE RHEOLOGY OF ITALIAN ALKALINE MAGMAS)

Alessandro Vona

A.A. 2010/2011

Relatore: Dott.ssa Claudia Romano **Coordinatore: Prof. Domenico Cosentino**

Correlatore: Dott. Daniele Giordano

Content

1. Introduction

Understanding how the magma below an active volcano evolves with time and predicting possible future eruptive scenarios for volcanic systems, is crucial for the hazard assessment and risk mitigation in areas where active volcanoes are present. The viscous response of magmatic liquids to stresses applied to the magma body (for example in the magma conduit) controls the fluid dynamics of magma ascent. Adequate numerical simulation of such scenarios requires detailed knowledge of the viscosity of the magma. Magma viscosity is sensitive to the liquid composition, volatile, crystal and bubble contents. High temperature, high pressure viscosity measurements in magmatic liquids involve complex scientific and methodological problems. Despite more than 50 years of research geochemists and petrologists have been unable to develop a unified theory to describe the viscosity of complex natural systems.

Viscosity (η) is defined by Newton as the internal resistance to flow and assumed to be the proportionality between shear stress (τ) and strain rate ($\dot{\gamma}$) ($\tau = \eta\dot{\gamma}$). It is a critical property governing the efficiency of transport processes of molten geomaterials. It controls eruption dynamics and affects physico-chemical processes such as degassing and crystallization in magmas. The viscosity of naturally-occurring magmas can span more than 15 orders of magnitude (10^{-1} to 10^{14} Pa s) primarily in response to variations in melt composition (X), volatile content, temperature (T), pressure (P), as well as the proportions and distributions of suspended solids and vesicles. (Webb and Dingwell, 1990; Dingwell et al., 1992; Dingwell, 1996a; Papale, 1999; Llewellin et al., 2002; Llewellin and Manga, 2005; Vetere et al., 2006; Ardia et al., 2008; Giordano et al., 2009). Heat production (viscous heating) or loss, due to either friction or cooling at the conduit wall during ascent of magma toward the surface, are also features observed in natural environments strongly affecting magma viscosity (Rosi et al., 2004; Costa et al., 2007; Giordano et al., 2007).Viscosity can be also significantly affected by the choice of applied stress-strain regime (e.g., Caricchi et al., 2007, 2008; Costa et al., 2009; Petford, 2009; Mueller et al., 2010).

A silicate melt behaves as a Newtonian fluid when the viscosity at a certain temperature is independent of changes in shear stress or strain rate. If the viscosity depends on the shear stress or strain rate, the melt behaves as a non-Newtonian fluid. Silicate melts behaves as non-Newtonian fluids, only when the shear rate approaches the relaxation rate (Webb and Dingwell, 1990).

A large number of experimental studies (e.g., Dingwell et al., 1996; Richet et al., 1996; Stevenson et al., 1998; Whittington et al., 2000, 2001; Romano et al., 2003; Giordano et al., 2004, 2009; Vetere et al., 2007, 2008; Ardia et al., 2008,) and numerical models (e.g., Russell et al., 2003;

Giordano and Dingwell, 2003; Giordano et al., 2006, 2008; Hui and Zhang, 2007) of the P-T-X dependence of the viscosity of silicate melts have been recently performed demostrating the considerable recent progress in our understanding of magmatic liquids. At a fixed temperature viscosity varies by orders of magnitude as a function of composition (Richet, 1984) and for certain compositions it can also depend on the oxygen fugacity (Dingwell and Virgo, 1987 and Mysen, 1988). An increase in temperature decreases the viscosity since the structural rearrangements in the melt are easier because both the free volume and the configurational entropy increases (Richet, 1984). Most silicate melts show a non-Arrhenian behaviour, reflecting a non-linear relation between the $\log\eta$ vs. 1/T.

However, during a significant part of their history, many magmas are at temperatures below their liquidus; consequently, they contain suspended crystals and, in the case of near-surface magmas and lavas, bubbles. The presence of crystals or bubbles transforms the behavior of magmas from simple Newtonian fluids to more complex rheological materials. Although a certain number of experimental and modeling studies have investigated the rheological properties of different natural magmas at *subliquidus* temperature (Shaw, 1969; Gay et al., 1969; Spera et al., 1988; Pinkerton et al., 1992; Pinkerton and Norton, 1995; Sato, 2005; Sato and Ishibashi, 2007; Ishibashi, 2009) or of synthetic silicate suspensions (Lejeune and Richet, 1995; Costa, 2005; Caricchi et al. 2007; Costa et al., 2009; Muller et al., 2010), no general parameterization exists to determine the rheological properties of multiphase systems. Factors influencing multiphase rheology are the chemical evolution of the suspending fluid during crystallization and/or bubble segregation, the suspended particles concentration, their shape, mean size, size distributions and maximum packing fraction, as well as their ability to modify the rheological properties of the continuous fluid. All these factors affect the rheological response of magmas and eventually the onset of Non-Newtonian behavior in intermediate- to and high-concentration suspensions.

In this work, a detailed investigation of the rheological properties of crystal-bearing and bubble-bearing magmas was performed.

As a step towards the characterization of the effect of crystals on the rheology of magmatic liquids (Chapter 4), we have investigated the high temperature rheological behavior of natural basaltic magmas from Stromboli and Etna volcanic systems during cooling and crystallization in a concentric cylinder apparatus. Moreover a new measurement technique has been developed to measure high temperature viscosity of synthetic liquids with different amount of particles of known shape and crystal size distribution.

The effect of the contemporary presence of bubbles and crystals on natural trachytic samples from the 1538 Monte Nuovo eruption by unconfined uniaxial deformation experiments (Chapter 5)

was also investigated. Comparing the data from this study with those by Caricchi et al. (2008) (on th effect of crystals on the rheology of Monte Nuovo magma), the net effect of vesicles was estimated.

In Chapter 6 the dependence of oxidation state on shear viscosity of a trachybasaltic melt from Etna has been measured using the concentric cylinder method and a gas mixing furnace. The viscosity variation due to different Fe^{2+}- Fe^{3+} ratios is discussed in terms of the structural role of iron in natural silicate melts.

Finally, in Chapter 7 the run products derived from the rheological measurements during isothermal crystallization experiments on basaltic materials from Stromboli and Etna were used to investigate the kinetics of the crystallization process as a function of the degree of undercooling.

2. Theoretical and experimental background

2.1 Structure and Viscosity of Silicate Liquids

2.1.1. Structure of silicate melts

SiO_4^{4-} tetrahedra are the principal building blocks of silicate crystals and melts. The oxygen connecting two of these tetrahedral units is called a "bridging oxygen" (BO) (Fig. 2.1). The "degree of polymerisation" in these material is proportional to the number of BO per cations that have the potential to be in tetrahedral coordination T (generally in silicate melts: Si^{4+}, Al^{3+}; Fe^{3+}; Ti^{4+} and P^{5+}). The "T" cations are therefore called, the "network former cations". More commonly used is the term non-bridging oxygen per tetrahedrally coordinated cation, NBO/T. A non-bridging oxygen (NBO) is an oxygen that bridges from a tetrahedron to a non-tetrahedral polyhedron (Fig. 2.1). Consequently the cations constituting the nontetrahedral polyhedron are the "network-modifying cations".

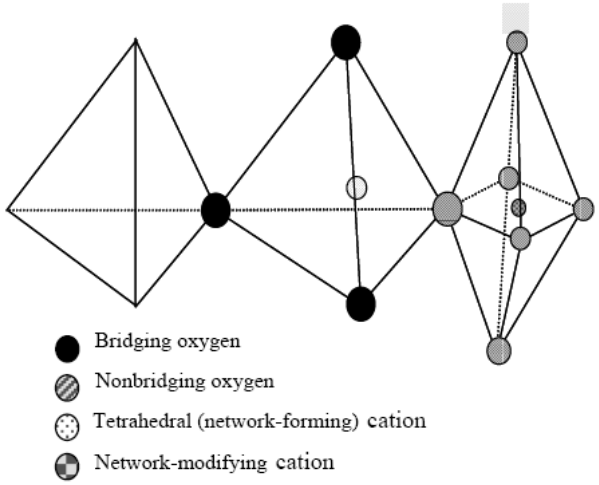

Fig. 2.1. Sketch of nonbridging oxygen per tetrahedrally coordinated cations (NBO/T) (Mysen, 1988)

Addition of other oxides to silica (considered as the base-composition for all silicate melts) results in the formation of non-bridging oxygens.

Most properties of silicate melts relevant to magmatic processes depend on the proportions of non-bridging oxygens. These include, for example, transport properties (e.g. Urbain et al., 1982; Richet, 1984), thermodynamic properties (e.g. Navrotsky et al., 1980; Stebbins et al., 1983), liquid

phase equilibria (e.g. Kushiro, 1975; Ryerson and Hess, 1980) and others. In order to understand how the melt structure governs these properties, it is necessary, first, to describe the structure itself and then, relate this structural information to the properties of the materials. To the following analysis is probably worth noting that despite the fact that most of the common extrusive rocks have NBO/T values between 0 and 1, the variety of eruptive types is surprisingly wide.

In view of the observation that nearly all naturally occurring silicate liquids contain cations (mainly metal cations, but also Fe, Mn and others) that are required for electrical charge-balance of tetrahedrally-coordinated cations (T), it is necessary to characterize the relationships between melt structure and the proportion and type of such cations.

Mysen et al. (1985) suggested that, as the "network modifying cations", occupy the central positions of non-tetrahedral polyhedra, and are responsible for the formation of NBO, the expression NBO/T can be rewritten as:

$$\frac{NBO}{T} = \frac{1}{T}\sum_{i=1}^{i} nM_i^{n+} \qquad (2.1)$$

where is M_i^{n+} the proportion of network modifying cations, i , with electrical charge n+. Their sum is obtained after subtraction of the proportion of metal cations necessary for charge-balancing of Al^{3+} and Fe^{3+}, whereas T is the proportion of the cations in tetrahedral coordination. The use of Eq. 2.1 is controversial and non-univocal because it is not easy to define "a priori" the cation coordination. The coordination of cations is in fact dependent on composition (Mysen, 1988). Eq. 2.1 constitutes however the best approximation to calculate the degree of polymerisation of silicate melt structures.

2.1.2. Viscosity of Silicate Melts: Relation with Structure

In Earth Sciences it is well known that magma viscosity is principally function of liquid viscosity, temperature, crystal and bubble content.

The viscosity of the pure liquid is a function of composition, temperature and pressure. Neglecting, at the moment, the influence of pressure as it has very minor effect on the melt viscosity up to about 20 kbar (e.g. Dingwell et al., 1993; Scarfe et al., 1987), it is known that viscosity is sensitive to the structural configuration, that is the distribution of atoms, in the melt. Therefore the relationship between "network modifying" cations and "network forming/stabilizing" cations with viscosity is critical to the understanding the structure of a magmatic liquid and vice versa.

The main forming/stabilizing cations and molecules are: Si^{4+}, Al^{3+}, Fe^{3+}, $T^{,4+}$, P^{5+} and CO_2 (e.g. Mysen, 1988). The main network modifying cations and molecules are: Na^{+}, K^{+}, Ca^{2+}, Mg^{2+}, Fe^{2+}, F^{-}, and H_2O (e.g. Mysen, 1988). However, their role in defining the structure is often controversial. For example, when there is a charge unit excess their roles are frequently inverted.

The observed systematic decrease in activation energy of viscous flow with the addition of Al (Riebling, 1964, 1966; Urbain et al., 1982; Rossin et al., 1964) can be interpreted to reflect decreasing the "(Si, Al) – bridging oxygen" bond strength with increasing Al/(Al+Si). There are, however, some significant differences between the viscous behaviour of aluminosilicate melts as a function of the type of charge-balancing cations for Al^{3+}. Such a behaviour is the same as shown by adding some units excess to a liquid having NBO/T=0.

Increasing the alkali excess (AE) results in a non-linear decrease in viscosity, which is more extreme at low contents. In detail however, the viscosity of the strongly peralkaline melts increases with the size r of the added cation (Hess et al., 1995; Hess et al., 1996).
Earth alkaline saturated melt instead exhibit the opposite trend although they have a lower effect on viscosity (Dingwell et al., 1996; Hess et al., 1996).

Physical, chemical and thermodynamic information for Ti-bearing silicate melts mostly agree to attribute a polymerising role of Ti^{4+} in silicate melts (Mysen, 1988). The viscosity of fully polymerised melts depends mainly on the strength of the Al-O-Si and Si-O-Si bonds. Substituting the Si for Ti results in weaker bonds. Therefore as TiO_2 content increases the viscosity of the melts is reduced (Mysen et al., 1980). Ti-rich silica melts and silica-free titanate melts are some exceptions that indicate octahedrally coordinated Ti^{4+} (Mysen, 1988).

The most effective network modifier is H_2O. For example, the viscosity of a rhyolitelike composition at eruptive temperature, decreases by up to 1 and 6 orders due to the addition of an initial 0.1 and 1 wt%, respectively (e.g. Hess and Dingwell, 1996). Such an effect nevertheless strongly diminishes with further addition and tends to level off over 2 wt% .

Iron content as Fe^{3+} or Fe^{2+} also affects melt viscosity. Because NBO/T (and consequently the degree of polymerisation) depends on $Fe^{3+}/\Sigma Fe$ also the viscosity is influenced by the presence of iron and by its redox state (Cukierman and Uhlmann, 1974; Dingwell and Virgo, 1987; Dingwell, 1991). The situation is even more complicated as the ratio $Fe^{3+}/\Sigma Fe$ decreases systematically as the temperature increases (Virgo and Mysen, 1985). Thus, iron-bearing systems become increasingly more depolymerised as the temperature is increased. Water also seems to provide a restricted contribution to the oxidation of iron in relatively reduced magmatic liquids, whereas in oxidized calk-alkaline magma series, the presence of dissolved water will not largely influence melt ferric-ferrous ratios (Gaillard et al., 2001).

How important the effect of iron and its oxidation state in modifying the viscosity of a silicate melt (Dingwell and Virgo, 1987; Dingwell, 1991) is still unclear and under debate. On the basis of a wide range of spectroscopic investigations, ferrous iron behaves as a network modifier in most silicate melts (Cooney et al., 1987; and Waychunas et al., 1983 give alternative views). Ferric iron, on the other hand, occurs both as a network former (coordination IV) and as a modifier. As a network former, in Fe^{3+}-rich melts, Fe^{3+} is charge balanced with alkali metals and alkaline earths (Cukierman and Uhlmann, 1974; Dingwell and Virgo, 1987).

In chapter 6 the effect of oxidation state on the viscosity of a basalt from Etna has been investigated through high-temperature viscometry with the concentric cylinder method in controlled CO-CO_2 atmosphere. The obtained viscosity data have been then compared to previous data from similar studies on Fe-rich synthetic melts (e.g. Dingwell and Virgo, 1987; 1988; Dingwell, 1991) and basaltic melts (Bouhifd et al., 2004).

Further investigations are necessary to fully understand the structural complexities of the "degree of polymerisation" in silicate melts.

2.2. Crystal-bearing magma rheology

With few exceptions, previous experimental determinations on the effect of crystals on the rheology of liquids have been performed either on materials related to ceramics or on simplified systems such as a) synthetic analogues (e.g., syrups, gelatins, silicon oils) with mono- or bi-disperse particle size distribution of simple morphology (e.g. Marti et al., 2005; Pabst et al., 2006; Mueller et al., 2010) or b) high-T compositionally simplified silicate liquids with single crystalline phases of various shape from sub-rounded to elongated (e.g. Lejeune and Richet, 1995; Caricchi et al., 2007; Champallier et al., 2008).

Very few studies have evaluated the multiphase rheology of crystal-bearing natural silicate melts (e.g., Ryerson et al. 1988; Pinkerton and Stevenson, 1992; Lejeune and Richet, 1995; Pinkerton and Norton, 1995; Sato, 2005; Caricchi et al., 2008; Ishibashi and Sato, 2007; Ishibashi, 2009; Costa et al., 2009; Petford, 2009). Even fewer data are available describing the rheology of crystal- plus bubble-bearing melts (e.g., Lavallée et al., 2007).

Viscosity is defined as the resistance to flow under specific applied stress (σ) conditions and it is expressed by complex functions of applied stress and resulting strain (γ) and strain-rates (e.g., Herschel and Bulkley, 1926). For a Newtonian liquid, $\sigma = \eta\dot{\gamma}$ where η is the Newtonian viscosity.

The presence of a solid phase or a gaseous phase to form a solid or bubble suspension can yield non-Newtonian behavior, expressed in the more general equation:

$$\sigma = \sigma_0 + K\dot{\gamma}^n \quad (2.2)$$

where σ_0 is a stress threshold to be overcome in order to have flow, namely the yield stress; K is the *flow consistency* (which corresponds to shear viscosity at $\dot{\gamma}$=1 s^{-1}) and n is the *flow index* which describes the degree of Non-Newtonian behavior being equal to 1 for Newtonian fluids, n>1 for shear-thickening and n<1 for shear-thinning fluids. The apparent viscosity is defined as $\eta = \sigma/\dot{\gamma}$. measured at a particular stress or strain rate.

From Eq. (1), assuming zero yield stress, the relative viscosity (ratio between stress and strain rate divided by the viscosity of the suspending liquid, η_l) can be written as:

$$\eta_r = \frac{K}{\eta_l}\,\dot{\gamma}^{n-1} \quad (2.3)$$

where $K_r = K/\eta_l$ represent the relative consistency.

In a two-phase material the average viscosity η varies continuously between the values of each constituent (η_1 and η_2) as a function of the relative concentration of one phase (ϕ).

As a first approximation, the variation of the relative parameters can be described by two end-member models (series and parallel models, or Voigt and Reuss bounds) consisting in the arithmetic and in the geometric mean value η_a and η_g, respectively (Voigt,1928; Reuss, 1929; Guéguen and Palciauskas, 1992; Vigneresse and Tikoff, 1999; Ji and Xia, 2002), in which the transport property for each phase is weighted according to its respective volumetric percentage :

$$\eta_a = \phi\eta_1 + (1-\phi)\eta_2 \quad (2.4)$$

$$1/\eta_g = \phi/\eta_1 + (1-\phi)\eta_2 \quad (2.5)$$

Although these laws allow to describe the viscosity of two well-mixed viscous fluids, they are not suitable when the two phases have very different properties, as in the case of a suspension of rigid particles within a viscous fluid. They therefore represent the upper and lower bounds for the effective bulk viscosity of the two-phase material (Fig. 2.2).

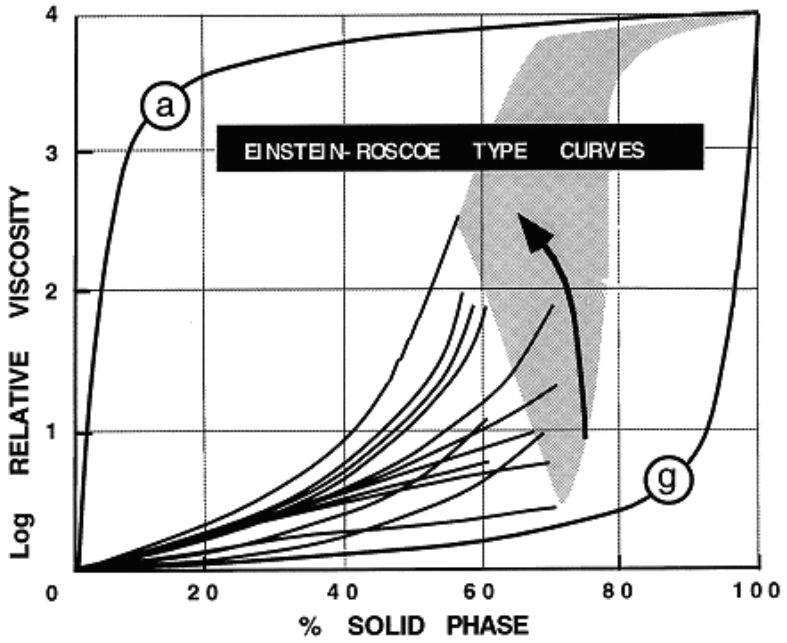

Fig. 2.2. Relative viscosity (η_s/η_m) as a function of solid fraction showing the Voigt (a) and Reuss (g) bound. The solid suspensions curves lie in between the two bounds. (from Vigneresse and Tikoff, 1999).

In general, an increasing crystal content of suspensions generates a sigmoidal increase in viscosity (Lejeune and Richet, 1995). For low solid fractions, the viscosity increases slowly with the particle volume fraction (ϕ), close to the geometrical mean ("Reuss bound"; Reuss, 1929), and the suspension maintains a Newtonian rheological behavior (strain-rate independence).

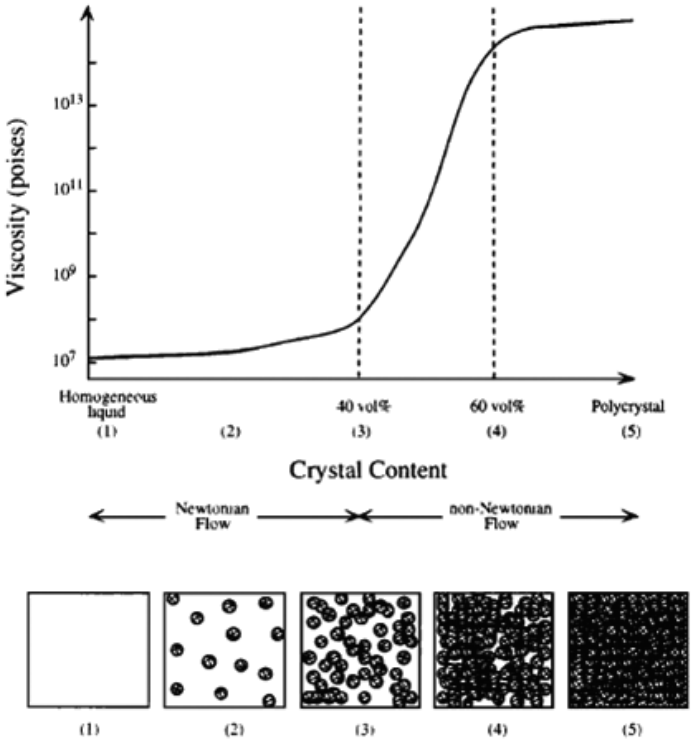

Fig. 2.3. Viscosity-crystal fraction relation for solid suspensions. (from Lejeune and Richet ,1995)

When ϕ exceeds a critical value (ϕ_c), particles start to interact with each other and a solid network of particles begins to form, causing a strong increase in viscosity and the onset of non-Newtonian flow, characterized by Bingham-like rheology (with yield strength) and/or shear thinning effects.

As the solid fraction is further increased another rheological threshold, corresponding to the maximum packing density of solid particles (ϕ_m), causes the viscosity to approach the Voigt bound (Voigt, 1928). At this point the system behaves essentially as a single phase solid material and flow ceases, eventually culminating in brittle failure if additional stress is applied to the material. (Fig. 2.3).

It is thus useful to distinguish the three following concentration regimes (c.f. Rutgers 1962a,b; Thomas, 1965; Pabst et al. 2006; Mueller et al. 2010): (1) a dilute flow regime, where the viscosity increase is nearly linear and rheology is Newtonian; (2) a semi-dilute regime, where the viscosity exhibits a higher order dependence on crystal content, but rheology remains Newtonian and (3) a concentrated regime, where the suspension shows a rapid increase in viscosity and the onset of Non-Newtonian behavior. These regimes are defined not only on the basis of crystal concentration, but also on the basis of crystal shape, crystal size and shape distribution and orientation of particles. The effects of those parameters are discussed in this section.

For suspensions of spherical particles, Rutgers (1962a,b) and Thomas (1965) found the upper limit for the dilute regime at $\phi \leq 0.02$ and $\phi \leq 0.01$, respectively, and that of the semi-dilute regime at $\phi_c \leq 0.25$. For monodisperse suspensions of elongated particles, Doi and Edwards (1978) defined these regimes as functions of particle aspect ratios (R=long axis/short axis) (Fig.2.4).

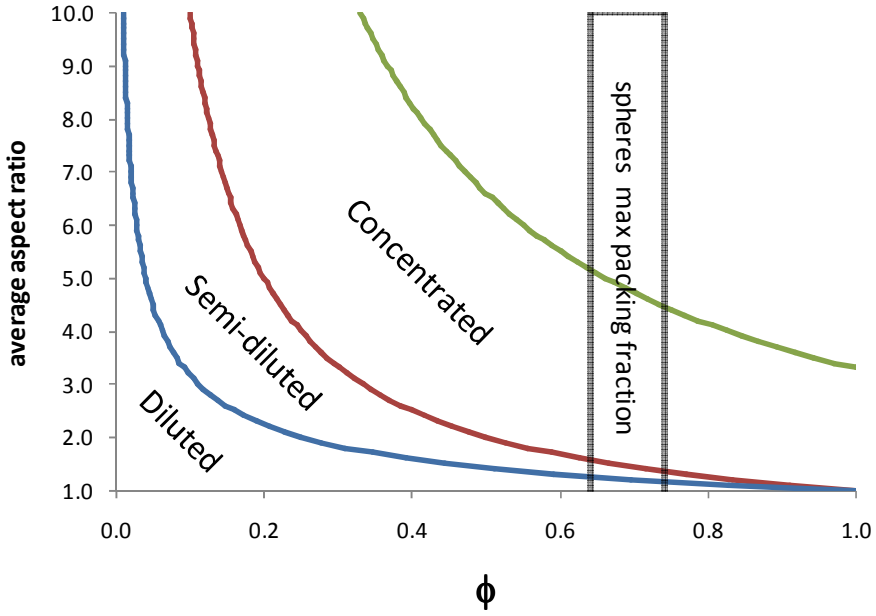

Fig. 2.4. Concentration regimes for monodisperse suspensions as a function of aspect ratio and crystal content after Doi and Edwards (1978). Fields are separted by the conditions: diluted $\phi < 1/R^2$; semi-diluted $1/R^2 < \phi < 1/R$; concentrated $\phi < 3.3/R$.

To predict the viscosity of liquids containing solid suspended particles in the dilute and semi-dilute concentration regimes, different derivations of the equations of Einstein (1906) and Roscoe (1952) are commonly used.

For the simplest system of a very *dilute suspension* of solid spherical monodisperse particles (ϕ<0.03), Einstein (1906) calculated that the viscosity follows the equation:

$$\eta_r = (1 + B\phi) \tag{2.6}$$

where η_r is the relative viscosity and B is the Einstein coefficient, an adjustable parameter which is commonly assumed to be equal to 2.5, although, alternative values ranging from 1.5 to 5.5 have been given (e.g., Jeffrey and Acrivos, 1976; Pabst et al. 2006).

To expand the range of applicability to higher crystal fractions, incorporating the effects of hydrodynamically interacting particles (in the *semi-dilute* regime), Roscoe (1952) introduced an equation known as the Einstein-Roscoe (ER) equation, which considers the maximum packing density of solid particles (ϕ_m):

$$\eta_r = \left(1 - \frac{\phi}{\phi_m}\right)^{-2.5} \tag{2.7}$$

For monodisperse spherical particles, ϕ_m ranges from a maximum of 0.74 when the particles show the most compact ordered hexagonal arrangement (Shaw, 1965) to 0.60 for less compact, disordered arrangements (Marsh, 1981). The ER equation set with the value of ϕ_m=0.60 (determined empirically by Marsh (1981) using Shaw's (1969) viscosity data), is appropriate to describe relative viscosity increase for particle fraction ϕ < ca. 0.3-0.4 (below the onset of non-Newtonian behavior) for a suspension containing uniform spherical or equantly shaped particles, and has been used extensively in the simulation of natural magmas (e.g. Ryerson et al., 1988; Pinkerton and Stevenson, 1992; Lejeune and Richet, 1995). However, as demonstrated by Sato (2005), the ER equation is not applicable to natural magmas containing elongated crystals (i.e. tabular plagioclase), as both ϕ_m and the exponent (Eq. 4) vary as functions of the textural attributes of the particles and the total applied stress, σ.

Krieger and Dougherty (1959) in order to apply ER the equation to a larger range of non-spherical particle rheology provided the following general KD-equation:

$$\eta_r = \left(1 - \frac{\phi}{\phi_m}\right)^{-B\phi_m} \tag{2.8}$$

For values of Bϕ_m=2 and 2.5, Eq. (2.8) yields the MP and ER equations, respectively (Fig. 2.5).

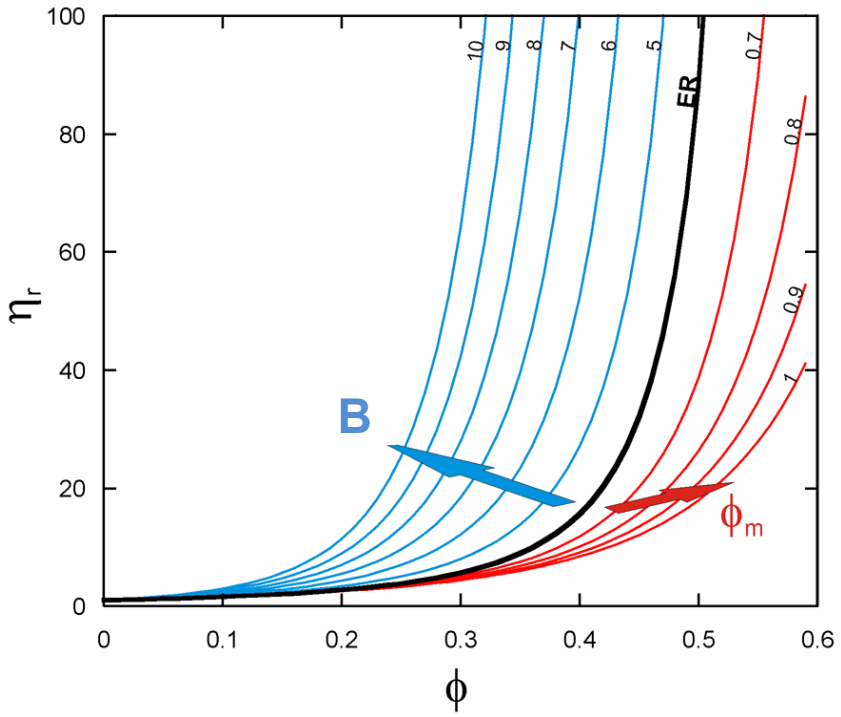

Fig. 2.5. Relative viscosity – solid fraction relation calculated with KD equation (Krieger and Dougherty, 1959) with different values of B and ϕ_m. The Einstein-Roscoe equation (black line) is calculated for ϕ_m=0.6 and $B\phi_m$=2.5 (i.e. $[\eta]$=4.167). Blue lines correspond to increasing values of B =5, 6, 7, 8, 9, 10 at constant ϕ_m=0.6. Red lines correspond to increasing values of ϕ_m=0.7, 0.8, 0.9, 1 at constant B =4.167.

It has been observed that both B (sometime referred to as "intrinsic viscosity") and ϕ_m are very sensitive to the axial ratio (R) of spheroids. Overall, B, contrarily to ϕ_m, increases as the particles shape deviates from an isotropic form (Jeffery et al., 1922). Based on the MP equation (having an exponent value of 2) and measurements on monodisperse particles of varying aspect ratios, Kitano et al. (1981) and Pabst et al. (2006), and Mueller et al (2010), respectively, propose different expressions for the dependence of the ϕ_m from R-parameter which correlate linearly and via a first order inverse function to such a parameter. These are single parameter expressions. Compared to Kitano et al (1981) and Pabst et al (2006) the expression formulated by Mueller et al (2010) (Eq. 2.9), has the advantage of always providing positive values for both B and ϕ_m.

$$\phi_m = \frac{2}{0.321\bar{R}+0.302} \qquad (2.9)$$

The effect of the particle size distribution on the viscosity of spherical suspensions was studied by Farris (1968). In his theory, the finer particles in a bimodal suspension behave essentially as a fluid with respect to the coarser particles if the size ratio (small to large) is <0.1 and interactions are negligible. Using this concept, the viscosity of bimodal and multimodal suspensions can be calculated from the unimodal viscosity data of each size. From this theory, the dependence of bimodal particle sizes (expressed as the diameters of the smaller and the bigger particles) on ϕ_m was found experimentally by Chong et al. (1971). Kansal et al. (2002) performed numerical simulations on the effect of the particle size distribution on ϕ_m for spherical particles and showed that ϕ_m increases for wide size distribution (up to ϕ_m=0.87 for a polydisperse random sphere packing).

Orientation of anisotropic particles also has an important effect on suspension rheology. Donev et al. (2004) showed that anisotropic particles with a preferred orientation have a higher ϕ_m, providing a more ordered packing structure with ϕ_m increasing from 0.64 to 0.74 as dispersion of particle orientation decreases.

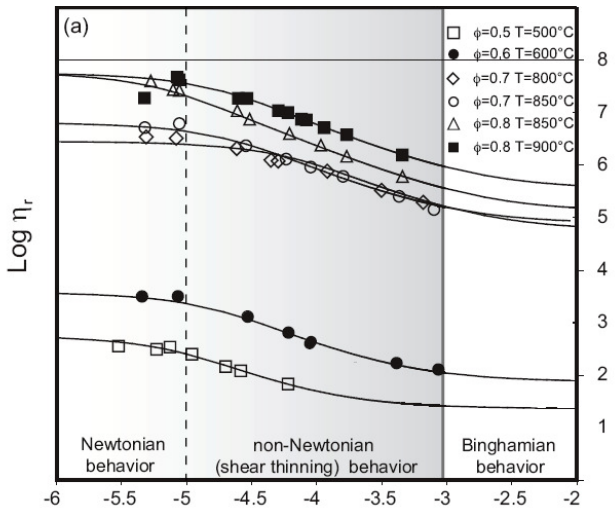

Figura 2.6. Evolution of different rheological behaviours as a consequence of increasing strain rate. (from Caricchi et al. 2007)

None of the above equations account for the strain rate dependence of viscosity. For *concentrated suspensions* it is observed that the rate of deformation strongly affects the rheological response. At high crystal fractions, increasing deformation rate yields the transition from Newtonian to non-Newtonian rheological behavior (Fig.2.6; Krieger, 1972; Van der Werff and de Kruif, 1989; Brückner and Deubener, 1997; Deubener and Brückner, 1997; Caricchi et al., 2007). At low strain rates (Brückner and Deubener, 1997; Scott and Kohlstedt, 2006; Caricchi et al., 2007), the increase of relative viscosity depends mainly on the textural characteristics of the crystalline phases (Newtonian behavior). Increasing the strain rate above a certain threshold results in a decrease of

the apparent viscosity, a non-Newtonian behavior known as shear thinning (e.g. Webb and Dingwell, 1990) until a minimum value is reached. This minimum represents the onset of pseudo-Bingham behavior in which the relative viscosity is lower than in the Newtonian field but is no longer dependent on the strain rate (Fig. 2.7).

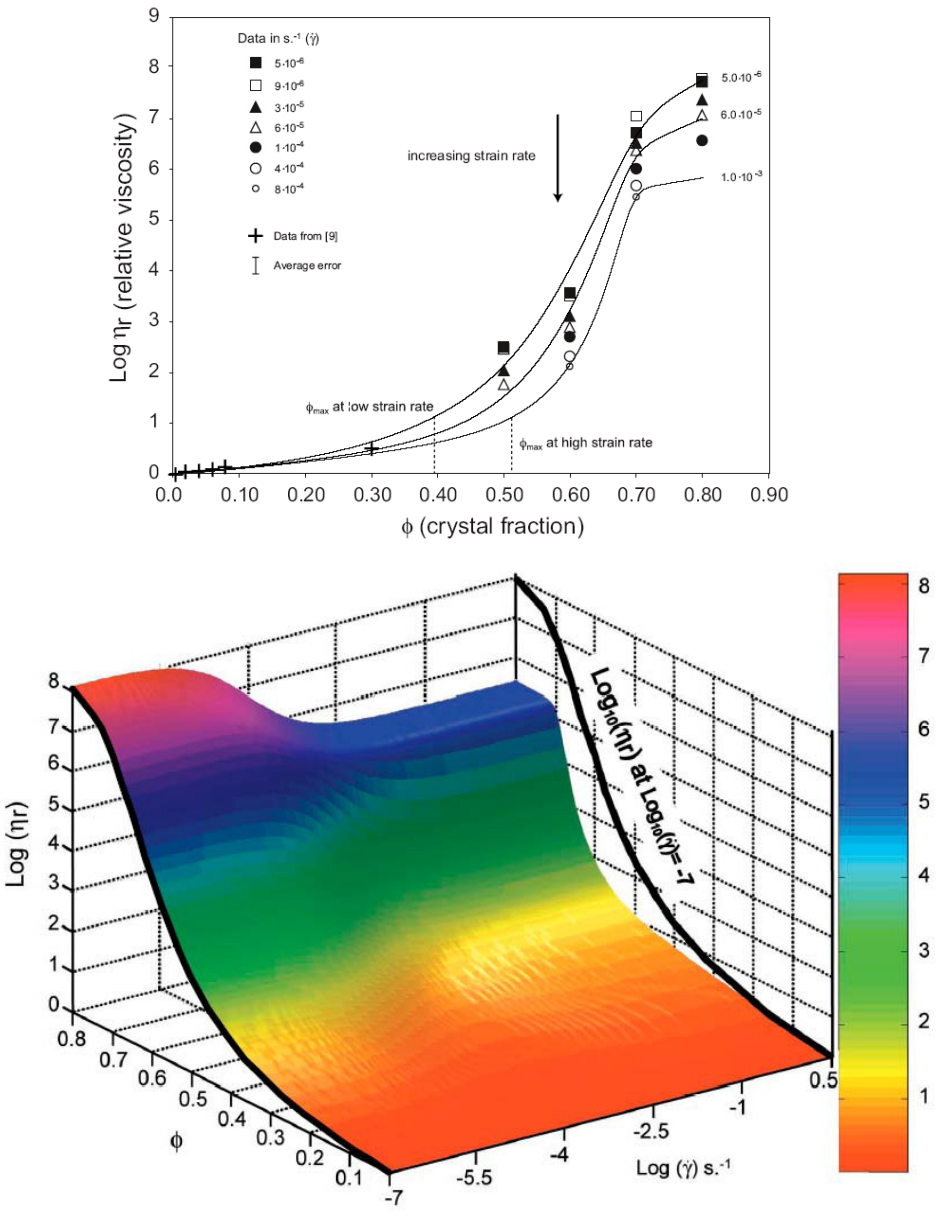

Fig. 2.7. (a) Deformation experiments from Caricchi et al. (2007), on spherical quartz particles suspended within a haplogranite synthetic melt, showing the relation between relative viscosity and crystal fraction at different strain rates. **(b)** 3D plot of the prediction model by Caricchi et al. 2007. Increasing strain rate results in a decrease in relative viscosity (shear thinning) and the shift of ϕ_c (here named ϕ_{max}) towards higher crystal content (from Caricchi et al. 2007).

Starting from Eq. (2.3), Ishibashi (2009) and Mueller et al. (2010) proposed two parametrizations obtained by modifications of the above reported strain rate independent KD and MP equations, respectively, to take into account of the shear thinning effect on the rheology of suspensions.

On the basis of their study on monodisperse suspensions with different aspect ratios, Mueller et al. (2010) provided relationships for K and n as a function of ϕ/ϕ_m and ϕ/ϕ_m and R, respectively:

$$\frac{K}{\eta_l} = \left(1 - \frac{\phi}{\phi_m}\right)^{-2} \tag{2.10}$$

$$n = 1 - 0.2R\left(\frac{\phi}{\phi_m}\right)^4 \tag{2.11}$$

With these expressions the relative consistency of monodisperse suspensions is completely described by the Maron-Pierce equation (MP), while the flow index *n* captures the role of shear thinning on the suspension rheology.

Ishibashi (2009) provided a modified strain rate dependent KD equation based on rheological measurements on natural balsaltic magmas:

$$\eta_r = \left(1 - \frac{\phi}{\phi_m}\right)^{-B_1\phi_m[1+\lambda \ln(1-\phi/\phi_m)\ln \dot{\gamma}\,]} \tag{2.12}$$

where $\phi_m = 0.6$ (as in the ER equation), $B_1 = 5.46$ represents the intrinsic viscosity at $\dot{\gamma} = 1\ s^{-1}$ and $\lambda = 0.118$ is an empirical constant which takes the shear thinning effect into account. However, the fitting parameters are not related in any way to the textural features of their suspension, such as crystal shape, crystal shape dispersion, crystal size dispersion and orientation dispersion, such that the parameterization cannot be further generalizable to other suspensions.

A more empirical parameterization of the relative viscosity, valid for low to medium-high concentrated suspensions of spherical particles was proposed by Costa (2005) and then modified by Caricchi et al. (2007) and Costa et al. (2009) to take into account the rate ($\dot{\gamma}$) dependence of the suspension rheology.The relation between relative viscosity and the solid fraction is given by:

$$\eta(\phi) = \frac{1+\varphi^\delta}{[1-F(\varphi,\varepsilon,\gamma)]^{B\phi^*}} \tag{2.13}$$

where

$$F = (1-\xi) erf\left[\frac{\sqrt{\pi}}{2(1-\xi)}\varphi(1+\varphi^{\gamma})\right] \quad (2.14)$$

with $\varphi = \phi/\phi*$ where ϕ*, ξ, γ and δ are empirical parameters that depend on the deformation rate and B is the Einstein coefficient. Although this model can successfully predict the multiphase rheology of suspensions varying from ϕ = 0.1 - 0.8 isotropic particles for a wide range of strain rates, it fails when the aspect ratio of the solids increases.

To date, a general model predicting the rheological behavior of magmatic suspension as a function of crystal content, crystal anisotropy, crystal size distribution and strain rate has yet to be formulated. In this study we have determined the *subliquidus* viscosity of Stromboli and Etna basalts and compared the results with existing predictive models. With this knowledge, we address the relative importance of temperature, residual melt evolution, crystallizing phases and their textural features on the rheological behavior of magmas.

2.3. Bubble-bearing magma rheology

In bubble-melt mixtures, the bubbles can either increase or decrease the shear viscosity of a suspension depending on the dynamic regime (Manga et al., 1998; Spera and Stein, 2000; Llewellin et al., 2002a,b; Rust and Manga, 2002a; Stein and Spera, 2002, Llewellin and Manga, 2005). The relative viscosity ($\eta_r = \eta_s(\phi)/\eta_l$, where $\eta_s$is the suspension viscosity and η_l is the viscosity of the liquid phase) is a function of the gas volume-fraction ϕ, that may increase or decrease with increasing ϕ depending on the conditions of shear and the bubble-relaxation time λ. The quantity λ is a measure of the timescale over which a bubble can respond to changes in its shear environment. For a single bubble in an infinite medium:

$$\lambda = \frac{\eta_0 R}{\Gamma} \quad (2.13)$$

where R is the undeformed bubble radius and Γ is the bubble–liquid interfacial tension. There is some evidence that λ is an increasing function of ϕ (Oldroyd, 1953; Oosterbroek and Mellema, 1981; Loewenberg and Hinch, 1996; Llewellin et al., 2002), however, Rust et al. (2003) show that the dependence of λ on ϕ is rather weak so, for simplicity, it is proposed that Eq. (2.13) is used for all ϕ.

The effect of bubbles on the magma rheology depends on the type of magma flow, that can be simplified as "steady" or "unsteady" (Llewellin and Manga, 2005).

A flow is decribed as "steady" when the condition of shear have remained constant for a time before present $t \gg \lambda$ (Llewellin et al., 2002; Rust and Manga, 2002). Manga and Loewenberg (2001), Llewellin et al. (2002), Rust and Manga (2002) and Stein and Spera (2002) show that, for a steady flow, the viscous regime is controlled by the capillary number Ca, given by:

$$Ca = \lambda\dot{\gamma} = \frac{\lambda\eta_0 R}{\Gamma} \tag{2.14}$$

where $\dot{\gamma}$ is the shear strain-rate. *Ca* describes the relative importance of viscous stresses, which tend to deform the bubbles, and interfacial stresses, which tend to restore them to sphericity. Since the flow is steady, *Ca* refers to the equilibrium between these forces, hence, the bubble shape is also stable (bubbles are described as relaxed) and is referred to as the equilibrium deformation. The magnitude of equilibrium bubble-deformation, therefore, depends on *Ca*. If $Ca \ll 1$, interfacial tension forces dominate and bubbles are approximately spherical (e.g., Taylor, 1934). If $Ca \gg 1$, viscous forces dominate and bubbles will be elongate (e.g. Hinch and Acrivos, 1980). The effect of bubble shape on viscosity can be explained as follows: Bubbles deform flow lines within the suspending medium, which tends to increase viscosity; bubbles provide free-slip surfaces within the suspending medium, which tends to decrease viscosity. For small *Ca* (bubbles are almost spherical) flow-line distortion is great and free-slip surface area is small, hence, $\eta_r > 1$; for large *Ca* (bubbles are elongate) flow-line distortion is small and free-slip surface area is great, hence, $\eta_r < 1$.

In principle, if the shape of bubbles can be determined as a function of *Ca* and ϕ then the rheology of the suspension can predicted (e.g., Batchelor, 1970). The problem, however, lies in determining bubble shape. For dilute suspensions, analytical results are available for small deformations (e.g., Taylor, 1934) and highly elongate bubbles (e.g., Hinch and Acrivos, 1980). Models are also derived for intermediate deformation (e.g., Wu et al., 2002). In general theoretical results for bubble shape agree well with experimental measurements (e.g., Rust and Manga, 2002; Hu and Lips, 2003; Yu and Bousmina, 2003). When the suspension is no longer dilute, however, the interactions between bubbles affect their shapes and consequently the rheology. Unfortunately, the rheology can be predicted accurately only if the bubble shape is accurately known (Cristini et al., 2002).

However, if the shear strainrate is changing, the flow is unsteady. In fact, Llewellin et al. (2002a,b) have shown that there are degrees of steadiness of flow which can be described using the dynamic capillary number *Cd*, given by:

$$Cd = \lambda \frac{\ddot{\gamma}}{\dot{\gamma}}$$

where $\ddot{\gamma}$ is the rate of change of shear strain-rate. *Cd* compares the timescale over which the bubbles can respond to changes in their shear environment (the bubble-relaxation time λ) with the timescale over which the shear environment changes (of order $\dot{\gamma}/\dot{\gamma}$). If $Cd \ll 1$, the bubbles are able to respond continuously to the changes in shear environment. Consequently, the bubbles are always approximately in their equilibrium deformation and the flow is approximately steady. Since the flow is approximately steady, the dynamic regime is controlled by the capillary number *Ca*. If, however, $Cd \gg 1$, the shear environment is changing too rapidly for the bubbles to respond, therefore the bubbles are unrelaxed. Since the bubbles never reach their equilibrium deformation, *Ca* is undefined and the flow is described as unsteady. In an unsteady flow, the bubbles do not have time to respond elastically to changes in shear, hence, they behave as if they have no bubble–liquid interfacial tension. Since there is, effectively, no elastic force affecting the shape of the bubbles, their response to the local shearing of the suspending liquid is purely viscous and, since they have negligible viscosity, they deform passively with the suspending liquid. This decreases the distortion of flow-lines around the bubbles leading to a decrease in the viscosity of the suspension as ϕ increases (Llewellin et al., 2002a). In summary: if $Cd \ll 1$, flow is approximately steady so regime is determined by considering *Ca*; $Cd \gg 1$ denotes unsteady flow and viscosity decreases with increasing gas volume-fraction.

Just as rheology can be calculated from knowledge of bubble shapes for steady flows, so too can the rheology for unsteady flows if the evolution of bubble shape is known (e.g., Tucker and Moldenaers, 2002). Several recent studies have made progress in developing models for the time-dependent deformation of bubble shape and rheology in a variety of flow geometries (e.g., Maffettone and Minale, 1998; Jansseune et al., 2001; Jackson and Tucker, 2003; Yu and Bousmina, 2003).

In this study we investigated the rheology of a natural sample derived from the Monte Nuovo eruption (Phlegrean Fields) containing ca. 45 % open porosity and a crystal content of ca. ϕ=0.47 with respect to the solid fraction. The experiments were performed at temperatures ranging from the galss transition temperature to the eruptive temperatures (600-700°C). The measurements allow to address the relative importance of the combined presence of crystals and vesicles and vesicles alone on the viscosity variation of natural magmas.

3. Experimental Methods

3.1. Overview

As seen in the previous section, the presence of suspended particles (crystals and/or bubbles) in a magma strongly affect the rheological properties of the magmatic mixture. The relative viscosity can increase due to both hydrodynamic and mechanical interaction among particles (crystals and bubbles) or decrease if the suspended particles can alter their shape under the applied stress (bubbles). A high particle content may also induce non-Newtonian behavior. The variation of viscosity and the non-Newtonian flow depend on factors such as the particle volume fraction, particle shape, spatial arrangement distribution of particles, particle size and the size- and shape-distributions of the particles (e.g. Costa et al., 2009; Petford, 2009; Mueller et al. 2010).

Given these complex dependencies, experiments devoted to the parameterization of suspension rheology have to be carefully planned 1) under variable deformational regimes and 2) for variable crystal content, shape, size and orientation. Further, the accurate characterization of textural features of the investigated samples before and after experimental deformation is essential. It is not infrequent that the different textural and compositional features of samples to be investigated determine the experimental technique to be adopted. For example, the presence of large crystals, common for lava dome products, requires the investigation of large samples in order for the results to be representative of the natural magmas. These lavas are commonly erupted at temperatures corresponding to high viscosity values (close to the glass transition interval) and thus the experiments must involve the application of high stresses of the order of several hundred MPa (e.g., Caricchi et al., 2007, 2008; Lavallée et al., 2008; Cordonnier et al., 2009) in order to induce flow.

A common experimental technique employed in the determination of rheological properties of crystal- and volatile-bearing samples (e.g., Caricchi et al., 2007, 2008; Champallier et al., 2008) at elevated temperature and confining pressure under both compressional and torsional modes is the Paterson-type deformation apparatus (Paterson and Olgaard, 2000). Uniaxial compression devices which allow for unconfined stresses can also be used to investigate the rheological response of multiphase materials (Quane et al., 2004; Lavallée et al., 2008; Robert et al., 2008a,b; Cordonnier et al., 2009). The techniques above mentioned allow viscosity determinations between10^{8} and 10^{14} Pa s at strain rates of 10^{-6} to 10^{-2} s^{-1} (Caricchi et al., 2007, 2008; Robert et al., 2008a, b). In addition, to our knowledge, Robert et al. (2008a) is the only study which investigated the deformation of vesicle-bearing sintered volcanic materials under water pressure conditions.

The high-temperature low-viscosity rheology of crystal- and/or bubble-bearing magmatic mixtures is commonly investigated by applying a constant rotational stress or strain-rate at *subliquidus* conditions using concentric cylinder methods (e.g., Stein and Spera, 2002; Ishibashi, 2009). On the other hand, concentric cylinders or cone-plate rheometers can also be used to determine low-T low-viscosity rheology of synthetic analogues (e.g., Llewellin et al., 2002; Pabst et al., 2006; Mueller et al., 2010). These techniques are used to measure viscosities between 10^{-2} and 10^{5} Pa s and deformation rates ranging from approximately 10^{-4} and 10^{-1} s^{-1}, depending on the specific experimental geometry.

3.2. Experimental measurements

3.2.1. High Temperature Viscometry (T>1000°C)

3.2.1.1. Concentric Cylinder Method

High temperature viscosity measurements were carried out at 1 atm at LMU (Munich) using a Brookfield DV-III+ viscometer head (full range torque of 7.2 x 10^{-2} Nm) and at RomaTre University (Rome), using a Anton Paar RheolabQC viscometer head. Viscosity determinations were performed following the methods and procedures described by Dingwell (1986, 1989a,b) (Fig 3.1 shows details of the furnace). Natural and synthetic materials were first melted in a large thin-walled Pt crucible in a Nabertherm $MoSi_2$ box furnace at T=1400°C for a few hours, until visual inspection indicated homogenization and the complete loss of bubbles from the samples. The melts were quenched in air, and the samples were removed from the crucibles by drilling and percussion. Chips of glass were loaded into a $Pt_{80}Rh_{20}$ cylindrical crucible (5.1 cm in height, 2.56 cm inner diameter, 0.1 cm wall thickness) and remelted in a box furnace heated by $MoSi_2$ elements. High temperature viscosity measurements were carried out using a Brookfield DV-III+ viscometer head (full range torque of 7.2 x 10^{-2} Nm) following the methods and procedures described by Dingwell (1986, 1989a,b). The spindle used for this study was similar to the one described by Dingwell and Virgo (1988) with dimensions 0.32 mm in diameter, 42 mm in length with a 45° conical tip to reduce end effects. The viscometer was calibrated against DGG-1 standard glass, for which the temperature-viscosity relationship is accurately known. With this equipment, viscosity can be measured in the range from 0.1 to 10^{5} Pa s, with an accuracy of ± log η = 0.05 Pa s (Hess et al., 1996).

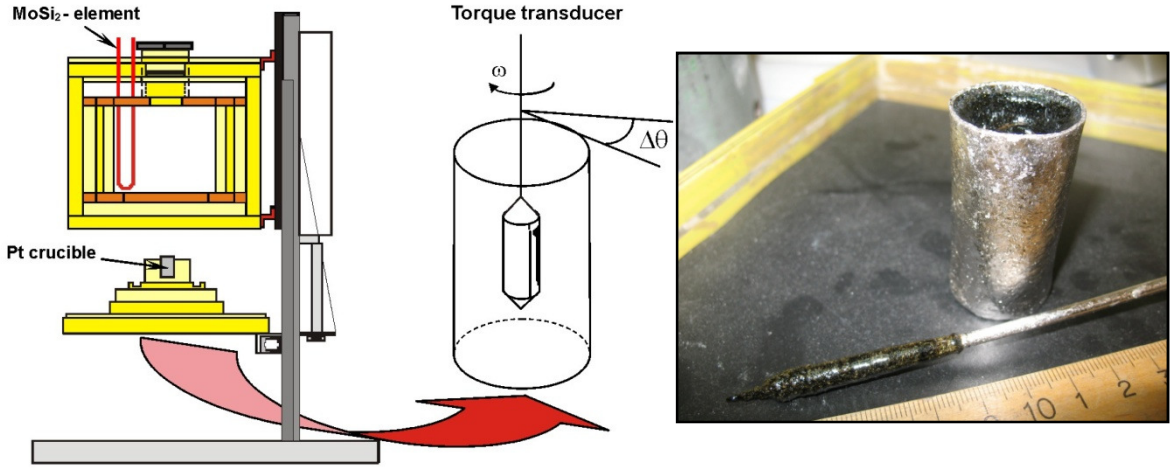

Fig. 3.1. Sketch of the concentric cylinder apparatus (left) and picture of crucible and spindle quenched at the end of an experiment.

In this study, the ratio of the inner to outer radius of the cylinder (R_i/R_o=0.125) corresponds to a "wide-gap geometry" for concentric cylinder measurements. This geometry is preferred to the narrow-gap system (R_i/R_o>0.97) as it does not present problems of achieving parallel alignment and it works better with suspensions containing large particles. As suggested by Krieger and Maron (1954), the shear stress/shear rate relationship over the interval of shear rates in the gap can be described by the following simplified Herschel-Bulkley (1926) power law equation (Eq. 2.2):

$$\sigma = K\dot{\gamma}^n \tag{3.1}$$

For this geometrical assemblage the values of shear stress and shear rate taken at the inner cylinder are given by:

$$\dot{\gamma} = \frac{2\Omega}{n\left(1-\left(\frac{R_i}{R_o}\right)^{2/n}\right)} \tag{3.2}$$

$$\sigma = \frac{M}{2\pi R_i^2 h} \tag{3.3}$$

where Ω is the angular velocity (rad/s), *M* the measured torque and *h* the effective immersed length of the spindle. However, the wide gap setup has the disadvantage that the shear-rate is not only dependent on the geometrical characteristics of the adopted assembly but it also depends on the flow index value (*n*). Using Eqs. (3.2) and (3.3) a flow curve (σ-$\dot{\gamma}$) can be built to describe the rheological behavior of the studied suspensions. The value of *n* can be determined by plotting *M*

versus Ω on a double logarithmic basis and taking the slope at the value of Ω under consideration (e.g., Ishibashi, 2009). The results obtained for our measurements, using this method, are given in section 4.

3.2.2. Low Temperature Viscometry (T= 600°C-800°C)

3.2.2.1. Parallel Plate technique

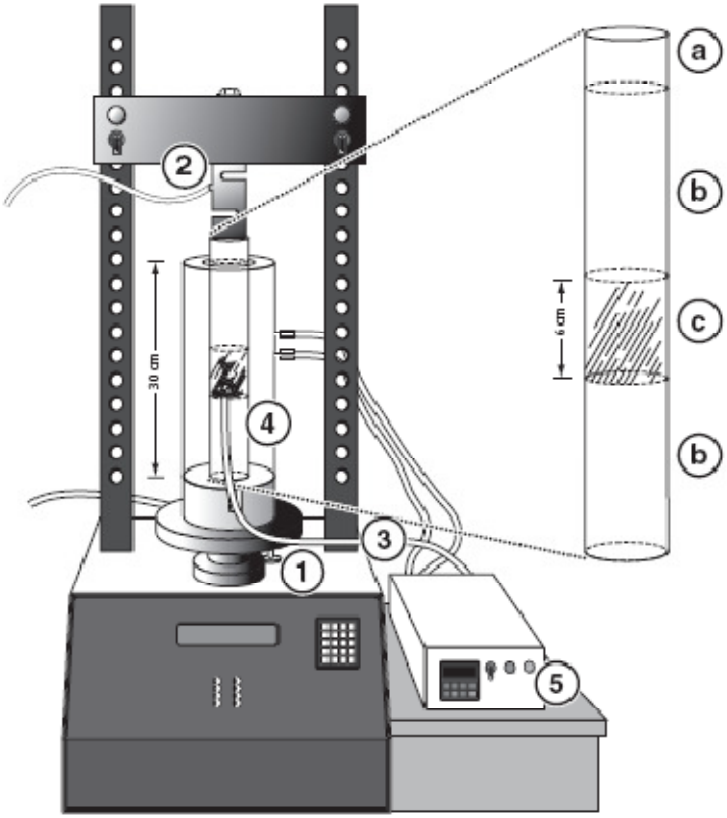

Fig. 3.3. Schematic representation of the Volcanology Deformation Rig (VDR). Base unit is a Geocomp Corporation Load Trac II load frame with LVDT displacement transducer (1), and load cell with an 1136 kg limit (2). Basic load frame is modified for high-T experiments by adding thermocouple (3), fiber-insulated furnace (4), and temperature controller (5). The sample assembly comprises a steel spacer (a) attached to the load cell and two high temperature ceramic pistons (b) located above and below the sample (c) (from Quane et al., 2004).

Measurements on Monte Nuovo trachytic samples were performed using a volcanology deformation rig (VDR) at UBC (Vancouver) and RomaTre University (Rome) (Fig. 3.3). The press, which has been previously described by Quane et al. (2004), is constituted by a LoadTrac II loadframe manufactured by Geocomp Corporation. The unit performs both constant displacement rate and constant load tests. Displacement is achieved by controlling the position of the bottom

platen using an electronic stepper motor with a displacement speed range from 5×10^{-6} to 2.5×10^{-2} cm/s and measured using a built-in linear variable differential transformer (LVDT) displacement transducer with a 7.6 cm travel range and 0.00013 cm resolution. Load is measured using an S-type load cell attached to a fixed crossarm.

Samples can be loaded at rates from zero to 1.9 kg/s, and the maximum attainable load is 1136 kg with 0.086 kg resolution. High temperatures are attained by a Zircar-type FIH fiber insulated heater tube furnace. The furnace has helically wound, Fe-Cr-Al alloy resistance wire elements embedded in a rigid body of high-temperaturerefractory fiber, is 30.5 cm long, and has inner and outer diameters of 7.6 and 15.25 cm, respectively. It is seated on the steel base and surrounds the lower piston, the sample and most of the upper piston. The furnace generates temperatures up to 1100 °C. A K-type thermocouple is used to monitor and control temperature during the experiment.
The press was calibrated on solid glass cores (10 × 25 mm) of NIST (NBS) standard reference material (SRM) 717a (borosilicate glass) under constant load and dry conditions at temperatures (550–600 °C; see Robert et al., 2008). The resulting experimental accuracy corresponds to 0.2 log units (Robert et al. 2008).

Using the parallel plate technique, the shear viscosity of the cores is computed for a given applied load (F; N), sample volume (V; m3), sample length at time t (L; m), and rate of shortening (∂L/∂t; m/s) using the "no-slip" (Eq. 3.4), and "perfect-slip" (Eq. 3.5) models of Gent (1960) (cf. Dingwell et al. 1993):

$$\eta_{ns}(Pa \cdot s) = \frac{2\pi L^5 F}{3V\frac{\partial L}{\partial t}(2\pi L^3 + V)} \tag{3.4}$$

and

$$\eta_{ps}(Pa \cdot s) = \frac{L^2 F}{3V\frac{\partial L}{\partial t}} \tag{3.5}$$

respectively.
The "no slip" equation is used for the case in which the surface area of contact between the melt and the parallel plates remains constant and the cylinder bulges with increasing deformation. The "perfect slip" equation is used for the case in which the surface area between the cylinder and the plate increases with deformation and the cylinder does not bulge.

4. Rheology of Crystal-bearing magmas

In order to evaluate the effect of the presence of crystals on the rheology of melts, experimental measurements were performed on remelted samples derived from natural rocks (Stromboli and Etna) and on synthetic samples produced by melting known amounts of oxides.

High temperature viscosity measurements on crystal bearing melts were performed with a concentric cylinder apparatus for both natural and synthetic materials.

On remelted natural samples, a continuous measurement of viscosity was performed during isothermal crystallization experiments (section 4.1).

For the synthetic material, the samples were periodically removed from the furnace and a known discrete amount of corundum crystals was added on the top. The viscosity variation was measured during the sinking of the particles (section 4.2).

At the end of the measurement, the stirring spindle was removed and the samples were taken out from the furnace and allowed to cool in air within the platinum crucible. The post-run products were then drilled and the cylindrical cores (20 mm diameter x 40 mm lenght) were sliced at surfaces parallel and perpendicular to the rotational axis, to subsequent chemical and textural analyses.

4.1. High temperature Rheology of Crystal-bearing Magmas from Stromboli and Etna

4.1.1. Sample Selection

The viscosity measurements were performed on re-melted samples of natural rocks derived from two active volcanic systems: Stromboli (15th March 2007 paroxysmal eruption) and Etna (1992 lava flow eruption).

In the next section a brief volcanological outline of the two volcanic systems is given, as well as the locations where the samples were collected.

4.1.1.1 Volcanological Outline

- *Stromboli*

In the last 1400-1800 years, the basaltic volcano of Stromboli have shown a steady behavior (Rosi et al. 2000), characterized by the persistence of Strombolian explosive activity and the continuous streaming of gas from the summit craters.

The "normal activity" (Barberi et al. 1993) consists of intermittent mild explosions (10-20 min period), which throw in the atmosphere a small amount of liquid and solid materials (scoriaceous bombs, lapilli and ash) up to 200 m above the craters. Periodically, the normal activity is interrupted by erupting crises consisting in lava flow emissions, that can be associated or not to more violent explosions (paroxysm).

The effusive eruptions can happen by overflowing from the active craters or from vents opened some hundreds of meters below the craters, in the Sciara del Fuoco volcano-tectonic depression, which behaves as a morphological constrain to the flow (Barberi et al., 1993).

The energy of paroxysmal eruptions throws the erupted material, consisting in pomiceous and scoriaceous bombs, lapilli and ash, from several hundreds to few kilometers above the craters (Barberi et al., 1993; Landi et al., 2009).

Two different types of magma have been recognized feeding the present-day activity of Stromboli (Rosi et al., 2000; Métrich et al., 2001; Francalanci et al., 2004; Landi et al., 2009). Despite a similar bulk composition, ranging from HK- to shoshonitic basalt, they show strong differences in terms of texture and matrix glass composition.

Highly porphyritic (HP; Landi et al., 2009) degassed shoshonitic basalt is erupted either as dense scoriae or lava flows during normal activity and effusive episodes. It contains about 50% phenocrysts, including, on average, 33 vol.% plagioclase An_{60-90}, 12 vol.% clinopyroxene Mg#=0.73-0.91 and 5% vol.% olivine Fo_{70-73}.

A nearly aphyric volatile-rich high-K basalt (low porphyritic, LP; Landi et al. 2009) is instead erupted as pomiceous material, only during the paroxysmal events.

In contrast, a nearly aphyric volatile-rich high-K basalt (low porphyritic, LP; Landi et al., 2009) is erupted as pumiceous material, exclusively during paroxysmal events.

The HP magma, which feeds the normal activity, resides in the upper part of the volcano. It is continuously refilled by deeper hot volatile-rich LP magma batches, which periodically intrude the shallow reservoir, crystallizing by decompression and volatile loss at low pressure (Métrich et al., 2001; Francalanci et al., 2005). Evidence of continuous mixing between LP and the HP magmas

have been observed in textural, mineralogical, chemical and isotopic studies (Francalanci et al., 1999, 2004, 2005; Landi et al., 2004, 2006, 2008; Armienti et al., 2007; Fornaciai et al., 2009). According to this model, the steady state behavior of the plumbing system is a consequence of the balance between magma refilling and magma expulsion.

The present study has been carried out on a pomiceous sample emitted during the 15th March 2007 paroxysmal eruption, collected few months after the explosion on Pizzo Sopra la Fossa site (Fig. 4.1).

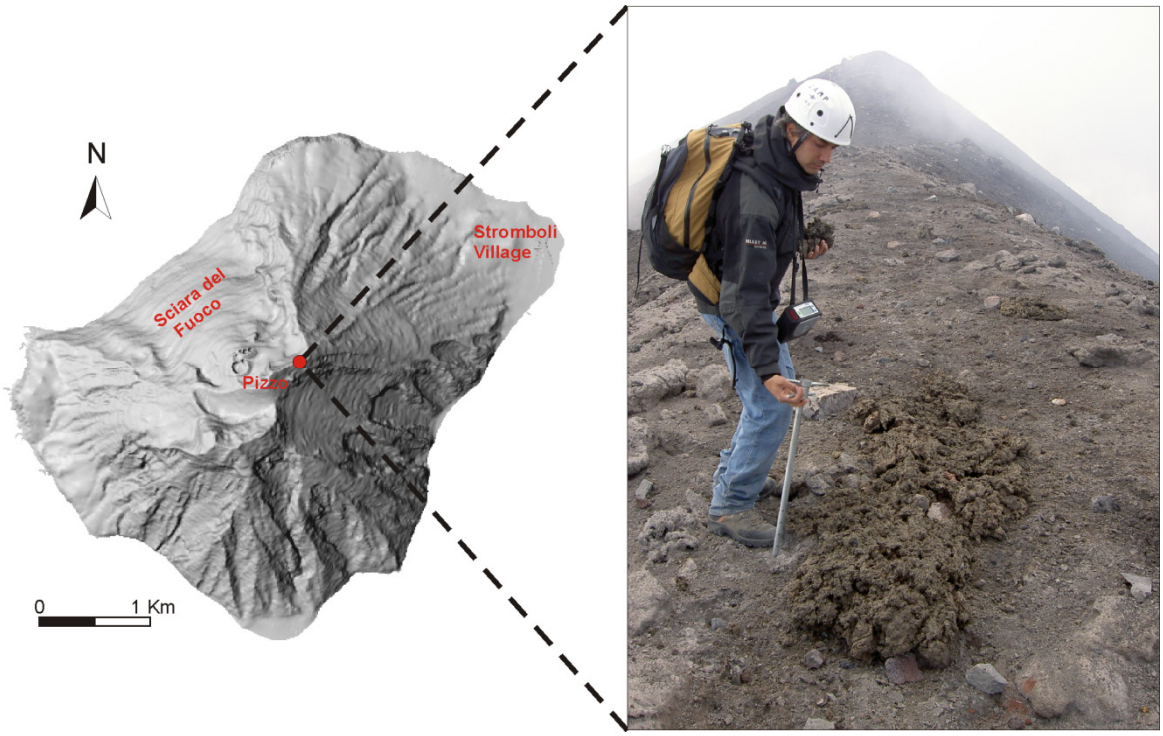

Fig. 4.1. Map of Stromboli island and sampling location (red circle) of the golden pumice from the 15th March 2007 paroxysmal eruption, used for viscosity measurements in the present study.

The explosion, generated by the rapid ascent of volatile-rich LP magma, occured after 16 days of HP lava emission and produced a plume which deposited ash and pomiceous lapilli/bombs. The pumices are nearly aphyric (<5% crystals), with microphenocryst of clinopyroxene (Fs_{5-8}, Wo_{45-48}) and olivine (Fo_{82-91}) in a HK-basaltic glassy matrix. In terms of bulk rock composition, they belong to the high-K calc-alkaline suite and they have similar composition characteristics of the pumices from the previous paroxysm on the 5th April 2003 (Landi et al., 2009; Fig. 4.2).

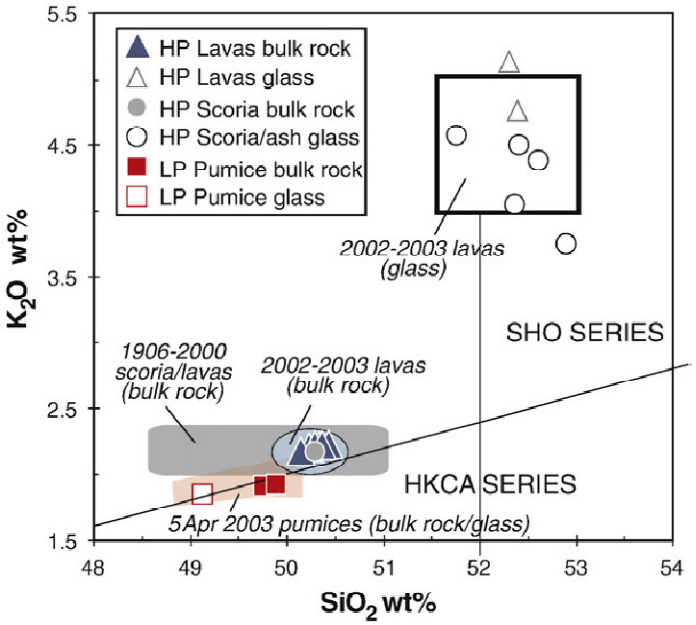

Fig. 4.2. K_2O vs. SiO_2 classification diagram (Peccerillo and Taylor, 1976) for products emitted during the 2007 eruptive crisis. Bulk rock and glass matrix compositions of lavas (triangles) and scoriae (circles) are similar and belong to the shoshonitic series (HP magma). Pumices from the 15th March 2007 paroxysm (squares) show a narrower compositional range between bulk rock and matrix and fall in the HK Calc-Alkaline field (LP magma). The ranges of compositions belonging to the 2002-2003 eruption (Landi et al., 2006; Métrich et al., 2005; Francalanci et al., 2008) and to 1906-2000 scoriae and lavas (Landi et al., 2006) are also plotted for comparison (from Landi et al., 2009).

- *Etna*

Volcanism in the Mount Etna area began at about 500 ka, when both submarine and subaerial tholeiitic lavas were erupted in the "Pre-etnean Gulf"(Condomines et al., 1982; Gillot et al., 1994; Armienti et al., 2004). During its eruptive history, resulting in the building of a complex of several composite volcanoes, Mt. Etna showed a continuous shift in composition through time of the primary magma towards alkali olivine basalt (Tanguy et al., 1997). Basaltic and slightly more differentiated trachybasaltic lavas have dominated the whole Etnean eruptive history (Fig. 4.3a), although occasional pulses of differentiation, by extensive low-pressure fractionation, produced trachyandesites and trachytes (Chester et al., 1985; D'Orazio et al., 1997). Trachybasalts are the prevalent volcanic products of Mt. Etna and they generate from a small degree fractionation of mafic phases from the primary basaltic magma at 8-10 kbar (Tanguy et al., 1997).

The most recent acitivity of Mt. Etna (starting since 1971) is characterized by a pronounced increase in the K2O/Na2O ratio which moves the lava composition into the field of potassic trachybasalts since the condition Na2O-2<K2O is satisfied (Clocchiatti et al., 1988; Armienti et al., 1994; Fig. 4.3b).

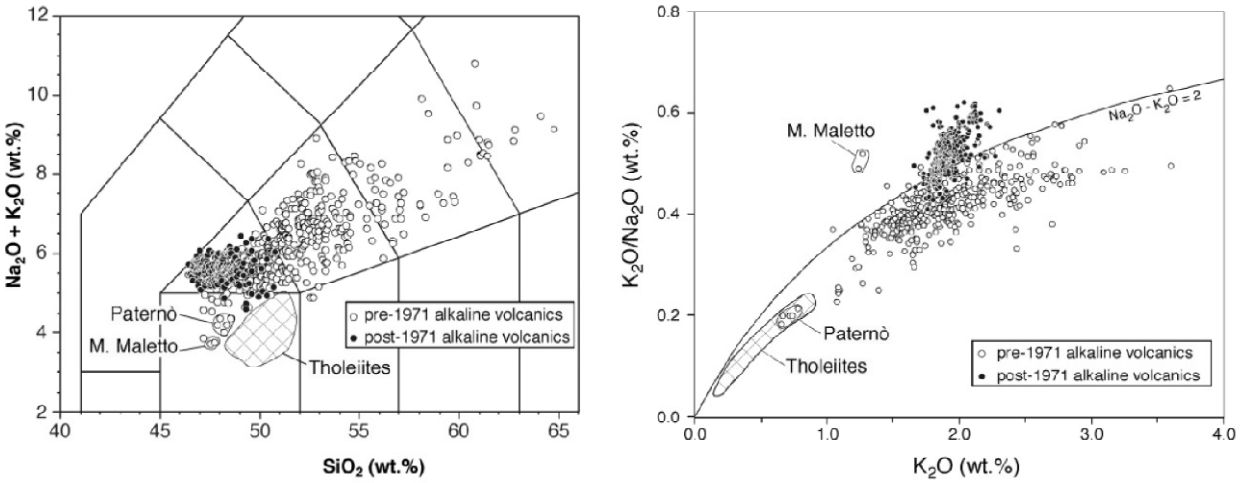

Fig. 4.3. (a) TAS classification diagram for Mt. Etna volcanic (after Le Bas et al., 1986). The composition of the most recent erupted lavas are confined within the trachybasalt field. (b) Potassium enrichment in the post-1971 lavas as shown by the K_2O/Na_2O vs. K_2O diagram. Both (a) and (b) are from Armienti et al. (2002).

The samples used for viscosity measurement in this study is the same studied by Giordano and Dingwell (2003) and was collected from the 1991-1993 eruption from the lava flow field in Val Calanna ca. 6.5 km from the eruptive fissure (Calvari et al., 1994). The 1991-1993 Etna eruption (Fig.4.4) represents one of the most prolonged and volumetrically significant observed at Etna in the last three centuries (Calvari et al., 1994; Armienti et al., 1994).

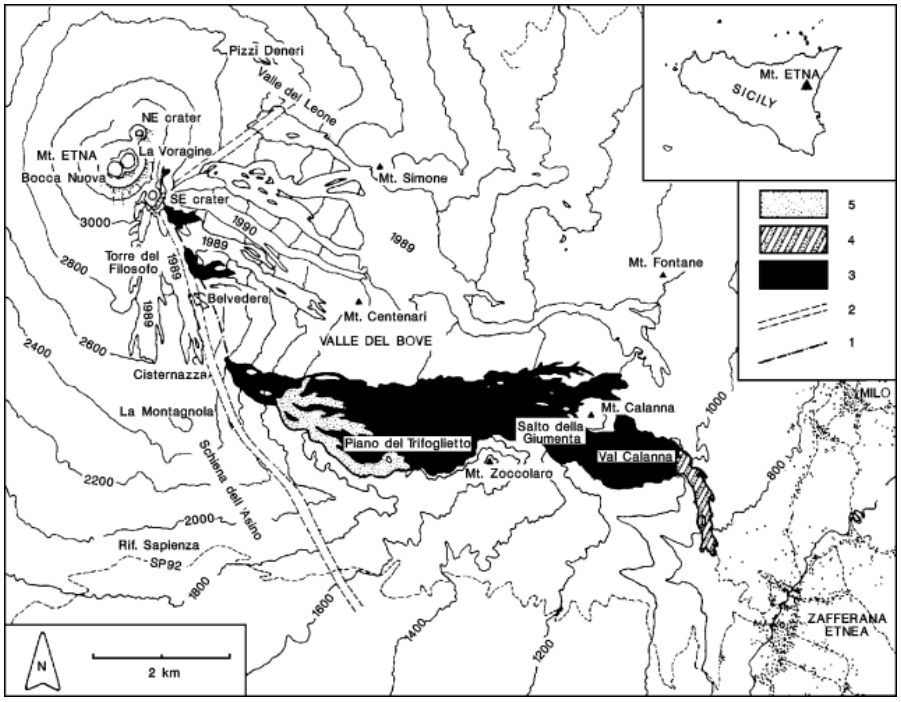

Fig. 4.4. Sketch map of Mt. Etna eastern section showing the lava flow field formed in 1991-1993 eruption (black area; from Calvari et al., 1994).

A detailed study of the petrography of the lavas belonging to this eruption has been provided by Armienti et al. (1994). They observed that most of the analyzed samples show a Porphyritic Index in the range between 30 and 33 vol.% of phenocrysts, although lower values were found for the first two lava flows that spread at the base of South East Crater (~19 vol.%) and higher values were found sporadically in the Valle del Bove flow field (~35 vol.%). The most abundant phase as phenocryst is plagioclase (~17-20 vol.%) followed by olivine and clinopyroxenes (~6-11 and ~2-4 vol.%, respectively). The only exception is represented by the less porphyritic samples from the base of the South East Crater which showed a reversed plagioclase/mafic mineral ratio. All minerals are present also as microlites with variable amounts of glass in the groundmass.

4.1.2. Sample Preparation and Chemical Analyses

The starting glasses used for the viscosity determination were prepared by fusion of the total rock. The fusions were performed in thin-walled platinum crucibles with a $MoSi_2$ furnace at T=1400-1500 °C. After several hours of melting, the samples were removed from the furnace and allowed to cool in air in the Pt crucible.

Tab. 4.1. Electron microprobe analyses of the starting materials (wt%)

	Stromboli HK-basalt	Etna trachybasalt
SiO_2	50.35 (±0.16)	48.16 (±0.23)
TiO_2	0.92 (±0.05)	1.69 (±0.06)
Al_2O_3	17.18 (±0.10)	17.10 (±0.11)
FeO_{tot}	-	-
FeO	1.71 (±0.11)	2.49 (±0.10)
Fe_2O_3	7.04 (±0.12)	8.60 (±0.10)
MnO	0.18 (±0.04)	0.19 (±0.02)
MgO	6.28 (±0.06)	5.38 (±0.08)
CaO	11.64 (±0.16)	10.36 (±0.07)
Na_2O	2.33 (±0.04)	3.69 (±0.05)
K_2O	1.85 (±0.05)	1.91 (±0.03)
P_2O_5	0.53 (±0.07)	0.43 (±0.06)
Fe^{3+}/Fe_{tot}	0.79	0.76
MgO/FeO_{tot}	0.78	0.53
Na_2O/Na_2O+K_2O	0.56	0.66
CaO/Al_2O_3	0.68	0.61
SM[a]	31.41	31.56
NBO/T[b]	0.47	0.45

Compositions are normalized to a total of 100 wt%.
Numbers in brackets correspond to 1σ standard deviation.
[a] Structure Modifiers parameter. On a molar basis (mol%) of oxides, SM is the sum of all structure modifier oxides, as defined by Giordano and Dingwell (2003).
[b] Non-bridging oxygen per tetrehedra on a molar basis (Mysen, 1988).

The anhydrous glass compositions were chemically analyzed by electron microprobe and the iron speciation was determined by titration with a standard solution of potassium permanganate. The results are reported in Tab.4.1.

In the standard TAS classification grid (Le Bas et al., 1986; Fig.4.5) the analyzed samples range in composition from HK-Basalt (Stromboli) to Trachybasalt (Etna).

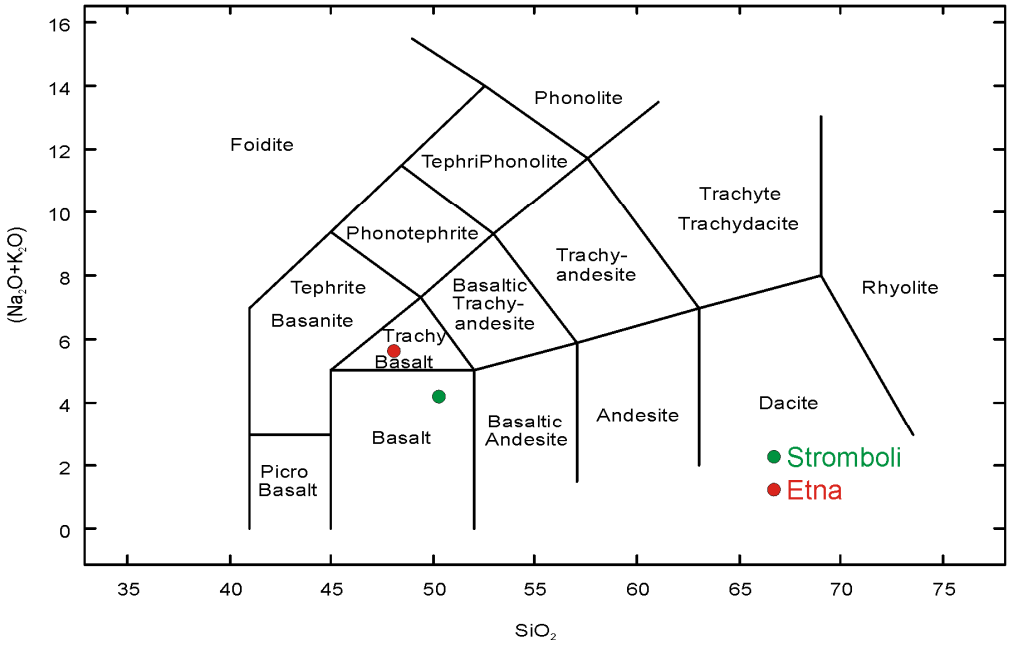

Fig. 4.5. Chemical composition of the investigated products. The chemical range of the samples is given according to the T.A.S. (Total Alkali Silica) diagram (after Le Bas et al., 1986) reporting the values of the total alkali (Na_2O+K_2O) content vs. the SiO_2 (wt%). Table 4.1 reports the chemical compositions as determined by microprobe analyses.

Despite a slight difference in composition (especially in SiO_2 and Na_2O+K_2O wt.%), the two samples display practically identical degree of polymerisation, expressed by the SM parameter (the sum of all the structure modifier oxides in mol%, as calculated by Giordano and Dingwell, 2003), or by the NBO/T parameter (non-bridging oxygen divided by tetrahedrically coordinated cations in mol%, as defined by Mysen, 1988) (Etna: SM=31.56; NBO/T=0.45; Stromboli: SM=31.41; NBO/T=0.47).

4.1.3. Pure Liquid Viscosity Determination

The pure liquid viscosity was measured in steps of decreasing temperature of 25°C/min and one hour equilibration time for each step. Once the required steps were completed the temperature was

increased to the initial value to check if any instrumental drift had occurred. No such drift was observed (see procedures in Dingwell and Virgo, 1988).

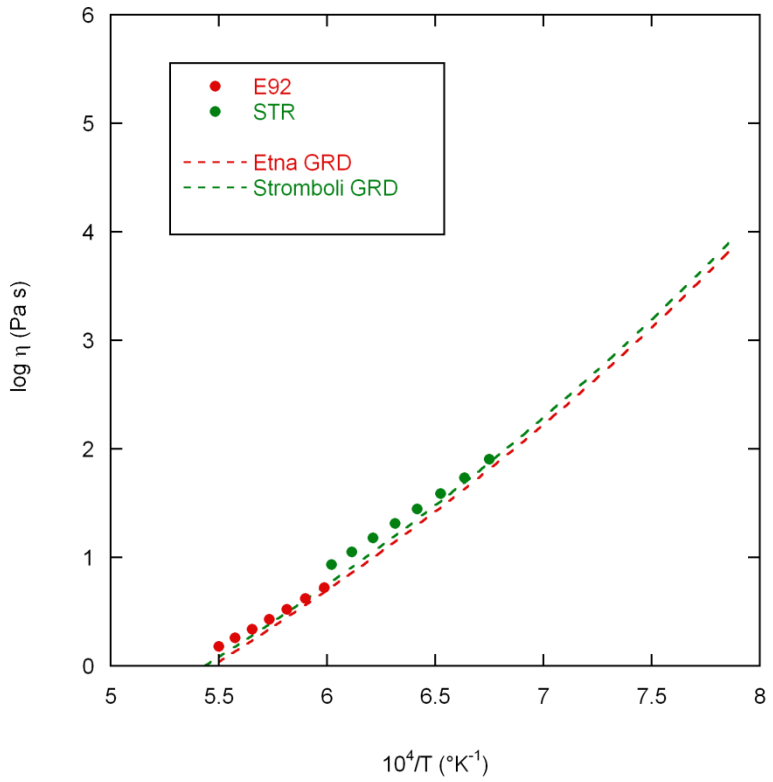

Fig. 4.6. Pure liquid viscosity of the starting materials in log unit (Pa•s) against the reciprocal of temperature (Arrhenian plot). Measured values of Stromboli HK-basalt (STR) are from this study; values of Etna trachybasalt (E92) have been measured by Giordano and Dingwell (2003). Broken lines represent the viscosity predictions for each sample according to GRD model (Giordano et al., 2008).

Tab. 4.2. High-temperature viscosity data of the starting material.

Stromboli basalt		*Etna trachybasalt*	
T(°C)	log η (Pa s)	T(°C)	log η (Pa s)
1387.7	0.93	1544.7	0.18
1362.1	1.05	1520.1	0.26
1336.4	1.18	1495.5	0.34
1310.7	1.31	1470.9	0.43
1285.0	1.45	1446.3	0.52
1259.4	1.59	1421.7	0.62
1233.7	1.74	1397.1	0.72
1208.0	1.90		

Dry viscosity determinations in the above liquidus field for the starting materials are reported in Fig.4.6. In the present study, we measured the high-temperature viscosity on the Stromboli HK-basalt (STR) for T=1210-1390°C, while data for Etna (E92) were measured by Giordano and Dingwell (2003) (Tab.4.2).

Viscosity data show an increase of ca. 1 order of magnitude in the investigated range of temperature (Stromboli: T=1208-1388°C, Etna: T=1397-1545°C), in good agreement with the prediction model "GRD" by Giordano et al. (2008). The studied compositions show similar trends as a consequence of almost identical NBO/T and SM parameters (see Section 4.1.2).

4.1.4. Crystal-bearing Melt Rheology

Prior to initiation of the *subliquidus* experiments, the melt was stirred continuously at 1400 °C, for ca. 5 h to ensure that the crystalline phases of the natural mineral assemblage were fully dissolved. Subsequently, the temperature of the melt was lowered rapidly to that of the measurement dwell temperature and held constant until a stable reading of the viscosity value was achieved. The initial rotational speed was set to ω=20 rpm for experiments carried out on Stromboli material and to ω=2.5 rpm for Etna samples (translating into a maximum strain rate of ca. 4.3 s^{-1} and ca. 0.5 s^{-1}). The software controlling the spindle speed automatically halves the speed when maximum torque is reached (due to crystallization). The viscosity reading typically achieved a steady value after 10^4-10^5 s (interpreted here as equilibrium in the crystallization process at that temperature). Once that equilibrium conditions were reached, the rotational speed was varied to evaluate its effect on the rheological response of our suspension. The rotational speed was allowed to decrease stepwise and subsequently increase to its original value and was left in the new position for a long enough time (transient) to obtain a new stable reading (on the order of tens of minutes). No drift in the viscosity reading due to the variation of rotational speed was observed in any of our experiments allowing us to conclude that our measurements were highly reproducible. Before the samples were removed from the furnace we checked that no residual torque, indicative of yield strength, was present at the no-stir condition (ω = 0 rpm). At the end of each experiment, the stirring spindle was removed and the melt attached to the spindle was quenched in water. A comparison between the materials quenched in water and in air indicated that no appreciable crystallization took place during cooling in the crucible. The post-run products were then drilled and the cylindrical cores (20 mm diameter x 40 mm length) were sectioned at surfaces parallel and perpendicular to the rotational axis (Fig. 4.7), to permit subsequent chemical and textural analyses.

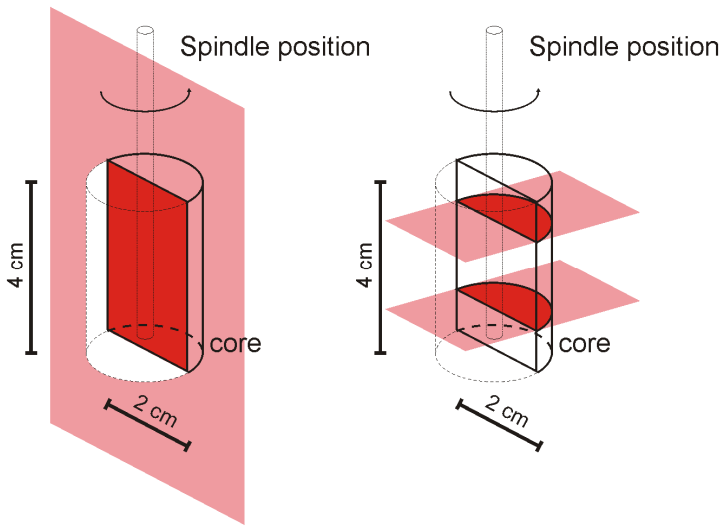

Fig. 4.7. Thin section orientation: one longitudinal (left) parallel to the spindle direction and two transversal (right) at 1 cm distance from the top and from the bottom of the core respectively.

4.1.5. Results

The temporal evolution of apparent viscosity readings during the isothermal crystallization experiments are reported in Fig. 4.8. We can observe a non linear viscosity increase with time for all of the analyzed curves. The curves are constituted by successive series of ramps and plateaus. The first early stage (<0.1 x 10^5 s) ramp, likely to be attributed to the thermal relaxation of the melt to the new temperature conditions (from T=1400°C to the temperature of the measurement), is commonly followed by a plateau, whose length typically exhibits an overall decrease with increasing undercooling. After this stage, an extensive viscosity increase is observed followed by a secondary plateau and, in one case, additional plateaus and ramps. Rotational speeds during crystallization are reported in Fig. 4.8. Measurements were terminated when a stable value of apparent viscosity was achieved in a time range between 0.7-4.8 x 10^5 s (from ca. 1 day to one week). Table 4.3 reports the shear rate values at the final stable reading stage ($\dot{\gamma}_f$) together with those corresponding to the maximum values ($\dot{\gamma}_i$) as observed at the beginning of each measurement.

On Stromboli HK-basalt, seven isothermal crystallization experiments were performed in the temperature range between T=1187.5-1151.5°C (Fig. 4.8a). The experiment run at the lowest temperature (T=1151°C) showed a rapid increase in apparent viscosity and the reading reached the instrumental limit after ca. 3x10^4 s. For this reason, the measurement automatically stopped and it could not be used in the present study, as no sample was collected. All of the other experiments

reached stable values of viscosity in a time span between 0.7 and 1 x 10^5s. At the end of the measurement the viscosity increased by a factor ranging from 2 to 37 times; as an inverse function of temperature. The largest increase was observed at T=1156.7°C. The final viscosity ranged between 2.3 and 3.7 log Pa s.

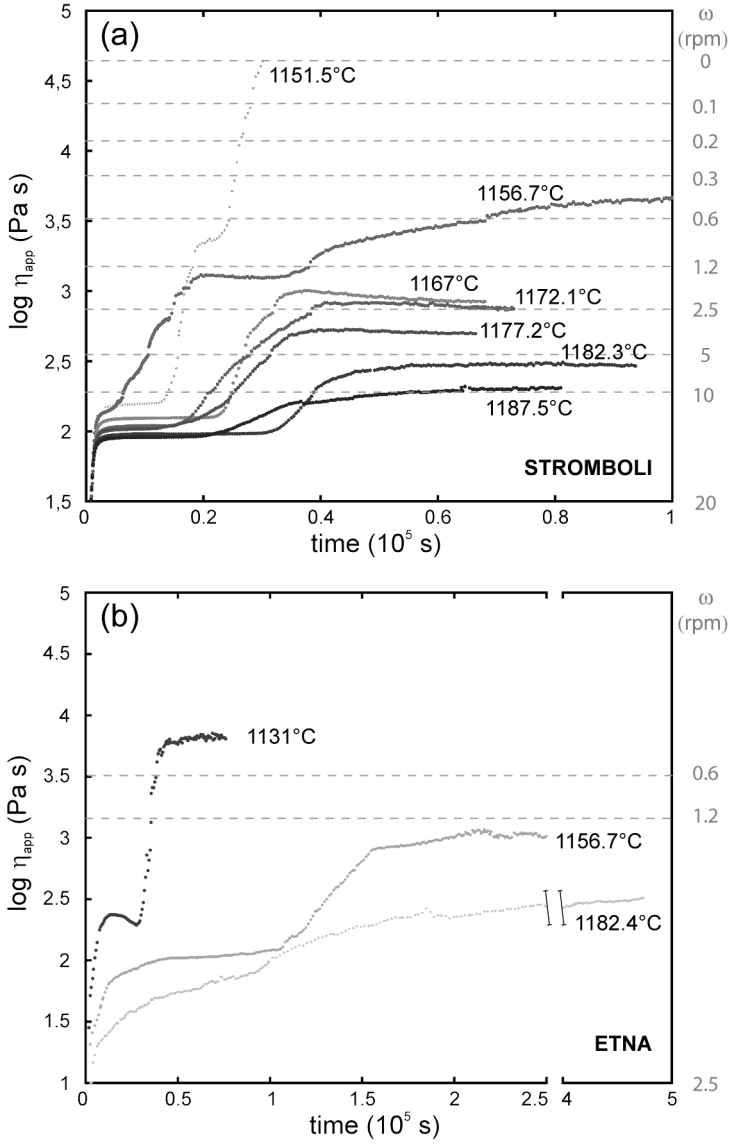

Fig. 4.8. Time variation of viscosity for Stromboli HK-basalt (a) and Etna trachybasalt (b) at *subliquidus* conditions. For a clearer view, the time axis on the (b) graph is broken between 2.5-4 x 10^5 s. The right Y scale refers to the values of rotational speed adopted (expression of deformation rates). The rotational speed varies in a step-wise fashion, halving each time the maximum viscosity (corresponding to the maximum torque allowed) for each speed is reached.

Fig. 4.8b displays the results of three isothermal crystallization experiments performed on Etna trachybasalt. Viscosity reached stable values of 2.50, 3.07, and 3.79 log Pa s, at T=1182.4°C, 1156.7°C, and 1131°C, respectively.

Table 4.3. Results of subliquidus viscosity measurements

Sample	*Stromboli*						*Etna*		
Run	SGP7	SGP5	SGP4	SGP1	SGP3	SGP6	E92-1	E92-2	E92-3
T(°C)	1187.5	1182.3	1177.2	1172.1	1167.0	1156.7	1182.4	1156.7	1131
$\dot{\gamma}_i$(s^{-1})	4.26	4.26	4.26	4.26	4.26	4.26	0.53	0.53	0.53
$\dot{\gamma}_f$(s^{-1})	2.18	2.24	1.13	0.56	0.58	0.14	0.54	0.56	0.14
log η_0 (Pa s) [a]	2.28	2.33	2.38	2.41	2.44	2.54	2.61	2.70	2.91
η_{app} (Pa s) -a	263 (2.18)	364 (2.24)	602 (1.13)	901 (0.56)	964 (0.58)	5180 (0.14)	355 (1.09)	1127 (0.56)	6264 (0.14)
η_{app} (Pa s) -b	267 (1.09)	377 (1.12)	628 (0.56)	935 (0.27)	1032 (0.28)	5503 (0.07)	361 (0.54)	1172 (0.27)	6699 (0.07)
η_{app} (Pa s) -c	271 (0.54)	391 (0.56)	657 (0.27)	970 (0.13)	1099 (0.14)	5702 (0.05)	366 (0.26)	1216 (0.13)	6967 (0.05)
η_{app} (Pa s) -d		406 (0.27)				6058 (0.02)		1262 (0.07)	
K (Pa s)	268	379	606	874	918	4360	356	1092	5181
n	0.98	0.95	0.94	0.95	0.91	0.91	0.98	0.95	0.90
R^2	0.999	0.999	0.999	0.999	0.998	0.998	0.999	0.999	0.999
K_R (K/η_0)	1.42	1.78	2.50	3.40	3.35	12.63	0.88	2.20	6.40
ϕ_{Glass} (vol%)	0.890	0.875	0.861	0.863	0.821	0.728	0.934	0.842	0.794
$\phi_{Plagioclase}$ (vol%)	0.107	0.122	0.134	0.130	0.172	0.229	0.057	0.133	0.176
$\phi_{Pyroxene}$ (vol%)	-	-	-	-	-	0.027	-	-	0.043
ϕ_{Spinel} (vol%)	0.003	0.003	0.005	0.006	0.007	0.016	0.009	0.025	0.020
$\bar{R}$ [b]	6.13	6.98	6.91	6.85	6.90	7.25	5.57	6.15	6.57
ϕ_m [c]	0.4010	0.3801	0.3817	0.3831	0.3820	0.3741	0.4160	0.4004	0.3900

Note: Number in brackets correspond to the applied strain rate in s^{-1}.
(a) viscosities of residual melts (η_0) have been calculated using GRD model by Giordano et al. (2008) with a correction factor of +0.2 log units (see text).
(b) calculated via Equation (18).
(c) calculated after Mueller et al. (2010).

The effect of varying the deformation rate of the equilibrium suspensions is reported in Fig. 4.9; a slight decrease in viscosity with increasing shear rate has been observed for low temperature experiments for both Etna and Stromboli magmas. The largest decrease occurs at the lowest investigated temperature for both Stromboli and Etna where the apparent viscosities show a decrease from 6058 to 5180 Pa s (from 3.78 to 3.71 on log scale) with increasing shear rates from 0.02 to 0.14 s^{-1} and from 6967 to 6264 Pa s (from 3.84 to 3.80 on log scale) with increasing shear rates from 0.05 to 0.14 s^{-1} respectively.

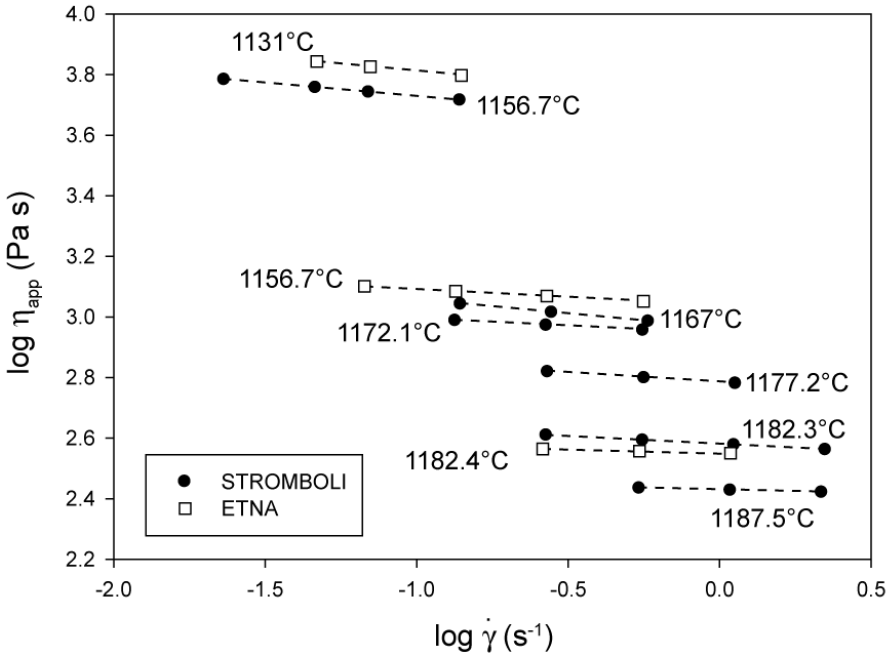

Fig. 4.9. Variation of the logarithm of the apparent viscosity with respect to the logarithm of strain rate.

4.1.6. Post-Run Phase Chemistry

The chemical compositions of the crystalline phases and the melts were analyzed at the CNR – Istituto di Geologia Ambientale e Geoingegneria in Rome, using a Cameca SX50 electron microprobe equipped with 5 WDS spectrometers and EDS Link eXL system, under analytical conditions of 15 kV accelerating voltage, 15 nA beam current and 10 μm beam diameter to reduce K and Na volatilization. To better investigate possible chemistry variations within each sample, analyses were performed systematically along profiles orthogonal to the spindle direction).

4.1.6.1 Melt Chemistry

The analyses of the chemical compositions of the residual melts are reported in Tab. 4.4. For Strombolian magmas, with decreasing temperature, the crystallization process generates liquid compositions showing increasing SiO_2, MgO and K_2O, and decreasing Al_2O_3 and CaO content. The concentration of FeO_{tot}, TiO_2 and K_2O remains approximately constant for all samples. (Fig. 4.11). The experiments run at the lower temperatures (SGP3 and SGP6) show some heterogeneity in chemical composition as demonstrated by their higher standard deviations in Tab. 4.4. Such variability is related to inhomogeneous spatial distribution of the crystalline phases in the samples (see below). This effect is most evident in the sample SGP6 (at the lowest investigated temperature) where the chemical variation of the residual melt results from an inhomogeneous spatial distribution of clinopyroxene and iron oxides, both of which are only present near the stirring spindle (Fig. 4.12a).

In the SGP3 experiments clinopyroxene is absent. The heterogeneity, evident in a SiO_2-FeO_{tot} variation diagram (Fig. 4.12b) is the result of an heterogeneous distribution of iron oxides in the samples. For lower temperature runs (SGP3 and SGP6) two different domains are recognizable as a function of the distance from the spindle: a silica-rich iron-poor zone in the inner part of the core (close to the spindle) and a silica-poor iron-rich zone toward the wall of the core (far from the spindle).

The same kinds of variations have been observed on the low temperature runs of products from Etna samples (E92-2 and E92-3), but are absent in the sample run at T=1182.4 (E92-1). Decreasing temperature causes slight decreases in SiO_2, Al_2O_3 and CaO, whereas MgO, TiO_2 and K_2O display slight enrichment trends. (Fig. 4.13).

Table 4.4. Chemical composition of starting materials and residual melts

Sample	*Stromboli*														*Etna*							
Run	Starting material		SGP7		SGP5		SGP4		SGP1		SGP3		SGP6		Starting material		E92-1		E92-2		E92-3	
T(°C)			1187.5		1182.3		1177.2		1172.1		1167.0		1156.7				1182.4		1156.7		1131	
SiO_2	50.35	(0.16)	51.13	(0.12)	51.26	(0.13)	51.35	(0.19)	51.36	(0.21)	51.29	(0.40)	51.42	(0.62)	48.16	(0.23)	51.09	(0.13)	50.70	(0.49)	50.55	(0.35)
TiO_2	0.92	(0.05)	1.03	(0.03)	1.03	(0.05)	1.05	(0.04)	1.07	(0.04)	1.08	(0.05)	1.15	(0.05)	1.69	(0.06)	1.82	(0.04)	1.78	(0.05)	1.93	(0.04)
Al_2O_3	17.18	(0.10)	15.59	(0.11)	15.39	(0.12)	15.29	(0.10)	15.09	(0.13)	14.91	(0.11)	14.49	(0.17)	17.10	(0.11)	16.34	(0.08)	15.73	(0.16)	15.28	(0.30)
FeO_{tot}			8.47	(0.11)	8.44	(0.10)	8.41	(0.16)	8.41	(0.17)	8.59	(0.42)	8.65	(0.56)			8.01	(0.11)	8.56	(0.47)	8.82	(0.28)
FeO	1.71	(0.11)													2.49	(0.10)						
Fe_2O_3	7.04	(0.12)													8.60	(0.10)						
MnO	0.18	(0.04)	0.2	(0.03)	0.21	(0.03)	0.19	(0.04)	0.2	(0.05)	0.2	(0.04)	0.23	(0.04)	0.19	(0.02)	0.22	(0.03)	0.21	(0.04)	0.22	(0.04)
MgO	6.28	(0.06)	7.15	(0.12)	7.25	(0.07)	7.27	(0.12)	7.47	(0.09)	7.58	(0.10)	7.77	(0.12)	5.38	(0.08)	5.43	(0.08)	6.02	(0.16)	6.08	(0.23)
CaO	11.64	(0.16)	11.43	(0.12)	11.35	(0.13)	11.35	(0.10)	11.39	(0.11)	11.26	(0.08)	11.12	(0.16)	10.36	(0.07)	10.36	(0.13)	10.17	(0.20)	10.05	(0.31)
Na_2O	2.33	(0.04)	2.34	(0.06)	2.37	(0.07)	2.34	(0.06)	2.35	(0.07)	2.33	(0.05)	2.3	(0.05)	3.69	(0.05)	4.07	(0.08)	3.98	(0.04)	4.09	(0.16)
K_2O	1.85	(0.05)	2.05	(0.04)	2.09	(0.05)	2.12	(0.05)	2.13	(0.06)	2.19	(0.06)	2.22	(0.08)	1.91	(0.03)	2.05	(0.04)	2.20	(0.03)	2.27	(0.18)
P_2O_5	0.53	(0.07)	0.6	(0.05)	0.6	(0.04)	0.61	(0.06)	0.53	(0.09)	0.55	(0.05)	0.65	(0.06)	0.43	(0.06)	0.61	(0.04)	0.64	(0.04)	0.71	(0.06)
Total	99.17		99.27		99.22		99.50		98.61		99.21		99.34		99.41		98.96		99.14		99.36	

Note: Oxyde compositions are normalized to a total of 100 wt%. Number in brackets correspond to 1σ standard deviation. Measured totals are also reported.

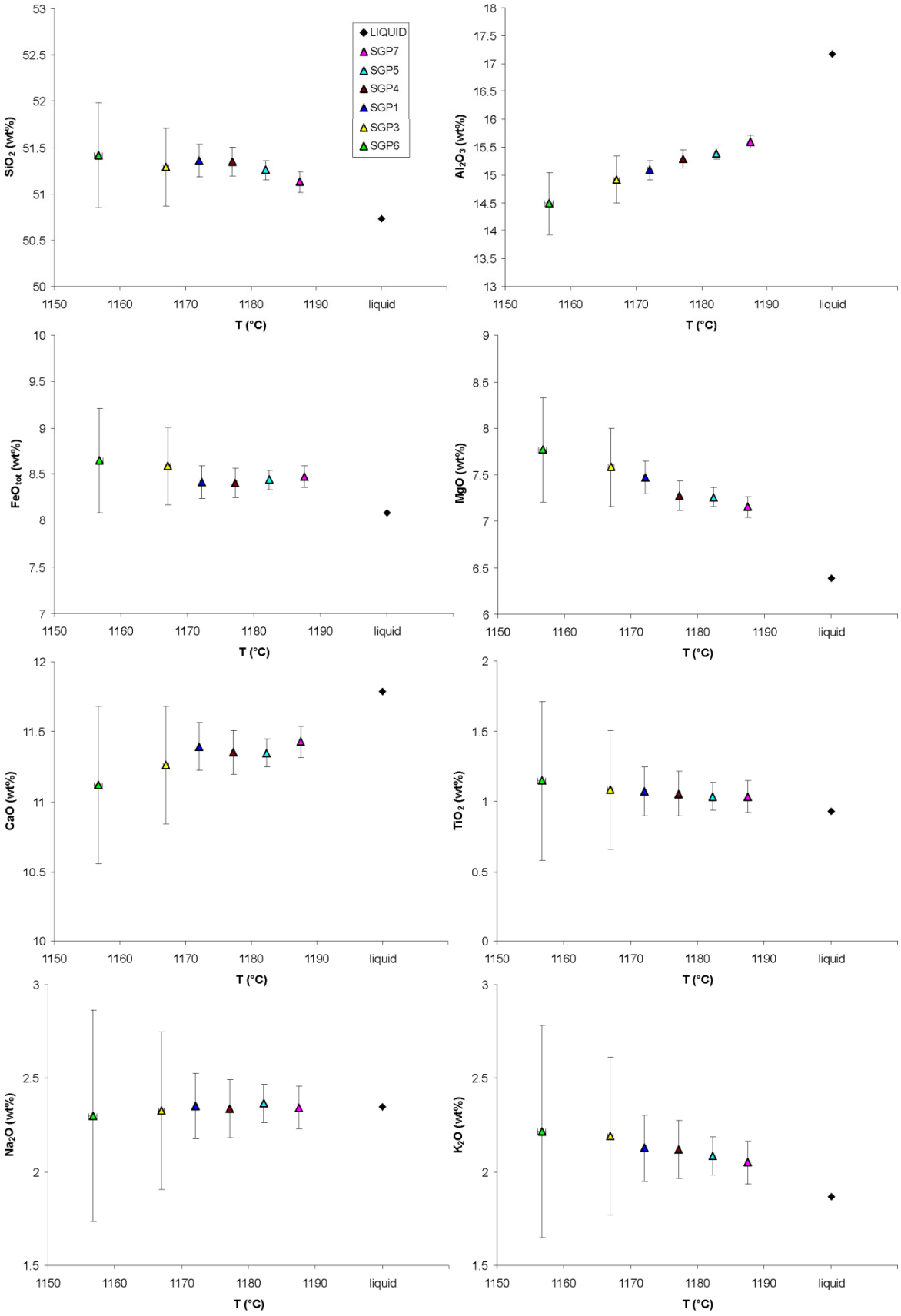

Fig. 4.11. Chemical evolution of the suspending liquid from Stromboli as a function of experimental temperature. The plotted error bar is relative to ±1σ (Tab.1). The composition of the starting material (liquid) is plotted as reference.

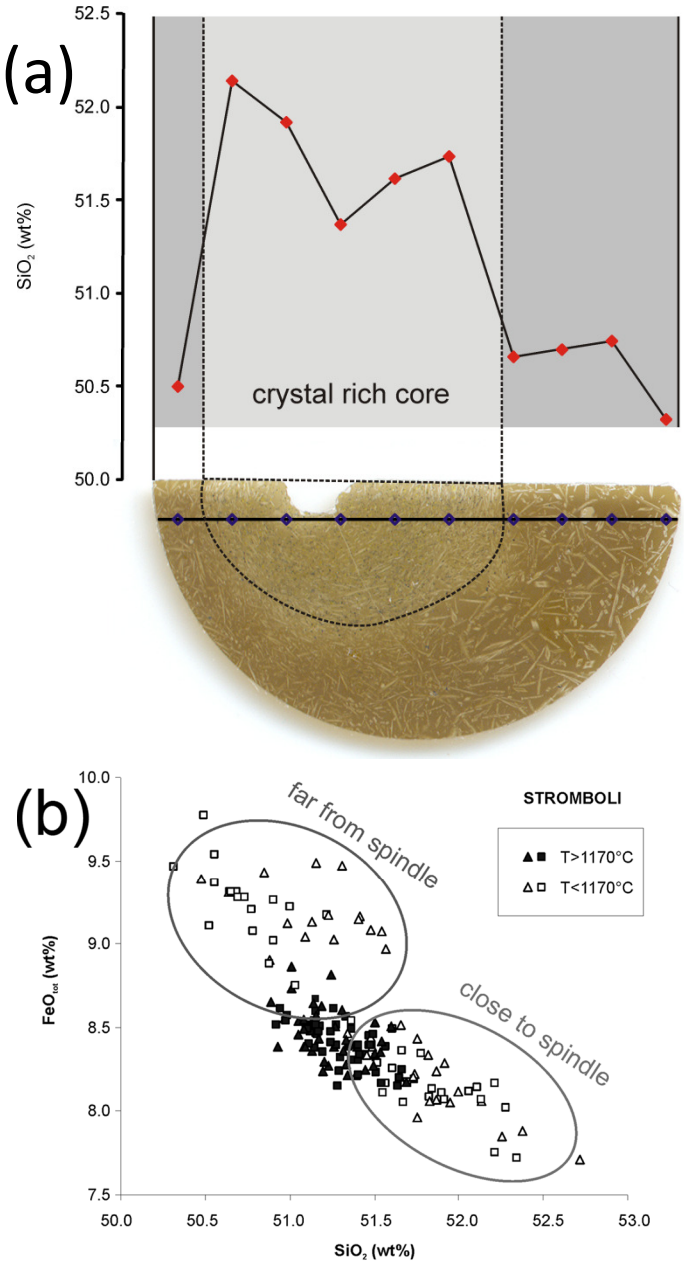

Fig. 4.12. (a) (a) Chemical and textural heterogeneity observed on the lowest temperature measurement from Stromboli (SGP6). The apparent position of the spindle, which appears to be offset, is an artifact due to the drilling procedure, not to a non-centered position of the spindle during the measurement. Black dots represent the spots of the microprobe analyses. The variation in SiO_2 along the sample is also reported. (b) FeO_{tot} vs. SiO_2 variation diagram on Stromboli run products. Heterogeneities in chemical composition increase in the low temperature experiments (run SGP3 and SGP6, open symbols), where two different domains were recognized as a function of the distance from the spindle.

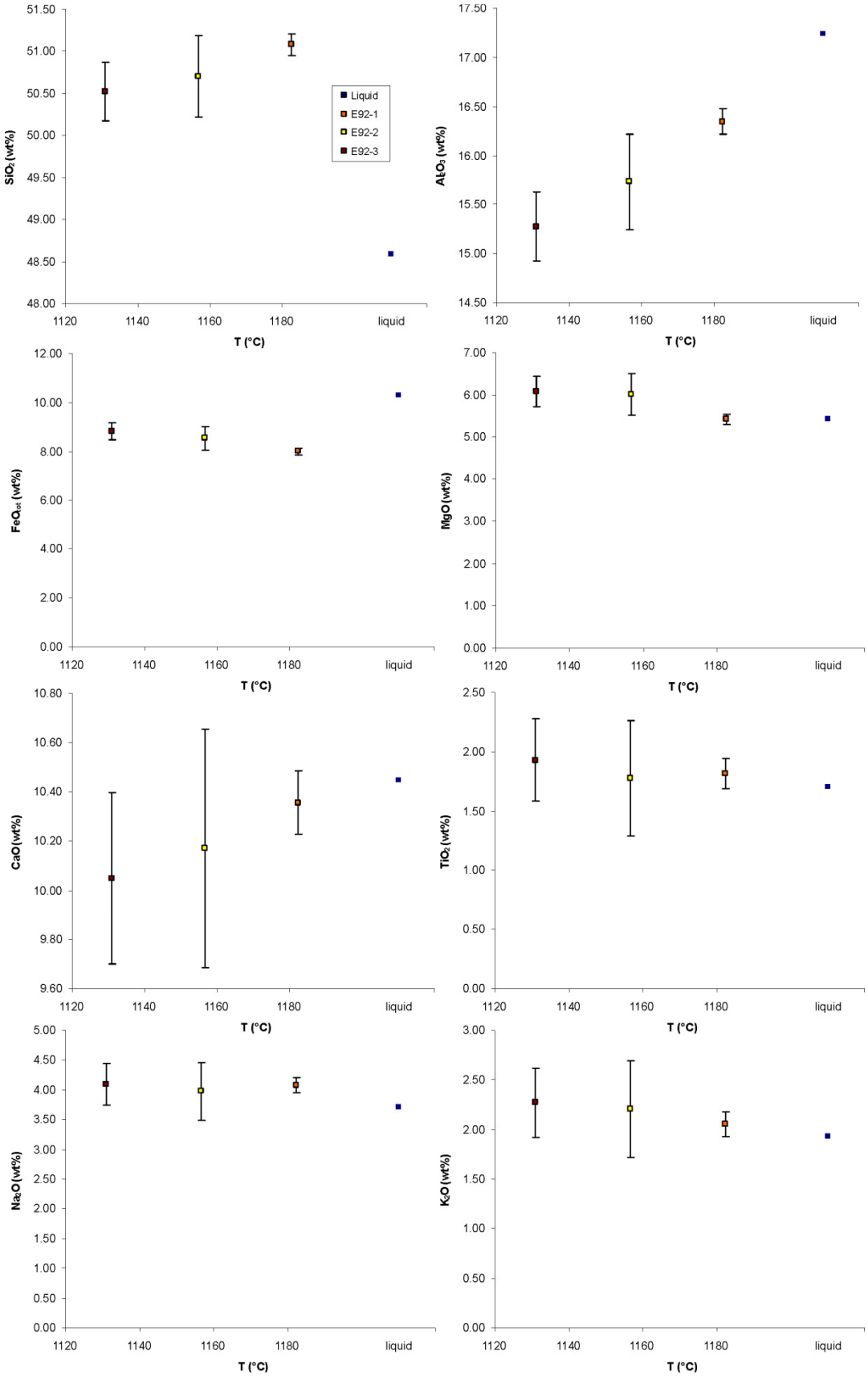

Fig. 4.13. Chemical evolution of the suspending liquid from Etna as a function of experimental temperature. The composition of the starting material (liquid) is plotted as reference.

4.1.6.2 Crystal Chemistry

Spinel and plagioclase are the high-T mineralogical assemblage. Plagioclase composition ranges between An_{79-72} for Stromboli and between An_{72-64} for Etna (Fig. 4.14a), well within the range of natural magmas. The anorthite content is found to be a direct function of temperature. Low temperature experiments also exhibit the formation of augite, occurring only at 1157°C on Stromboli (SGP6) and at 1131°C (E92-3) on Etna, the lowest temperature at which measurements could be performed within the allowed viscosity range (Fig. 4.14b). Olivine was not observed, despite its presence in natural samples of both Stromboli and Etna materials. The absence of olivine can be explained by the high oxygen fugacity conditions adopted in the present study, which favor the crystallization of the spinel phase.

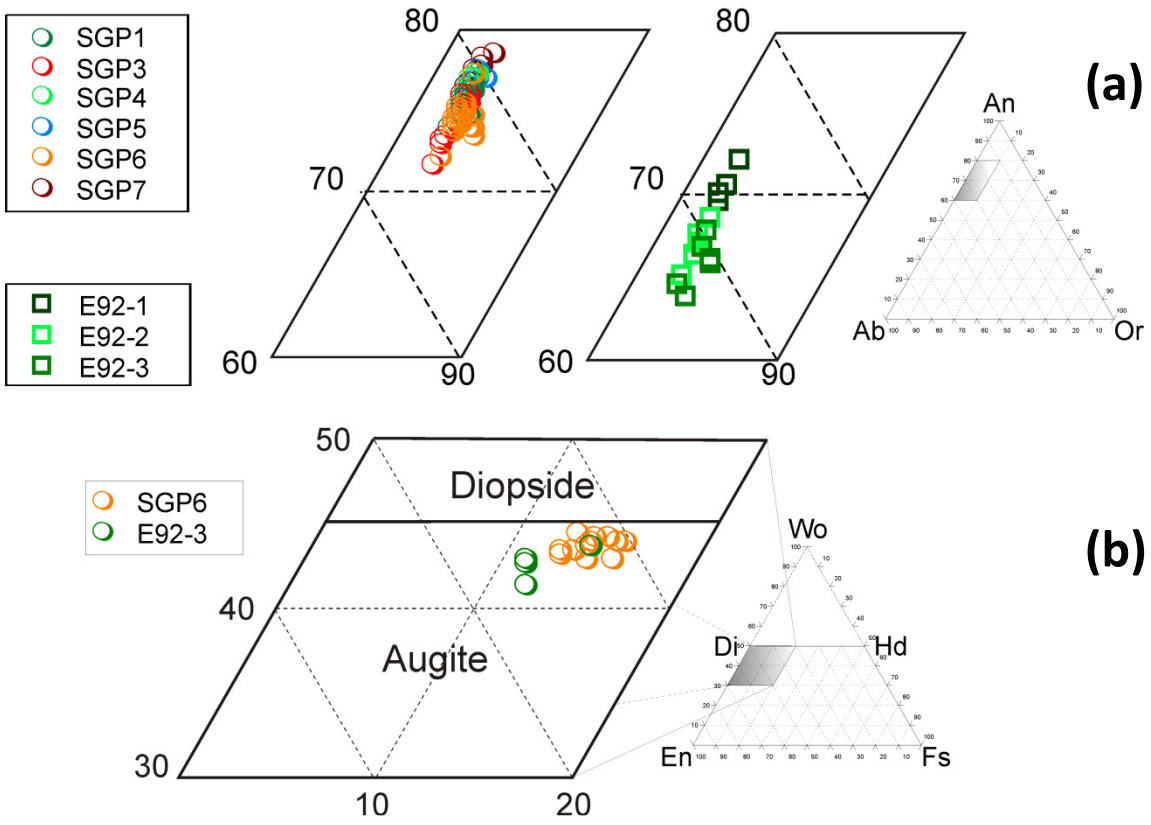

Fig 4.14. Classification diagrams for (a) plagioclase derived from crystallization experiments on Stromboli, Etna, and (b) clinopyroxene, crystallized during the lowest temperature experiments run on Stromboli (SGP6, T=1156.7°C) and Etna (E92-3, T=1131°C) samples.

4.1.7. Textural Analysis

The post-run products were drilled and cylindrical cores of ca. 4 cm length and 2 cm diameter were obtained. Thin sections were then prepared for each sample with orientation parallel and orthogonal respect to the spindle position (see Fig. 4.7).

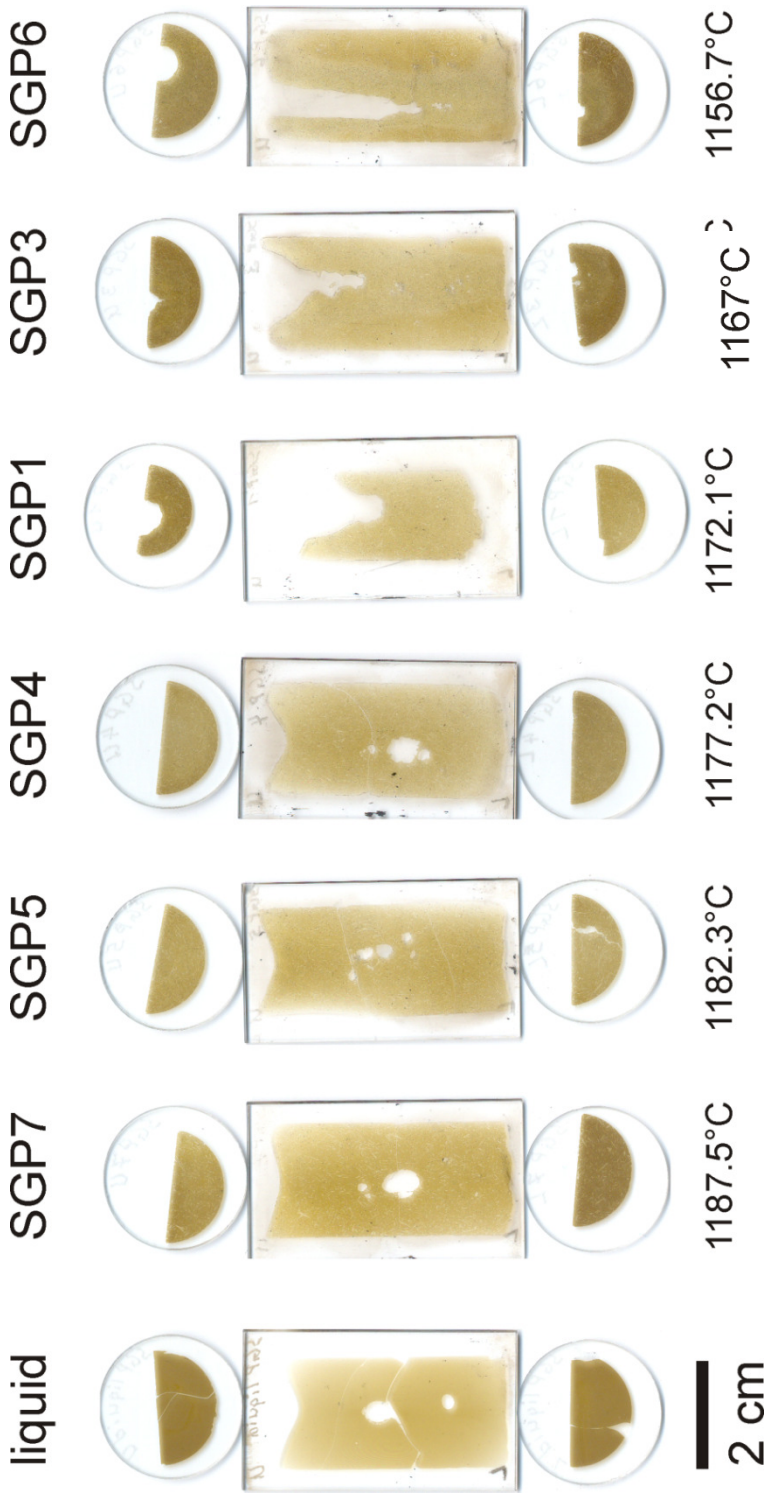

Fig. 4.15. Pictures of sectioned cores from crystallization experiments on Stromboli HK-basalt.

In Figg. 4.15-4.16, photographs of the whole set of sections are reported. The former position of the spindle, before it was removed, is clearly visible on the sections relative to low temperature experiments, when the viscosity is high enough to prevent any rearrangement of the melt, while it is recorded as holes of trapped air at the high temperature experiments.

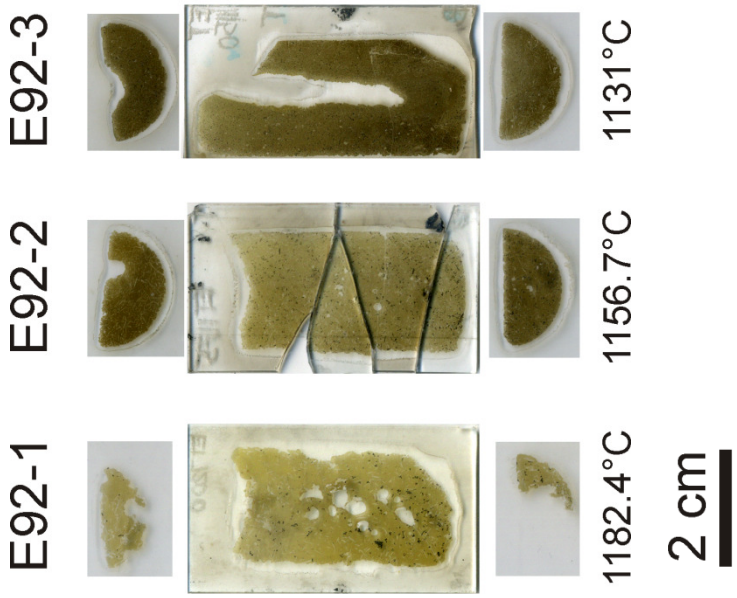

Fig. 4.16. Pictures of sectioned cores from crystallization experiments on Etna trachybasalt (E92-1, E92-2, and E92-3).

Backscattered electron images (BSE) of the longitudinal thin sections were collected with a Philips XL30 SEM at the LIME laboratory of Roma Tre University. Picture profiles were taken at ca. 1 cm from the top and ca. 1 cm from the bottom of the core. For each experimental run, an area between 25 and 55 mm^2 has been digitally analyzed. Depending on the magnification used (between 40x and 100x for the more crystalline samples), the lowest measurable size ranged between 4 and 1.7 μm. Between 100 and 4000 plagioclase, clinopyroxene and spinel crystals were contoured for each sample using Corel Draw© and ImageJ software, and binary images were obtained (Fig. 4.17). Adjacent crystals forming clusters were then separated by drawing white lines in order to isolate the single crystals. For each crystal, the intersection length, width, area and orientation were then measured with ImageJ software. Length and width are expressed as the major and minor axis of the equivalent area ellipse. The results of the analyses are reported in Tab. 4.5.

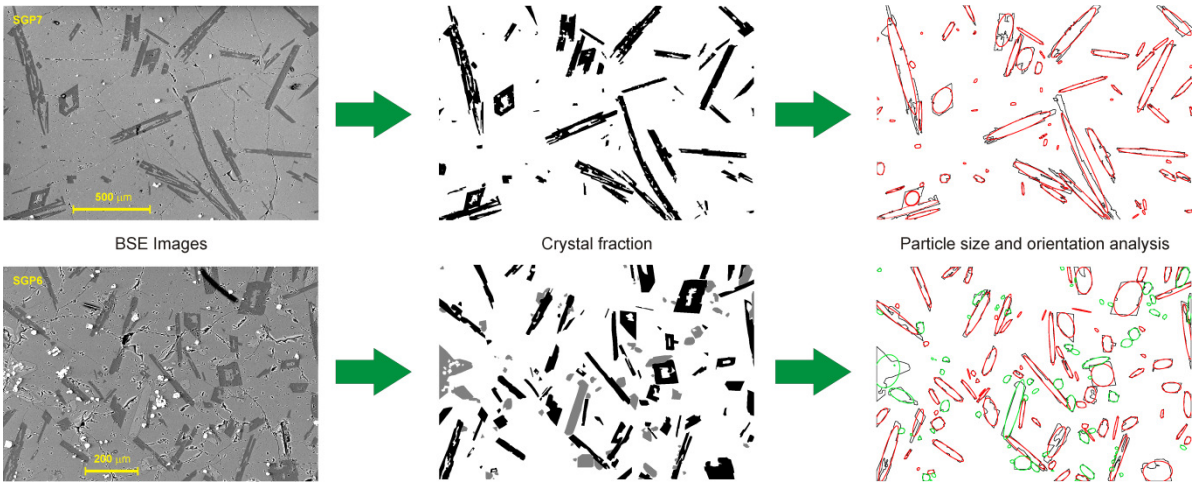

Fig. 4.17. Image analyses procedure. As an example, two pictures relative to the crystal poor (SGP7) and the crystal rich (SGP6) sample from Stromboli are reported. The BSE images were converted in binary images and then the measurement of the textural parameters were performed. On the right side, the shapes of the equivalent area ellipse used to approximate the real crystal shape are reported.

Table 4.5. Results of textural analysis

	Stromboli							*Etna*			
Run	SGP7	SGP5	SGP4	SGP1	SGP3	SGP6		E92-1	E92-2	E92-3	
Investigated area (mm^2)	37.365	50.450	57.495	28.545	51.056	24.302		46.394	43.183	23.159	
Phase	plg	plg	plg	plg	plg	plg	cpx	plg	plg	plg	cpx
Number of crystals	753	1568	2387	960	3927	3293	692	102	1048	1027	388
Number density (mm^{-2})	20.153	31.080	41.517	33.631	76.916	135.503	28.475	2.199	24.269	44.346	16.754
Surface area (mm^2)	2.630	4.500	6.000	2.880	7.380	3.510	0.526	1.765	4.750	2.202	0.359
Mean size L (mm)	0.114	0.109	0.990	0.096	0.088	0.066	0.047	0.282	0.140	0.104	0.039
Minimum size L (mm)	0.007	0.007	0.007	0.007	0.007	0.004	0.031	0.030	0.010	0.006	0.006
Maximum size L (mm)	0.875	0.923	0.997	0.848	0.952	0.512	0.125	1.266	1.069	0.853	0.243
Mean size W (mm)	0.028	0.260	0.024	0.024	0.021	0.016	0.028	0.061	0.030	0.019	0.022
Minimum size W (mm)	0.003	0.003	0.003	0.003	0.003	0.002	0.017	0.006	0.004	0.003	0.002
Maximum size W (mm)	0.151	0.170	0.176	0.168	0.111	0.104	0.081	0.210	0.188	0.108	0.125

The overall crystal fraction (Tab. 4.3) varies between ϕ=0.06 at 1182°C (Etna) and ϕ=0.27 at 1157°C (Stromboli). Heterogeneities have been investigated along profiles perpendicular to the rotational axis (Fig. 4.18). While high temperature experiments exhibit a homogeneous distribution of plagioclase crystals along the entire crucible, at low temperature (SGP6 and E92-3), the pyroxene is unevenly distributed, present only in the internal part of the sample, near the stirring spindle. In Stromboli sample SGP6, the presence of clinopyroxene is compensated by a lesser amount of plagioclase, so that the overall crystal content remains constant. In contrast, in Etna sample E92-3, a difference of ca. 0.05 ϕ between the clinopyroxene-bearing core and the crucible wall is observed. The standard deviation in the crystal content, due to the analyses of the textural features of each image and to the heterogeneity in the crystal distribution, has be estimated to be equal to 0.014 (0.025 for sample E92-3).

The small heterogeneities in the phase distribution are related to different nucleation processes as a function of the distance from the spindle, as the phase assemblage at any point is in equilibrium with the liquid phase, as already discussed previously. In the presence of a laminar flow, and with negligible temperature gradients, the crystallization of pyroxene could be initiated by random density fluctuations due to an imperfect alignment of the spindle. In such cases, the exact characterization of the phase distribution in the sample becomes even more important. Plagioclase frequently shows a skeletal habit and is elongated in shape, while clinopyroxene is only slightly elongated and spinel is spherical, tending to form clusters.

The true shape of crystals has been estimated by optical means in thin sections and by the study of 2D intersections on the binary images. Assuming that the shape of crystals is independent of their size, we found a relation between the axis measured on selected oriented crystals and the mode of the width/length ratio of all crystal intersection through the plane oriented parallel to the spindle direction (Fig. 4.19). For plagioclase, although the shape of the curves remains almost constant, a slight decrease in the mode value can be observed (from 0.16 to 0.12) as the temperature decreases, which we interpret as indicative of increasing average aspect ratio from ca. 7 to 8.3. Clinopyroxene and spinel are more equant and have average aspect ratios of 2 and 1, respectively.

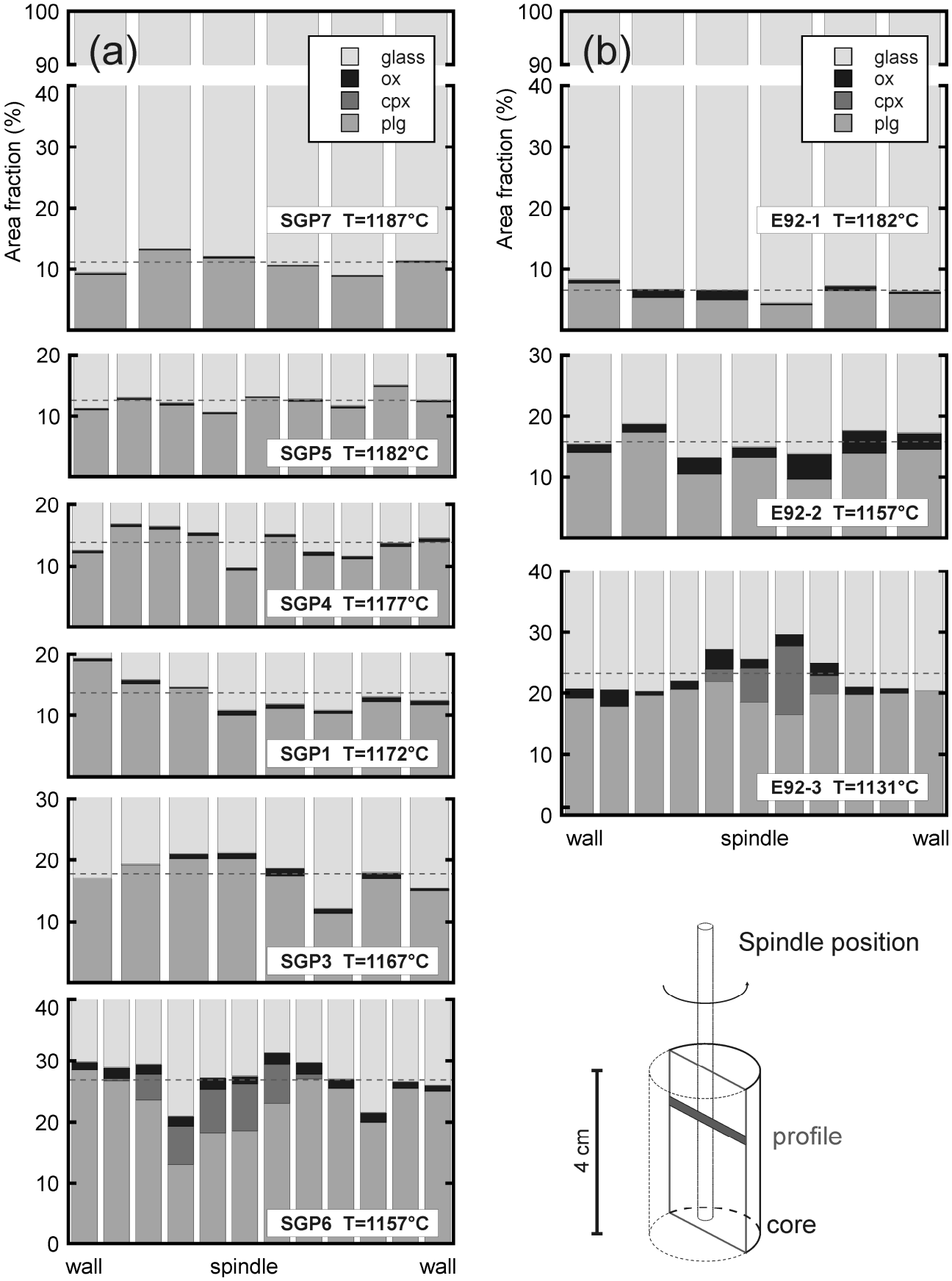

Fig. 4.18. Crystal fractions expressed as 2D intersection area fraction for (a) Stromboli and (b) Etna experimental runs. Each bin corresponds to one single analyzed picture along the section profile. The number of bins depends on the picture magnification (greater for the low temperature experiments) and subordinately on the overlapping width between pictures. Dashed lines represent the average total crystal fraction as reported in Tab. 4.3.

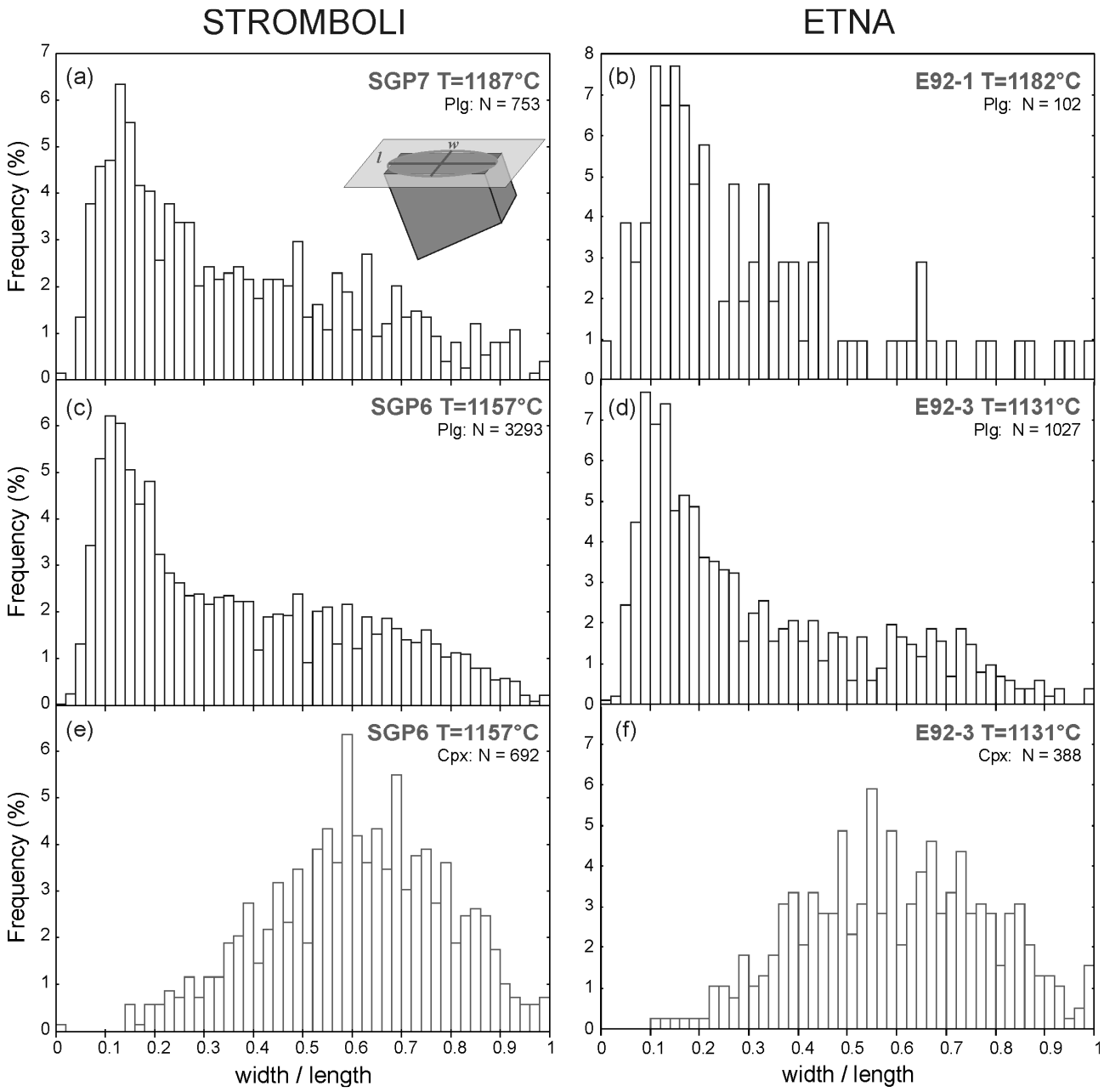

Fig. 4.19. Frequency distribution of 2D interception width/length (w/l) ratios of plagioclase (a-d) and clinopyroxene (e-f) crystals, cut on sections parallel to the spindle direction. (a-d) High and low temperature plagioclase interception for Stromboli (a,c) and Etna (b,d). A decrease in the mode value with decreasing temperature is observed on both starting materials. (e-f) Clinopyroxene interception distributions observed at low temperature experiments on both Stromboli and Etna indicate a less elongated shape.

Plagioclase crystals tend to be aligned according to the flow direction at low temperature as shown in Fig. 4.20, where the high- intermediate- and low-temperature experiments on Stromboli are reported (SGP7, SGP4 and SGP6 respectively). The orientation of the particles could be due to particle rotation in shearing flow. At lower T, where both volume fraction and aspect ratio of the plagioclase crystal are higher, we observe a slightly higher alignment of particles. This agrees well with the observation (Mueller et al., 2010) that the expected particle orientation distribution is a function of aspect ratio: more anisotropic particles rotate faster when perpendicular to the flow lines (thefore spending less time in this position) and slower when aligned to the flow lines (more time). We observe statistically a higher proportion of aligned particles in the case of more elongated crystals (low T) than in the case of more equant particle (high T) as illustrated in Fig. 4.20. At equilibrium conditions, the viscosity response to rotational speed variation is immediate, and no shear weakening behavior (decrease in viscosity with time) is observed. We infer that, at equilibrium conditions, the orientation of crystals does not change with time.

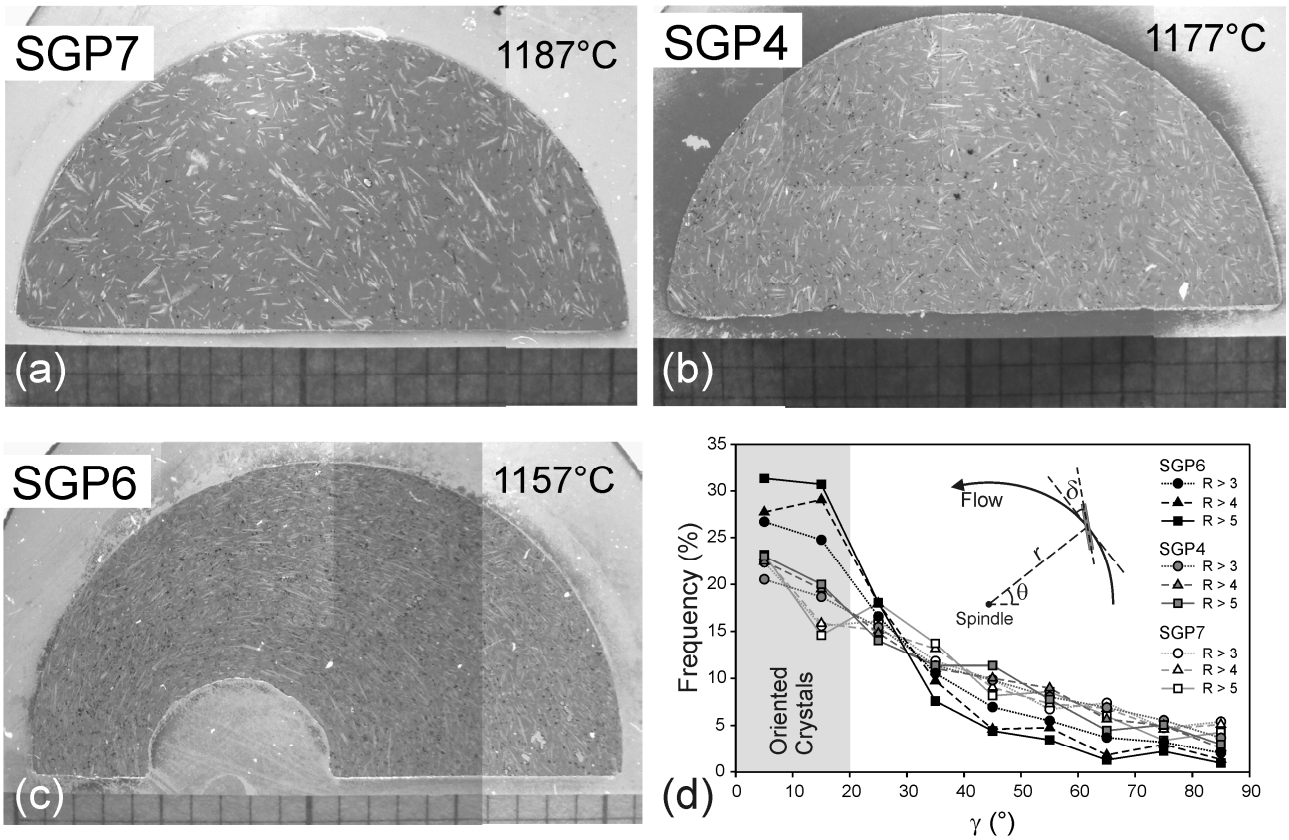

Fig. 4.20. (a-c) Orientation distribution of plagioclase at (a) 1187°C, (b) 1177°C (c) 1157°C on Stromboli samples from sections cut through planes orthogonal to the rotation axis. (d) Frequency distribution of δ angle (i.e. angle between crystal long axis and circular flow line). A decrease in orientation dispersion with decreasing T is observed. Low T sample (SGP6) shows a slight decrease in orientation dispersion with increasing aspect ratio R. As in Fig. 4.12, the non centered position of the spindle in SGP6 sample (c) is an artifact of the drilling procedure.

In Fig. 4.21 the distribution of crystal size is described by the commonly used CSD diagram (Marsh, 1988; Cashman and Marsh, 1988). A stereological conversion can be obtained using the equation proposed by Higgins (1994) for polydisperse populations of different shapes:

$$n_V(L) = \frac{n_A(L)}{(0.64 \cdot D')} \quad (4.1)$$

where $n_V(L)$ and $n_A(L)$ are the crystal *number density* per unit volume and per unit area, respectively, calculated for each size class (L+ΔL) and D' is the mean size calculated via:

$$D' = \frac{(X+Y+Z)}{3} \quad (4.2)$$

where X is the midpoint of the interval ΔL whereas Y and Z are calculated by the known values of crystal shape. The population density is then obtained by the volumetric number density $n_V(L)$ dividing it by the width of the interval ΔL:

$$n'_V(L) = \frac{n_V(L_{XY})}{L_Y - L_X} \quad (4.3)$$

The unit of population density is mm^{-4}, as it is given by the number density (mm^{-3}) divided by the length of the bin interval. Plotted against the crystal size, the natural logarithm of the population density shows a linear trend, as commonly found in rocks. In the case of our experiments, the linear trend can be assumed to derive from a constant nucleation rate of crystals, directly controlled by the degree of undercooling of the melt and hence by the experimental temperature, and growth rate of crystals dependent on crystal sizes (Marsh, 1998). The differences in the slopes of the examined curves hence reflect differences in crystal size distributions, with the high temperature experiments displaying the maximum polydispersity.

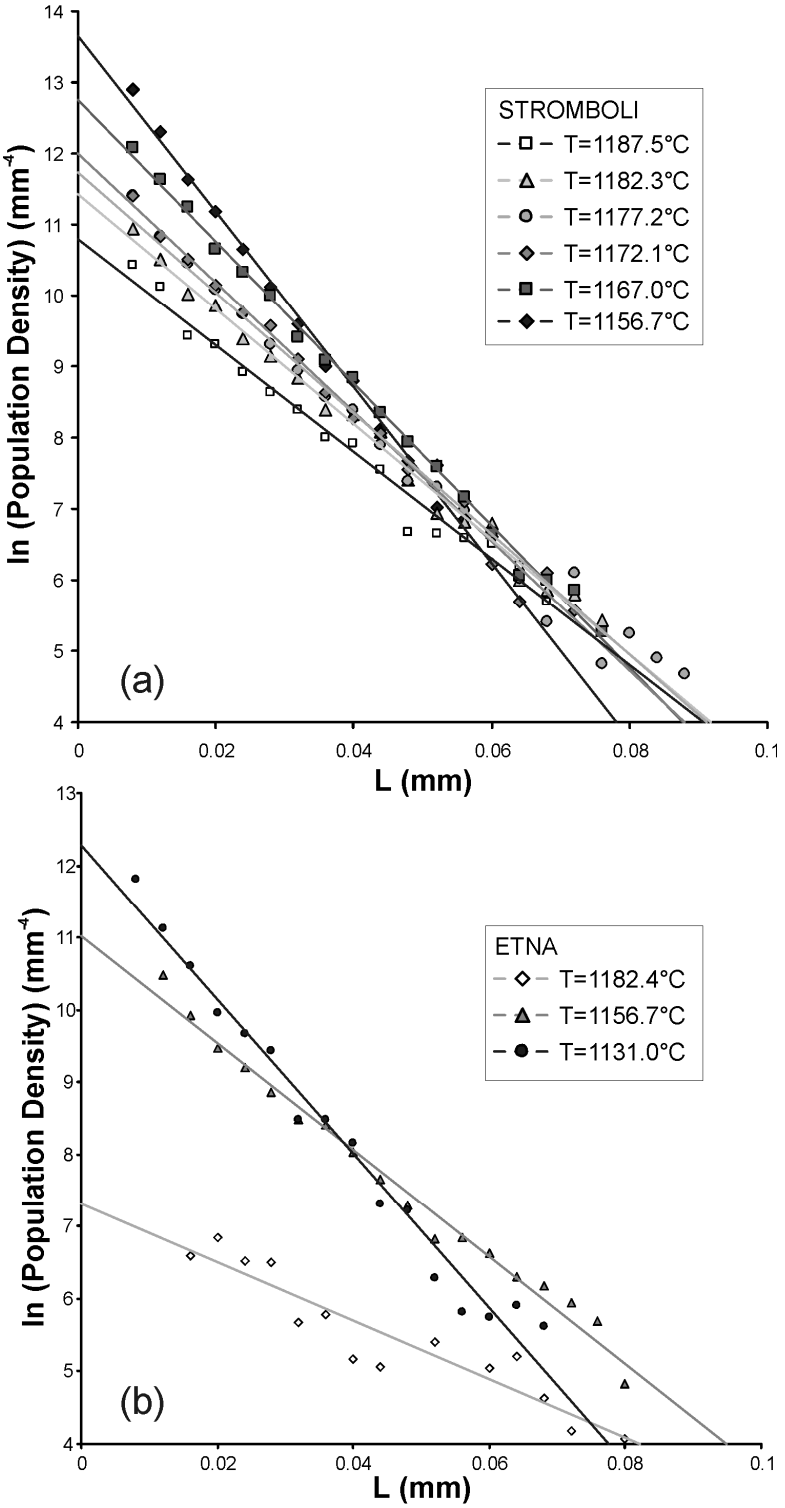

Fig. 4.21. Crystal size distribution diagram of plagioclase crystals for Stromboli (a) and Etna (b) experimental runs. The dispersion of crystal sizes decrease with temperature as shown by the decreasing of the slope of the linear regression (solid lines).

4.1.8. Discussion

Fig. 4.8 reports the temporal evolution of apparent viscosity readings during the isothermal crystallization experiments.. A non linear viscosity increase with time is observed in all of the analyzed curves. These are constituted by a initial plateau, probably associated with the incubation time of nucleation, followed by a ramp and a final plateau. In the case of experiment SGP6 (T=1156.7 °C- Stromboli), a second ramp and second plateau is also discernible. The ramps (which express the increase of viscosity with time) are likely associated with nucleation and/or crystallization processes. In the case of experiment SGP6, the second ramp and plateau reflect a more complex behavior, as a hiatus in nucleation and crystallization or the crystallization of a second phase. This second plateau however does not match with any gap in the CSD curve (Fig. 4.21) indicating that the nucleation of a second phase (clinopyroxene) rather than a pulsatory behavior in the crystallization process is the more likely explanation. The lengths and shapes of plateaus and ramps describing the viscosity variation with time for all experiments do not correlate simply with temperature. A further potential complication affecting the shape of the apparent viscosity-time curve is given by the deformation regime during crystallization. As mentioned above, the viscometer automatically halves the rotational speed when the torque reaches its maximum value during viscosity increase, thus yielding different strain rate versus time patterns, which in turn may influence crystallization kinetics at the different stages. The change in the crystallization pattern induced by halving the strain rate could result in a viscosity variation and possibly be recorded in the slope of the viscosity-time curve. However, within the sensitivity of our measurements, we do not observe any appreciable systematic variation of viscosity versus time versus strain rate (shown as rotational speed in Fig. 4.8) which could be related to this mechanism.

Measurements were terminated when a stable value of apparent viscosity was achieved. At the equilibrium conditions, T trends correlate perfectly with both viscosity and crystal content, as high temperatures correspond to lower viscosity and lower crystal contents (Tab. 4.3).The experimental time needed to achieve a steady value was longer for Etna than for the Stromboli samples, up to 4.8 x 10^5 s for the highest temperature experiment (T=1182.4°C). Such differences in steady state achievement time might be attributed to slower crystallization kinetics in Etna trachybasalt, due to lower initial deformation rates ($\dot{\gamma}_i$=0.53 s^{-1}) and higher incubation times for crystal nuclei (Kouchi et al., 1986). We cannot rule out that at longer measurement times, crystallization could proceed leading to further viscosity increases, (especially for the lower temperature experiments). However, it should be stressed that the achievement of phase equilibria is not the aim of this study and that on

the contrary, rheological equilibrium, in the form of stable values of apparent viscosity, was reached in all experiments.

The chemical and textural analyses performed on the post-run charges correspond only to the final stable viscosity readings. The transient behavior, i.e. the plateaus and ramps related to the crystallizing liquid are not further investigated in this section.

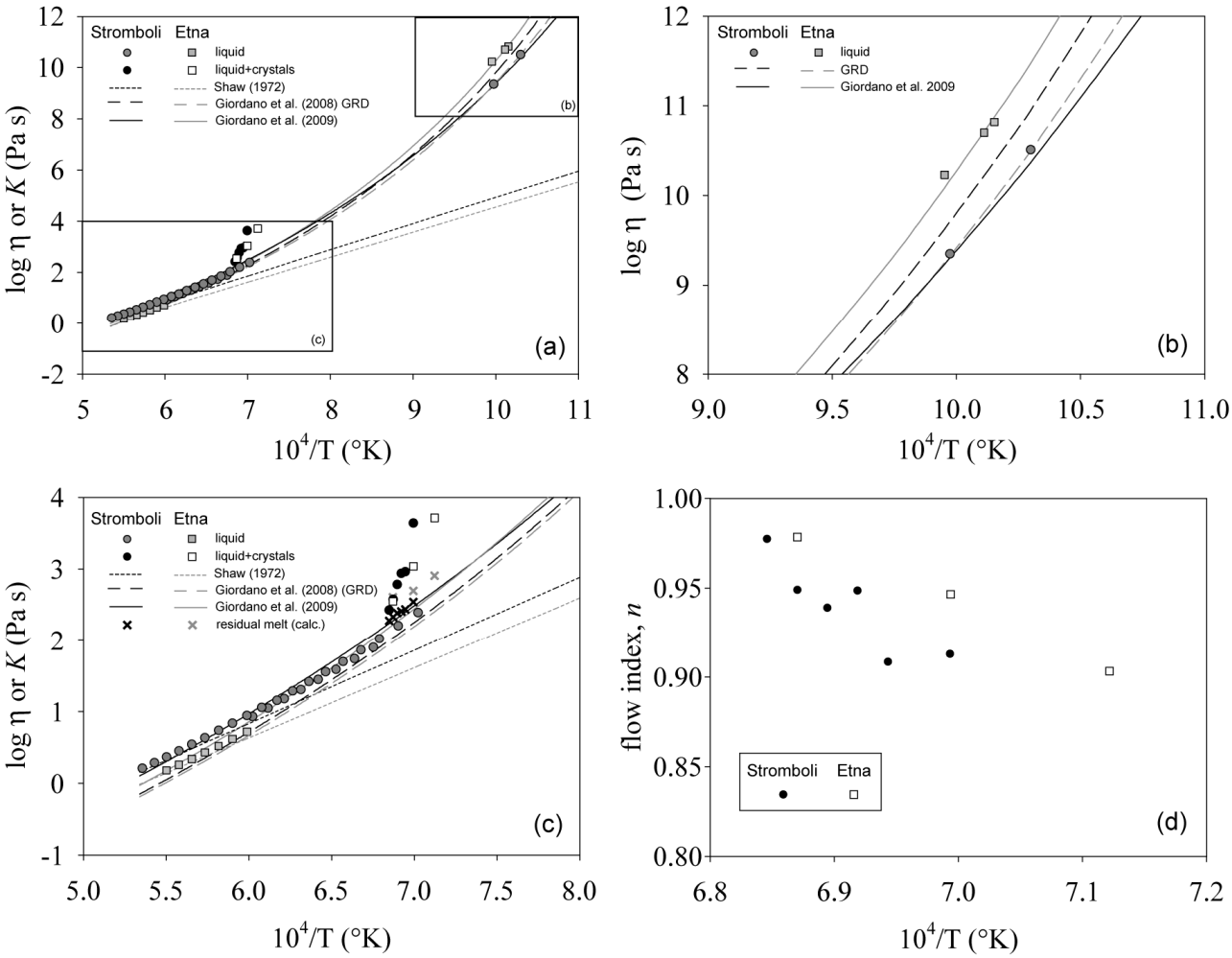

Fig. 4.22. a) Flow consistency K (equal to Newtonian viscosity at $\dot{\gamma}$ =1 s-1) and viscosity of the investigated basalts against the reciprocal temperatures. The measured pure liquid viscosities at high and low T are from Giordano et al. (2006) and the present study for Stromboli (grey circles) and from Giordano and Dingwell (2003) for Etna (grey squares). Data are compared to the viscosity models from Shaw (1972; dotted line), Giordano et al. (2008; GRD, dashed lines) and with the equation obtained by Giordano et al. (2009; solid lines). The subliquidus measurements on Stromboli (black circles) and Etna (white squares) are also reported. b) Low T liquid viscosity data for Stromboli and Etna and models from Giordano et al. (2008; GRD) and equation obtained by Giordano et al. (2009). The equations of Giordano et al. (2009) better reproduce the experimental data compared to the GRD model. c) High T viscosity of the liquid and consistency of the magmatic suspensions. The subliquidus measurements on Stromboli (black circles) and Etna (white squares) are also reported and show a strong departure from the pure liquid viscosity of the starting material. Also reported the viscosity of the residual melt composition as a function of T calculated with the GRD model with a 0.2 log units correction (see text). d) the flow index (n) values of subliquidus measurements on Stromboli (black circles) and Etna (white squares) are plotted against the reciprocal temperatures, showing the onset of a slight shear-thinning behavior with decreasing temperature.

The net effect of crystals on the viscosities of magmatic suspensions is commonly expressed in terms of relative viscosities, defined as the ratio between the measured apparent viscosity of the suspension and that of the suspending liquid. In order to calculate the viscosity of the residual melt upon crystallization, we have to refer to the existing prediction models which allow to calculate viscosity from the liquid compositions.

Figures 4.22a,b,c compare our experimental data with the various predicting models of viscosity, in terms of viscosity (η) or consistency (K, which equals the viscosity for Newtonian fluids) as a function of inverse T. The original model (Shaw, 1972) considered a Arrhenian variation of viscosity with T. We can observe, as already previously recognized for several liquid compositions, that the results of the Arrhenian parameterization of viscosity strongly diverge from the liquid viscosity data, the discrepancy being higher at lower T. The other two parameterizations presented are taken from Giordano et al. (2008) (GRD in the following) and Giordano et al (2009) who also analyzed Etna and Stromboli compositions. Both parameterizations make use of a Vogel Fulcher Tamman (VFT) equation ($\log \eta = A + B / (T - T_0)$, where A, B, and T_0 are adjustable constants) accounting for the non-Arrhenian temperature dependence of viscosity and are considered more reliable in predicting viscosity of the pure liquid compositions.

In order to define a strategy to best calculate the viscosity of the residual melt and to reduce possible sources of errors, we tried to assess the reliability of the two different parameterizations. The GRD model allows calculating the viscosity of any liquid as a function of composition and T , whereas the Giordano et al (2009) model calculates the liquid viscosity for Etna and Stromboli liquids at any temperature.

In Fig. 4.22a,b,c the differences between the measured and calculated viscosity in both the high and low temperature intervals are reported. Measured data (symbols in the figure) for Etna are from Giordano and Dingwell (2003), whereas data from Stromboli are from Giordano et al. (2006) and the present investigation (Tab. 4.6). From Fig. 4.22b and 4.22c we can observe that the predicting model of Giordano et al. (2009) is capable of better reproducing our experimental results compared to the GRD model. In particular, at high temperature (Fig. 4.22c) the calculated RMSE (Root Mean Square Error) by using the GRD and Giordano et al (2009) parameterizations are respectively of 011 and 0.06 log units for Etna liquid and 0.18 and 0.13 log units for Stromboli liquid. These differences are greater at low T, with RMSE values of 0.55 and 0.08 log units and 0.22 and 0.14 log units for Etna and Stromboli liquids, respectively (Fig. 4.22b). We are however compelled to use the GRD model, because it allows viscosity calculations as a function of the residual melt composition. As the two predicting models differ by 0.2 log units (The GRD model predicts viscosity values 0.2 log units lower than Giordano et al. 2009 model) at the *subliquidus* T, in order

to reduce possible sources of errors, we apply a correction of 0.2 log units of viscosity to the calculation obtained by using the GRD model.

Table 4.6. Measured viscosity of the pure liquids

Stromboli basalt [(a)]		*Stromboli basalt* [(b)]		*Stromboli basalt* [(b)]		*Etna trachybasalt* [(c)]	
T(°C)	log η (Pa s)	T(°C)	log η (Pa s)	T(°C)	log η (Pa s)	T(°C)	log η (Pa s)
1387.7	0.93	1593.9	0.21	1323.2	1.29	1544.7	0.18
1362.1	1.05	1569.3	0.28	1298.6	1.42	1520.1	0.26
1336.4	1.18	1544.7	0.37	1274.0	1.56	1495.5	0.34
1310.7	1.31	1520.1	0.45	1249.4	1.70	1470.9	0.43
1285.0	1.45	1495.5	0.54	1224.8	1.86	1446.3	0.52
1259.4	1.59	1470.9	0.64	1200.2	2.02	1421.7	0.62
1233.7	1.74	1446.3	0.74	1175.6	2.21	1397.1	0.72
1208.0	1.90	1421.7	0.84	1151.0	2.39	731.6	10.23
		1397.1	0.95	729.5	9.35	715.9	10.70
		1372.5	1.06	697.9	10.51	711.9	10.82
		1347.8	1.16				

[(a)] This Study; [(b)] Giordano et al. (2006); [(c)] Giordano and Dingwell (2003).

Fig. 4.22c shows the development of the consistency *K* as a function of the inverse temperature for the *subliquidus* experiments. We can observe that below T=1190°C entrance into the *subliquidus* field is marked by a cut-off in the curve, i.e, a sharp departure from the pure liquid curve, consequent to the presence of suspended crystals and chemical evolution of the residual melt. The viscosities of the residual melt composition, calculated with the strategy outlined above, are also reported.

In Fig. 4.22d the flow index *n* with inverse temperature is presented. We observe a steady decrease of the flow index parameter (a measure of the degree of non-Newtonian behavior) as a function of inverse T for both Etna and Stromboli melts from $n \approx 1$ at high temperature (Newtonian behavior) to $n \approx 0.90$ at low temperature, indicative of a weak non-Newtonian shear-thinning behavior.

We then calculated the relative viscosity, defined as the ratio between the measured apparent viscosity of the suspension and that of the residual liquid calculated as described above (Tab.4.3). In Fig. 4.23 the relative viscosity as a function of the crystal fraction ϕ is shown. As expected, the relative viscosity increases with increasing ϕ at constant shear strain rate, from nearly 1 at ϕ=0.06 up to 15-17 (according to the applied shear rate) for the most crystallized sample with ϕ=0.27,

describing a curve that deviates strongly from the Einstein-Roscoe equation and from the recent strain-rate dependent model by Costa et al. (2009), also reported in the figure. We interpret this deviation as due to the elongation of crystal phases (mean aspect ratio between 6 and 7.2), compared to isotropic particles that were used to calibrate those models. In Fig. 4.23 we can also observe that the increase of the relative viscosity as a function of ϕ is slightly higher at lower shear strain-rate and that the shear strain-rate dependence of the relative viscosity increases with increasing ϕ, in agreement with recent literature data (c.f. Caricchi et al., 2007; Ishibashi, 2009).

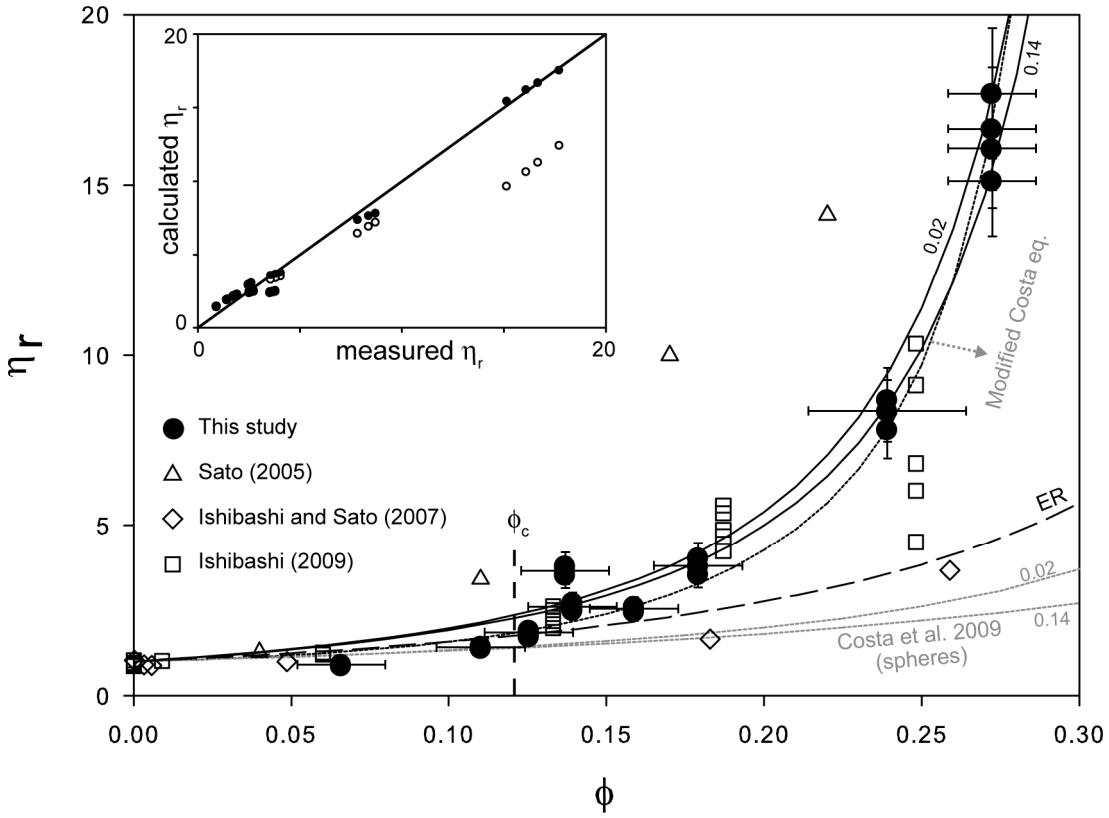

Fig. 4.23. Relative viscosity as a function of crystal fraction (ϕ). Black circles represent data obtained from this study. Error in the relative viscosity value is = ±0.05 log units. Horizontal errors refer to the crystal content standard deviation equal to 0.014 (0.025 for sample E92-3). Data from Sato (2005; open triangles), Ishibashi and Sato (2007; open diamonds) and Ishibashi (2009; open squares) are also reported. Dashed line describes the Einstein-Roscoe equation (ER); grey dotted lines show the prediction model by Costa et al. (2009) calculated for spherical particles and strain rate of 0.14 and 0.02 s^{-1}. Black dotted line represents a new fitting of our data using Costa et al. (2009) equation (fittings parameters are reported in the text). Solid lines refer to the fitting according to the modified KD equation (eq. 4.9) with $\alpha = 0.06$ and $\phi/\phi_m = 0.37$ at shear rate of 0.14 and 0.02 s^{-1}. The insert shows a comparison between the measured values of this study (black circles) and those calculated using Ishibashi (2009) model (open circles).

The Etna and Stromboli basalts show Newtonian behavior at T > 1175°C in the experimental $\dot{\gamma}$ range (2.24-0.02 s^{-1}). At T<1175°C a slight decrease in apparent viscosity with increasing shear rate (shear thinning) has been observed. No yield strength of the suspensions has been observed even for

the more crystal-rich samples. The critical volume fraction of crystals ϕ_c at the onset of non-Newtonian behavior (onset of concentrated regime) is ϕ_c=0.12-0.14. This value is markedly lower than the values proposed by other studies containing isotropic particles (e.g. Ryerson et al., 1988; Lejeune and Richet, 1995) but agrees well with the range of values found by Ishibashi (2009). These low values are attributable to the highly anisotropic nature of the suspended particles in this study which favors grain interactions at lower concentration. (Hoover et al., 2001; Saar et al., 2001; Ishibashi, 2009). ϕ_c is not affected by the orientation of the particles (higher orientation would yield lower ϕ_c values) as particles show preferred orientation only at higher cystal content and lower experimental temperature (Fig. 4.20).

The onset of non-Newtonian behavior has been attributed in the past to several causes (de Brujin; 1951; Stickel and Powell, 2005; Mueller et al., 2010). In our study, all measurements were performed in a hydrodynamic regime where Brownian motion and particle inertia are negligible, as indicated by both their high Peclet numbers ($Pe>10^8$) and low Reynolds numbers ($Re<10^{-8}$). Moreover, small Stokes numbers ($St<10^{-7}$) indicate that uncoupling between the fluid and solid phase (leading to non-Newtonian behavior) is not present (Coussot and Ancey 1999; Mueller et al., 2010). Mueller et al. (2010) argue that for the $Pe>>10^3$ and $Re<<10^{-3}$ regimes, shear thinning could be caused by localized viscous heating of the suspending fluid. However, Ishibashi and Sato (2007) rule out viscous heating for their experiments on basalts and suggest either the decrease in particle orientation dispersion or the decrease in intergrain interaction, as indicated by Ryerson et al. (1988), as the cause of shear thinning behavior. In our case we observe a slightly higher shear-thinning effect at lower T, where a higher concentration or more oriented particles is observed. Therefore, alignment of particles could be responsible for the shear-thinning effect. However, the higher particles concentration could lead at the same time to larger grain dispersive forces (decreasing intergrain interaction, Ryerson et al., 1988) and possibly larger viscous heating effects (Mueller et al.,2010). The viscous heating effect for our liquids calculated according to Bird et al. (1987) for the shear rate conditions of our experiments is found however to be negligible.

The only other experimental studies of natural magmas in a comparable range of deformation rate and crystal content are those of Sato and Ishibashi (Sato, 2005; Ishibashi and Sato, 2007, Ishibashi, 2009). Their results are included in Fig. 4.23 for comparison. A similar behavior of increasing relative viscosity with increasing crystal fraction can be observed for the Sato (2005) and Ishibashi (2009) viscosity data on plagioclase-bearing basalts from Fuji volcano, at plagioclase mean aspect ratios of 12.9 and 8.5, respectively. The strong increase in relative viscosity observed by Sato (2005) at very low crystal content may be due to the very high aspect ratio of plagioclase crystals in those experiments. In contrast, for the olivine-bearing basaltic lava, investigated by

Ishibashi and Sato (2007), the lower aspect ratio of plagioclase (ca. 4) and the presence of granular olivine, leads to a very different trend of weak viscosity increase as a function of crystal content, in better accord with the ER equation. The authors argue that, for low average aspect ratios ($\bar{R}$ <4-6.5), the effect of crystal shape on the intrinsic viscosity parameter can be counterbalanced by the effect of the dispersion of crystal sizes which yields an increase of the ϕ_m parameter and a significant reduction of the effective volume fraction ϕ/ϕ_m.

Our data agree well with the viscosity data obtained by Ishibashi (2009) for crystal contents up to ϕ=0.2. The similarity of the results presumably result from very similar aspect ratios of the plagioclase crystals in both studies. However, for higher values of ϕ , the shear rate dependence of the suspensions of this study is found to be weaker (n=0.90) than that found by Ishibashi (2009) at ϕ=0.25 (n=0.82). Such a difference could be linked to the presence of sub-rounded clinopyroxene in our low temperature experiments, which complicates the suspension rheology to that of a bimodal polydisperse suspension. We wish to stress that comparison between our results and the data presented by Sato (2005) and Ishibashi (2009) must remain semi-quantitative, as the normalization procedure adopted in those studies differ from our procedure. Sato (2005) and Ishibashi (2009) calculate the residual liquid viscosity by using the Arrhenian viscosity model of Shaw. Such a normalization procedure may induce significant errors in the relative viscosity calculation, especially at lower temperatures, where the non-Arrhenian behavior of magmas is more pronounced.

We fitted all of our data, irrespective of the strain rates, with the equation by Costa et al. (2009) (Eqs. 2.13-14). The resulting curve is presented in Fig. 4.23 and the new calculated parameters are the following: ϕ^* = 0.274; ξ = 0.0327; γ = 0.84; (δ was fixed as in Costa et al. 2009: δ = 13- γ). The results are quite satisfactory and can be used to parameterize the multiphase rheology of a suspension with the same textural features of our liquids (average aspect ratio, crystal size and shape distribution).

However, in order to obtain a more general parameterization of the multiphase rheology of different suspensions, the effects of crystal shape anisotropy and crystal size distribution must be derived. To take into account the crystal shape, the values of ϕ_m have been calculated on the basis of the average aspect ratio using Eq. (2.9) (Mueller et al., 2010), which has been calibrated to empirically fit their data on analog suspensions containing monodisperse particles of fixed aspect ratio. We calculated the average aspect ratio ($\bar{R}$) according to the following equation:

$$\bar{R} = \frac{\sum \phi_i \bar{R}_i}{\phi} \tag{4.4}$$

where ϕ_i and $\bar{R}_i$ are the crystal fraction and the mean aspect ratio of phase *i*. The resulting $\phi_m(\bar{R})$ values show a small but detectable decrease as a function of increasing crystal content, from 0.42 to 0.37. A good way to describe and fit the relative viscosity data is to separate the consistency (which takes the same value as η at $\dot{\gamma}$ = 1 s^{-1}, Eq. 2.3), from *n*, which captures the role of shear thinning. In this way, the two separate contributions to viscosity are easily visualized and the relative viscosity can then be obtained by the combination of these two quantities.

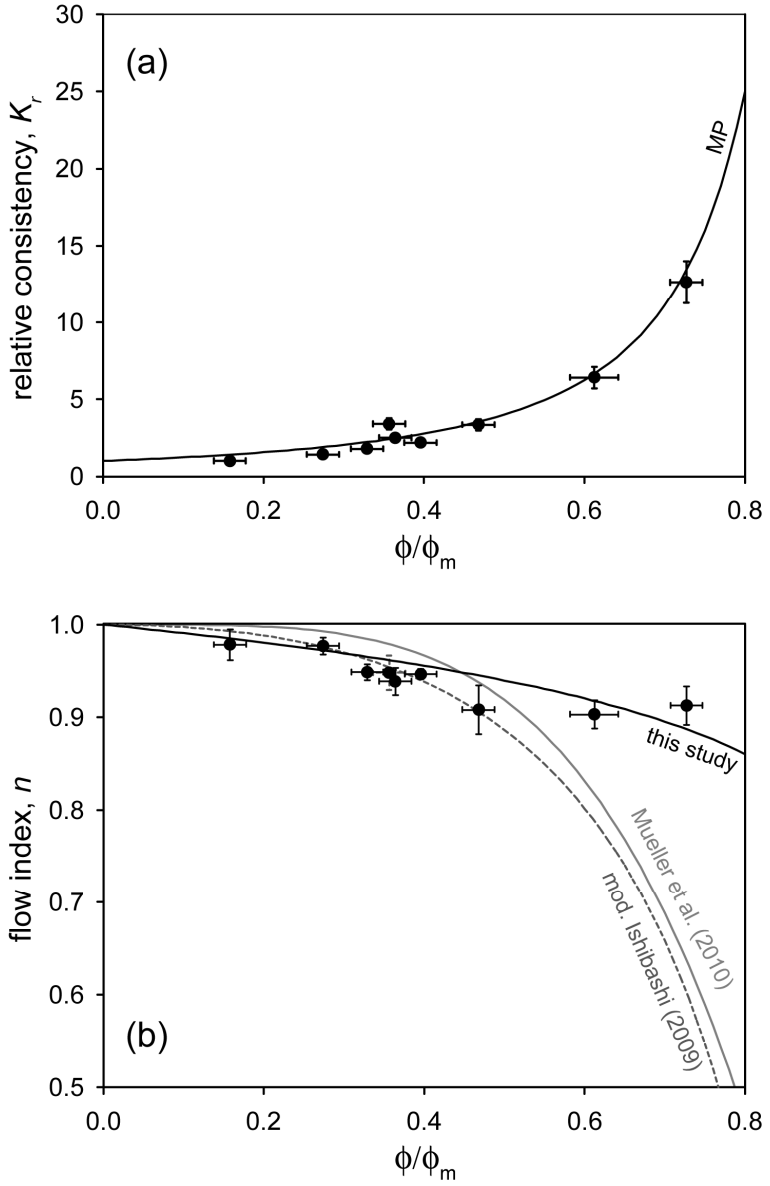

Fig. 4.24. (a) Relative consistency (K_r) vs. normalized crystal fraction (ϕ/ϕ_m). Black circles refer to data from this study; solid line shows the Maron-Pierce relation. Values of ϕ_m are calculated according to Eq. (2.9) by Mueller et al. (2010). (b) Flow index (*n*) vs. normalized crystal fraction (ϕ/ϕ_m). Black circles refer to data from this study. Grey solid line refers to Eq. (2.11) by Mueller et al. (2010), calculated for R=6.5; grey dashed line refers to the modified Ishibashi (2009) equation (Eq. 4.5). Black solid line refers to Eq. (4.6) adopted in the present study.

The relative consistencies ($K_r = K/\eta_l$) are reported in Fig. 4.24a as a function of the calculated ϕ/ϕ_m. With this representation, all our measured values collapse onto the curve using the Maron-Pierce equation confirming that crystal shape is a first order parameter that affects the increase in suspension viscosity, through the dependency of axial ratio on ϕ_m, compared to other observed textural parameters. The effects of the observed crystal size distributions and that of the orientation dispersions on ϕ_m appear to be negligible compared to the effect of crystal shape. In fact, all of our measured values and the Mueller (2010) data pertaining to monodisperse particles present different crystal size distributions and orientation dispersions and despite this, they all converge into a single master curve relating aspect ratio to suspension consistencies.

As illustrated previously (Fig. 4.22d), with increasing crystallization a weak shear thinning (n<1) effect has been observed. The observed values of flow index (n) as a function of crystal fraction are shown in Fig. 4.24b. In Fig. 4.24b the equation proposed by Mueller et al. (2010; Eq. 2.11) for a R=6.5 is also reported. Moreover, from the equation proposed by Ishibashi (2009; Eq. 2.12) a relation for $n(\phi/\phi_m)$ can be derived if $B\phi_m=2$ is assumed (as in MP-equation) as:

$$n = 1 - 2\lambda\left[ln\left(1 - \frac{\phi}{\phi_m}\right)\right]^2 \quad (4.5)$$

where λ=0.118 as in the Ishibashi (2009) study. Eq. (4.5) is also reported in Fig. 4.24b.

Our data are consistent with both equations, except at crystal content ϕ/ϕ_m>0.5. The reason for this discrepancy is probably the difference in the suspensions of the studies, therefore differences in crystal size, crystal shape and orientation distribution, although those dependencies are difficult to constrain. Whereas the consistency of the investigated suspensions seem to be perfectly described by only one parameter, ϕ_m, which in turn is only affected by the crystal shape, the non-Newtonian character of the suspension has indeed a more complex relation with the textural features of the suspension. We empirically fitted our data in Fig. 4.24b to the following equation:

$$n = 1 + 2\alpha \log\left(1 - \frac{\phi}{\phi_m}\right) \quad (4.6)$$

We stress that given the paucity of existing experimental data on polidisperse suspensions, a general functional form for the effect of textural parameters on the non-Newtonian character of the suspension does not exist nor can one be provided at the moment. This equation is only valid for our specific polidispersity, as far as the non-Newtonian character is concerned.

To visualize the results of the parameterization in terms of relative viscosity and to allow a easier comparison with literature data, we combined the two equations (2.10 and 4.6) for consistency and *n*, into a general equation. From the comparison of Eqs. (2.3) and (2.8), we obtain the following equation (Ishibashi , 2009):

$$-B\phi_m = \frac{\log(K_r)}{\log\left(1-\frac{\phi}{\phi_m}\right)} + (n-1)\frac{\log(\dot{\gamma})}{\log\left(1-\frac{\phi}{\phi_m}\right)} \quad (4.7)$$

Substitution of Eqs. (2.10) and (4.6) into Eq. (4.7) produces the expression:

$$-B\phi_m = -2[1-\alpha\log(\dot{\gamma})] \quad (4.8)$$

Substituting Eq. (4.8) into the KD equation (Eq. 2.8) the following general expression can be derived:

$$\eta_r = \left(1-\frac{\phi}{\phi_m}\right)^{-2[1-\alpha\log(\dot{\gamma})]} \quad (4.9)$$

Equation (4.9) was used to fit our data leaving α as an adjustable parameter, in order to account for errors due to the Maron-Pierce approximation ($B\phi_m = 2$) and errors due to the calculation of the flow index *n*. The ϕ_m values were calculated using Eq. (2.9), which takes into account the crystal shape factor The α value obtained is = 0.06 with R^2= 0.995. The results of the modeling are reported in Fig. 4.23 for the low T strain rates (where shear thinning effects are visible). The quality of the fitting is difficult to visualize in this type of representation as neither strain rate variations nor ϕ_m variations are visible. As an example, two curves are shown, referring to maximum and minimum shear strain rates and ϕ_m conditions of the low T data of Stromboli liquids.

In the insert, calculated versus measured relative viscosities for our data are reported using the modeling presented here and the Ishibashi (2009) model. As it can be seen, the model equation reproduces very well all the experimental data. At high crystal content, the Ishibashi (2009) model underestimates the relative viscosity in comparison with our data. The discrepancy between the two model equations is due to the use of a fixed ϕ_m = 0.6 in the Ishibashi (2009) parameterization. Decreasing values of ϕ_m as the particles become more elongated, as parameterized in Eq. (2.9), yields a higher value of relative viscosity with respect to that predicted by Ishibashi (2009).

We stress that the differences in the various function form of the equation presented in Fig. 4.24b refers only to shear thinning effects which, in the case of our experiments, are minor compared to the effect of crystals on consistency.

Our results demonstrate that the crystal shape factor is of paramount importance ,through the ϕ_m dependency on aspect ratio, in influencing the rheological behavior of a crystal-bearing magma and thus should not be neglected. Any numerical simulation of magma dynamics should take into account the shape of crystals as it can drastically affect the rheological behavior and hence the eruptive style of a volcano (explosive vs. effusive). The effects of crystal size dispersion, crystal shape dispersion (bimodal in our low temperature experiments) and orientation dispersion seem to be minor on ϕ_m and therefore K, but can be incorporated in the α parameter, which in turn controls the shear-rate dependence of the magma suspension rheology. Further experiments with different crystal size and crystal shape dispersion will be needed, in order to evaluate such a dependency for different suspensions.

Compared to previous studies on the high temperature rheological behavior of magmatic suspensions (Sato, 2005; Ishibashi and Sato, 2007; Ishibashi, 2009), the method we utilize in this study allows better control of important experimental constraints: (1) continuous viscosity readings during isothermal crystallization allow detection of the achievement of a constant viscosity value with time, indicative of equilibrium in the crystallization process. At these stable conditions, it is safe to perform measurements under varying deformation regimes, as the changes of the suspension features (driven by crystallization) are negligible; (2) textural features of crystal phases are not perturbed from periodically inserting and removing the measuring spindle with varying experimental conditions. In this manner, time dependent behavior (thixotropy), caused by rearrangement of elongated particles and possible disequilibrium conditions caused by re-crystallization due to spindle insertion can be minimized. (3) the present method also allows for analysis of nearly the entire post run product, whose textural attributes can be thus accurately characterized.

4.1.8. Summary

Viscosity measurements have been performed on basaltic melts from Stromboli and Etna during crystallization. At the investigated *subliquidus* temperatures (1131°C<T<1187°C) a strong increase in viscosity has been observed as a consequence of the presence of crystals (ϕ=0.06-0.27). At T > 1175°C and ϕ up to 0.12-0.14 both studied compositions behave as Newtonian liquids, while at lower temperature, the increase in crystal content leads to the onset of a weak shear thinning

behavior (n=0.9). A strong departure from the well-known (strain-rate independent) Einstein-Roscoe equation and from the strain-rate dependent model by Costa et al. (2009) for spherical particles has been observed. The origin of this discrepancy is ascribed primarily to the effect of elongated plagioclase in increasing crystal interactions at low ϕ.

The effect of crystal shape can be evaluated using the equation proposed by Mueller et al. (2010) to derive the value of ϕ_m assuming a mean aspect ratio $\bar{R}$. Such a dependence can be modeled effectively with a Maron-Pierce equation (Maron and Pierce, 1956). Using this representation we confirm that crystal shape is a first order parameter that affects the increase in suspension viscosity (relative to other observed textural parameters). The crystal size distribution and crystal shape heterogeneity (at low T experiments) could be controlling parameters of the strain-rate dependence of the investigated suspensions.

We present a new parameterization of the relative viscosity as a function of crystal content which combines the Mueller et al. (2010) equation for consistency with a modelization of the non-Newtonian character of the liquid suspension which takes into account the crystal shape effect and the polidispersity of the suspension.

Crystal size distributions and crystal shape heterogeneities are included in the α parameter, an empirical constant which takes into account the shear thinning effect. The combination of these equations permits us to parameterize for the first time the effect of crystal shape on the rheology of natural magmatic suspensions.

The explosive versus effusive eruptive style of a volcano strongly depends on the rheology of magma which is in turn controlled by the concentration and shape of crystals. Any modeling pertaining to magma dynamics in the conduits, from convection and crystal settling in the magma chamber to volatile exsolution, degassing and fragmentation along the conduit and emplacement rate and dimensions of lava and pyroclastic flows, should therefore take into account the complexity of the rheology of magmatic suspensions, as revealed by this study.

4.2. High temperature Rheology of Crystal-bearing synthetic Haplogranitic melt

In addition to the *subliquidus* rheology measurements on natural magmas from Stromboli and Etna, another approach was followed to characterize the effect of crystals on the rheology of magmatic liquids. We have investigated the high temperature (977°C and 1080°C) rheological

behavior of a synthetic melt (HPG8Na20, Hess et al., 1995) with different content of corundum crystals in a concentric cylinder apparatus. The starting composition is different from that of a typical basalt and it was chosen because of its similar NBO/T value (NBO/T=0.51) compared to the Stromboli and Etna basalt (NBO/T=0.47 and 0.45, respectively). If the chemical composition imposes a great constraint on the rheological behavior in the low-temperature high-viscosity regime, where contribution due to the chemical mixing of the cations become important, in the high-temperature, low-viscosity regime, the overall strength of the melt, mainly represented by the average NBO/T of the liquid, is the most important parameter affecting viscosity and the anhydrous composition becomes of secondary importance.

The variation of crystal content was achieved by adding corundum crystals to the melt at constant temperatures above the *liquidus*. Using this technique, complexities in the interpretation of the experimental results can be avoided, because the melt composition does not change as a result of changing temperature and partial crystallization. Considering that the corundum solubility does not change significantly, the melt composition remains basically unchanged upon variation of temperature.

4.2.1. Sample Preparation and Experimental Technique

We have chosen a haplogranitic melt composition (HPG8, Holtz et al. 1992) which lies near the 1-Kbar (P_{H2O}) ternary minimum in the system SiO_2-$NaAlSi_3O_8$-$KAlSi_3O_8$. To this basis composition we have added 20 wt% of Na_2O (HPG8Na20). The obtained composition is close to that studied by Hess et al. (1995) (Tab.1).

Table 4.7
Nominal composition of the starting material

	wt %	Mole fraction
SiO_2	62.80	0.669
Na_2O	23.63	0.244
Al_2O3	10.19	0.064
K_2O	3.38	0.023
total	100.0	1

The melts investigated in the present study were generated by direct fusion of powder mixes of oxides (SiO_2 and Al_2O_3) and carbonates (Na_2CO_3 and K_2CO_3) at 1 atm and 1500°C. The fusions were performed in thin-walled crucibles with a $MoSi_2$ box furnace. The partially fused products of this initial fusion were then transferred in the crucibles to the viscometer furnace, and a stirring spindle was entered into the sample from above. The samples were fused for hours until inspection of both the stirring spindle and the crucible, removed periodically from the melt, indicated that the melts were homogeneous and bubble-free. The melts were removed from the furnace, poured on a steel plate and allowed to cool in air. To improve the homogeneity, the obtained glasses were crushed and the material were loaded in the measurement crucible ($Pt_{80}Rh_{20}$, see section 3.2.1).

The pure liquid HT viscosity was measured following methods and techniques described in section 3.2.1, in the 977-1490°C temperature range and rotational speed of 40 rpm.

The crystal-bearing melt rheology measurements were performed isothermically at T=1000°C and T=1100°C. The experiments were performed on the HPG8Na20 plus corundum system. The chosen corundum crystals are 1.37 mm long in average with a standard deviation of 0.25. Their aspect ratio is slightly elongated ranging from 1 to 3 with an average of 1.4 and a standard deviation of 0.2. Thus, the resulting building network is on a first order comparable to the one of mono-dispersed spheres which simplifies the whole system complexity.

For each experiment, 35 g of HPG8Na20 sample was melted and periodically (ca. every one hour) removed from the furnace to add a discrete amount of corundum crystals at the surface of the crucible. Then, the crucible was loaded back in the furnace to continue the measurement during the sinking of the particles. Three experiments were performed (A5, A6 and A8) with different amount of particles added at each step: 1 g for a total of 7 g in experiment A5, 2 g for a total of 14 g in experiment A6 and 3 g for a total of 24g in experiment A8. Rotational speed adopted varied between 2.5 and 5 rpm, which translates into strain rates from 5.65 x 10^{-1} to 1.12 s^{-1}.

4.2.2. Results

The results of high temperature viscosity measurements on the HPG8Na20 melt (before any crystal was added) are presented in Tab. 4.8 and in Fig. 4.25 in a viscosity vs. temperature plot. With decreasing temperature from 1490.4°C to 977°C an increase of about 2.2 $\log_{10}$ units has been observed.

Table 4.8 Pure liquid viscosity data for HPG8Na20

T (°C)	1490.4	1439.0	1387.7	1336.4	1310.7	1285.0	1259.4	1233.7	1208.0	1182.4	1079.7	977.0
log η (Pa s)	0.79	0.93	1.09	1.25	1.34	1.43	1.52	1.61	1.70	1.80	2.33	2.92

Fig. 4.25 shows the viscosity vs. temperature plot for data from this study. For comparison, viscosity data for the same haplogranititc melt with different excess of sodium from Hess et al. (1995) and for Stromboli and Etna samples investigated in section 4.1 are also reported. Data from this study converge with data on HPG8Na20 from Hess et al. (1995) and are fitted by the same TVF equation proposed by the authors for this composition:

$$\log \eta = -2.38 + \frac{4178}{T(°K)-463} \qquad (4.10)$$

The results of the viscosity measurements on the synthetic suspension of HPG8Na20 composition are reported in Tab. 4.9. For experiments A5 and A6 all the measurements were performed at T=977°C, whereas for experiment A8 the measurements were run at two temperatures 977°C and 1080°C for the lower and higher crystal fractions, respectively, because of high viscosity achieved by the suspension in the two final particles addition steps (A8-20 and A8-24) and the related technical difficulties in removing the stirring spindle from the sample.

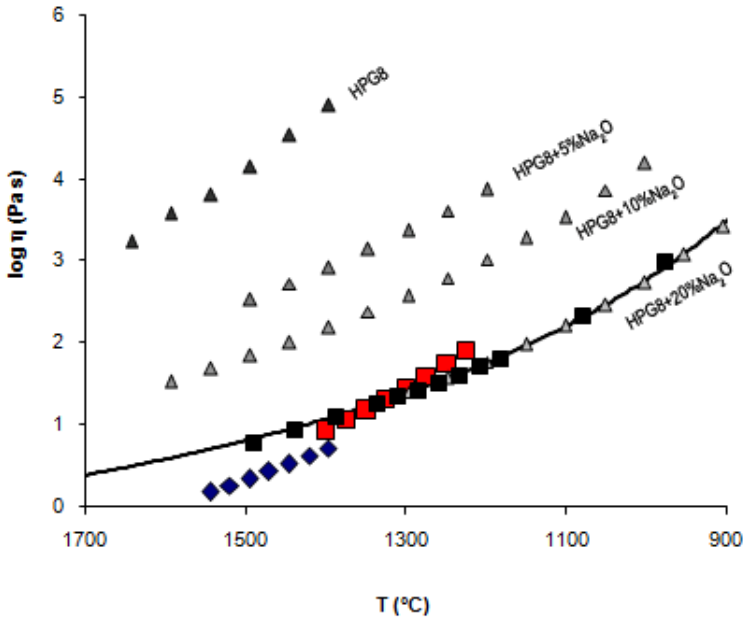

Fig. 4.25. Concentric cylinder viscometry data of the synthetic melt HPG8Na20 (black squares). Remelted samples from Stromboli and Etna (red and blue, section 4.1) and haplogranites with different sodium excess (0-20 wt%, triangles, from Hess et al. 1995) are reported for references. Black line represent the TVF fitting for HPG8Na20 from Hess et al. (1995).

Fig. 4.26 shows an example of the viscosity evolution with time (A5 experiment). Between each curve the sample has been removed from the furnace and new amounts of particles were added. Each curve shows a decrease in viscosity due to heating and relaxation of the suspension until the achievement of a stable value. The mean value of such viscosity plateau has been considered as indicative of the viscosity value of the suspension and reported in Tab. 4.9.

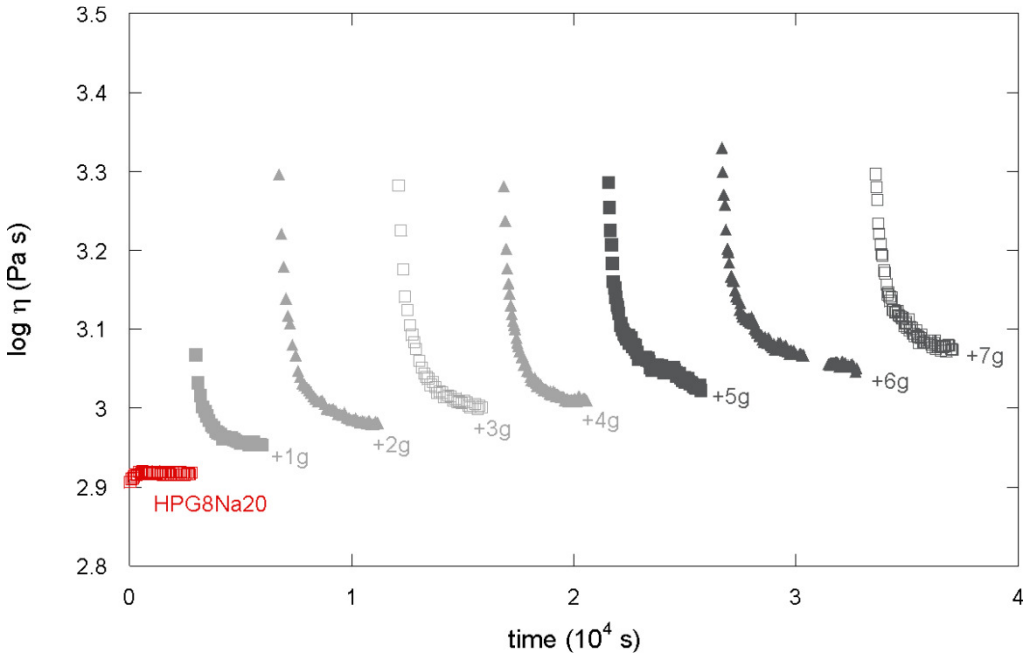

Fig. 4.26. Time variation of viscosity for experiment A5 in the HPG8+Na20 system.

The viscosity increased monotonously with increasing particle fraction in all the experiments up to 3.6 times the viscosity of the pure liquid in the more crystal-rich suspension (A8-24). Once the viscosity achieved the stable value, the rotational speed has been varied to check for any effect of the deformation rate on the viscous response of the suspension, indicative of Non-Newtonian behavior. No measurement showed a detectable variation of viscosity with changing strain rates, suggesting that at this experimental conditions all the investigated suspensions behaved as Newtonian fluids.

Table 4.9 Results of viscosity measurements in the HPG8Na20+corundum system

Sample	Added Crystals (g)	T (°C)	η (Pa s)	η_r	$\phi^{(n)}$	$\phi^{(ia)}$
A5-1	1	977.0	909.96	1.09	0.02	-
A5-2	2	977.0	967.96	1.16	0.03	-
A5-3	3	977.0	1017.67	1.22	0.05	-
A5-4	4	977.0	1032.77	1.24	0.07	-
A5-5	5	977.0	1069.67	1.29	0.08	-
A5-6	6	977.0	1143.14	1.37	0.10	-
A5-7	7	977.0	1204.65	1.45	0.11	0.12
A6-2	2	977.0	980.73	1.18	0.03	-
A6-4	4	977.0	1077.85	1.30	0.07	-
A6-6	6	977.0	1179.35	1.42	0.10	-
A6-8	8	977.0	1267.57	1.52	0.12	-
A6-10	10	977.0	1322.50	1.59	0.15	-
A6-12	12	977.0	1438.95	1.73	0.18	-
A6-14	14	977.0	1605.30	1.93	0.20	0.21
A8-4	4	977.0	1064.14	1.28	0.07	-
A8-8	8	977.0	1221.27	1.47	0.12	-
A8-12	12	977.0	1394.59	1.68	0.18	-
A8-16	16	977.0	2009.79	2.43	0.22	-
A8-20	20	1079.7	472.11	2.91	0.26	-
A8-24	24	1079.7	588.88	3.63	0.30	0.27

$^{(n)}$ nominal crystal fraction; $^{(ia)}$ image analysis crystal fraction

4.2.3. Crystal Fraction Determination

Two approaches were followed two determine the crystal fraction of the studied suspension: 1) calculation based on the physical properties of the liquid and corundum ('nominal' in Tab. 4.9) and 2) from textural analysis of thin sections of the post-run material ('image analysis' in Tab. 4.9).

For the first method, the densities of the glass and the corundum crystals at the investigated temperatures were calculated. The density of the HPG8Na20 glass was firstly determined at room temperature with the Archimedean buoyancy method in toluene and air (accuracy of ± 0.2%).

Then, the high temperature densities of the melt have been calculated using the thermal expansivity $dV/dT=12.28x10^{-4}$ cm^3 mol^{-1} $°C^{-1}$ for the glass and $dV/dT=26.45x10^{-4}$ cm^3 mol^{-1} $°C^{-1}$ for the melt (after Knoche et al.1995) and the glass transition temperature equal to 500.85 °C (after Hess et al. 1996) (Fig. 4.27). With increasing temperature, density of HPG8Na20 decreases from 2.491 g/cm^3 at room temperature to 2.321 and 2.299 g/cm^3 at 977°C and 1080°C, respectively. On the contrary, the density of corundum can be assumed constant (3.689 g/cm^3) in the investigated temperature range, due to its low thermal expansivity ($8.1x10^{-6}$ cm^3 mol^{-1} $°C^{-1}$; Fiquet et al., 1999). Given the weight of glass and particles, and knowing the high T density of the materials, the volume fraction of crystals can be easily calculated. The results are reported in Tab. 4.9. The crystal fraction increases continuously for each experiment up to maximum ϕ of 0.11, 0.20 and 0.30 for A5, A6 and A8 respectively.

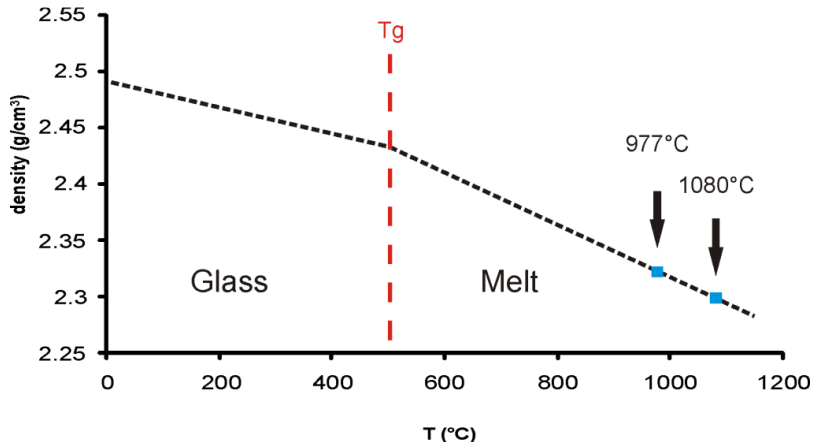

Fig. 4.27 Density vs. temperature relationship of HPG8Na20 material, calculated with thermal expansivities values given by Knoche et al. (1995) and assuming a glass transition temperature (Tg) of T=500.85°C (Hess et al., 1996). Blue squares represent the values at the investigated temperatures adopted for crystal fraction calculations.

At the end of the measurements the stirring spindle was removed and the sample was allowed to cool in air in the platinum crucible. The post-run products were then drilled and the cylindrical cores (20 mm diameter x 40 mm length) were sectioned at surfaces parallel to the rotational axis (Fig. 4.28).

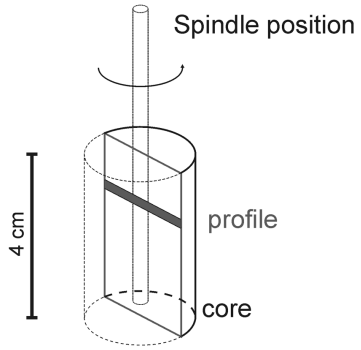

Fig. 4.28. Sketch of a sectioned post run product. Image analyses were performed along profiles orthogonal to the rotational axis.

Photomicrograph profiles were taken for each sample with an optical microscope along directions orthogonal to the rotational axis (see Fig. 4.28). The pictures, reported in Fig. 4.29, were digitalized, crystals were contoured and the crystal fraction was measured using ImageJ software on the binary images. The results are shown in Tab. 4.9 and show a good agreement with nominal values obtained by the physical properties of the materials. In particular, for experiments A5 and A6 the discrepancy is of only 1% crystal fraction, while it is slightly higher for experiment A8 (3% crystal fraction).

On this basis, the nominal crystal fraction has been retained to be representative of the real fraction, also for the intermediate measurement steps, in which no sample was collected and no direct measurement of crystal content could be performed through image analysis.

(a)

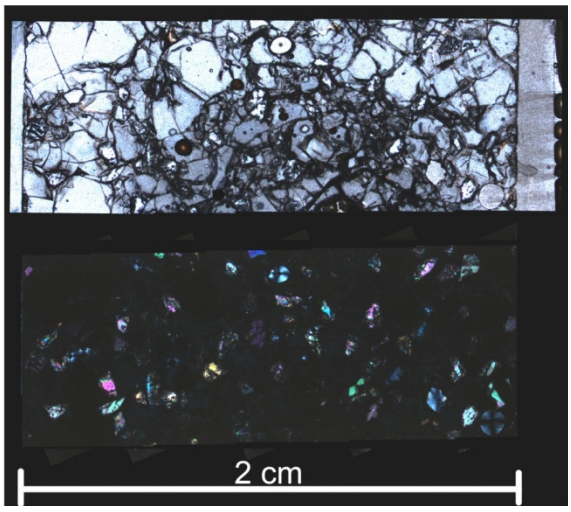

(b)

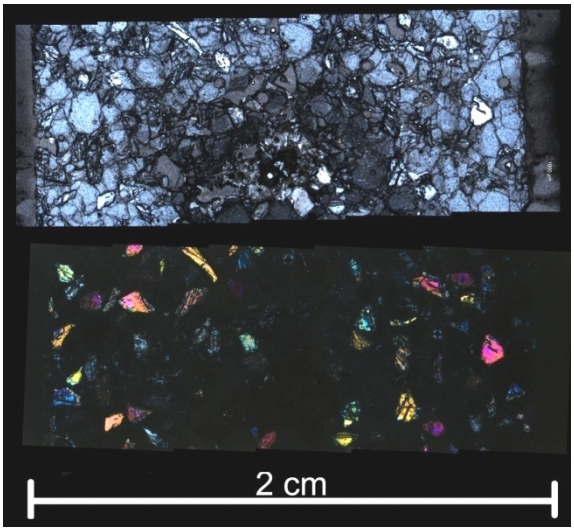

(c)

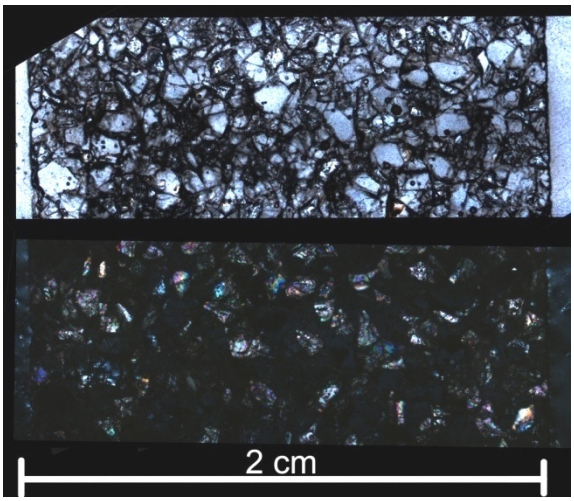

Fig. 4.29. Photomicrographs of post-run products A5 (a), A6 (b) and A8 (c) in plane and cross polarized light. Corundum particles are better observable in crossed light, due to higher interference color contrast. The crystal fraction obtained by digital analysis is ϕ=0.12, 0.21, 0.27 for A5, A6 and A8, respectively.

4.2.4. Fitting of Experimental Data

In Fig. 4.30 the viscosity variation with increasing crystal fraction is expressed as relative viscosity, that is the ratio between the measured apparent viscosity and the viscosity of the suspending liquid. The main advantage of the adopted method consists in a stronger control on the viscosity of the synthetic liquid, that does not change composition during measurements, as it is not subjected to crystallization and differentiation processes. The viscosity of the pure liquid has been determined at the measurement temperature before any particle was added; it is in perfect agreement with the values found by Hess et al. (1995) for the same melt composition and ranges

from 2.33 to 2.92 $\log_{10}$ Pa s at T=1080°C and T=977°C, respectively. Normalizing the measured apparent viscosity to these values, the obtained relative viscosities show a monotonous increase from nearly 1 to 3.6, for the most crystal rich sample (Tab. 4.9).

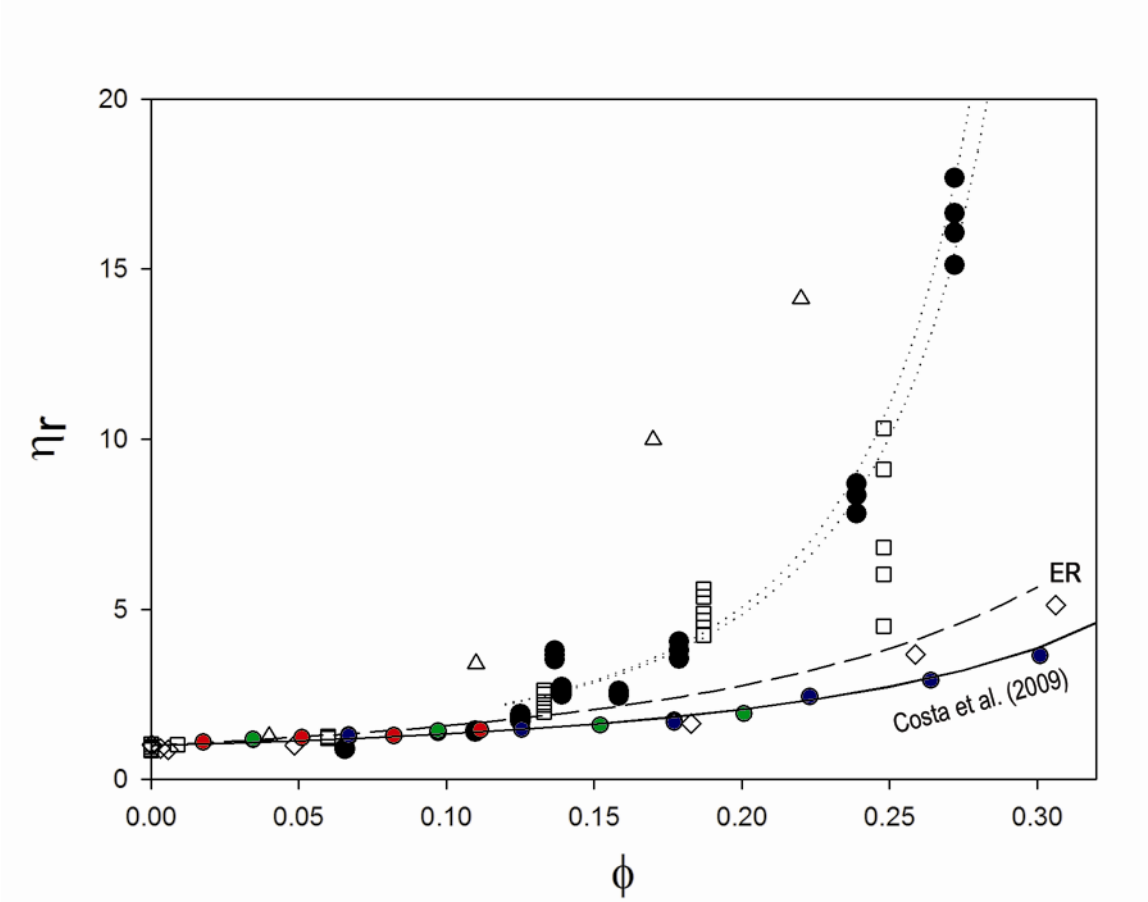

Fig. 4.30. Relative viscosity as a function of crystal fraction (ϕ). Colored circles represent data obtained from this study on the HPG8Na20+corundum system: A5 (red), A6 (green) and A8 (blue). Data from this study on Stromboli and Etna basalts (section 4.1; black circles), from Sato (2005; open triangles), Ishibashi and Sato (2007; open diamonds) and Ishibashi (2009; open squares) are also reported. Dotted lines refers to the fitting obtained for elongated particles on Etna and Stromboli (see section 4.1.8) at 0.14 and 0.02 s^{-1}; dashed line describes the Einstein-Roscoe equation (ER); solid lines shows the prediction equation by Costa et al. (2009) calculated for spherical particles at strain rate ranging from 0.565 to 1.12 s^{-1}.

For comparison, in Fig. 4.30 data from measurements on natural remelted samples from Stromboli and Etna (discussed in section 4.1) and from previous works on basaltic compositions (Sato, 2005; Ishibashi and Sato, 2007; Ishibashi, 2009) are reported.

The observed increase in relative viscosity of the HPG8Na20+corundum system is consistent with those observed in those study for crystal fraction up to ca. ϕ=0.10-0.12. However, for higher fractions those studies (with the exception of data from Ishibashi and Sato (2007)) show a rapid increase that lead to a departure from the Einstein-Roscoe equation and at above ϕ=0.12-0.15 the onset of a weak shear thinning Non-Newtonian behavior. However, the present study did not show

such departure from the Einstein-Roscoe equation and displayed values of relative viscosity 10 times lower than Stromboli suspension at ϕ= ca. 0.27. Moreover, no dependence of the apparent viscosity on the deformation rate was detected. As discussed in detail in section 4.1, the main reason of these differences is the particle shape anisotropy. Data from Stromboli and Etna and those from Sato (2005) and Ishibashi (2009) are relative to suspensions containing highly elongated particles. On the other hand, as mentioned above, the corundum crystals selected for this study have an average aspect ratio of 1.4 and the resulting suspension can be regarded as a first approximation as mono-dispersed spheres suspension.

The relative viscosity variation is lower than that predicted by the commonly used Einstein Roscoe equation (ER; eq. 2.5) with ϕ_m=0.6 (Marsh, 1981), whereas it is in good agreement with that predicted by the recent empirical model by Costa et al. (2009) for the adopted strain rates.

The polynomial equation

$$\eta_r = 1 + B\phi + B_1\phi^2 + \ldots \quad (4.7)$$

commonly used in the semi-diluted regimes with B=2.5 anb B_1=14.1 (Guth and Gold, 1938; Fig. 4.31) seems to reproduce the data only for ϕ_m<0.15, whereas it overestimates the relative viscosity at intermediate concentration and underestimates it at higher ϕ.

The fit of our data with the Maron-Pierce (MP) and with the Krieger-Dougherty (KD) models are reported in Fig. 4.31. The Maron-Pierce fit (with ϕ_m as the only adjustable parameter) yields a value of ϕ_m=0.6412 (R^2=0.988). The two parameter (ϕ_m and B) Krieger-Dougherty fit yield values of ϕ_m=0.6390 and B=3.10 (R^2=0.988). The similar values of ϕ_m and the exponent of the equations (2 for the MP and Bϕ_m=1.985 for the KD) leads to nearly overlapping curves (almost indistinguishable in Fig. 4.30). The determined value of ϕ_m are very close to the value of ϕ_m=0.64 determined for the random close packing of spheres by Rintoul and Torquato (1996) and to the value of ϕ_m=0.633 found by Mueller et al. (2010) in their measurements on spherical particles suspensions.

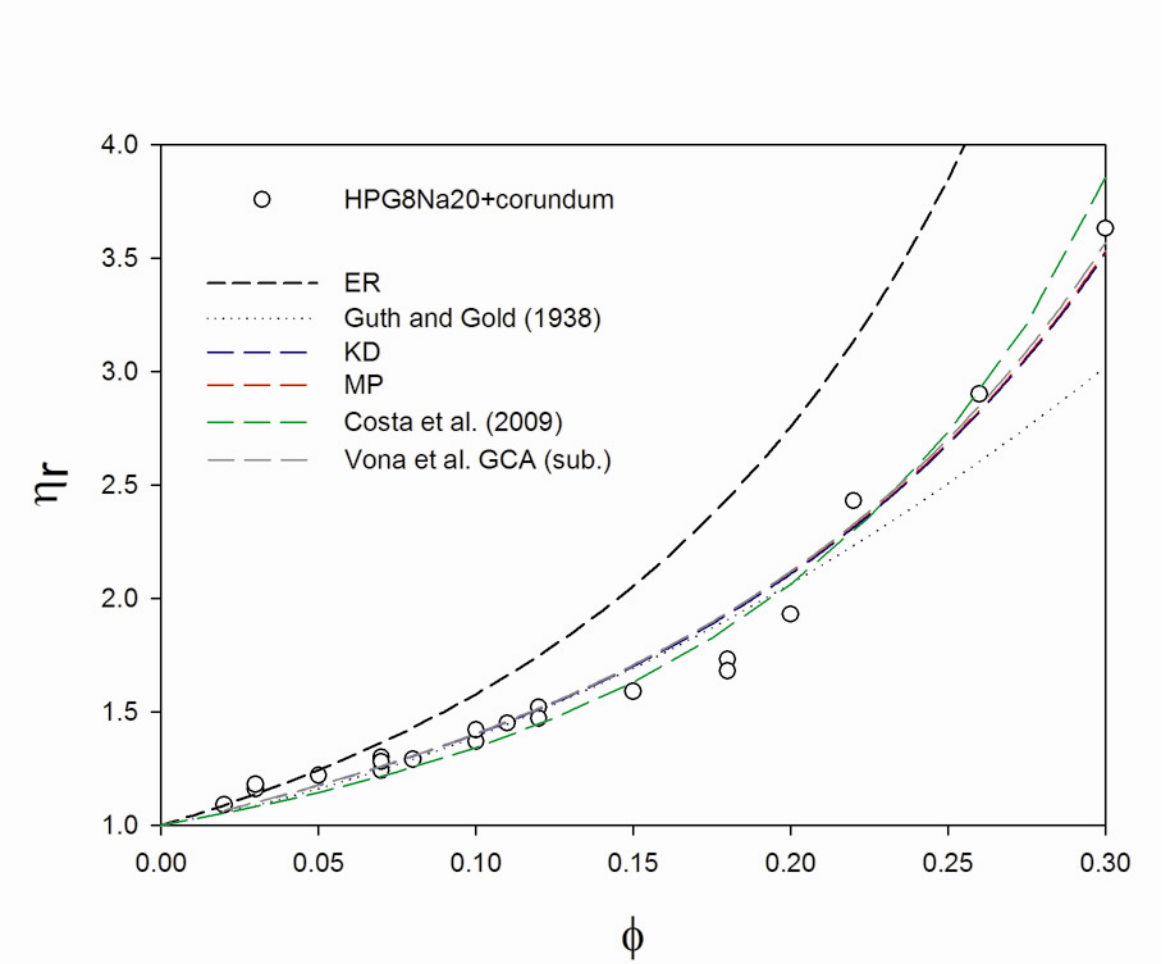

Fig. 4.30. Results of fitting of HPG8Na20+corundum system relative viscosity data (circles) as a function of crystal fraction (ϕ) in the dilute and semi-dilute fields.

Finally, the data set was fitted by the equation 4.5, proposed in section 4.1.8 (Vona et al. GCA, in Fig. 4.31), obtained by fitting of data from Stromboli and Etna, which takes into account the elongated shape of particles and the strain-rate dependence on viscosity. The fitting, with the Maron-Pierce derived value of ϕ_m=0.6412, and $B_1=2/\phi_m$ yields a α parameter value of 0.055 (R^2=0.983). This value is in agreement with that found for Stromboli and Etna (α =0.06) for different ϕ_m (0.37-0.41). Also the curve obtained by this fitting nearly overlaps the MP and KD curves, as there is no effect of strain rate (and hence the magnitude of α is small) in the studied suspensions. As in the previous discussions (section 4.1.8) we suggest that the effect of crystal size dispersion and crystal shape dispersion can be incorporated in the α parameter, and that the value of 0.055 can be reasonably taken as the minimum possible value, being it relative to homogeneous equant particles.

4.2.5. Summary

A new technique is proposed to investigate the high temperature rheology in synthetic silicate melts systems. Such method allows to measure viscosity of crystal-bearing melt in a concentric cylinder apparatus. Discrete amounts of particles are put at high temperature at the top of the melt and stirring produces sinking of the particles. Viscosity measurements are performed once the particles have reached their equilibrium position. Compared to the natural samples measurements (performed in dynamic crystallization regime), this technique has the advantage of allowing complete control on particle characterization (mean size, shape, size distribution, etc.) and on viscosity of the suspending liquid, as no differentiation process is involved.

Data obtained in this study at T=977°C and T=1080°C on a synthetic haplogranitic melt with 20% sodium excess (HPG8Na20) containing equant shaped corundum crystals indicate that the presence of crystals yield an increase of viscosity of a factor 3.6 at ϕ=0.30. Such increase is in agreement with that observed by many authors on spherical particles. The results have been compared to previous study on natural magmas, which yield a more rapid increase in relative viscosity, as well as the onset of Non-Newtonian behaviors. The reason of the different behavior is given by the elongated shape of the crystallizing crystalline phase (plagioclase and pyroxenes) in those measurements, and the consequent increase of interactions between particles, which leads to stronger increase in viscosity. The data set was fitted by the known Maron-Pierce and Krieger-Dougherty equations yielding values of maximum packing fraction of ϕ_m=ca. 0.64, comparable to the values presented in literature (ϕ_m =0.67, Rutgers, 1962a; ϕ_m =0.64, Rintoul and Torquato, 1996; ϕ_m =0.633, Mueller et al., 2010) for monodisperse suspensions of spheres. Data were also fitted by the KD derived equation proposed in section 4.1.8 and calibrated for highly anisotropic particles (plagioclase aspect ratio of ca. 6-7). The similar obtained values of α extend the validity and applicability of this equation to equant-shaped particles in the range of the studied strain rates, leaving the value of ϕ_m as the only needed parameter. More experiments are needed to better constrain the α parameter variation, especially in function of different size shapes and dispersions. Moreover a systematic study at different particle shapes and size distribution with the technique developed in this study could be used as a fundamental reference tool for the characterization of the effects of crystals on the viscosity of natural magmas.

5. Rheology of Crystal- and Vesicle-bearing Magma from Monte Nuovo

5.1. Introduction

The 1538 eruption of Monte Nuovo was characterized by two phases with contrasting eruptive styles. After a first stage of phreatomagmatic activity, which produced a tuff cone, the second phase was explosive and the products were emplaced on the top of the tuff cone (Piochi et al., 2005; D'Oriano et al., 2005; Di Vito et al., 1987). The second phase was more markedly magmatic and in contrast with the similar chemistry of the products with respect to the first phase, the textures of the scoria and the micro-crystals content were more variable reaching in some case 100 vol. % (D'Oriano et al., 2005). These differences in physical properties of magmas are due to different processes occurring during the rise inside the volcanic conduit, and reflect changes in the rheology of the erupted materials.

In order to characterize the rheology of partially crystallized trachytic magmas characteristic of the second stage of activity of the 1538 AD Monte Nuovo eruption, we performed a series of controlled deformation rate experiments using an unconfined uniaxial deformation apparatus to investigate the rheological response of cylinders of natural samples.

5.2. Sample Selection and Characterization

A detailed description of the deposits can be found in previous studies (D'Oriano et al., 2005; Piochi et al., 2005). Scoriaceous products of 10 to 50 cm in diameter were collected from the so called Lower Member (LM; D'Oriano et al., 2005) and from the two subunits (UM1 and UM2) of the Upper Member, distinctive for the first and the second stage of activity of the 1538 AD Monte Nuovo eruption, respectively.

Approximately 150 sample cores of 22-25.7 mm in diameter and 35–50 mm in lengths were drilled from samples collected in the field. The faces of the cylinders were parallelized by grinding to perform accurate geometrical measurements of the sample volumes. Open porosity was computed by taking the difference between the calculated volume of the cylindrical samples and the volume measured for the same sample using a helium pycnometer. Similarly, the bulk density was

quantified from the weight of the sample and the cylindrical volume, whereas the matrix density was calculated from the weight of the sample and the volume measured by the helium pycnometer.

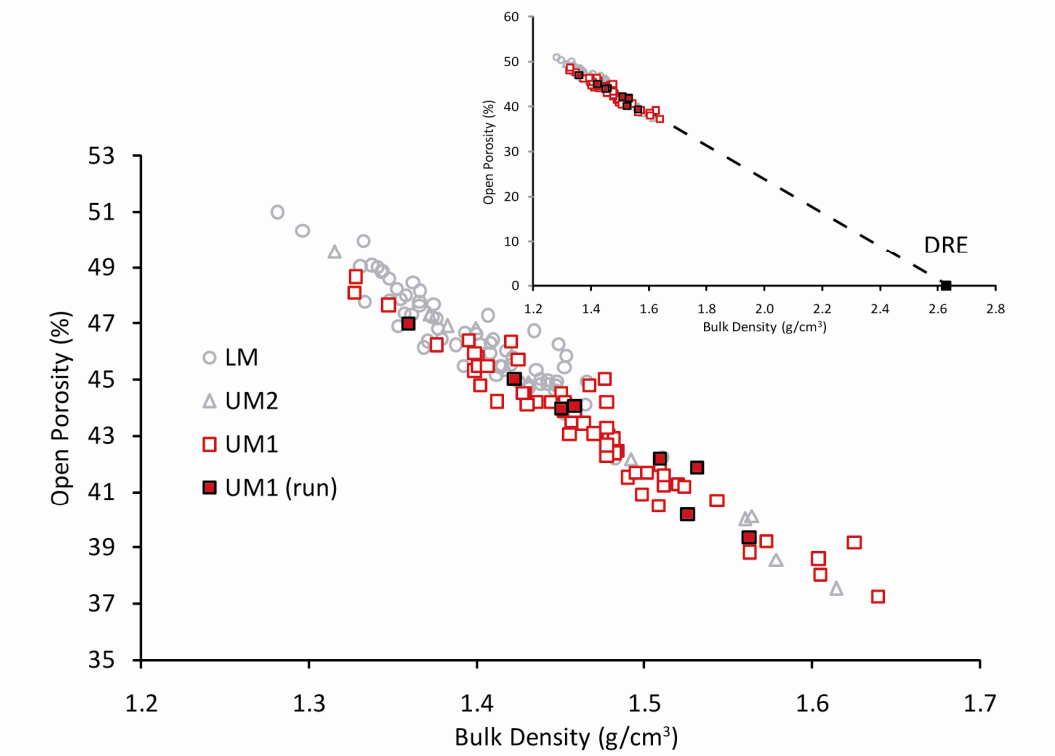

Fig. 5.1. Density measurements for the analyzed specimen from Monte Nuovo. Grey circles: LM samples; grey triangles: UM2 samples; red squares: UM1 samples. Filled red squares represent the UM1 samples used for viscosity determinations. Open porosity vs. Bulk Density. Open porosity was calculated taking the difference between the core volume and the volume measured by pycnometry. Sample Density is the ratio between the sample weight and the volume of the core. In the inset the value of the dense rock equivalent (DRE) measured by pycnometry on sample powder is reported.

All the analyzed specimen showed a bulk density ranging from 1.3-1.6 g/cm^3 (Fig. 5.1). Samples from the LM unit showed the higher average porosity ranging from 0.42-0.51%, compared to sample from the UM unit (UM1 and UM2) ranging from 0.37-0.50%. Considering the higher matrix density from LM samples (2.54-2.76 g/cm^3) compared to UM samples (UM1: 2.53-2.66 g/cm^3; UM2: 2.57-2.63 g/cm^3), the higher vesicularity observed in LM samples has been interpreted to be caused by higher number of fractures. For this reason, the experimental investigations were conducted on nine cores from the Upper Member (UM1) with a variation in open porosity ranging between 39 and 47%. The dense rock equivalent density (DRE) has been measured on sample powder and is 2.63 g/cm^3. The samples investigated in this work have been previously studied by Caricchi et al. (2008) in a work on the effect of crystals on the rheology of Monte Nuovo magmas. The analyses of the UM samples are reported in Tab. 1. Both bulk rock and matrix glass compositions are trachytic and the mineral assemblage is composed of dominantly plagioclase and K-feldspar, clinopyroxene, magnetite and biotite. The overall crystal fraction is $\phi = 0.47$.

Tab. 5.1. Electron Microprobe Analyses (wt%) of UM samples from Caricchi et al. (2008).

	Bulk Rock	Matrix Glass
SiO_2	60.33	61.66
TiO_2	0.43	0.57
Al_2O_3	19.39	19.48
FeO	3.23	3.55
MgO	0.24	0.34
MnO	0.22	0.25
CaO	1.79	1.11
Na_2O	5.85	4.85
K_2O	7.21	7.85
P_2O_5	0.02	0.04
Total	98.70	99.69

5.3. Experimental Results

Uniaxial deformation experiments were performed isothermically by deforming crystal- and vesicle-bearing cylindrical specimen at constant displacement rates (CDR) or at constant load (CL). Both methods produce constant strain rates measurements (Fig. 5.2).

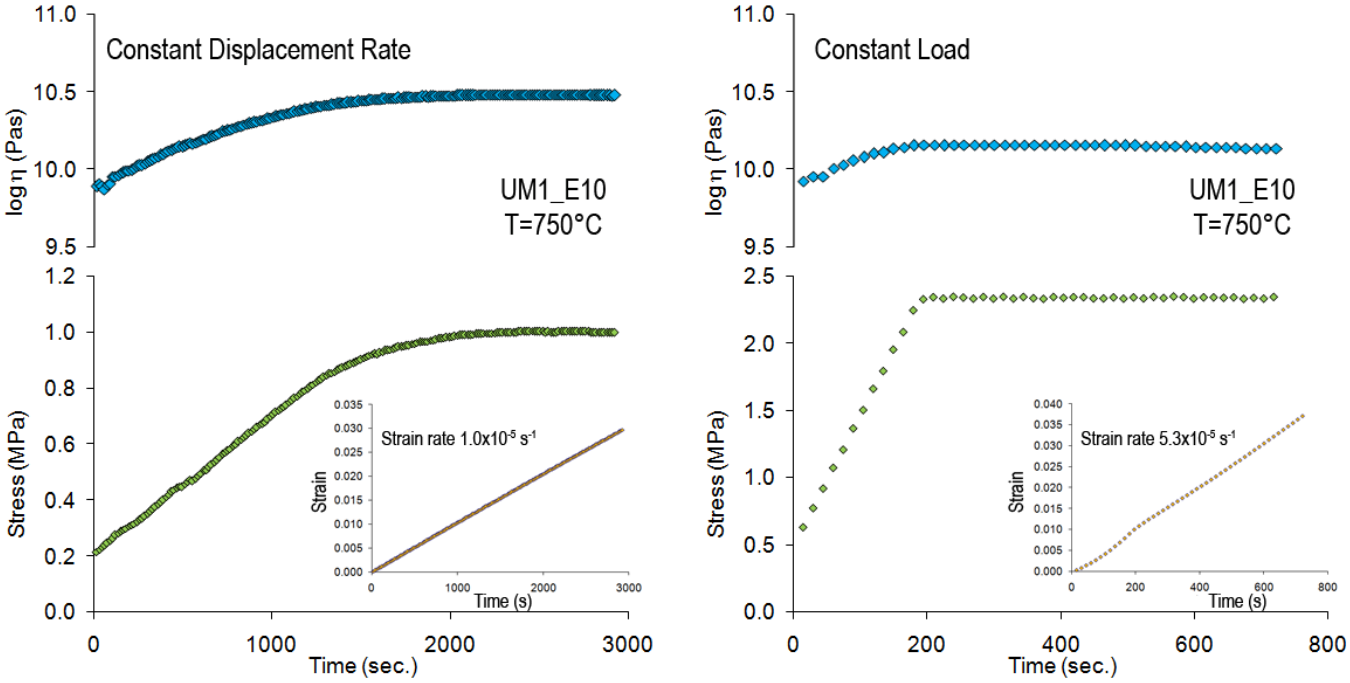

Fig. 5.2. Viscosity vs Time (upper diagram), Stress (due to the applied load) vs Time (lower diagram) and Strain vs Time (inset in the lower diagram) (the slope of this latter curve is the strain-rate) paths deriving from a constant displacement-rate (a) and a constant load (b) type of measurement on UM1_E10 sample at T=750°C. Stress in the figures is calculated as applied to the sample surface; viscosity is calculated after Gent (1960).

Table 5.2. Summary of the performed experiments

Sample	Method	T(°C)	Porosity (%)	Strain Rate (s^{-1})	Stress (MPa)	Total Strain (γ)	Log η_{matrix}	Log η_{eff}	Log η_{rel}
UM1_E4	CSR	600	0.39	*9.6E-06*	*25.25*	*0.051*	*13.59*	*11.87*	*-1.72*
UM1_E7	CSR	640	0.45	2.8E-06	8.52	0.023	12.41	11.96	-0.46
	CSR			3.0E-06	9.64	0.010	12.41	12.00	-0.42
	CSR			5.6E-06	12.32	0.027	12.41	11.81	-0.60
UM1_B15	CSR	650	0.44	9.1E-07	11.40	0.022	12.14	12.58	0.44
	CSR			5.7E-07	11.31	0.003	12.14	12.81	0.67
	CSR			3.2E-07	9.80	0.004	12.14	12.98	0.84
UM1_E1B	CSR	700	0.40	3.1E-06	4.08	0.015	10.91	11.60	0.69
	CSR			6.1E-06	4.73	0.015	10.91	11.39	0.48
	CSR			1.0E-06	2.42	0.007	10.91	11.86	0.95
	CSR			1.1E-07	1.55	0.001	10.91	12.69	1.78
UM1_E2A	CSR	725	0.42	9.8E-06	2.69	0.038	10.35	10.92	0.57
	CSR			5.8E-06	2.14	0.007	10.35	11.06	0.71
	CSR			2.8E-06	1.68	0.007	10.35	11.26	0.91
	CSR			9.8E-07	1.29	0.005	10.35	11.61	1.26
	CSR			1.9E-05	3.78	0.021	10.35	10.80	0.45
UM1_E10	CSR	750	0.47	1.0E-05	1.00	0.030	9.84	10.48	0.64
	CSR			1.0E-06	0.50	0.006	9.84	11.17	1.33
	CL			5.3E-05	2.34	0.037	9.84	10.14	0.30
	CSR			1.1E-05	1.16	0.048	9.84	10.50	0.66
	CSR			1.1E-06	0.49	0.005	9.84	11.14	1.30
	CSR			1.2E-07	0.34	0.001	9.84	11.86	2.02
	CSR			3.3E-06	1.33	0.063	9.84	11.06	1.22
UM1_B14	CSR	750	0.44	2.9E-05	2.44	0.038	9.84	10.39	0.55
	CSR			5.6E-05	3.24	0.033	9.84	10.25	0.41
	CSR			9.6E-05	4.16	0.056	9.84	10.11	0.27
UM1_E1A	CSR	800	0.40	2.9E-06	1.00	0.025	8.91	11.01	2.09
	CSR			5.7E-06	1.53	0.023	8.91	10.91	2.00
UM1_A12	CSR	800	0.42	1.1E-05	1.79	0.016	8.91	10.77	1.86
	CSR			3.1E-05	2.23	0.011	8.91	10.33	1.42
	CSR			5.8E-05	2.59	0.014	8.91	10.15	1.24
	CSR			*1.0E-04*	*1.89*	*0.432*	8.91	*9.25*	*0.32*

Values in italic print represent measurements at which a constant stress at flow was not achieved due to the failure of the sample (UM1_E4) or the onset of shear weakening (UM1_A12).

In CDR measurements (Fig. 5.2a), the stress needed to maintain a constant deformation increases with time until it reaches a stable value, whereas in CL measurements (Fig. 5.2b) the strain rate adjusts with time to a stable value under a fixed stress. The experiments were carried out at temperature varied between 600 and 800 °C and applied strain rates between 10^{-7} and 10^{-4} s^{-1}. The stress is calculated as the ratio between the applied force and the core surface. It is an apparent stress, that equals the effective stress applied on the sample only if the sample is vesicle-free. In fact, in a porous material the effective stress is distributed only on the solid matrix. The effective surface of stress application can be calculated, as a first approximation, as the ratio between V_{matrix} and core height. For the studied materials, which have a porosity of ca. 0.50, the effective stress would be about 2 times higher than apparent stress. However, for the purpose of this study, it is convenient to deal with apparent stress, that allows to compare data with vesicles-free materials and then to derive the net effect of the presence of vesicles on the rheology of magmas.

On each UM1 core, from 1 to 7 steps of deformation were performed at different strain rates. The results of the measurements are reported in Tab. 5.2.

All samples showed an elastic response followed by strain hardening (increase stress with increasing strain) and final flow at constant stress (Fig. 5.2). Two exception are represented by experiment UM1_E4 (run at T=600°C the lowest investigated temperature) and by experiment UM1_A12 (T=800°C) (Fig. 5.3). In UM1_E4 (Fig. 5.3a) the transition between viscous and brittle behavior has been crossed at strain rate of about 10^{-5} s^{-1} and stress of 25.25 MPa, resulting in the failure of the sample. On the other hand, the last deformation step in experiment UM1_A12 (Fig. 5.3b) was performed at strain rate of 10^{-4} s^{-1} and it lasted until the achievement of a total strain γ = 0.43, a strain much higher than those obtained on the rest of the experimental dataset (γ <0.07). The test showed an increase of stress up to a peak at 2.82 MPa and then a continuous decreasing of

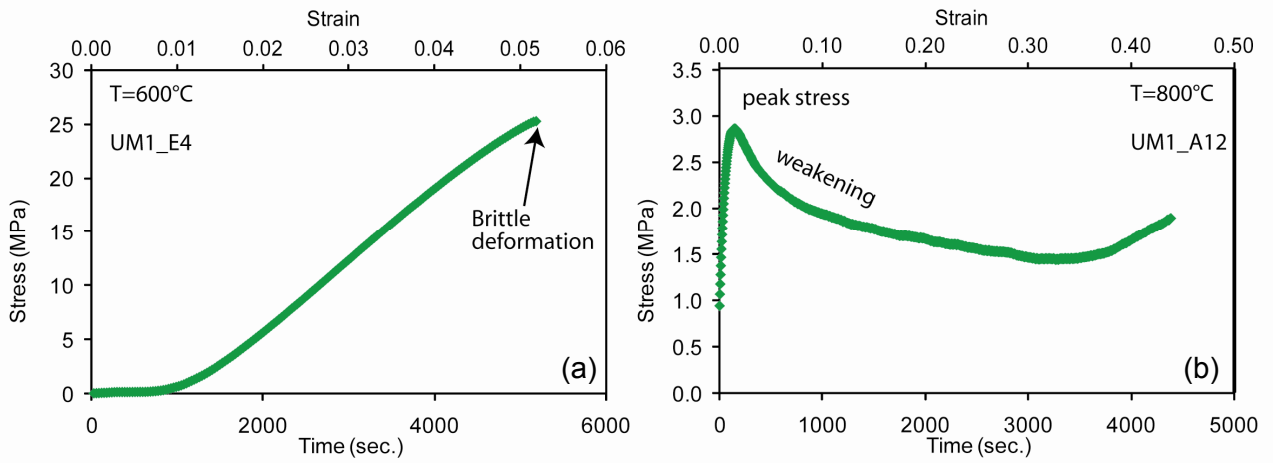

Fig. 5.3. Evolution of applied stress with increasing strain and time at (a) T=600°C (UM1_E4) and (b) T=800°C (UM1_A12).

stress with deformation increasing (stress weakening) and a stable value of stress at flow was not achieved.

On experiment run at T=650°C (UM1_B15) and on the two measurements performed at the lowest strain rate at T=700°C and T=750°C (UM1_E1B: $\dot{\gamma} = 1.1\text{x}10^{-7}$ s^{-1}; UM1_E10: $\dot{\gamma} = 1.2\text{x}10^{-7}$ s^{-1}) the displacement recorded by the device transducer was close to the minimum displacement that could be resolved by the instrument. As a consequence the measurements show high noise on data values due mainly to an apparent steplike (not continuous) deformation at the small scale. For this reason the accuracy of these measurements may be not satisfying and they will be treated as 'high uncertainity' measurements in the following sections.

In Fig. 5.4 the stress-strain rate relationships at flow condition of the deformation experiments are reported.

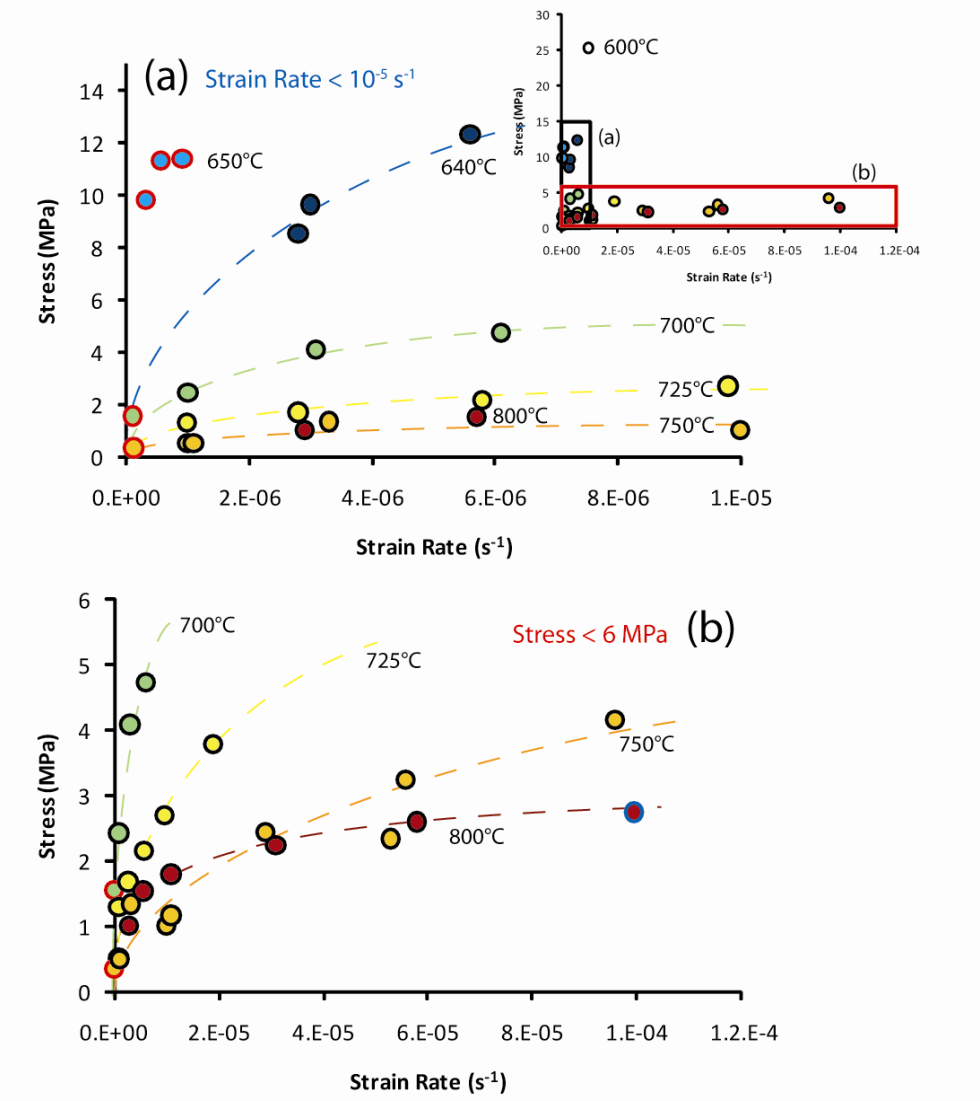

Fig. 5.4. Stress vs. Strain Rate plot for UM1 samples at different temperatures. For a clearer view the whole dataset (reported in the inset) is divided in two fields: high stress – low strain rate (a) and low stress – high strain rate (b). Experiment UM1_E4 run at T=600°C is present only in the inset due to the high stress reached before the onset of brittle behavior. Red-outlined circles represent measurement with low accuracy (see text).

In a logarithmic representation of stress vs. strain rate at flow (Fig. 5.5), a log linear relation can be observed at T=640-750°C. As a first approximation, the lines relative to this temperature interval are subparallel and seem to be equally spaced. Also the measurements at 800°C show a log linear correlation, before the onset of shear weakening at $\dot{\gamma} = 1\text{x}10^{-4}$ s^{-1}, but are characterized by a less steep slope.

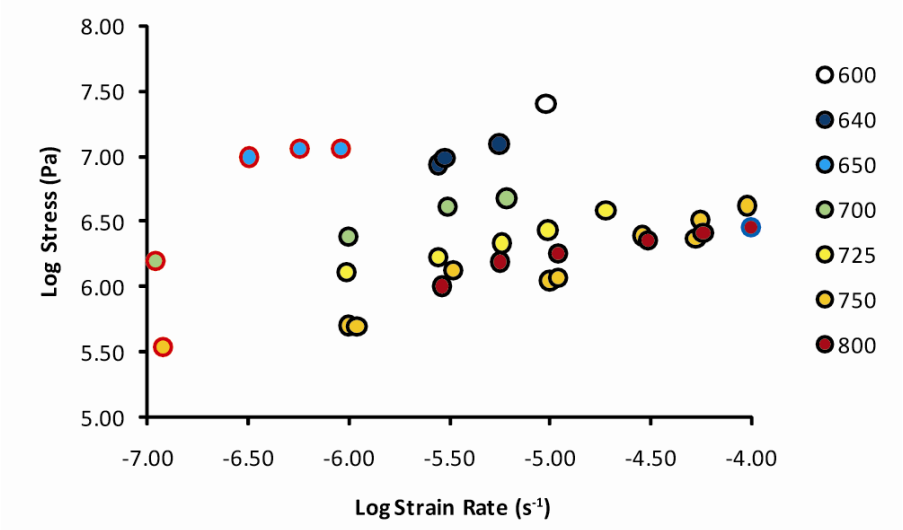

Fig. 5.5. Diagram illustrating the maximum stress reached during flow of the material at different temperatures (600°C-800°C).

From stress and strain rate data, the effective viscosity has been calculated during data collection using "no slip" (Eq. 5.1) and "perfect slip" (Eq. 5.2) models by Gent (1960) (Fig. 5.2).

$$\eta_{ns}(Pa \cdot s) = \frac{2\pi L^5 F}{3V\frac{\partial L}{\partial t}(2\pi L^3 + V)} \quad (3.5)$$

$$\eta_{ps}(Pa \cdot s) = \frac{L^2 F}{3V\frac{\partial L}{\partial t}} \quad (3.6)$$

The values of effective (real) viscosities at flow conditions are reported in Fig. 5.6, and the values of apparent viscosity (calculated as $\eta_{app} = \sigma/\dot{\varepsilon}$) are also reported for comparison. While apparent viscosities are always higher of about 0.5 $\log_{10}$ units, viscosities calculated by the "no-slip" and the "perfect-slip" models are almost identical. The discrepancies are below 0.03 $\log_{10}$ units at all investigated conditions. Based on the geometry of the run-product cores, in particular those derived by higher strain experiments, which showed some bulging, we chose the "no-slip" end-member model to describe the rheology of the studied samples.

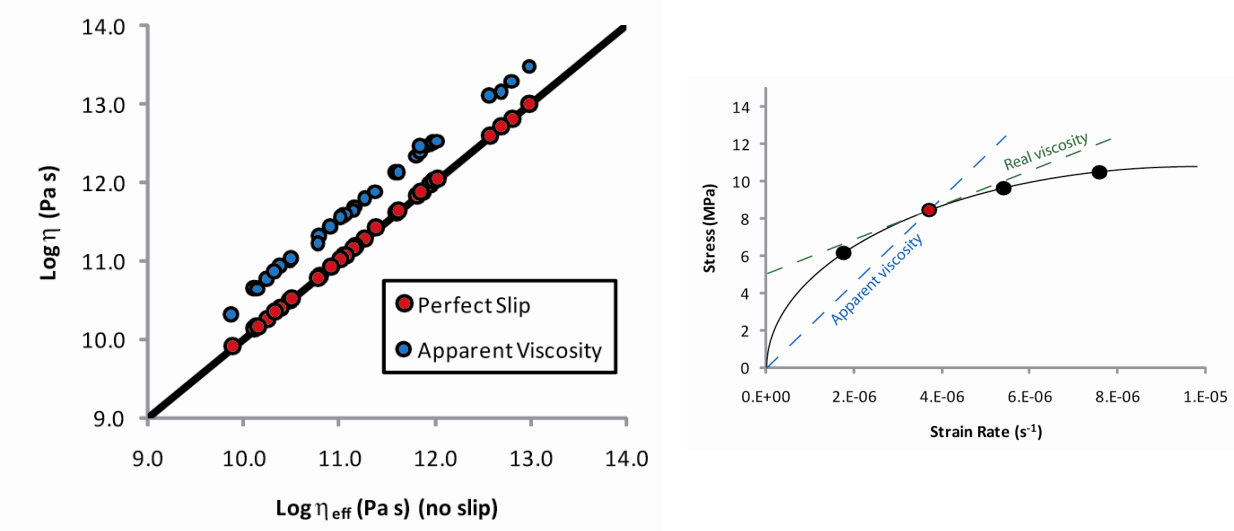

Fig. 5.6. Effective viscosity determination. (left side) Almost identical values were obtained by "no slip" (x axis) and "perfect slip" (red circles) end-member models of Gent (1960). On the contrary apparent viscosities (blue circles) show a sistematic shift of ca. 0.5 $\log_{10}$ units. (right side) Theoretical difference between apparent and real (or effective) viscosity for a shear thinning material.

The effect of strain rates on the viscosity of natural magma from Monte Nuovo is reported in Fig. 5.7. At all studied temperature, the viscosity decreases monotonously with increasing strain rate. A maximum decrease was observed for experiment UM1_E10 run at T=750°C where viscosity at $\dot{\gamma}=10^{-6}$ s^{-1} is 1.1 $\log_{10}$ units higher than at $\dot{\gamma}=5.3 \times 10^{-5}$ s^{-1}. In the range of deformation rates of this study Monte Nuovo magma behaves always as shear thinning rheological material and no bingham-like behavior (i.e the viscosity is not more dependent on the applied strain rate) has been observed also at the highest investigated strain rates (10^{-4} s^{-1}).

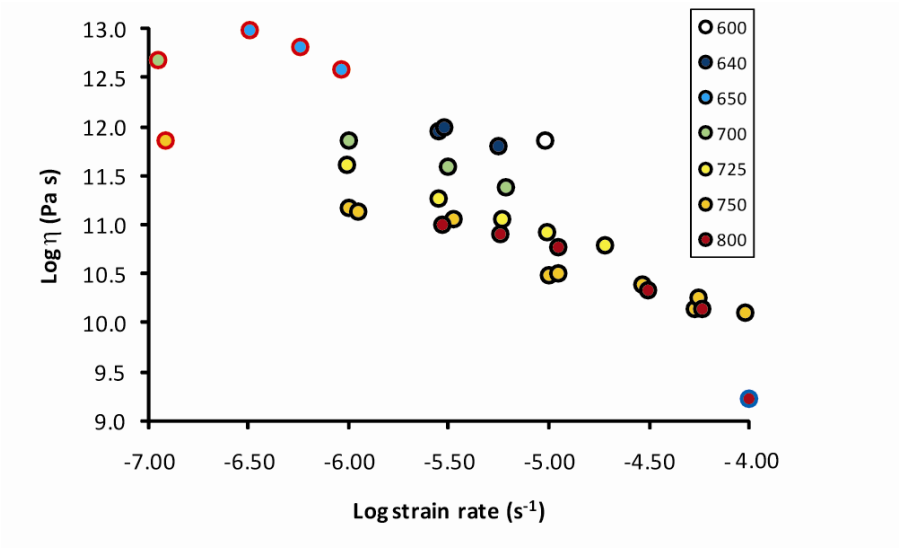

Fig. 5.7. Variation of viscosity (computed with the "no slip" model by Gent (1960) as a function of applied strain rate.

5.4. Post-run Products Characterization

At the end of the measurements, the experimental cores were analyzed to determine the change in porosity due to deformation. Volcanic rocks contain two types of porosity: connected and isolated. Connected is defined as the volume fraction of pores that are connected to each other and can be physically accessed by gas or fluid. Isolated porosity is defined as the volume fraction of porosity that is isolated by the skeletal framework and cannot be accessed by gas or fluid. The total porosity of a rock (Φ_T) is given by the sum of connected and isolated porosities and is:

$$\Phi_T = \frac{V_{\Phi_T}}{(V_{DRE} + V_{\Phi_T})} \tag{5.2}$$

where V_{DRE} is volume of the dense rock equivalent (e.g., powder) and $V_{\Phi T}$ is the volume of the total pore space in the sample. Connected (Φ_C) and isolated (Φ_I) porosities are given by:

$$\Phi_C = \frac{V_{\Phi_C}}{(V_{DRE} + V_{\Phi_C} + V_{\Phi_I})} \tag{5.3}$$

$$\Phi_I = \frac{V_{\Phi_I}}{(V_{DRE} + V_{\Phi_I})} \tag{5.4}$$

The corresponding densities are defined on the basis of how they are measured.

The dense rock equivalent (DRE) density of the sample (ρ_{DRE}) is the density of the rock framework of the sample alone (e.g., no porosity) and was measured on samples of rock powder by He-pycnometry. Powdering the sample ensures that there are no pores and that the He-pycnometry experiment measures the true volume (V_{DRE}) of a fixed mass of rock powder (M_R).

$$\rho_{DRE} = \frac{M_R}{V_{DRE}} \tag{5.5}$$

The skeletal density (ρ_{sk}) is the density of the rock and the isolated porosity. Using He-pycnometry, the gas infiltrates the samples connected pores but cannot access the isolated pores. Therefore, the He-pycnometry experiment measures the volume of the rock/solid framework and the isolated (inaccessible) pores (e.g., the skeletal volume: $V_{DRE} + V_{\Phi I}$).

$$\rho_{sk} = \frac{M_R}{(V_{DRE} + V_{\Phi_I})} \quad (5.6)$$

The bulk density (ρ_B) was measured on cores of rock samples using the mass (M_R) and a bulk volume estimated from the geometry of the core ($\pi * L * r^2$), when the cylindrical shape was preserved (e.g. pre-run cores and low strain measurements). For high strained post-run cores (UM1_E10, UM1_B14 and UM1_A12), which showed a departure from perfect cylindrical shape due to compression and bulging, the bulk volume was determined by Archimedean buoyancy on the samples coated with paraffin. The paraffin coatings were performed by immersing the sample in a bath of liquid paraffin (T=100 °C). Samples were weighed before and after the paraffin coating, in order to calculate the mass of the applied paraffin. The paraffin density (0.834 g/cm^3) was used to extract the bulk volume of the samples. The bulk volume incorporates the volume of the rock (V_{DRE}), as well as, the volume of connected ($V_{\Phi C}$) and isolated ($V_{\Phi I}$) porosity.

$$\rho_B = \frac{M_R}{(V_{DRE} + V_{\Phi c} + V_{\Phi_I})} \quad (5.7)$$

The results of porosity and density determinations of the experimental material at pre- and post-run conditions are reported in Tab. 5.3.

The effect of the deformation on the amount of vesicles of the investigated materials is quite small, as all the post-run products show a total porosity reduction ranging from about 0-1.5% compared to the starting material (Fig. 5.8). One only exception is given by the high strained experiment UM1_A12, for which a decrease of about 12% was measured. However such a value is associated to a large error derived from technical difficulties in the paraffin coating procedure due to the strongly irregular shape of the product. However, because the main part of the strain was achieved during the last deformation segment at strain rate of $1x10^{-4}$, we retain that in all the other segments the sample undergone a similar porosity reduction as sample UM1_E1A, run at the same experimental temperature. Another uncertainty could be associated to the measure on sample UM1_E4, of which only a part of the original core was recovered after the brittle failure. Fig. 5.6 shows that the total porosity decreases both in term of isolated and connected porosity, roughly as a function of the strain of the material. Considering that the porosity of the starting materials varies of about ±4% (Fig. 5.1), we can conclude that, with the above mentioned exceptions, at the experimental conditions of this study (i.e. low strain), the evolution of porosity with time during

deformation tests could have a secondary role in determining the rheological properties of the samples.

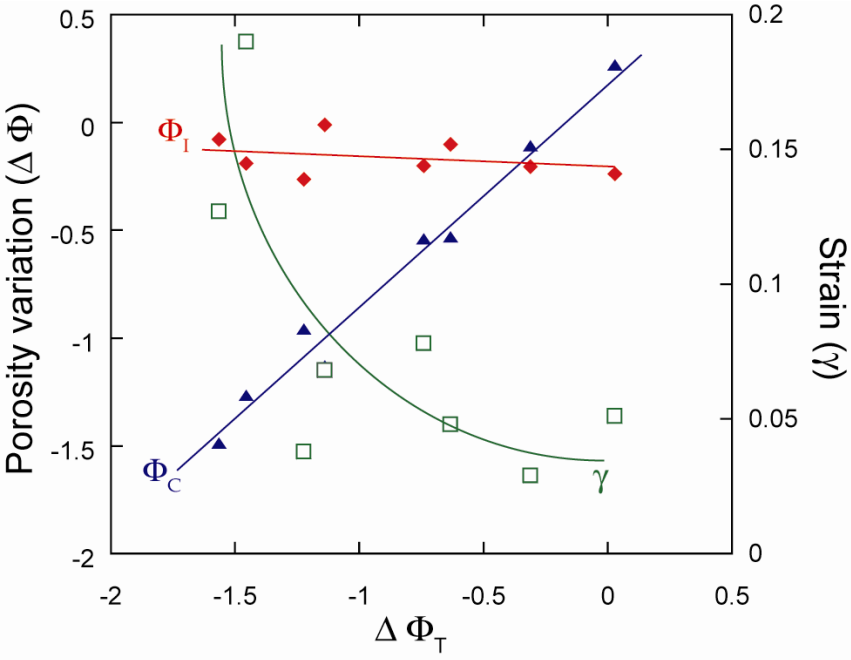

Fig. 5.8. Post-run isolated (Φ_I: red diamonds) and connected (Φ_C: blue triangles) porosity variation of investigated samples as a function of total porosity variation (Φ_T) and strain (γ). High strained sample UM1_A12 is not reported due to high uncertainty in the post-run porosity determination.

Table 5.3. Porosity and density determinations of investigated materials.

		Pre-run					Post-run					
	T (°C)	ρ_B	ρ_{sk}	Φ_T	Φ_C	Φ_I	ρ_B	ρ_{sk}	Φ_T	Φ_C	Φ_I	Total Strain (γ)
UM1_E4	600	1.563	2.576	40.56	39.34	1.22	*1.56*	*2.586*	*40.59*	*39.61*	*0.98*	*0.051*
UM1_E7	640	1.423	2.587	45.90	45.02	0.87	1.452	2.589	44.76	43.89	0.86	0.068
UM1_B15	650	1.459	2.578	44.52	43.41	1.11	1.467	2.587	44.21	43.31	0.91	0.029
UM1_E1B	700	1.542	2.549	41.36	39.52	1.84	1.574	2.562	40.13	38.56	1.58	0.038
UM1_E2A	725	1.524	2.595	42.03	41.25	0.77	1.544	2.604	41.29	40.72	0.57	0.078
UM1_E10	750	1.359	2.563	48.30	46.96	1.34	1.398	2.574	46.84	45.70	1.15	0.190
UM1_B14	750	1.477	2.589	43.81	42.93	0.88	1.519	2.593	42.24	41.44	0.80	0.127
UM1_E1A	800	1.499	2.549	42.97	41.19	1.79	1.516	2.554	42.34	40.65	1.69	0.048
UM1_A12	800	1.521	2.610	42.16	41.73	0.43	*1.841*	*2.611*	*29.99*	*29.49*	*0.50*	*0.432*

Densities (ρ_B and ρ_{sk}) are expressed in g/cm^3; Porosities (Φ_T, Φ_C, Φ_I) are in vol%. Values in italics print represent measurements with high uncertainities.

5.5. Fitting of Experimental Data

To derive a general flow law for the natural porous samples from Monte Nuovo eruption, stress (τ) and strain rate ($\dot{\gamma}$) experimental data were fitted using the three parameter Herschel-Bulkley (Herschel and Bulkley, 1928):

$$\tau = \tau_0 + K\dot{\gamma}^n \quad (5.6)$$

where τ_0 is the yield stress (Pa) below which there is no flow, K is the flow consistency (which takes the same values as η evaluated at $\dot{\gamma}$=1 s^{-1} and is expressed in Pa s) and n is the flow index (dimensionless) which defines the degree of non-Newtonian behavior. When τ_0=0 and n=1, the model describes a Newtonian fluid; when τ_0>1 and n=1, the model describes a Bingham fluid, and when τ_0=0 and n<1 or n>1, the model describes respectively a pseudoplastic (shear thinning) or a dilatant (shear thickening) fluid. Characterizing a liquid in terms of these three parameters gives a much richer description of its rheology than is possible with a single value of apparent viscosity.

Data obtained at $\dot{\gamma}$=10^{-7} s^{-1} and from UM1_A12 at $\dot{\gamma}$=10^{-4} s^{-1} were not included in the fitting. The results of the data fitting are reported in Tab. 5.4. The fitting is good across the whole dataset (R^2=0.955-0.991) and the accuracy increases with increasing temperature, mainly as a consequence of the wider investigated range of strain rates (Fig. 5.9).

At all the temperatures the value of yield stress τ_0 is approximately equal to zero (τ_0=0.0003-0.008 Pa), hence the parametrization reduces to that of a simple two parameters power law equation:

$$\tau = K\dot{\gamma}^n \quad (5.7)$$

Tab. 5.4. Fitting parameter of the Herschel-Bulkely model

T (°C)	τo (Pa)	log K (Pa s)	n	R^2
640	2.86e-4	9.56	0.470	0.955
700	1.02e-3	8.53	0.353	0.964
725	8.28e-3	8.68	0.447	0.991
750	2.29e-4	8.89	0.562	0.981
800	1.48e-3	7.49	0.252	0.981

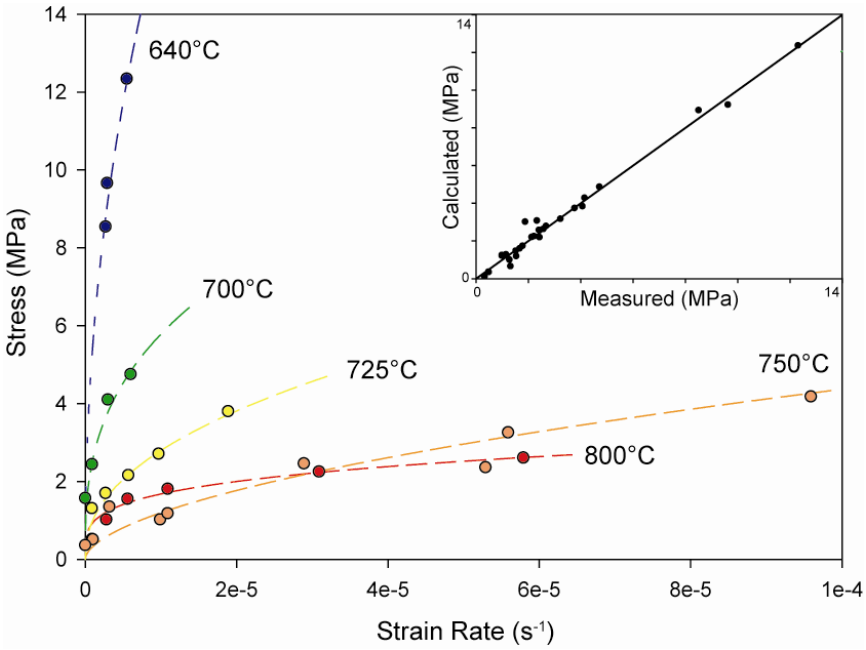

Fig. 5.9. Stress vs. Strain Rate diagram showing the results of data fitting with the Herchel-Bulkley equation (dotted lines) in the temperature range 640-800°C (see table 5.4 for fitting parameters). The inset shows the comparison between measured and calculated values of stress in MPa.

In Fig. 5.10 the flow parameters are reported as a function of temperature. No simple relation can be extracted between parameters and T. In general, flow consistencies decrease with increasing temperature from K=9.56 $\log_{10}$ unit at T=640°C to K=7.49 $\log_{10}$ unit at 800°C, while flow index n is in the 0.46±0.1 range at T<750°C, while it assumes a lower value at T=800°C (n=0.25).

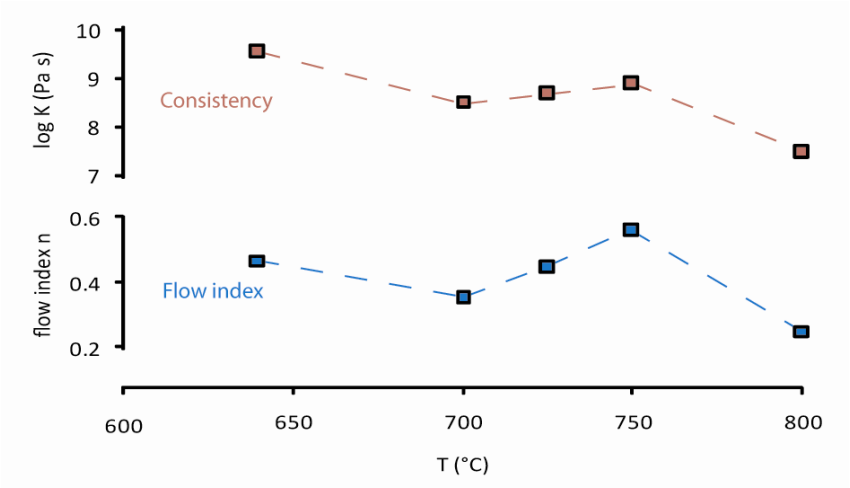

Fig. 5.10. Herschel-Bulkley parameters at the different experimental temperatures.

5.6. Discussion

The principal results of this study indicate that the Monte Nuovo magma behaves as a non-Newtonian (shear thinning) fluid at T=640-750°C at strain rates between 10^{-6} and 10^{-4} s^{-1}. Only one experiment (UM1_E4) performed at lower temperature (T=600°C) and $\dot{\gamma}=10^{-5}$ s^{-1}, showed a pure brittle behavior. At the highest investigated temperature (T=800°C), which is close to the estimated temperature of Monte Nuovo eruption (850±40 °C, Piochi et al., 2005; Caricchi et al., 2008), at strain rate of 10^{-4} s^{-1} the onset of stress weakening (continuous decreasing of stress with increasing deformation) was observed. Knowing the position of the onset of stress weakening is important because beyond this threshold the application of a fixed stress to the material can induce a strong acceleration of the flow process. Post-run analyses of the sample where stress weakening was observed showed clear evidence of strain localization (concentration of strain in a discrete portion of the material), revealed by the preferential alignment of crystals. Moreover, macroscopic fractures were observed, indicating that the measurement was performed at the limit between the plastic and the brittle field.

With the above mentioned exception, shear thinning behavior has been observed in all the measurements, including those performed at the lower temperatures and strain rates. Caricchi et al. (2008) studied the net effect of crystals on the rheology of Monte Nuovo. The study was performed on the same natural samples of the present work, after annealing of the starting materials through hot isostatically pression (HIP) in order to remove any porosity. Measurements were performed with a Paterson apparatus, at slight lower temperatures (T=550-630°C) and slight higher strain rates (between 10^{-6} and 4 x 10^{-4} s^{-1}). Caricchi et al. (2008) performed the measurements at confined pressure, hence avoiding the loss of structural H_2O from the glass during the experiments (0.86-1.54 wt%). The results of their experiments indicate that the vesicles-free crystal-bearing magma from Monte Nuovo has a Newtonian behavior at $\dot{\gamma}<10^{-4}$ s^{-1}, followed by non-Newtonian (shear thinning) and finally brittle behavior with increasing strain rates. In the present study, none of the measurements showed Newtonian behavior, even those performed at comparable temperature and low strain rate (i.e. UM1_E7; T=640°C) thus suggesting that a first effect of the presence of vesicles in the samples is that of reducing the Newtonian field and expand the field on shear thinning behavior.

In order to evaluate the combined effect of crystals and vesicles on the rheology of Monte Nuovo, data were normalized to the values of viscosity of the suspending liquid matrix. The viscosity of the glassy matrix of Monte Nuovo has been previously investigated as a function of

temperature and water content by Giordano et al. (2004) and a refined VTF parameterization was proposed by Giordano et al. (2009):

$$\log(\eta) = A_{VFT} + \frac{B_{VFT}}{T(K) - C_{VFT}} \quad (5.6)$$

where the pre-exponential factor A_{VFT} is a constant independent of composition (Russell et al., 2003; Giordano et al., 2008) and is equal to -4.55 and the effect of water (expressed in mol%) is incorporated into the B_{VFT} and C_{VFT} parameters:

$$B_{VFT} = 10449 - 101.63 \cdot H_2O \quad (5.7)$$

$$C_{VFT} = 303.7 - 193.8 \log(1 + H_2O) \quad (5.8)$$

The presence of H_2O leads to a general decrease of viscosity and the effect is considerably more pronounced at lower temperatures (Fig.5.11). In fact, at the investigated experimental temperatures (600-800°C) , 1 wt% of H_2O yields a decrease in the suspending liquid viscosity of 3.7 $\log_{10}$ units at 600°C and 2.2 log10 units at 800°C, compared to the anhydrous composition. Although the natural samples contain about 1 wt% of H_2O (cfr. Caricchi et al., 2008), we assume that for long duration measurements (1-2 hours) at unconfined conditions, almost all the water will exsolve. For this reason, we assumed that the liquid matrix is virtually anhydrous.

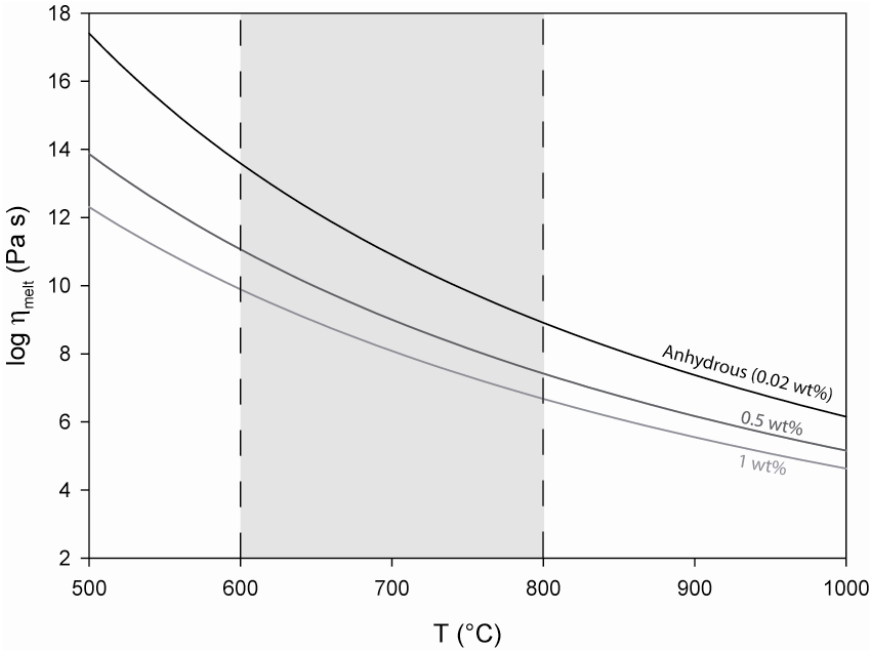

Fig. 5.11. Plot of the logarithm of liquid matrix viscosity as a function of temperature. Lines are calculated from Eq. 5.6-8 by Giordano et al. (2009).

The measured effective viscosity of the multiphase magma is always higher than the viscosity of the liquid matrix (Fig. 5.12a), except at T=640°C, where at the measured viscosity of 11.81-12 log Pa s corresponds a liquid viscosity of 12.41 log Pa s.

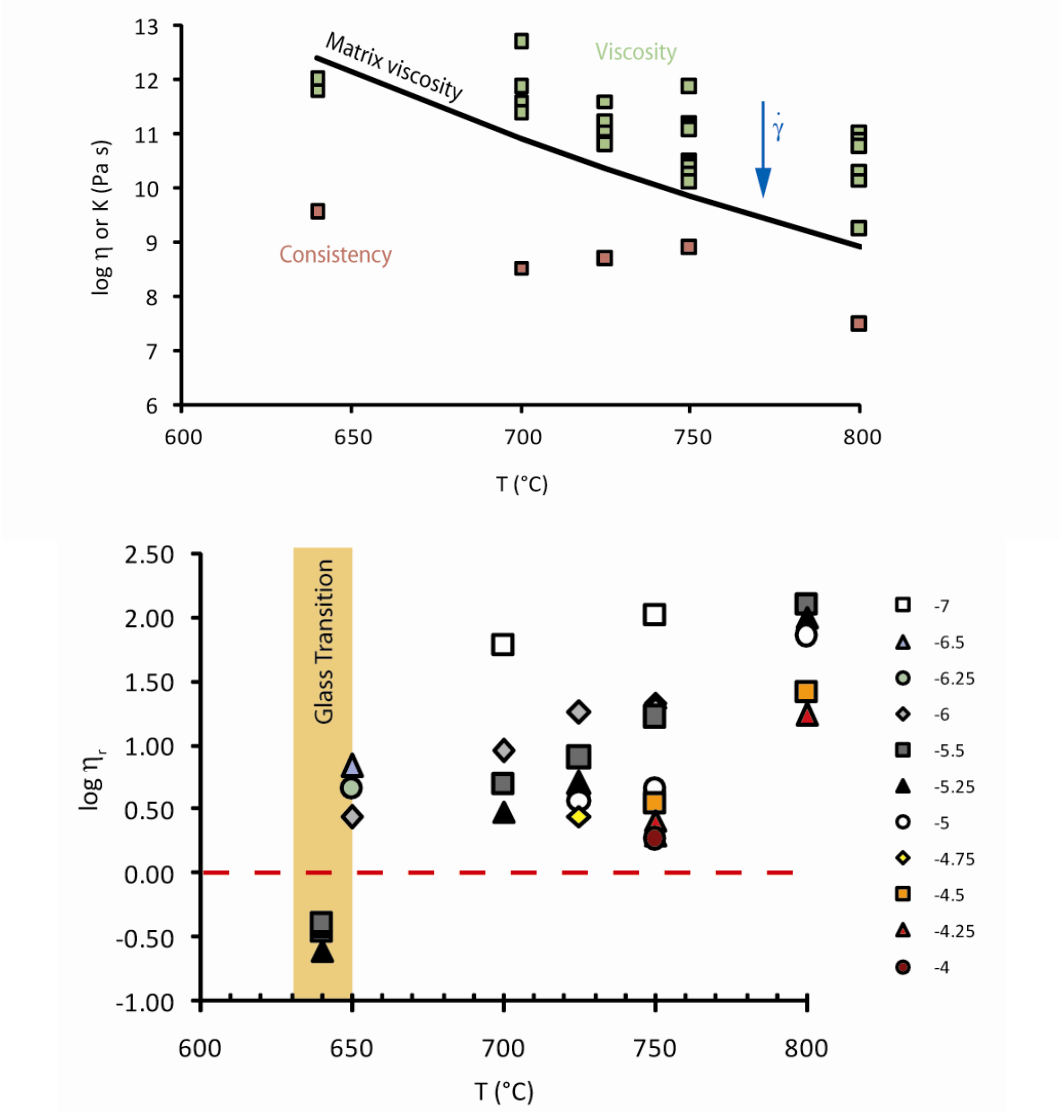

Fig. 5.12. (a) Comparison between viscosities of multiphase materials (green squares) and that of the suspending fluid (solid line). The value of consistency *K* are also reported (red squares). (b) Relative viscosities as a function of temperature at log strain rates between -7 and -4. Yellow area defines the glass transition interval after Giordano et al. (2005).

In Fig. 5.12a the magma consistencies are also reported. Consistency values are always lower than the viscosity of the liquid matrix at the same temperature. If consistencies are regarded as apparent viscosities at $\dot{\gamma}$=1 s^{-1}, the shifting between their values and those of the measured viscosity is a function of the degree of Non-Newtonian behavior (expressed by the flow index *n*) and the experimental strain rate range. For this reason, comparing consistency values to the viscosity of the liquid allows to obtain an absolute characterization of the material that is not connected to the

deformation rates at which each experiment was performed. The maximum relative consistencies K_r (expressed as K/η_{matrix}) are observed at T=640°C (K_r=-2.85 $\log_{10}$ units). With increasing temperature, the discrepancy between the liquid viscosity and the consistencies seems to decrease up to K_r=-0.95 $\log_{10}$ units at T=750°C and then increase again at T=800°C (K_r=-1.43 $\log_{10}$ units).

The values of relative viscosity (η_r), calculated as the ratio of the measured effective viscosity (liquid + crystals + vesicles) and the viscosity of the anhydrous liquid calculated after Giordano et al. (2009), are reported in Tab. 5.2 and plotted in Fig. 5.12b as a function of the experimental temperature. The effect of the contemporary presence of crystals and vesicles is that of increasing the viscosity of the magma, with respect to the suspending liquid phase alone, at T between 700-800°C and the investigated deformation rate. The amount of increase is clearly a function of applied strain rate (reflecting the shear thinning behavior) and of temperature. In fact, the maximum increase has been observed at 800°C where relative viscosities are between 1.24 and 2.09 $\log_{10}$ units, depending on the applied shear rate, and they decrease with decreasing temperature. Caricchi et al. (2008) also observed in their experiments the highest relative viscosity values associated with the lowest viscosity of the melt phase. They indicate that the enhanced rheological difference between crystals (i.e. feldspar, the dominant phase) and matrix in samples with the lowest matrix viscosity could result in an increase of relative viscosity at higher temperature. By comparing the activation energy (Ea) for plastic flow of the suspending melt (calculated by data from Giordano et al., 2004, for the glassy matrix composition with 0.86 wt% H_2O) with that of the feldspar (after Ribacki and Dresen, 2004), Caricchi et al. (2008) found comparable values at 500-600 °C (303 and 332±32 KJ/mol, respectively). With increasing temperature the difference between the activation energies become more marked (293 KJ/mol at T=600-700). Given the similarity of the Ea of plastic flow at low T, the authors argued that part of the deformation could be taken up by the suspended crystals. On the contrary, at higher temperatures the deformation is mostly concentrated on the melt phase, hence enhancing the effect of crystals as undeformable solids increasing the relative viscosity. Regardless of the Ea differences between crystals and liquids, which vary as a function of anhydrous composition and water content, it is important to note that even in our case, the relative viscosity increases at high temperature, when the plastic behavior of liquid and crystals differ the most.

At T=640°C we obtain a negative relative viscosity value (η_r= -0.60-0.46) (i.e. the viscosity of the suspension (melt+crystals+vesicles) is lower than the viscosity of the liquid matrix alone). At T=640°C, the suspending melt is close to (or even below) the glass transition (T_g=640±10 °C after Giordano et al., 2005; based on calorimetric measurements at cooling rate between 5-20 °K/min; Fig. 5.12b). If the glass transition region is crossed, the applied stress could be essentially

accommodated by brittle deformation (e.g. microfractures and vesicles breakage and coalescence), yielding negative relative viscosity values. Alternatively, the negative relative viscosity could be due to the normalization procedure adopted. In fact, at T close to T_g the kinetics of water exsolution (ca. 1 wt% in the starting material,) is very slow and part of the water could remain entrapped in the melt, even at the unconfined pressure conditions of the experiment. In the presence of water, the viscosity of the liquid would decrease, and this effect, if not taken into account in the normalization procedure, would result in lower relative viscosities.

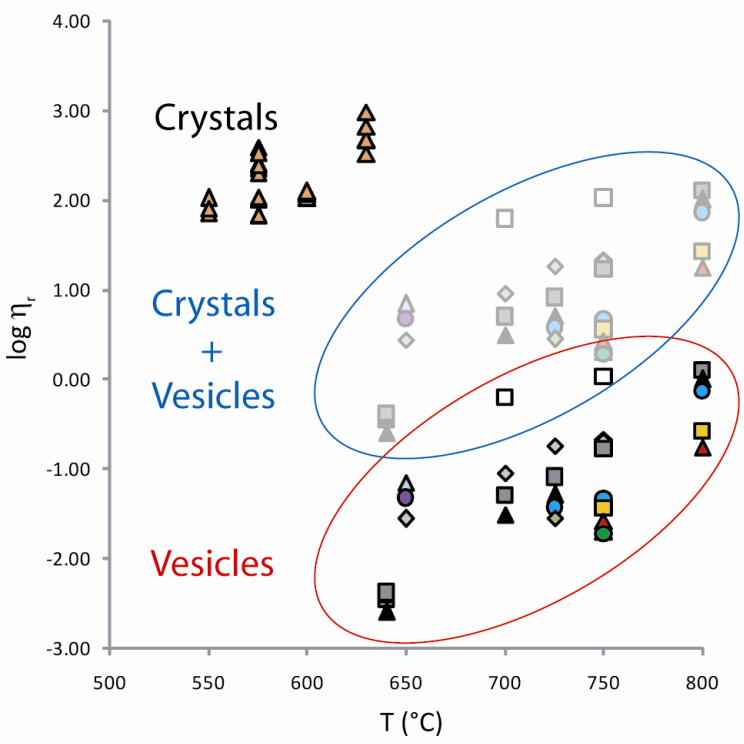

Fig. 5.12. Relative viscosity vs. temperature. The relative viscosities of the multiphase measurements (crystals + vesicles; blue ellipse) have been normalized for the net effect of crystals from data by Caricchi et al. (2008) (orange triangles) to derive the effect of only vesicles on the viscosity (red ellipse).

To provide an estimation of the net effect of the vesicles on the rheology of Monte Nuovo magma, the relative viscosities have been further normalized to the relative viscosities of Caricchi et al. (2008) on vesicle-free crystal-bearing magmas ($\eta_{r(v)} = \eta_{r(v+c)}/\eta_{r(c)}$). Provided that Caricchi et al. (2008) experiments were performed at slight lower temperature and that the relative viscosities seem to increase with increasing temperature from both their and the present study, such estimate represent the minimum expected result. To simplify the calculation we chose the values derived by experiments performed in the Newtonian field and for melts with the closer composition of the suspending matrix (i.e. water content 0.86 wt%). An average value of 2.00 $\log_{10}$ unit was

obtained from those measurements and was used to normalize the vesicle- crystal- bearing relative viscosities. With such normalization (reported in Fig. 5.13 the shift in relative viscosities yields values comprised between ca. 0 at 800°C and minimum strain rate (3x10-6 s^{-1}) and -2.70 log units at T=640°C and maximum strain rate (5.6x10^{-6} s^{-1}).

The effect of bubbles on the rheology of a magma can be of increasing or decreasing viscosity depending on the dynamic regime (Manga et al., 1998; Spera and Stein, 2000; Llewellin et al., 2002a,b; Rust and Manga, 2002a; Stein and Spera, 2002, Llewellin and Manga, 2005). In a steady flow (where the shear has remained constant for a time higher than the relaxation time of the bubbles) the viscous regime is controlled by the capillary number (see section 2.1.3 for details):

$$Ca = \frac{\dot{\gamma}\eta_0 R}{\Gamma} \quad (5.9)$$

When $Ca \gg 1$ viscous forces (expressed by $\dot{\gamma}$ and η_0) dominate over the bubble surface tension (Γ) and bubbles deform (e.g. Hinch and Acrivos, 1980), decreasing the viscosity.

On the other hand, when $Ca \ll 1$, interfacial tension forces dominate and bubbles are approximately spherical (e.g., Taylor, 1934) and in this case the viscosity increases as a function of bubble content. The decreasing of relative viscosity observed in the present work, indicates that at the experimental deformation and temperature range the rheological regime is $Ca \gg 1$. For this regime, Lewellin and Manga (2005) propose to estimate the relative viscosities using equations:

$$\eta_r = (1 - \phi)^{\frac{5}{3}} \quad (5.10)$$

$$\eta_r = \frac{1}{1+22.4\phi} \quad (5.11)$$

for minimum and maximum models, respectively. For the average vesicle fraction of the present work (ϕ=0.47) the relative viscosity derived from Eq. 5.10 and 5.11 is -0.46 and -1.06 $\log_{10}$ units, respectively (Fig. 5.12). The observed decrease of viscosity due to the presence of vesicles is higher and relative viscosities reach up to -2 $\log_{10}$ units varying as a function of T and stress-strain regime.

As stated above, the present investigation has been conducted on natural samples at 1 atm conditions. Therefore, the vesicles, connected to each other, are filled with atmospheric air. In natural pre-eruptive magmatic environments, magma bubbles are filled with pressurized H_2O vapor, and their pressure is a function of the magmatic pressure at equilibrium conditions and the

degassing process in a non-equilibrium process. The differences encountered could be due to the different pressure conditions which may affect the surface tension.

The present study can be applied to a lava flow emplacement case. We compared the data obtained at T=800°C in the present study, at the onset of shear weakening, with data from Caricchi et al. (2008), in which the same rheological response was observed. (Fig. 5.13). Caricchi et al. (2008) found a relation for the temperature dependence of the stress at the onset of shear weakening (namely, shear strength, τ_s):

$$log\ \tau_s = 3.1 \cdot 10^{-3} \cdot T + 6.4692 \qquad (5.12)$$

where $\tau_s$is in Pa and T in °C. Using Eq. 5.12 to extrapolate the data at eruptive temperatures (data point at 800°C), the obtained value is more than two orders of magnitude higher than the measured value for stress weakening on vesicles-bearing magma in the present work.

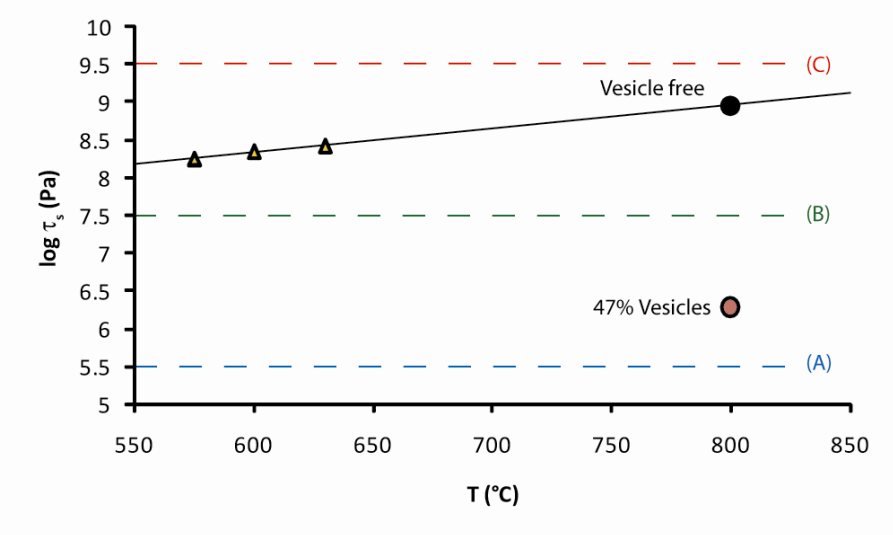

Fig. 5.13. The onset of shear weakening described in terms of shear strength of the material (τ_s) as a function of temperature. Triangles are shear weakening data for crystal-bearing vesicle-free measurements on Monte Nuovo samples by Caricchi et al. (2008). Black circle is an extrapolation at eruptive temperatures of data by Caricchi et al. (2008) obtained using the linear equation proposed by the authors (black line). Dashed lines (A, B, C) represent three theoretical conditions for the magma deformation (see text).

A lava flow with heterogeneities in terms of bubble content is simplified by the two end-members (vesicle free and 47% vesicles) in Fig.5.13. For a hypothetic stress of 5.5 log Pa (curve A) both regions are in the viscous regime. With increasing the stress (curve B, 7.5 log Pa), the vesicle free magma is still in the viscous field while the vesicle bearing melt will accommodate the deformation through brittle failure. Finally, at higher stress (curve C) both region of the magma will undergo to brittle behavior. Multiple switching from glassy to liquid behavior may occur during lava flow

emplacement of acidic magmas. (Tuffen et al., 2003; Gonnermann and Manga, 2005; Dingwell 2006). According to this mechanism, magma fragments can weld and be viscously deformed if shear stress decreases. As a result of this multiple switching, rhyolitic obsidian lava flows can reveal flow banding textures (Gonnermann and Manga, 2005). The amount of vesicles on the melt seems to strongly control the plastic vs. brittle behavior of the melt, therefore vesicles heterogeneities in the magma could also increase the flow banding formation.

It is interesting to note that while the presence of bubbles decreases noticeably the viscosity of the magma in the deformation regime of our experiments, at the same time the shear strength is also strongly reduced. From fiber elongation studies Webb and Dingwell (1990) found that the shear strength of magmas range from 350 MPa for rhyolitic compositions to approximately 250 MPa for more mafic melts. Similar values have been found in other studies (Romano et al., 1996 Mungall et al., 1996). According to Caricchi et al. (2008) the shear strength values range from 180 MPa at 575 °C to 258 MPa at 630°C. Extrapolation at 800°C yields an unrealistic high value of 900 MPa. In our case, brittle failure occurs at approximately 2 MPa and 800 °C. This extremely low shear strength is compatible with the behavior observed for vesicles- bearing magmas at different shear stress-shear strain rate conditions (Romano et al., 1996; Mungall et al., 1996; Stevenson et al., 1998) and it is related to the concentration of stress at the vesicle-melt interface which favors brittle failure. We therefore encounter a anomalous situation where the presence of bubbles on the one side enhances the fluidity of the magma yet at the same time leads to rapid onset of brittle fragmentation. Local heterogeneities due to variable degassing and crystallization kinetics can lead to regions of viscous deformation or brittle behavior and temporal crossing of the glass transition, yielding to the flow banding formation and the development of textural heterogeneities observed in many silicic obsidian lava flows.

5.6. Summary

Multiphase rheology of natural vesicles- and crystal- bearing magmas from Monte Nuovo have been investigated by uniaxial deformation experiments in the T range 600°C-800°C and strain rates between 10^{-7} and 10^{-4} s^{-1}. Brittle behavior of the magma has been observed at T<600°C and strain rates of 10^{-5} s^{-1} and at T=800°C for the higher applied strain rate (10^{-4} s^{-1}). All other experiments were performed in the viscous regime and Monte Nuovo magma showed always a non-Newtonian shear thinning behavior. Effective viscosity in the range of 10^{10}-10^{13} were calculated by the no slip model by Gent (1960). Fitting of experimental data using the Herschel-Bulkley model revealed that at the studied condition, no yield stress was present and yielded a parametrization of the flow

behavior in terms of consistency *K* and flow index *n*. Normalizing the measured multiphase viscosity (liquid+crystal+vesicles) to the viscosity of the suspending liquid (calculated after Giordano et al., 2009), the net combined effect of crystals and vesicles on the rheology was investigated. The relative viscosities indicated a dependence from experimental temperature and applied strain rate. Higher relative viscosities (up to 2.1 $\log_{10}$ units) were observed with increasing temperature and decreasing strain rates. Negative relative viscosities were observed at T=640°C, when the melt approaches the glass transition temperature (Giordano et al., 2005). To derive the net effect of vesicles on determining the rheology of Monte Nuovo magmas, the relative viscosity was further normalized to the relative viscosity obtained by Caricchi et al. (2008) on the same sample composition and no porosity. Normalization revealed that the presence of vesicles is a major impact on the rheology of magmas and can lead to a decrease of the viscosity of more than two orders of magnitude. At the same time, the presence of bubbles leads to a strong decrease in the shear strength of the magma and can lead to local and temporal variation in the deformation regimes (viscous vs. brittle) during a lava flow emplacement, which may result in the textural heterogeneities (flow banding) observed in many silicic obsidian lava flows.

6. Effect of Oxygen Fugacity on the Viscosity of Etna Basalt

As the melt structure directly influences the melt rheology, the structural role of iron in silicate melts and its change as a function of different oxidation state holds a primary role in determining the flow behavior of iron-rich materials as molten basalts. However current information regarding the effects of redox equilibria on the viscosity of iron-bearing melt is scarce and have predominantly focused on iron-rich simplified system (e.g. Dingwell and Virgo, 1987; Dingwell and Virgo, 1988; Dingwell, 1991).

The dependence of oxidation state on shear viscosity of a trachybasaltic melt from Etna has been measured using the concentric cylinder method and a gas mixing furnace. The measurements were performed under CO_2-CO mixtures at 1 atm and in a temperature range of 1300 to 1150°C. The experimental procedure involved a continuous measurement of viscosity during stepwise reduction of the melts. Melt chemistry was controlled by dip sampling the liquids at temperature. The resulting glasses were analyzed by electron microprobe and a volumetric FeO titration.

6.1. Sample Selection and Experimental Methods

The starting material for these experiments was the same of Giordano and Dingwell (2003) and of HT crystal-bearing melt rheology measurements of this study (E92, Etna Trachybasalt from 1992 lava flow; See Section 4.1).

The experimental procedure used is similar to that described by Dingwell and Virgo (1987) and in Section 3.2. However, unlike the other HT viscosity measurements carried out in the present work, the melt was reduced by flowing mixtures of CO_2-CO through the alumina muffle tube.

The viscometry determinations were initiated by equilibrating the melt sample in air at T=1300°C. After 1 hour, achieved a stable, time-invariant viscosity reading, the melt was reduced by flowing pure CO_2 gas, and then CO-CO_2 gas mixtures, through the tube furnace.

Four decreasing temperature steps were performed at T between 1300°C and 1150°C (1300 – 1220 – 1165 – 1150°C). The gas ratio was calculated from Deines et al. (1974) to maintain a constant oxygen fugacity of log fO_2=-9. For each temperature step, the melt was permitted to equilibrate to a time-invariance of the viscometer reading (5 to 7 days).

The composition and oxidation state of the melt was monitored by obtaining a melt sample after the temperature steps at 1300°C and 1220°C. The melts were sampled by dipping an alumina rod into the sample and drawing out a drop of liquid, which was then plunged into H_2O for quenching. Unfortunately at lower temperature (1165°C and 1150°C), the dipping procedure was hampered by

high viscosity and technical difficulties, therefore the melt could not be sampled. The samples obtained were then used for microprobe analysis and wet chemical volumetric determination of Fe^{2+} (Wilson, 1960).

6.2. Chemical Analysis

The results of electron microprobe analysis of the samples measured in air (E1300-a) and in controlled atmosphere at T=1300°C and T=1220°C (E1300-9 and E1220-9, respectively) are reported in Tab. 6.1, along with the oxidation state obtained by FeO titration and expressed as $Fe^{3+}/\Sigma Fe$.

Compared to the starting material, the run products show a slight enrichment in SiO_2 and Al_2O_3, together with a weak decreasing in FeO_T (10.31-7.84 wt%). The concentration of the other oxides remains approximately constant for all samples.

Iron speciation drastically changes for measurements conducted under CO-CO_2 mixture. Sample run in air at T=1300°C shows $Fe^{3+}/\Sigma Fe$=0.76, while both samples obtained at T=1300°C and T=1220°C at reducing conditions show an identical ratio $Fe^{3+}/\Sigma Fe$=0.18, reflecting the similar chemical potential of oxygen (Fig. 6.1).

Tab. 6.1. Electron Microprobe Analyses (wt%)

Sample	E1300-a	E1300-9	E1220-9
SiO_2	48.13	50.35	51.33
TiO_2	1.69	1.73	1.68
Al_2O_3	17.08	17.68	17.80
Fe_2O_3	8.59	1.56	1.59
FeO	2.49	6.61	6.39
MnO	0.19	0.20	0.17
MgO	5.38	5.28	4.92
CaO	10.35	10.21	9.57
Na_2O	3.68	3.91	3.93
K_2O	1.91	2.02	2.16
P_2O_5	0.43	0.42	0.41
Cr_2O_3	0.01	0.02	0.02
FeO_T	10.30	8.03	7.84
$Fe^{3+}+/\Sigma Fe^{2+}+Fe^{3+}$	0.76	0.18	0.18
$\log(fO_2)^{(a)}$	-1.46	-6.97	-7.61
$\log(fO_2)^{(b)}$	-1.96	-6.60	-7.33

(a) Calculated after Kress and Carmichael (1988);
(b) Calculated after Moretti et al. (2005)

The experimental oxygen fugacity was calculated on chemical basis adopting the models by Kress and Carmichael (1988) and Moretti (2005). The two models converge and indicate -log(fO_2)= 1.46-1.96 for the sample in air at T=1300°C, -log(fO_2)= 6.60- 6.97 for E1300-9 and -log(fO_2)= 7.33-7.61 for E1220-9. The discrepancy between these values and those calculated by gas-ratio in the furnace (-log(fO_2)=9; Deines et al., 1974) has probably a kinetic origin.

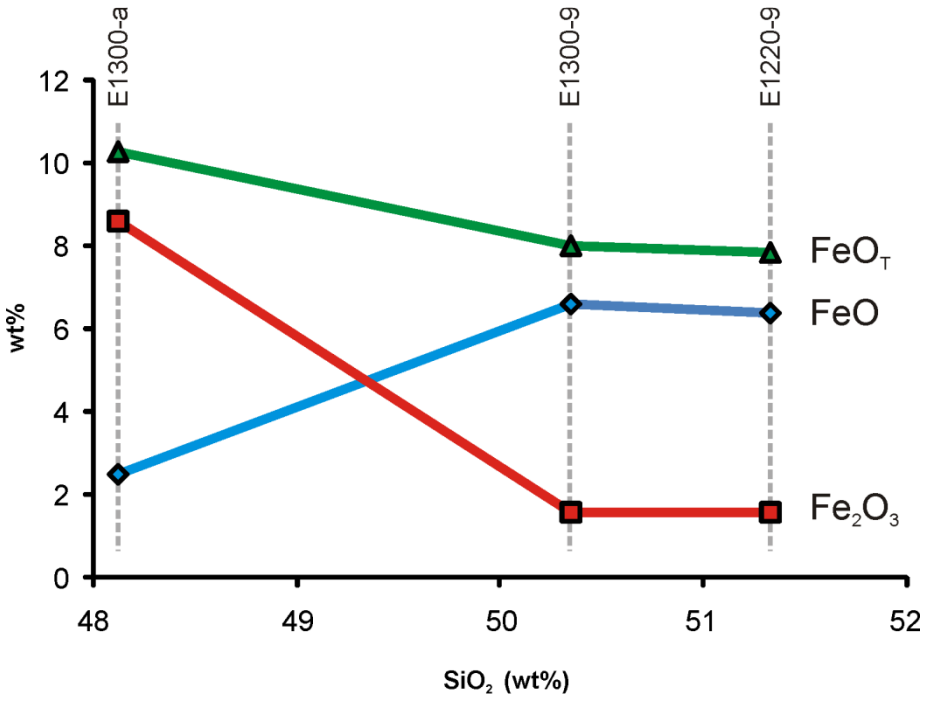

Fig. 6.1. Iron speciation of oxidated (E1300-a) and low-fugacity run products (E1300-9 and E1220-9). Slight decreasing of FeO_T and inversion of Fe^{2+}/Fe^{3+} ratio has been observed for measurements at low fugacity conditions.

6.3. Results

The results of the viscosity determinations on Etna basalt are presented in Tab. 6.2.

Tab. 6.2. Viscometry results.

T (°C)	log η (Pa s)	Sample
1300[(a)]	1.32	E1300-a
1300[(b)]	1.20	E1300-9
1220[(b)]	1.65	E1220-9
1165[(b)]	2.00	-
1150[(b)]	2.29	-

[(a)] air; [(b)] CO_2-CO atmosphere

At T=1300°C the decrease in melt viscosity is approximately 0.12 $\log_{10}$ units, from a viscosity of 20.9 Pa s for the most oxidized melt to a viscosity of 15.8 Pa s for the reduced melt. As expected, as temperature decreases, viscosity continuously increases up to 195 Pa s at T=1150°C.

Viscosity data are reported in Fig. (6.2), together with data from Giordano and Dingwell (2003) and data from *subliquidus* measurements described in section (4.1), both performed in air. From high- and low-temperature data from Giordano and Dingwell (2003) (Fig. 6.2 inset) , a Tammann-Vogel-Fulcher (TVF) fitting has been done and the resulting equation is:

$$\log \eta = -4.7147 + \frac{5827.339}{T(°K) - 611.5539} \qquad (6.1)$$

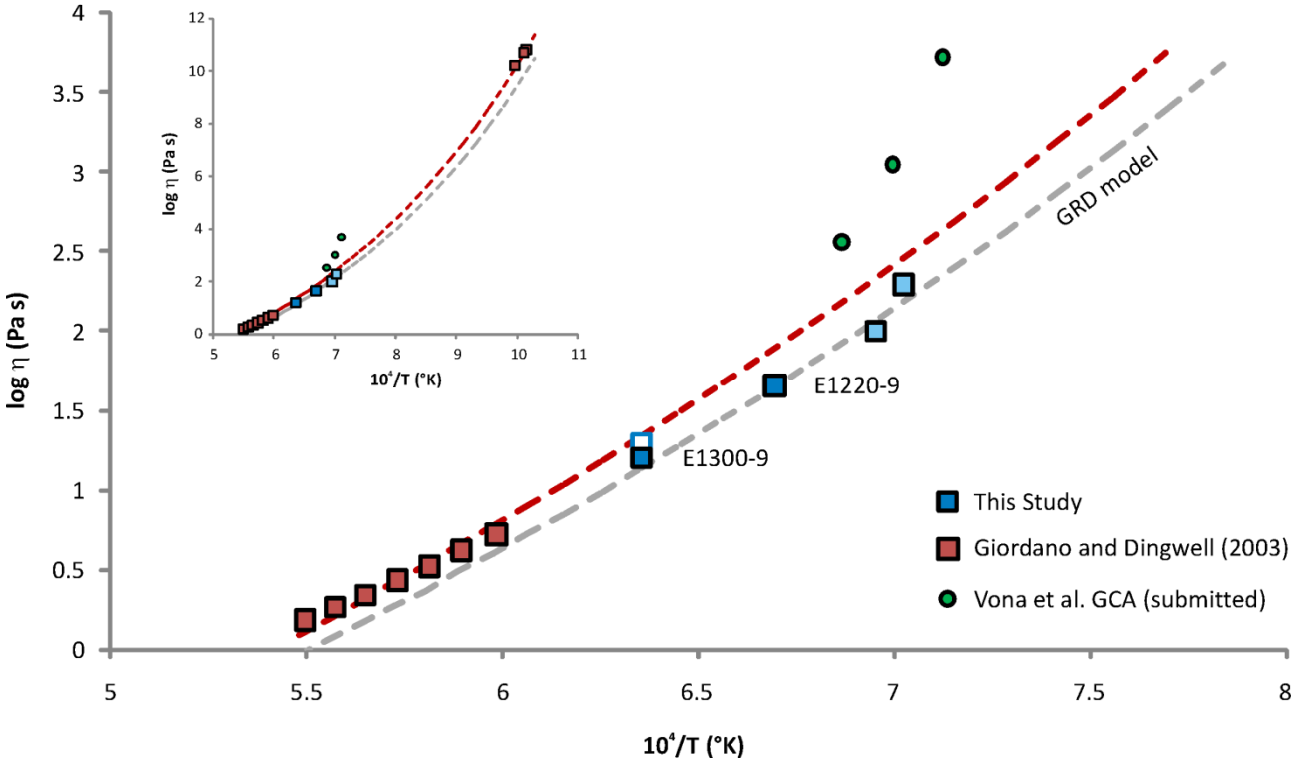

Fig. 6.2. Viscosity-temperature relation of investigated samples. Blue-white square represent measurement at T=1330°C in air before CO-CO2 fluxing (E1300-a). Dark blue squares are relative to reduced measurements at which a melt sample was collected (E1300-9 and E1220-9), while light blue squares represent viscosity measurements at which sampling has not been possible (see text). For comparison, HT and LT viscosity data carried out in air on the same composition by Giordano and Dingwell (2003) are reported (see inset). Red dashed line is relative to a TVF fitting of Giordano and Dingwell (2003) data and grey dashed line is the prediction of Giordano et al. (2008) viscosity model. Green circles are data for crystal-bearing viscosity measurements on the same composition from Vona et al. (GCA, submitted) described in section (4.1).

The calculated viscosities of the oxidated starting material, obtained on chemical basis by the prediction model by Giordano et al. (2008) (GRD) are also plotted in Fig. 6.2. The curve lies approximately 0.2 $\log_{10}$ units below the curve obtained with Eq. (6.1) .

Viscosity measurement in air at T=1300°C is perfectly described by Eq. (6.1), while measurements at low oxygen fugacity appear to have a slight lower viscosity, showing a maximum departure of 0.33 $\log_{10}$ units at T=1165°C.

6.4. Discussion

6.4.1. Effect of Oxidation State on Crystallization

Data from *subliquidus* measurements in air on the same composition at T ranging from 1182 to 1131°C, described in section X.X and reported in Fig. 6.2, show a strong departure from the pure liquid behavior as a consequence of the onset of crystallization (up to ϕ=0.21 at T=1131°C) of spinel + plagioclase + clinopyroxene phases. The same departure is not visible on the reduced measurements at comparable temperatures. Only at the lowest investigated temperature (T=1150°C) the more rapid increase in viscosity may indicate the onset of crystallization. However, the lacking of a melt sample for this temperature does not allow us to assert it with certainty.

It is known from literature (e.g. Mysen and Richet, 2005) that iron redox state has important consequences on solid-liquid phase equilibria. Thanks to its same charge and similar ionic radius, Fe^{2+} substitute for Mg^{2+} under reducing conditions in olivine and pyroxene. Under oxidizing conditions, the kinship of Fe^{3+} with Al^{3+} is in contrast much less marked, probably due to differences in effective ionic radii for the two network former cations (for $[4]Al^{3+}$, the ionic radius is 0.39 A, and for $[4]Fe^{3+}$ is 0.49 A, Shannon, 1976). Moreover, crystallization is enhanced under oxidizing conditions (Mysen and Richet, 2005). Such effect has been experimentally observed by Bouhifd et al. (2004) from isothermal creep experiments on an alkali basalt at T ranging from 930 to 950 °K and $Fe^{3+}/\Sigma Fe$ from 0.84 to 0.17. As in our study, the most reduced samples showed no increase of viscosity with time, whereas it increased o**f** several orders of magnitude for the oxidated samples, as a consequence of crystallization. Rogers and Williamson (1969) and Cukierman and Uhlmann (1974) found that Fe^{3+} acts as a nucleating agent in $CaO\text{-}MgO\text{-}Al_2O_3\text{-}SiO_2$ glasses and in an Fe-rich lunar composition. Beall and Rittler (1976) even claimed that oxidation of iron is the main factor controlling crystallization of basalt. This effect is probably due to the presence of oxides which act as heterogenous nucleation sites for other crystals.

6.4.2. Effect of Oxidation State on Viscosity

Most of the previous studies on the effect of oxidation state on magma viscosity have focused on simplified synthetic iron-rich melts (e.g. Williamson et al., 1968; Cukierman and Uhlmann, 1974; Toguri et al., 1976; Klein et al., 1983; Seki and Oeters, 1984; Dingwell and Virgo, 1987; Dingwell and Virgo, 1988; Dingwell, 1991). The results of these viscometry studies indicate that the effect of oxidation state on the viscosity of certain Fe-bearing silicate melts is of increasing viscosity as a function of the increase of oxygen fugacity and the results of previous structural studies provide evidence of differing structural roles for ferric and ferrous iron to explain such an effect.

In the traditional structural view of the role of iron in the silicate melt/glass, Fe^{3+} is considered to be present in the liquid in [4] coordination state and to act as a network former, therefore increasing the polymerization degree of the liquid and its viscosity, whereas Fe2+ is considered a network modifier , increasing the NBO/T and therefore reducing the viscosity of a melt. Increasing ratio of Fe3+/Fe2+ would therefore lead to an increase in viscosity (Dingwell and Virgo, 1987, 1988; Dingwell, 1991).

In a study on two melts in the system Na_2O-FeO-Fe_2O_3-SiO_2 at T between 1430 and 1200°C, Dingwell and Virgo (1987) observed that the reduction of viscosity is not a linear function of $Fe^{3+}/\Sigma Fe$ and the curvature of log viscosity vs. $Fe^{3+}/\Sigma Fe$ yields a composition invariance of melt viscosity at $Fe^{3+}/\Sigma Fe$ below 0.4.

From measurements at different oxidation state on a hedenbergitic melt ($CaFeSi_2O_6$) at 1400°C and 1340°C, Dingwell and Virgo (1988) found that the viscosity decreases with decreasing $Fe^{3+}/\Sigma Fe$ to intermediate values of ferric/total iron and then increases with further melt reduction. On the basis of ^{57}Fe Mössbauer spectroscopy, the authors argue that the initial decrease in melt polymerization is due to the tetrahedral-octahedral coordination transfer of ferric iron and the reduction of tetrahedrically coordinated ferric iron to non-tetrahedrically coordinated ferrous iron. At ferric/total iron = 0.2 both of these processes cease because the concentration of tetrahedral ferric iron in the melt is exhausted. Further melt reduction must consume octahedral ferric iron (Virgo and Mysen 1985). This process has a polymerizing effect on the melt, because the oxygen mol fraction is decreasing with respect to a constant number of tetrahedrically-coordinated cations.

In Fig. 6.3a data from this study on Etna basalt at T=1300°C are plotted together with data on iron-rich silicate melts from Dingwell and Virgo (1987) and Dingwell (1991) in a viscosity vs. oxidation state diagram (see figure caption for details). As described in section 6.3, the reducing condition lead to a decrease of 0.12 $\log_{10}$ units of the viscosity of the melt. The obtained data are not sufficient to distinguish a non linearity in such decrease, as the measurements were performed

only at two different oxidation states ($Fe^{3+}/\Sigma Fe$ = 0.76 and 0.18). However the relative decrease of viscosity seems to be lower than that observed by Dingwell and Virgo (1987) and Dingwell (1991) in their studies. In Fig. 6.3b the relative viscosity reduction is expressed as the ratio between the viscosity of the melt at different oxidation states and the viscosity of the melt measured in air. Our data indicate that a decreasing of $Fe^{3+}/\Sigma Fe$ from 0.76 to 0.18 yields a decrease in viscosity of about 10% .

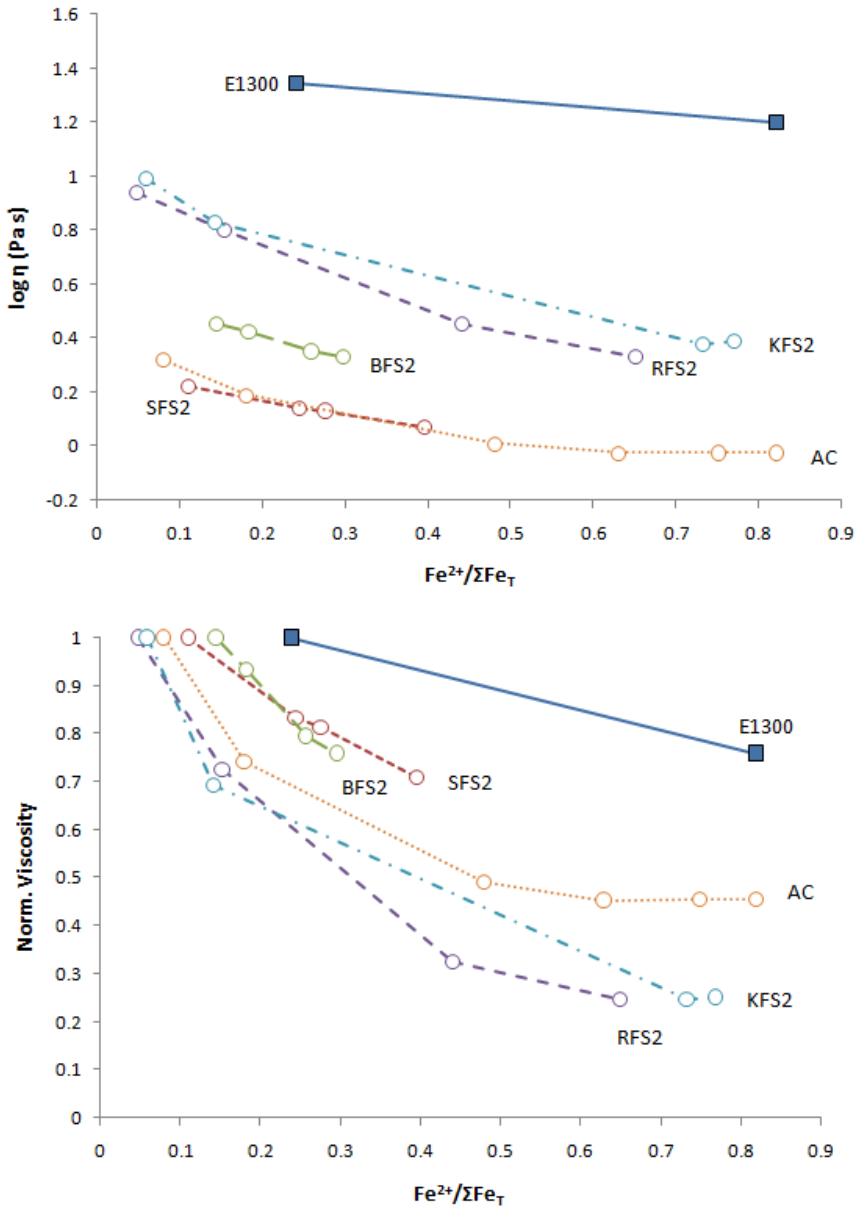

Fig. 6.3. (a) Oxidation state dependence of shear viscosity for Etna basalt at T=1300°C (blue squares). Oxidation state is expresses as ferrous/total iron. Data on synthetic materials from Dingwell and Virgo (1987) (AC: $NaFeSi_2O_x$), and Dingwell (1991) (SFS2: $Sr_{0.5}FeSi_2O_x$, T=1350°C; BFS2: $Ba_{0.5}FeSi_2O_x$, T=1345°C; RFS2: $RbFeSi_2O_x$, T=1470°C; KFS2: $KFeSi_2O_x$, T=1380°C) are reported for comparison. (b) Relative variation of viscosity as a function of $Fe^{2+}/\Sigma Fe_T$. The values of measured viscosity are normalized to the viscosity measured in air. The legend is the same as in Fig. (a).

The differences in the effect of fO_2 on our samples compared to the literature data can be related to two effects:

1) The absolute amount of iron in the liquid.

   The compositions investigated by Dingwell and Virgo (1987) and Dingwell (1991) are extremely iron-rich (>20 wt%) and the therefore any structural effect due to the change in the fO_2 is strongly enhanced for these compositions.

2) The natural liquid composition.

   Dingwell and Virgo (1987) observed that their studied composition (synthetic simplified systems), equilibrated in air at T>1000°C, contain 95% of iron present as tetrahedrally coordinated ferric iron. In more complex natural magmas, however, Al competes with Fe^{3+} for tetrahedral coordination, forcing some Fe^{3+} to enter higher coordination states ([5] or possibly [6] fold coordination state). (Mysen and Richet, 2005). As observed by Wilke et al. (2005) from XANES spectroscopy, in basaltic melts, regardless of oxidation state, both Fe^{2+} and Fe^{3+} can reside both in [4], [5], and [6] showing an average co-ordination around [5]. In general, it is not possible to determine with certainty the behavior of the ions in these structural states, if they act as network modifiers or network formers in the silicate network, therefore polymerizing or depolymering the silicate structure. For instance, Jackson et al. (1993) investigated by X-ray absorption spectroscopy the structural role of iron in SiO_2-FeO system and they proposed a network-like structure for Fe_2SiO_4 melt, with a local arrangement like that in crystalline phenakite (Be_2SiO_4) and willemite (Zn_2SiO_4) where each oxygen of a SiO_4 tetrahedron is shared with two Fe(II)O4 tetraehdra with [4]Fe^{2+}.

   Along the FeO-SiO_2 join, the Fe_2SiO_4 shows a maximum in viscosity, which confirms the polymerizing role of Fe^{2+}[4] in these glasses/melts. While it is not possible to determine with certainty if a [5] coordinate polyhedron behaves as a network former or modifier in the melt, it can be safely assumed that mixed coordination states for both Fe^{3+} and Fe^{2+} make any distinction between such species and their influence on physical properties even more blurred. This would certainly help explaining the smaller effect on viscosity here observed.

Finally, the viscosity reduction with decreasing oxidation state observed in this study is compared with that observed for basalts in the study from Bouhifd et al. (2004). Although their measurements were performed at lower temperatures (T=677°C and T=1127°C), data seem to be completely consistent, as they observed a reduction of 1.5 $\log_{10}$ units at T=677°C and of 0.3 $\log_{10}$ units at T=1127°C for oxidation state ranging from $Fe^{3+}/\Sigma Fe$=0.84 to 0.17. The effect of the redox state on viscosity seems to be more pronounced at lower than at higher temperatures and this would

explain the reduction of only 0.12 $\log_{10}$ units for $Fe^{3+}/\Sigma Fe$ = 0.76-0.18 observed at T=1300°C for Etna basalt.

6.5 Summary

Viscosity measurements have been performed on basaltic melts from Etna at low oxygen fugacity condition. At the investigated temperatures (1150°C<T1300°C), a slight decrease in viscosity has been observed in comparison with data expected from fitting of HT and LT viscosity measurements on the same liquid conducted in air by Giordano and Dingwell (2003). Data seem to follow the shape of the pure liquid curve, at least up to the lowest investigated temperature (T=1150°C). This behavior has been interpreted as no or minor crystallization taking place during measurements. Data obtained in this study (section 4.1), regarding HT rheology measurements on the same material, conducted in air at comparable temperature range (1131-1182°C), showed a rapid increase in viscosity and a departure from the pure liquid behavior, as a consequence of crystallization of spinel + plagioclase ± clinopyroxene. We thus infer that one major effect of low oxygen fugacity is the decreasing of liquidus temperature of the melt.

A comparison between two different oxidation state has been possible at T=1300°C where the reducted sample has been compared to the sample relative to the melt equilibrated in air ($Fe^{3+}/\Sigma Fe$ = 0.18 and 0.76, respectively). The viscosity decrease observed in the most reduced sample is smaller than the decrease observed by many authors on simplified iron-bearing silicate melts. We infer that this behavior is linked to the competition in natural systems between Fe^{3+} and Al in entering the tetrehedric structural sites. Being Al favoured in tetrahedrical coordination, part of Fe^{3+} is forced to behave as network-modifier also at high fugacity condition, thus the depolymerization of the melt when the reduction Fe^{3+}- Fe^{2+} takes place is limited. Our data seem to be consistent with those obtained by Bouhifd et al. (2004) on basalts, confirming that the effect of oxidation state on viscosity is more pronounced at lower than at higher temperatures.

Further investigation are needed to better describe the oxidation state-viscosity relationship for natural basaltic melts. Such investigations should permit to systematically investigate the basalt viscosity at different oxidation state. At the same time, structural studies (e.g. ^{57}Fe Mössbauer spectroscopy, XANES spectroscopy) are needed to continuously determine the structural role of Fe^{3+} and Fe^{2+} with changing fO_2 conditions.

7. Experimental determination of plagioclase crystal size distribution and crystallization kinetics of Stromboli and Etna basalts under stirring conditions

7.1 Introduction

The *subliquidus* rheological measurements performed on Stromboli and Etna basalts (described in Section 4) were conducted through isothermal crystallization experiments. To completely characterize the rheological behavior of magmatic suspensions, a detailed textural characterization of samples has been performed. The textural parameters analyzed (crystal fraction, crystal shape, size and orientation distributions) were then used to constrain a model for the effect of crystals on the rheology of magmatic suspensions. In addition, as they were performed with controlled chemical and physical conditions, the crystallization experiments can be used to explore the evolution of the texture and the crystallization kinetics of basalts under isothermal conditions and controlled deformation rate. In fact, the numbers, size and shapes of the crystals in a rock sample reflect the relative kinetics of nucleation and growth, which is in turn dependent on its solidification history. Controlling the cooling history by experimental studies, a quantitative relationships between the solidification process and crystallization kinetics can be provided. The observed textures of experimental samples can be then used to constrain nucleation and growth rate during crystallization. Applying the kinetics parameter to natural magmatic rocks can in turn constrain their solidification history. Since the introduction of crystal size distribution (CSD) analysis to petrological studies (Marsh, 1988; Cashman and Marsh, 1988), textural variations in igneous rocks have frequently been quantified in terms of changes in the CSD (e.g., Cashman, 1993) and a great deal of theory has been developed linking CSDs to kinetic processes (Marsh, 1998, 2007; Armienti, 2007).

7.2. Brief review of theory

7.2.1. Kinetics of crystallization process

Upon cooling, atoms constituting the magmatic liquids can turn into solid state by ordering in crystal lattice or keep a disordered structure forming natural glasses. The evolution of the system is

controlled by magma composition, which determines the kind of mineral forming, and from the magma cooling rate, which controls the available time for crystal nucleation and growth.

In a simplified monophasic system, at constant pressure, an equilibrium temperature (Te) exists when solid and liquid phases have equal Gibbs free energy (Fig. 7.1). However, the first nuclei of solid crystalline phase form only as the liquid is in the metastable field and a *liquidus* T (<Te) is reached, at a certain undercooling ΔT=Te-T.

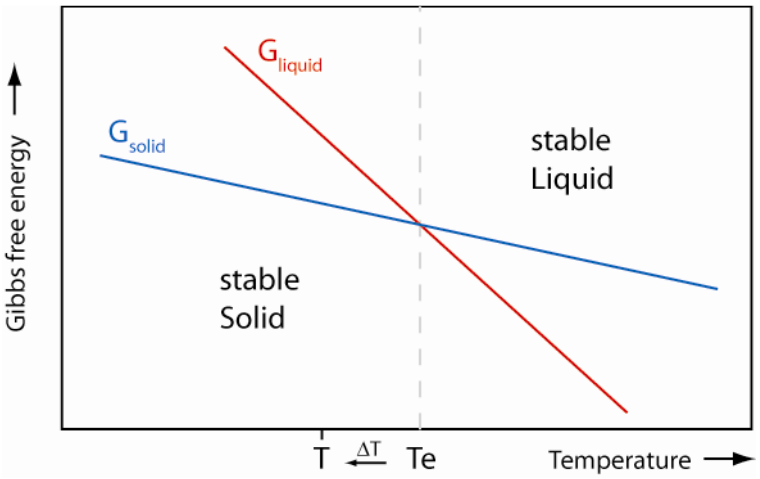

Fig. 7.1. Solid-liquid stability fields and Gibbs free energy variation.

At below *liquidus* conditions, atoms are continually added or removed from the clusters. Addition of new atoms reduce the energy of the system as particles ordered in crystalline lattice have lower energy with respect to particles free to move (volume or lattice energy contribution, ΔG_v). At the same time, bonds at the surface of the cluster are unsatisfied and there is a net increase in energy (surface energy contribution, ΔG_v). The sum of these two components gives the total energy of the cluster (ΔG_T). For very small crystal nuclei with elevated surface/volume ratio, the effect of surface energy hampering new aggregation prevails, while with increasing crystal dimensions volume contribution is dominating. As a result, with increasing cluster size the total energy rises to a peak and then descends (Fig. 7.2; e.g. Dowty, 1980, Higgins, 2006). When one of these clusters exceeds a critical radius, R_c, (representing the limit between cluster growth and dissolution) then it is energetically stable and a crystal nucleus is formed. Addition of further atoms to the nucleus is energetically favoured as it reduces the total energy. This process is termed homogeneous nucleation.

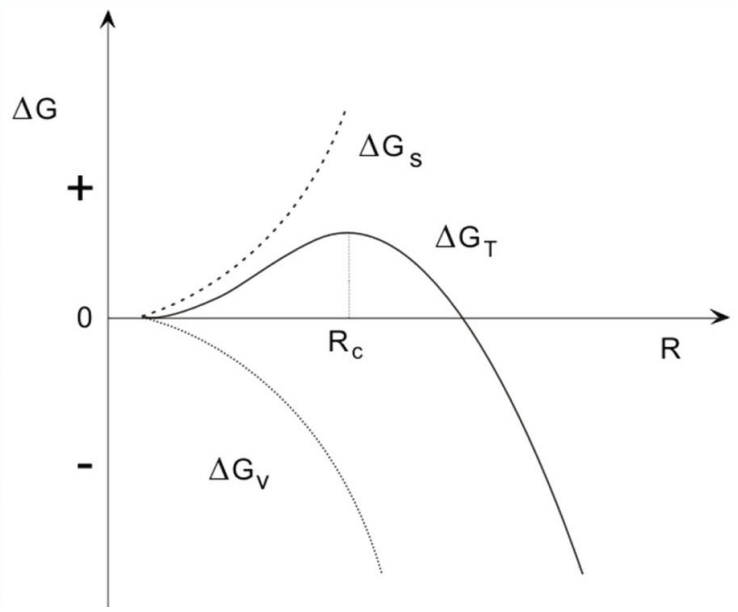

Fig. 7.2. Volume (ΔG_V), surface (ΔG_S) and total (ΔG_T) free energy variation in a simple liquid system during homogeneous nucleation. (from Peccerillo and Perugini, 2003).

The value of the critical radius is a function of the undercooling conditions ($\Delta T = T_{liquidus} - T_{system}$) and it assume infinite values for temperatures above *liquidus*. while it can markedly decrease for high values of ΔT (Fig. 7.3). At low undercooling no clusters reach the critical size and the nucleation rate is zero. With increasing undercooling, the nucleation rate increases rapidly to a peak and then diminishes.

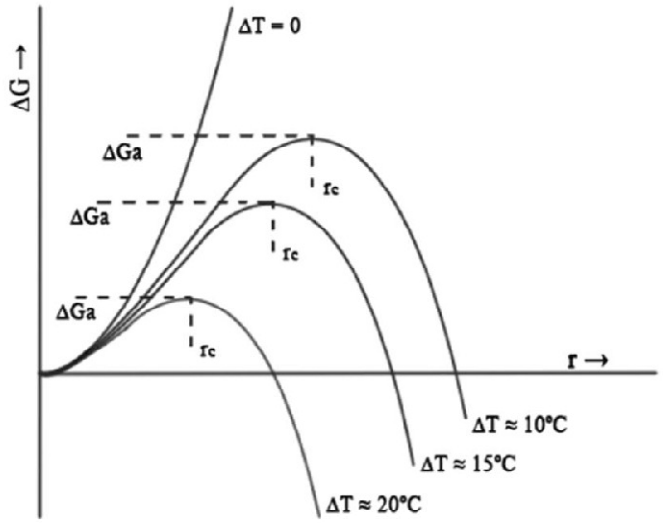

Fig. 7.3. Gibbs free energy of nuclei vs. size at different degrees of undercooling.

The activation energy needed for crystal nucleation strongly decreases if it occurs on the surface of existing host grains or bubbles, or on defect structures within crystals (heterogeneous nucleation). The surface energy of the cluster is lower, hence both the critical radius and energy barrier are lower (Fig. 7.4). Hence, formation of stable nuclei occurs at lower undercooling than for homogeneous nucleation. The energy further decreases if the host and the new phases show crystallographic similarity, expressed by the dihedral angle, θ (Figure 7.4).

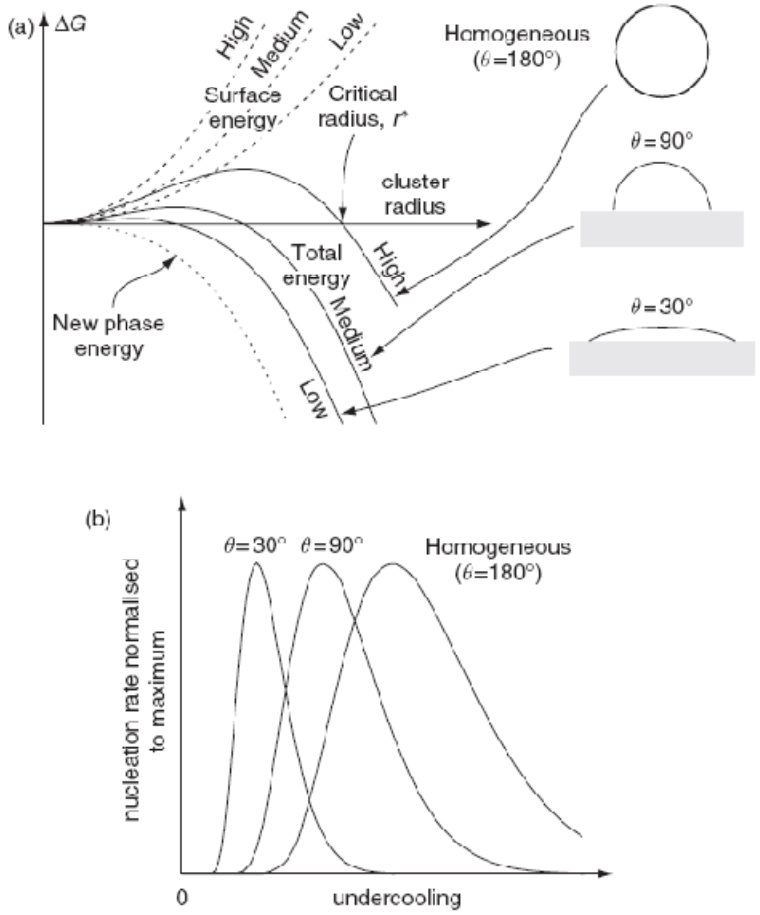

Fig. 7.4. (a) Gibbs free energy variation of an atomic cluster vs. cluster radius. For homogeneous nucleation (θ=180°) the surface energy is high and the critical radius is large. For heterogeneous nucleation (θ=30° and 90°) the surface energy is lower giving a lower critical radius. (b) Nucleation rate as a function of undercooling. For homogeneous nucleation and small degrees of undercooling the nucleation rate is zero. It increases rapidly to a peak and then diminishes with increasing undercooling. Heterogeneous nucleation reduces the undercooling necessary for nucleation (from Higgins, 2006).

The necessary undercooling is smallest when the new and host crystals are mineralogically identical and in the same orientation. However, in this case the greater ease of nucleation will be balanced by the lower concentration of the mineral component in the magma surrounding the growing host crystal.

As they are never completely liquid, the heterogeneous nucleation is the most common nucleation process in magmas. However, for large degrees of undercooling the extent of homogeneous nucleation can be more important.

Modeling of nucleation process is hampered by the difficulty in studying the small and unstable crystal nuclei. To this date the modeling is limited to simplified monophasic systems, and some differences between theoretical models and experimental results have been observed (Kirkpatrick, 1981; Cashman, 1990).

As they reached their critical size, the stable nuclei will grow to form well-developed crystals at a rate essentially controlled by three factors (Dowty, 1980):

(1) interface kinetics, the movement of material across the interface and its attachment on the crystal surface;

(2) material transport, the movement of material through the liquid;

(3) heat transfer, the removal of latent heat of crystallization from the interface.

Which of these processes is the dominant factor depends on the relative diffusion and heat transfer rates, the particular growth mechanism and the undercooling. Generally, interface kinetics is dominant at low undercooling, while either material transport or heat transfer becomes more important at high undercooling. However, because liquid silicates have high thermal diffusion with respect to the chemical diffusion, the heat transfer generally play a secondary role in magmatic systems (Dowty, 1980).

The mechanisms of attachment of atoms onto the crystal surface are divided into two main types, continuous growth and layer growth. In continuous growth, atoms are able to attach themselves wherever they land; this type of growth is normally associated with a rough or non-planar surface, which has a high concentration of unsatisfied bonds and therefore high surface energy. In layer or lateral growth, normally associated with a smooth, planar, or singular interface, with a low concentration of unsatisfied bonds and low surface energy, atoms are not strongly localized on the surface, although once they land there, there may be small probability of their leaving again. Atoms may move rather freely over the surface (surface diffusion), and are usually able to attach themselves permanently only at the edge of layers or steps, where they are in effect bonded to two surfaces. Crystals with macroscopically flat, crystallographically rational faces have presumably grown by the layer mechanism, whereas smoothly rounded crystals more probably have grown by the continuous mechanism. However it is not possible to make a sharp distinction between the two mechanism.

The material transport in crystal growth can be described in terms of atomic or molecular diffusion. Chemical diffusion is a process whereby the random thermally-activated movement of atoms in a material results in the net transport of atoms. This includes transport within the liquid phase (volume diffusion); across the interface (interface diffusion); in layer growth, parallel to the interface (surface diffusion), and from the surface onto the edge of a layer.

From all the factors described above we can distinguish two ideal scenarios determining the grow rate and then the shape of crystals:

1) the diffusion of material in the melt is fast enough to keep a constant composition at the interface and rate of crystal growth is controlled by the rate of integration of material to the surface (interface-controlled growth). Crystals which form under these conditions usually show well-developed equilibrium shapes;

2) the aggregation onto the surface is very fast and the material diffusion rate is not sufficient to feed new material to the crystal surface and its distribution is not homogeneous on the different crystal faces (diffusion-controlled growth). In this case, the elements aggregate mainly at the edge of the crystals, having no time to adjust diffusing along the surfaces. The resulting crystal shapes are from elongated to acicular or dendritic.

The process governing the growth rate (interface- vs. diffusion-controlled) is strongly affected by the undercooling regime. At low degrees of undercooling crystal growth is controlled by interface processes, as the growth rate (aggregation of atoms on the solid surface) is slow, while the diffusion processes are very effective. In contrast, for high undercooling the growth is diffusion-controlled, as the growth rate is fast and the diffusion processes are slowed by the higher viscosity of melt at lower temperature.

Although the crystal growth rate is favored by increasing undercooling, it is at the same time hampered by the increase in viscosity with decreasing temperature. For this reason, it increasing from zero at *liquidus* T ($\Delta T=0$) to a maximum for low degree of undercooling (where the viscosity increase is moderate). With increasing undercooling, the higher increase in viscosity cause the growth rates to slow and finally stop. In Fig. 7.5 the growth rate of a crystal is reported as a function of the undercooling. The comparison with the nucleation rate curve indicates that the maximum growth happens at lower degrees of undercooling with respect to the maximum nucleation. Such a difference have fundamental consequences on the development of the texture of magmatic rocks. In fact, for low undercooling there is low nucleation and high growth. At this conditions, typical of cooling large intrusive bodies, it is favored the formation of few crystal nuclei which can extensively grow to yield a coarse-grained texture. Increasing degrees of undercooling yield conditions at which the nucleation rate is maximum, while the growth rate is rapidly decreasing. As

a result, the formation of many nuclei with relatively low growth is favored and the resulting in medium- to fine-grained textures. Finally, for extreme degress of undercooling both nucleation and growth are small and tend to zero, and the formation of few little crystals and glass will form. Textures derived from medium to extreme undercooling conditions are typical of volcanic rocks.

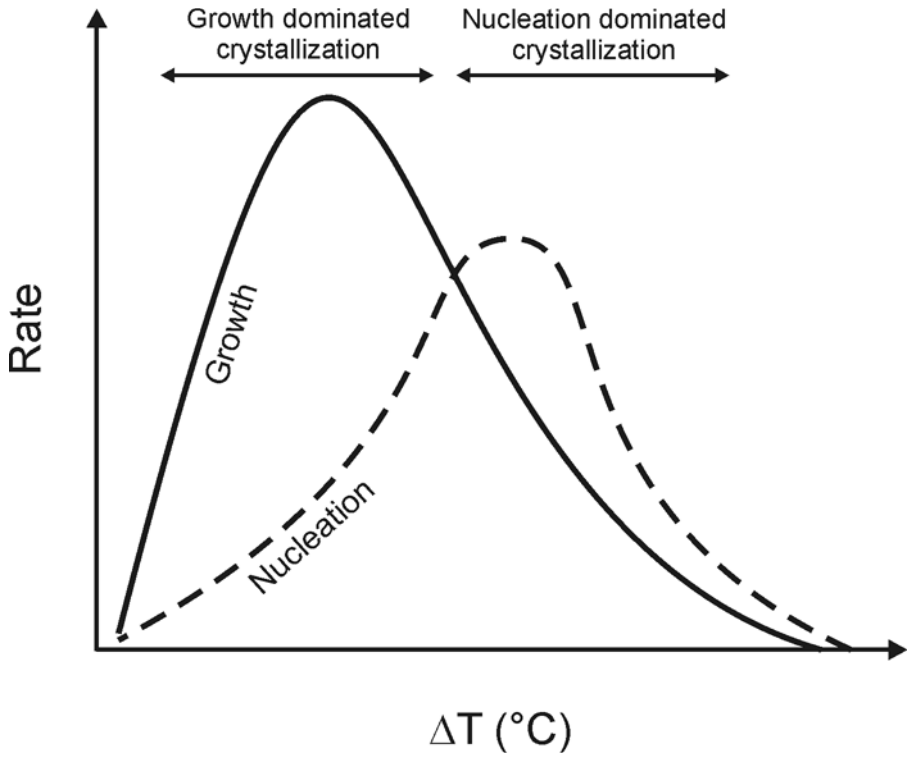

Fig. 7.5. Crystal nucleation and growth rates as a function of undercooling (redrawn from Peccerillo and Perugini 2003).

7.2.2. Crystal Size Distribution (CSD) theory

The process of nucleation is always followed by growth of the nuclei. The combination of nucleation and growth process will, in turn, affect the grain size distribution, i.e. the rock texture.

Crystal populations produced by kinetic processes alone are most commonly modeled using the Avrami equations (e.g. Lasaga, 1998). However, the solution of this equation requires knowledge of the variation of the nucleation rate with time, J (t), the growth rate with time and crystal size, G(t,l). Both of these are generally unknown and various models of their behavior have been proposed. The most common assumption is that the growth rate is independent of size and hence this variable can be simplified, although Eberl et al. (1998) have proposed that it is proportional to size. It cannot be overstated that independence of growth rate and size is for kinetic growth only: it is well established

that during coarsening (equilibration) the growth rate is size dependant (e.g. Voorhees, 1992). Both Gaussian (Lasaga, 1998) and exponential (Marsh, 1998) models for the variation of growth and nucleation rates with time have been proposed.

The method of crystal size distributions (CSDs) is a means of quantitatively describing crystal content as a function of size and of directly modeling crystallization in magmatic processes (Marsh, 1988).

The formulation of the problem of crystal size distributions employs the notion of population density, *n* (Randolph and Larson, 1971).

It is common in sedimentology to analyze particle sizes by plotting the cumulative number (*N*) of crystals against crystal size (see Fig. 7.6). The cumulative distribution is much more stable than the non-cumulative distribution because the number of crystals in each succeeding size range is added to the number of all smaller crystals and the ensuing total can only vary within definite limits. A size range containing no crystals, for example, would only affect *N* by holding it constant (i.e., zero slope), and not produce a strong spike in the curve. And the addition of a large number of crystals all of the same size would markedly increase the slope of the *N* curve, but the curve would not be unusually ragged, yet all the detailed information about the population (i.e., sizes and numbers) of crystals would be intimately reflected in the local changes in the slope of the *N* curve.

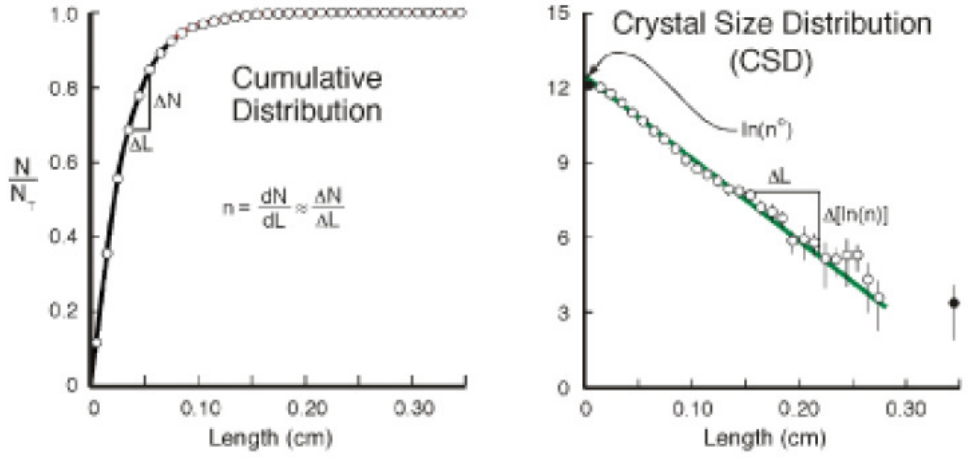

Fig. 7.6. Methods of representing crystal size measurements. The left diagram shows a cumulative distribution, the derivative or slope of which is a direct measure of population density (n) leading to the crystal size distribution (CSD) (right); the CSD slope and intercept are indicated (from Marsh, 1998).

The slope (*n*) of the *N* (cumulative number) curve is thus a measure of the population density, which will be a continuous function of crystal size *L*. That is,

$$n(L) = \frac{dN(L)}{dL} \tag{7.1}$$

It is clear that $n(L)$ is a function describing the number of crystals per unit length or size (L) of crystal (or particle) per unit volume of magma or rock. The units of $n(L)$ are thus number per length per unit volume or no./L^4. This is the fundamental variable upon which rests all further formalism concerning crystal size distributions. The relationship between $n(L)$ and $N(L)$ is shown graphically by Fig. 7.6.

If plotted in a ln(n) vs. L graph, data pertaining to many volcanic rocks show regularly an approximatively linear relation between the natural logarithm of the population density at size L and that size. This is particularly true for open magmatic systems, where there is a continuous input and output of material during the crystallization process (Marsh, 1988, Fig. 7.7).

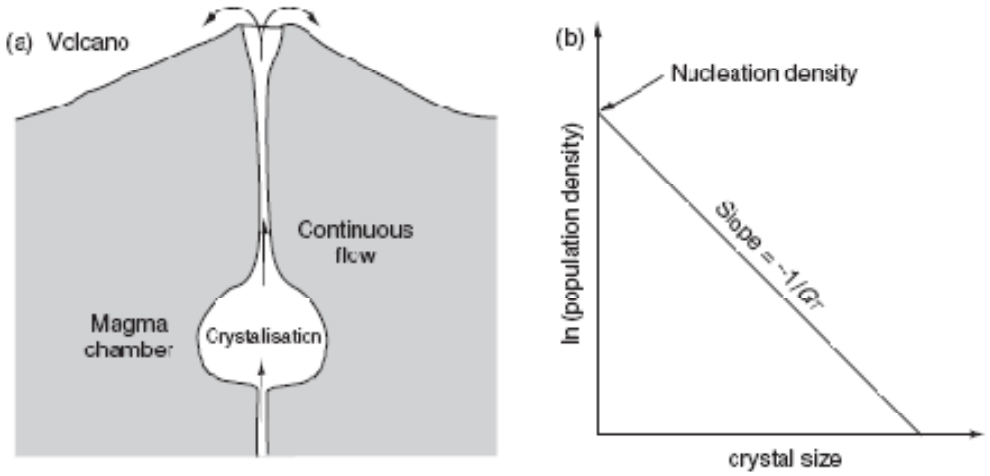

Fig. 7.7. (a) According to the steady-state crystallization model (Marsh, 1988), in a continuously erupting volcano magma enters the magma chamber from below and partial crystallization occurs in the chamber. An equal quantity of magma is withdrawn and erupts. (b) The CSD of a phase in the magma chamber is a straight line on graph of ln(population density) vs. size.

For one phase in the system:

$$n'_V(L) = n'_0(L)e^{-L/G\tau} \tag{7.2}$$

where $n'_V(L)$ is the population density of crystals for size L, $n'_0(L)$ is the final nucleation density, G is the growth rate and τ is the residence time. The characteristic length, C, is defined by:

$$C = G\tau \qquad (7.3)$$

This distribution is linear on a graph of ln (population density) versus size (L). The intercept is $\ln(n_V'(0))$ and the slope is -1/C. For steady-state systems the characteristic length equals the residence time multiplied by the growth rate. Although there are few geological systems that exactly resemble this simplified model, the variation of natural volcanic CSD curves from this general behavior can be investigated and the processes leading to their form can be described.

If the residence time is constant, but the nucleation density is increasing then the CSDs will be parallel (Figure 7.8). Increasing nucleation density could be produced by increasing undercooling. Increasing residence times for constant nucleation density will make the CSDs swing around a point on the vertical axis. Such a situation could occur if the magma chamber is expanding. Any combination of these two models is also possible. There is, however, no observational evidence so far that any geological system actually conforms to these models.

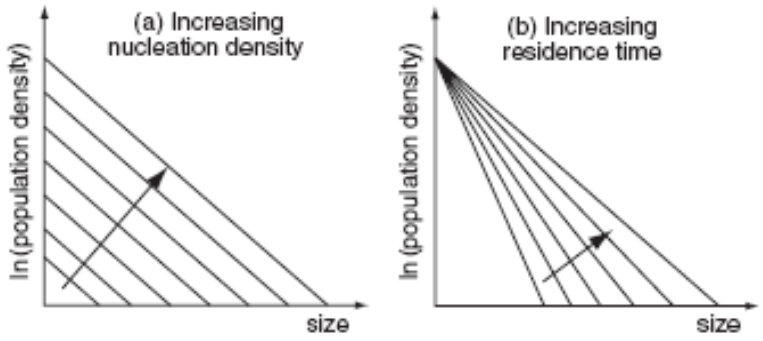

Fig. 7.8. Theoretical dispersion of CSDs in a continuously fed crystallization system with (a) variable nucleation density and (b) residence time.

Changes in the crystallization parameters during solidification, such as cooling rate, may change the characteristics of the CSDs. In general the system will take time to accommodate the new conditions and during that time the CSD will be curved on a classic CSD diagram (Marsh, 1988, Maaloe et al., 1989, Armienti et al., 1994). Such a transition will change the nucleation rate of the magma and initially produce a steeper part of the CSD at small sizes. However, with time the increased nucleation rate will propagate through the CSD as a step, until finally the CSD is again flat from end to end. Cashman (1993) proposed that primary curved CSDs could be produced at a constant cooling rate if there is a change in the nature of the phases precipitated. In this case there must be crystallization over a significant period of time in the two-phase field.

Obviously the steady-state approach of Randolf and Larson (1971) cannot be applied directly to closed-system crystallization. However, Marsh (1998) also examined closed systems and

discovered that a similar correlation can be produced under certain circumstances, although for high crystal contents the CSD is not linear for small crystals (Figure 7.9). In such a system the logarithmic – linear correlation is produced either by (1) exponentially increasing nucleation density with time J(t) at constant growth rate G, or by growth rate increases exponentially as a function of crystal size, G(L), nucleation rate being constant.

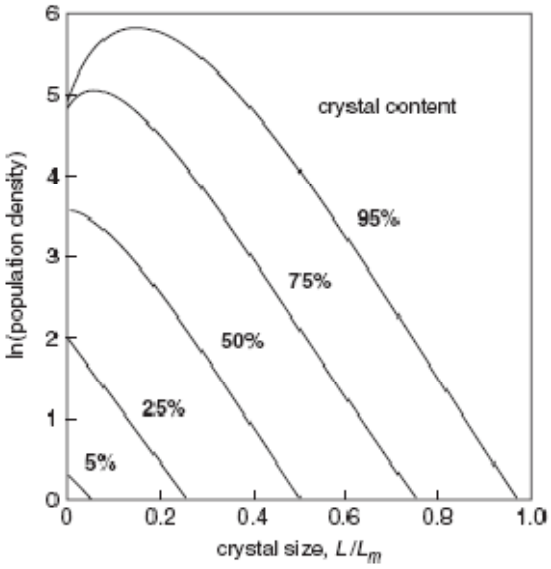

Fig. 7.9. Development of closed-system CSDs with increasing crystal content. Crystal sizes have been normalised to that of the largest crystal. The turn-down for small sizes reflects the lower magma volume and hence nucleation rate at high crystal contents. After Marsh (1998).

Obviously many complication can rise in each of the two ideal cases reported above (open and closed systems). Populations of crystals can be modified by mechanical processes, such as compaction, sorting and mixing. Some of these processes are closed, in that the total mass of the system is unchanged, others are open to the addition of crystals and magma. However, the CSD can provide a quantitative representation of petrographical data that can be used for evaluating, modeling and interpreting of natural rock textures. In particular, the CSDs can be described on the base of equation linking the number of crystals and their size to kinetic processes of nucleation and growth, as well as to the state at which the system is crystallizing (e.g. mixing, crystal settling, etc.). To achieve this goal quantitative data on the crystal growth rate are requested, at different degrees of undercooling. Experimental studies focused on the crystallization kinetics of volcanic rocks at different undercooling, with constrained crystallization time, provide a fundamental tool to better understand the natural volcanic rock textures, and consequently the magma eruptive dynamics.

7.3. Experimental Results

The technique used to perform the isothermal crystallization experiments on basaltic magmas from Stromboli and Etna has been already described in section 4.1.4. The experiments were carried out in air and at 1 atm, under stirring conditions, at different undercooling in the temperature range between T=1157-1187 °C for Stromboli and T=1131-1182 °C for Etna. Prior to lowering the temperature at *subliquidus* conditions, both magmas have experienced the same *superliquidus* treatment. They have been stirred continuously at T=1400°C for 5h to ensure that all the natural crystalline phases present in the starting materials were fully dissolved. Subsequently, the temperature of the melt was lowered rapidly to that of the dwell temperature. The main difference between the two datasets on Stromboli and Etna is given by the initial strain rate adopted during the crystallization experiments. Different initial deformation rates were applied by setting different stirring velocities for Stromboli and Etna starting material. The initial strain rate ($\dot{\gamma}_i$) applied to Stromboli samples was 4.26 s^{-1} while it was lower (0.53 s^{-1}) for Etna samples. Deformation rates automatically reduced during crystallization as a consequence of the viscosity increase. Details on the deformation rate vs. time path are reported in Fig. 4.8.

The *liquidus* temperatures were calculated using MELTS software (Ghiorso et al., 1995) for both compositions at the experimental conditions and gave similar values (T=1248°C and 1251°C for Stromboli and Etna, respectively).

The textural analyses performed to characterize the post-run products of isothermal crystallization experiments on basaltic magmas from Stromboli and Etna have been already detailed described in Section (4.1.7). The high temperature mineralogical assemblage is dominated by the presence of spinel (minor) and plagioclase with the occurrence of stable clinopyroxene only at the lowest temperatures (1157 °C and 1131°C for the Stromboli and the Etna samples, respectively). The overall crystal fraction (ϕ) varies between 0.06 and 0.27 and plagioclase crystal contents are between ϕ=0.11-0.23 for Stromboli and between ϕ=0.06-0.18 for Etna. MELTS simulations indicate the same crystallization sequence where the spinel is the *liquidus* phase and the onset of plagioclase and clinopyroxene crystallization occurring at T=1212°C and T=1194°C for Stromboli, respectively, and for Etna at T=1203°C and T=1182°C, respectively. For both Stromboli and Etna, the calculated crystallization onsets for clinopyroxene does not match with the first appearance in experiments which is always lower. As for the spinel, it is overestimated by the calculator, but the predicted increase of spinel mass with decreasing T is very similar to that found in experiments. The predicted plagioclase mass proportions fit quite well the values obtained by textural analyses for Stromboli. For Etna a discrepancy between measured and calculated values (~8%) was found at

the lowest temperature. On the basis of the calculated crystallization onsets, we derive that the experiments were run at undercooling (ΔT) varying from 24 to 45°C for Stromboli and from 21 to 72°C for Etna with respect to the plagioclase phase for the starting material.

Table 7.1. Results of CSD analysis.

	Stromboli						*Etna*		
Run	SGP7	SGP5	SGP4	SGP1	SGP3	SGP6	E92-1	E92-2	E92-3
T (°C)	1187.5	1182.3	1177.2	1172.1	1167	1156.7	1182.4	1156.7	1131
ΔT (°C)	25	30.2	35.3	40.4	45.5	55.8	20.6	46.3	72
Time (10^4 s)	5	5	4	4	4	(2-4)	40	20	7
ϕ_{Plg} (% vol)	0.11	0.12	0.13	0.13	0.17	0.23	0.06	0.13	0.18
Number density (mm^{-2})	20.15	31.08	41.52	33.63	76.92	135.50	2.20	24.27	44.35
Intercept $\ln(n_0)(mm^{-4})$	10.79	11.42	11.74	12.00	12.76	13.66	7.31	11.01	12.28
Slope (mm^{-1})	-74.9	-80.8	-84.9	-90.9	-99.8	-123.6	-40.3	-73.9	-106.8
R^2	0.984	0.992	0.984	0.988	0.996	0.994	0.881	0.986	0.977
J_{CSD} (m^{-3} s^{-1})	1.30E7	2.26E7	3.70E7	4.48E7	8.72E7	(1.73E8)	9.28E4	4.09E6	2.88E7
G_{CSD} (m s^{-1})	2.67E-10	2.47E-10	2.94E-10	2.75E-10	2.50E-10	(2.02E-10)	6.20E-11	6.77E-11	1.33E-10
G_{max} (m s^{-1})	2.88E-9	2.82E-9	3.45E-9	3.30E-9	3.20E-9	(2.76E-9)	4.53E-10	7.45E-10	1.64E-9

The temporal variations of viscosity have been used to constrain the time for the crystallization process. In fact, all the rheological measurements were stopped after the achievement of a time-invariant value of viscosity (a plateau in Fig. 4.8), which has been interpreted as indicative of a stable crystal content. In the following, the time to reach the plateau is considered as the time in which the crystallization process takes place (Tab. 7.1). One exception is given by the lowest temperature experiment on Stromboli (SGP6) showing a more complex temporal variation of viscosity which increased in a stepwise fashion with the formation of an intermediate plateau. The cause of this plateau is not known. One reason could be the saturation of plagioclase crystallization and the following ramp could be associated to the onset of clinopyroxene crystallization. In this case a value of t=2-4x10^4 s should be chosen. However, a secondary plateau was not observed for

Etna lowest temperature sample (E92-3) in which clinopyroxene is present. Due to the large uncertainty in determining the crystallization time, which could lead to major errors, SGP6 data will not taken into account when dealing with time-dependent considerations.

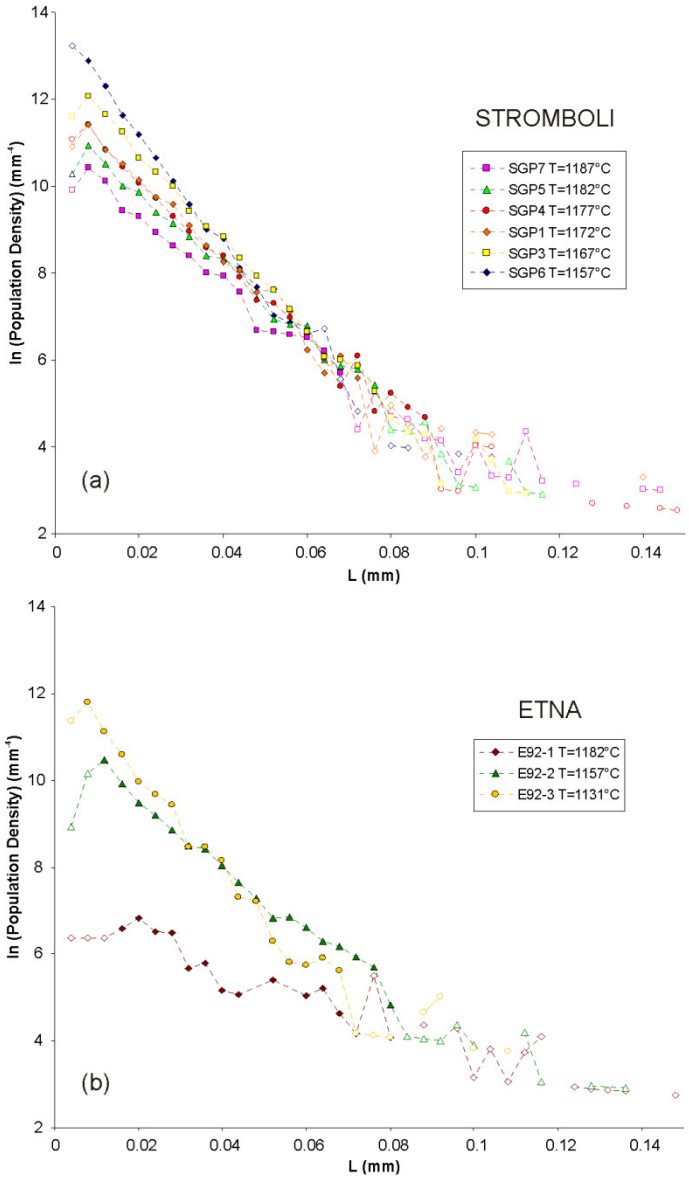

Fig. 7.10. CSD diagrams for Stromboli and Etna samples.

The crystallization time strongly differs between the two experimental datasets on Stromboli (between 4-5 x 10^4 s) and Etna (between 7-40 x 10^4 s). For instance, samples SGP5 (Stromboli) and E92-1 (Etna) were run at similar undercooling conditions ($\Delta T = 22.8 \pm 2.2$ °C) and achieved the viscosity plateau at t = $5x10^4$ s and t = $4x10^5$ s, respectively. The lower crystallization efficiency of sample E92-1 also determines a lower plagioclase crystal content (ϕ=0.06) at the rheological equilibrium with respect to SGP5 (ϕ=0.12). The same behavior can be observed by comparing

samples SGP3 (Stromboli) and E92-2 (Etna), both run at $\Delta T = 45.9 \pm 0.4$ °C. The crystallization time of SGP3 is $t = 4x10^4$ s, while it is $t = 2x10^5$ s for E92-2. The resulting plagioclase crystal fractions are $\phi=0.17$ and $\phi=0.13$, respectively.

Figure 7.10 shows the CSD diagrams for plagioclase phase obtained after the stereological correction on 2D textural measurements for both Stromboli (a) and Etna (b). They all present the same general shape, with a prominent linear section in their middle part. The downturn toward the small sizes is most probably an artifact derived from the image resolution. In fact, the spatial resolution of the images set the lowest measurable size at around 4 μm and the downturn seems to disappear for larger size. One exception is given by sample E92-1 on Etna run at 11872°C, presenting downward curvature at sizes lower than 20 μm, well within the range of measurable sizes. At the largest sizes, the number of crystals per unit area becomes too low to be representative, resulting in flattening of the CSDs.

7.4. Discussion

Stromboli and Etna magmas are characterized by very similar chemical compositions (Tab. 4.4) and *liquidus* temperature, and the post-run samples reflect this similarity showing the same mineralogical assemblage, constituted by spinel + plagioclase ± clinopyroxene (only at the lowest temperatures; Tab. 4.3). The observed differences in the time needed to achieve the 'rheological equilibrium' and the final crystal content as a function of the undercooling may be attributed mainly to the different stirring conditions.

As reported in previous studies (e.g. Uhlman et al., 1977; Tsuchiyama, 1983), the delay in nucleation (the time required until nucleation takes place; or incubation time) decreases with increasing ΔT. Moreover it is strongly affected by the presence of flow, decreasing with increasing deformation rate (Kouchi et al., 1983). From the viscosity-time paths in Fig. 4.8 these behaviors can be observed by focusing on the first flat part of the curves. These flats can be interpreted as the viscosities of the metastable liquids, before the crystallization takes place. Although it is not possible to quantify exactly the incubation time, as the nucleation at the first stages could yield no appreciable variation to the viscosity of the melt, a reduction of the flat length can be observed both with increasing undercooling within a single dataset (Stromboli and Etna) and with increasing deformation rate by comparing the two datasets.

In Figure 7.11 the final plagioclase contents are reported as a function of the undercooling. Both datasets on Stromboli and Etna show a linear trend that can be fitted by equations reported in the figure. Within each single series, crystal content continuously increases as a function of undercooling. Extrapolated to zero crystal fraction, both lines converge to zero, indicating a good agreement between the temperature values for the onset of plagioclase crystallization calculated by MELTS and those occurring in our experiments.

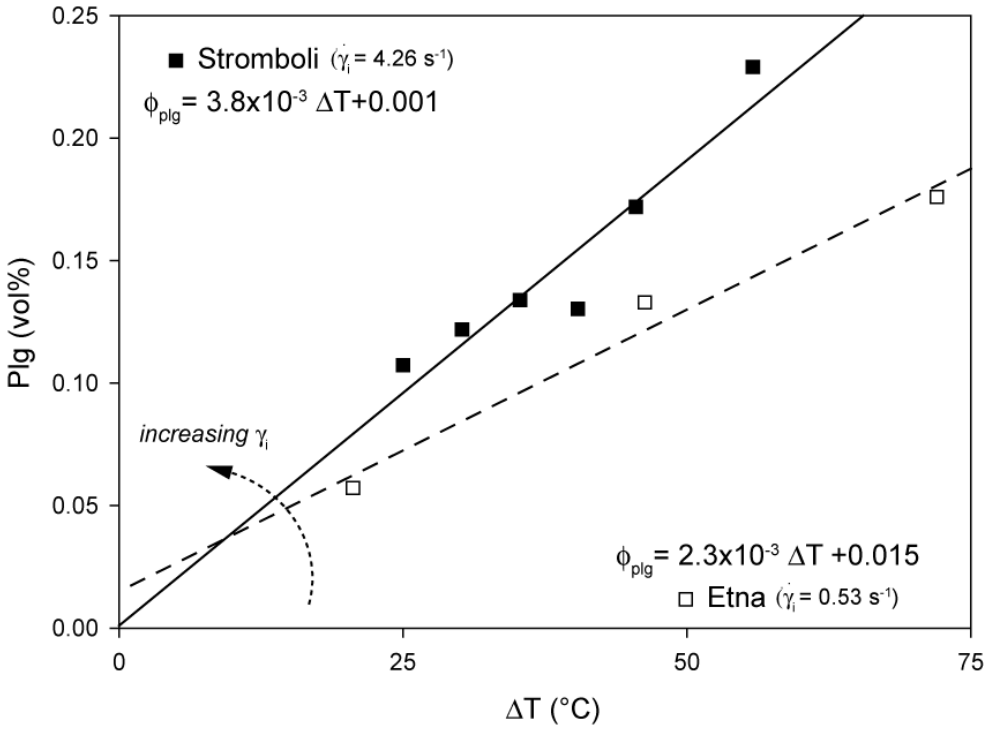

Fig. 7.11. Plagioclase content against undercooling for Stromboli (black squares) and Etna (empty squares). Solid (Stromboli) and dashed (Etna) lines represent the linear regression according to the equation reported in the diagram (R^2=0.90 and 0.98). The initial strain rates ($\dot{\gamma}_i$) for the two datasets are reported. Increasing $\dot{\gamma}_i$ yields a steeper slope.

However, with increasing degrees of undercooling the curves diverge with Stromboli data displaying a steeper slope with respect to Etna data, hence reaching higher crystal content for lower degrees of undercooling. Such a divergence can be addressed by the different kinetics of the crystallization process. A possible cause of this behavior could be that, although the initial nucleation density should be favored by higher degrees of undercooling and therefore in Etna experiments, the higher deformation rates applied on Stromboli samples could favor high nucleation density even at lower undercooling, possibly increasing the thermal fluctuation needed to stabilize the crystal nuclei. Given these initial conditions, the crystallization could then be facilitated by the lower degrees of undercooling on Stromboli experiments, with respect to Etna, where lower

experimental temperatures, and therefore higher liquid viscosity, could hinder atomic diffusion, hampering the crystal growth. In this framework, for Stromboli samples, the stirring-activated nucleation process, together with the low viscosity of the suspending liquid would permit, within the experimental time, the achievement of equilibrium crystal content (as testified by the good match between measured plagioclase amounts and those calculated by MELTS). In contrast, for Etna the occurrence of a slow, diffusion-limited growth, the equilibrium amount of crystal would not be reached in the experimental time-span, as highlighted by the discrepancy between MELTS calculation and measured crystal content.

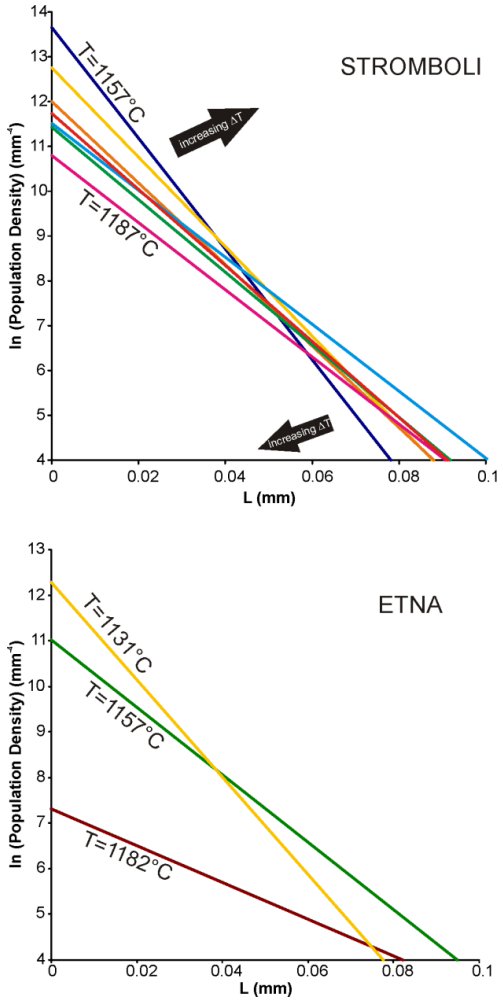

Fig. 7.12. Results of regressions of the linear section of the CSD curves (see also Fig. 4.21).

In order to interpret our results within the framework of existing CSD theories, the data were fitted to a linear equation of the form: $\ln(n) = \ln(n_0) + SL$. For this exercise, data at values of L smaller than the peak in the CSDs (related to the downward shape at low crystal sizes) were not

considered. For large values of L, size bins containing less than seven crystals were eliminated from the data set, because it was considered that these values are not statistically significant (Pupier et al., 2008). Plots of the log-linear part are reported in Fig. 7.12 and the result of the regression are reported in Tab. 7.1.

The curves continuously sharpen with decreasing experimental temperatures with slopes decreasing (i.e. assuming more negative values) from -74.9 to -123.6 mm^{-1} for Stromboli and from -40.3 to -106.8 mm^{-1} for Etna. Furthermore, an increase in the intercept, $\ln(n_0)$, values has been observed at lower experimental T from 10.79 to 13.66 mm^{-4} and from 7.31 and 12.28 mm^{-4} for Stromboli and Etna, respectively.

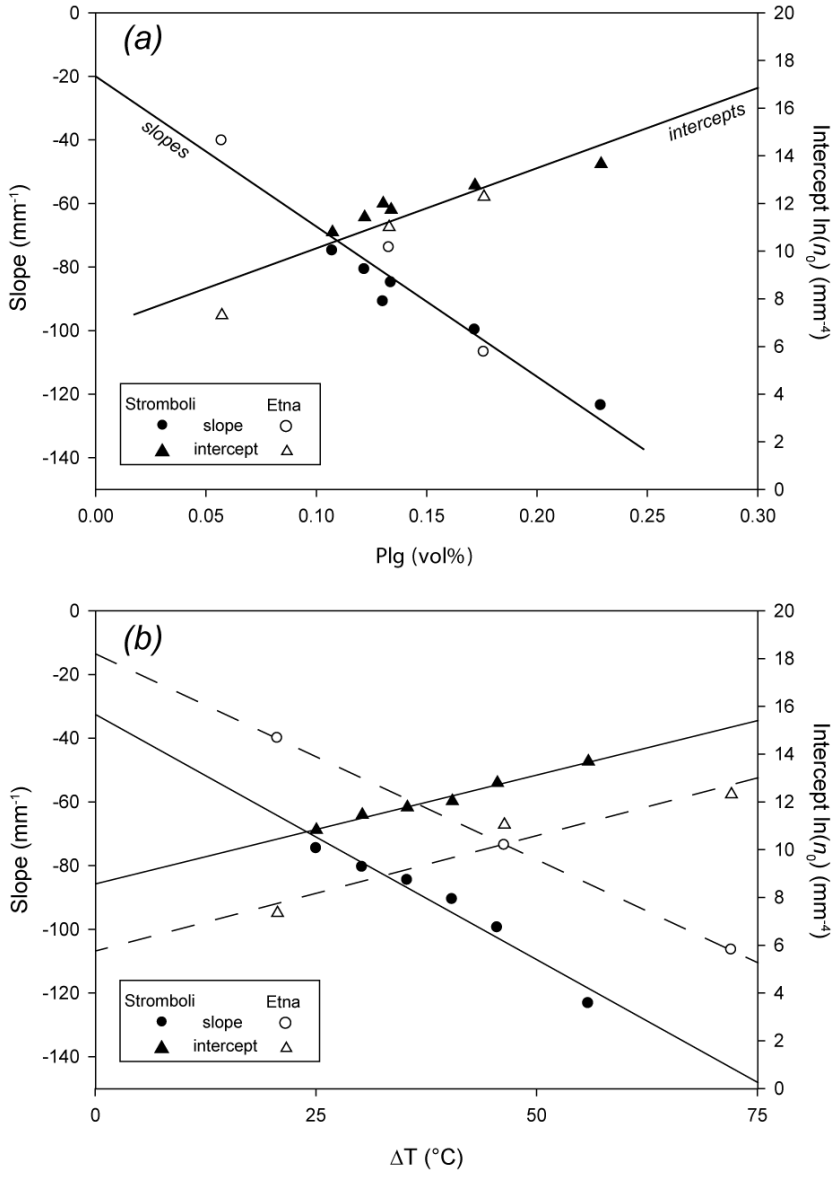

Fig. 7.13. (a) CSD slope and intercept variation as a function of plagioclase crystal content. for Stromboli (black symbols) and Etna (empty symbols). Solid lines refer to a unique linear fitting for both compositions. (b) CSD slope and intercept variation as a function of undercooling ΔT. Solid (Stromboli) and dashed (Etna) lines represent the fitting results given in Eqs. (7.6-7) and Eqs. (7.8-9), respectively.

As illustrated by Figure 7.12, within a single series, the contemporary intercept increasing and slope decreasing with increasing undercooling yields crystal size distributions progressively steeper at lower temperatures. The resulting 'fanning' behavior has been commonly observed in natural examples (e.g. Zieg and Marsh, 2002) and it is usually interpreted as the result of decreasing cooling rate through time in accordance with the thermal regime, with slow cooling producing flatter CSDs. Although in this work the experiments were run at isothermal conditions, our data agree well with this model, considering the analogy between a low cooling rate and low degrees of undercooling.

In Figure 7.13a the variation of the CSD slopes and intercepts are reported as a function of the plagioclase content. Both Stromboli and Etna data collapse on the same linear trends, indicating that for all the experimental conditions CSD slope and intercept are related through conservation of mass (Marsh, 2007). It seems therefore that the effect of the increasing flow does not affect the size distribution for a given crystal content, although it affects the overall crystal content. The relations are:

$$S = -472.5 * \phi_{Plg} - 20 \qquad (R^2=0.94) \qquad (7.4)$$

$$\ln(n_0) = 33.7 * \phi_{Plg} + 6.7 \qquad (R^2=0.83) \qquad (7.5)$$

The simple equations (7.4) and (7.5) directly correlate crystal content with CSD parameters for plagioclase crystallizing at isothermal condition. This means that the CSD curve can be easily predicted as a first approximation only using crystal fraction as an input parameter.

However, since the crystal fraction variation as a function of the undercooling is different for the two datasets (Fig. 7.11) a different evolution of the CSD parameters with varying undercooling ΔT is expected for Stromboli and Etna. Both slopes and intercepts describe a linear trend with increasing undercooling (Fig. 7.13b). The linear fitting yields the following equations for Stromboli:

$$S = -1.5417 * \Delta T - 32.8185 \qquad (R^2=0.95) \qquad (7.6)$$

$$\ln(n_0) = 0.0913 * \Delta T + 8.53 \qquad (R^2=0.98) \qquad (7.7)$$

While for Etna:

$$S = -1.294 * \Delta T - 13.7649 \qquad (R^2=1) \qquad (7.8)$$

$$\ln(n_0) = 0.0967 * \Delta T + 5.7231 \qquad (R^2=0.93) \qquad (7.9)$$

It can be observed from both the coefficients of the linear regression and graphically that the slopes and the intercepts for Stromboli and Etna have a similar gradient with increasing undercooling and show therefore sub-parallel trends, with a shifting factor that is probably linked to the effect of stirring on the crystal content vs. undercooling relation (Fig. 7.11). The use of Eqs. (7.6-7) and (7.7-8) can provide a simple estimate of the CSD parameters as a function of undercooling conditions for Stromboli and Etna series. In general, if the relation between degree of undercooling and crystal fraction is known as in Fig. 7.11, CSD parameter can be derived by either ϕ or ΔT by substituting the chosen parameter in the more general (7.4) and (7.5) equations.

As discussed by Marsh (1998) the observed log-linear decrease in population density as a function of crystal size can be explained, in a closed system, by two end-member scenarios. Either:

(1) nucleation rate J increases exponentially as a function of time and growth rate G is constant;

(2) growth rate G increases exponentially as a function of crystal size, nucleation rate being constant.

The first model has been widely adopted for modeling crystallization kinetics as a function of different cooling rates (e.g. Zieg and Lofgren, 2006). However, additional factors influencing the development of textures can be explained by crystal size dependent growth rate (Pupier et al., 2008). In general non-equant-shaped crystals display different growth rates along the different crystallographic axis, but for a given crystal face, growth rate is expected to be independent of crystal size (Zieg and Lofgren, 2006). In order to investigate if a size-dependent growth occurs in our experiments the frequency of the width/length ratios measured in 2D, which represent the X/Y ratio in 3D, are reported in Fig. 7.14 for different crystal sizes for experiments on Stromboli and Etna at high, intermediate and low temperatures.

A change in crystal shape depending on crystal size is visible as a general shifting towards higher width/length ratios with increasing sizes meaning that the thickness of crystals tablets (X) tends to increase more rapidly than their length (Y). For Stromboli (Fig. 7.14a-c) this effect seems to be slightly increasing with increasing undercooling although the maximum size class (w=0.06) at high undercooling in Fig. 7.14c could be statistically not representative due to the low number of crystal of this size (3% of the total analyzed crystals). For Etna it strikes that size-dependent shape occurs strongly at low degree of undercooling (Fig. 7.14d), diminishing at intermediate temperature (Fig. 7.14e) and finally increasing again at lower undercooling (Fig. 7.14f).

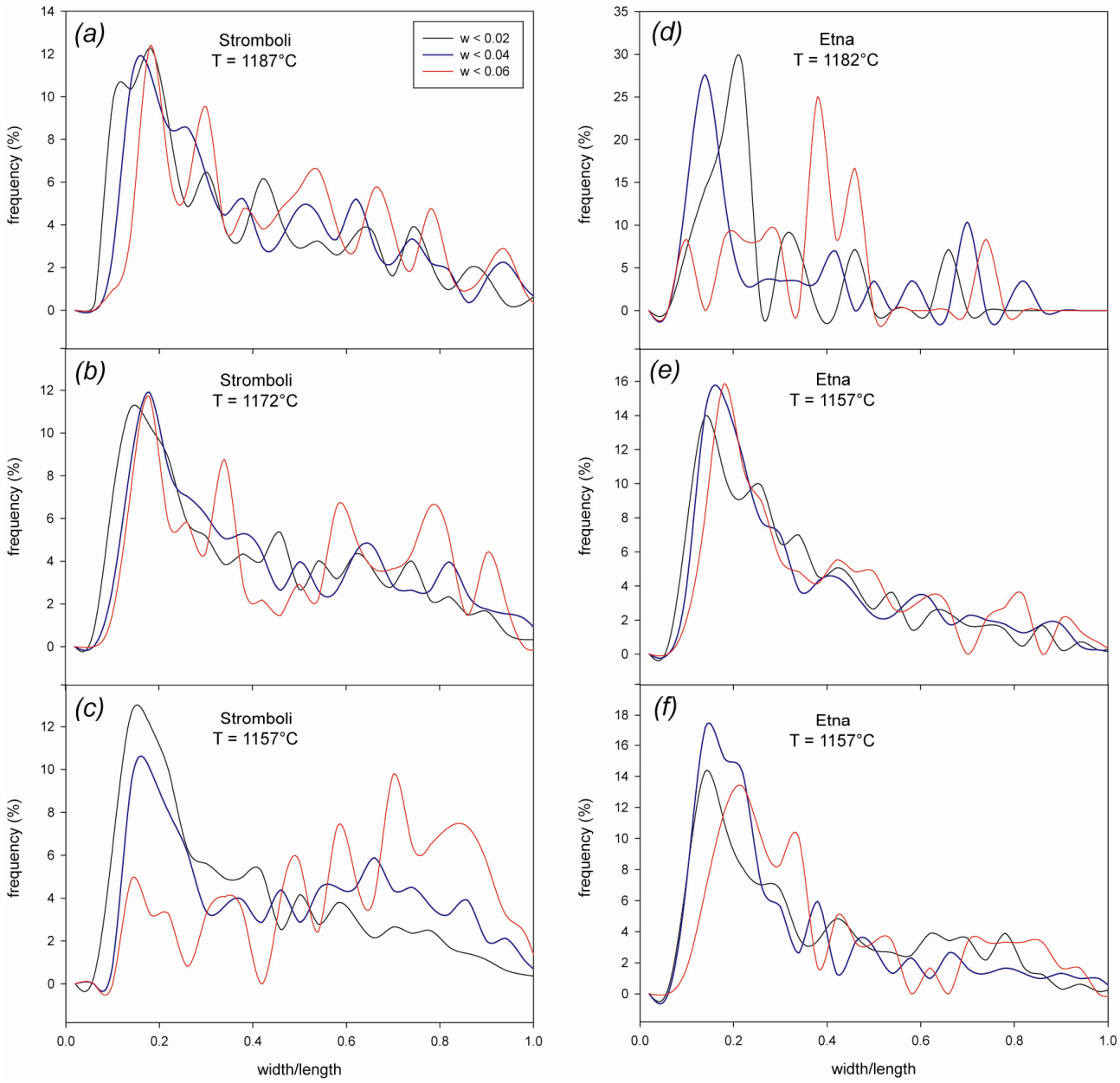

Fig. 7.14. Frequency distribution of 2D width/length ratios for different crystal sizes (w<0.02 mm, black; 0.02<w<0.004, blue; 0.04<w<0.006, red) at three representative experimental temperatures for Stromboli (a-c) and Etna (d-f) samples.

Crystal size dependent growth rate have been already inferred by Pupier et al. (2008) for experiments on plagioclase crystallization at different cooling rates. The authors interpret this process as due to crystal agglomeration. During crystallization the crystal fraction increases, which favors agglomeration, even if this effect is to some extent offset by the increase in viscosity of the liquid which will limit attachment by capillarity. In this study, the apparent size-dependent growth rate observed at the lowest temperature for both Stromboli and Etna could indicate crystal agglomeration. However, crystal agglomeration would result in flattening of CSDs toward large

sizes and steepening toward small sizes, thereby resulting in kinked CSDs (Burkhart et al. 1980; Marsh 1998; Pupier et al., 2008). High undercooling experiments on both Stromboli and Etna show no evidence of kinking, as they present clearly linear shapes. Therefore, crystal agglomeration process, if present, is not able to modify the CSDs and hence could be neglected. In contrast, for the high temperature experiment on Etna (Fig. 7.14d) the more reasonable explanation is that the size-dependent growth was caused by textural coarsening (or Ostwald Ripening; Higgins, 2002). This process occurs because small grains have a higher surface energy per unit volume than do larger grains. Therefore, to minimize energy in the system crystals smaller than a critical size will dissolve and 'feed' the growth of larger crystals. This can occur only when a crystal is held at a temperature close to its *liquidus* for a long period of time. Under these conditions, the nucleation rate is zero, but growth rate is high for crystals larger than the critical size. Material is transferred from one crystal to another by diffusion; hence, the process is much faster if the suspending liquid has low viscosity. High temperature experiment on Etna was run at ΔT=20°C and held at isothermal condition for t=4x10^5 s, a time long enough to retain that textural coarsening takes place. Another evidence of this process is given by the analysis of the CSD of this sample. The textural coarsening produces downward curvature at small size and possible rotation of the CSDs (Higgins 2002); on Etna High T sample (E92-1; Fig. 7.10) the downturn towards the small size occurs at size lower than 20 μm, well above the limit allowed by the analysis resolution. However, Etna High-T samples represent an exception, as this evidences were not observed on the other experiments of both datasets. Therefore, we retain that for the case of all other samples the crystal growth rate is not dependent of crystal size.

Following Zieg and Marsh (2002), if a size-dependent crystal growth rate is neglected, (therefore considering the end member scenario given above in point (1)), average growth rates and nucleation rate for L=0 can be derived on the basis of the interpretation of CSD parameters, from the slope and the intercept, as:

$$J = -\frac{n_0}{S\Delta t} \qquad (\mathrm{m^{-3}\ s^{-1}}) \qquad (7.10)$$

$$G = -\frac{1}{S\Delta t} \qquad (\mathrm{m\ s^{-1}}) \qquad (7.11)$$

The results of the calculation are reported in Tab. 7.1. In Figure 7.15 the values of calculated G and J are reported as a function of undercooling. Stromboli data always show higher values of both G and J with respect to Etna data. Stromboli growth rates G are not simply correlated with undercooling, however they display a relative small variation ranging between 2.5-3 x10^{-8} m/s. On

the other hand, a slight increase of G can be observed for Etna with decreasing temperature, from 0.6 x 10^{-8} to 1.3 x 10^{-8} m/s. Nucleation rates J always continuously increase with undercooling from 1.3 x 10^{7} to 8.72 x 10^{7} m^{-3} s^{-1} for Stromboli. As for Etna, nucleation rate assumes an extremely low value of 9.2 x 10^{4} m^{-3} s^{-1} at the highest undercooling experiment (ΔT=20°C), confirming that the crystallization process in this experiment is growth-dominated and that possible effects of textural coarsening occur. With increasing undercooling the nucleation rates increase continuously to values more comparable (yet lower) with those obtained on experiments on Stromboli material (up to 2.9 x 10^{7} m^{-3} s^{-1}).

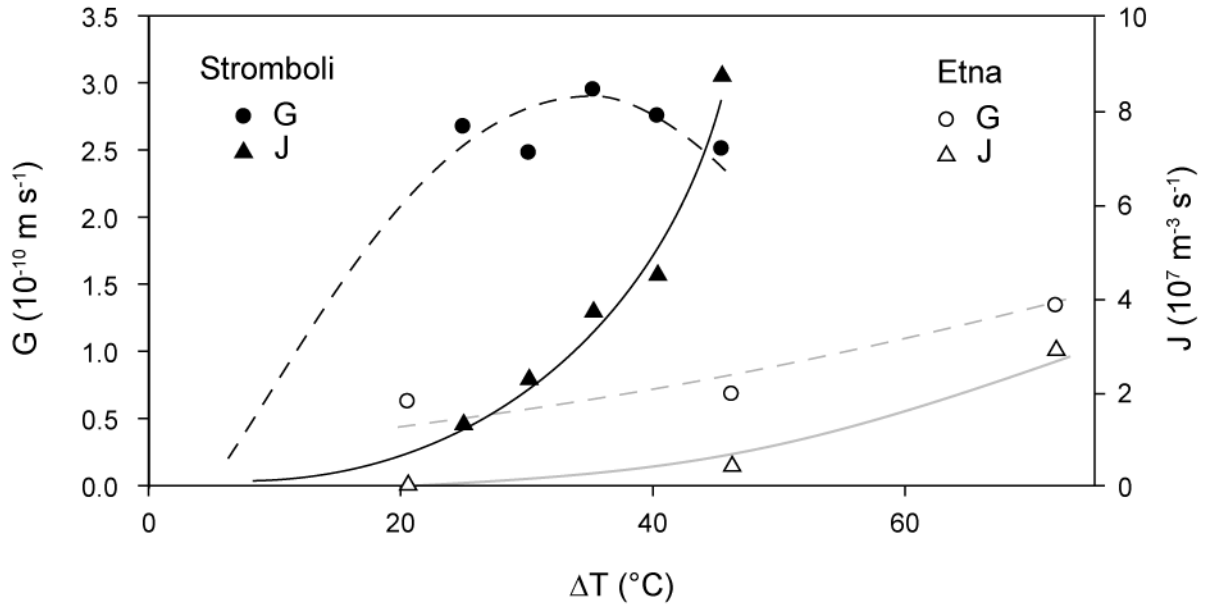

Fig. 7.15. Growth (G) and nucleation (J) rates obtained by CSD parameters against undercooling temperature. Growth rates for Stromboli (black circles) display a small variation with varying ΔT, while a slight increase can be observed for Etna (open circles). Both Stromboli (black symbols) and Etna (empty symbols) show increasing nucleation rate J with increasing ΔT.

To take into account the effect (e.g. crystal agglomeration and textural coarsening) leading to size-dependent growth we also calculated a maximum growth rate (G_{max}) from ratio between the size of the largest crystal and the experimental time (Tab. 7.1). The obtained values are about one order of magnitude higher than growth rates calculated by CSD parameters, and range between 2.8 x 10^{-9} m/s and 3.5 x 10^{-9} m/s for Stromboli and between 4.5 x 10^{-10} m/s and 1.64 x 10^{-9} m/s for Etna. The mean growth rate can, therefore, been bracketed by the values of G_{CSD} and G_{max}.

Both J and G values obtained in this paper are in agreement with those obtained experimentally by Pupier et al. (2008) from CSD data for plagioclase in basaltic magmas at different cooling rates and different *superliquidus* dwell times. For cooling rate ranging between 0.2-3 °C/h, the authors

estimate J values between 5.92 x 10^{6} $m^{-3}s^{-1}$ to 1.2 x 10^{10} $m^{-3}s^{-1}$ and G values between 6 x 10^{-11} m s^{-1} and 3.3 x 10^{-10} m s^{-1}. As a function of the *superliquidus* temperature and dwell times, they found that increasing the time above the *liquidus* strongly affects the values of J and G. For short dwell time and lower *superliquidus* temperatures they observed higher values of J and G. They interpreted this effect as the transition between heterogeneous (low superliquidus T and/or short dwell time) and homogeneous nucleation (high superliquidus T and/or long dwell time). In the present study, the melt was continuously stirred at high superliquidus temperature (T=1400°C) for 5 hours and all the natural crystalline phases were fully dissolved. Moreover the periodic inspection of the stirring spindle revealed that the liquid was completely degassed, therefore no pre-existing surface in the liquid was present, constituting a potential heterogeneous nucleation site. For this reason, we retain that the values of G and J in this study are relative to homogeneous nucleation.

Orlando et al. (2008) experimentally derived values of G for plagioclase and clinopyroxene for Etna basalt at undercooling similar to those explored in this study. The authors measured both the plagioclase overgrowth rims on crystal seeds (heterogeneous nucleation) and the size of microlites (homogeneous nucleation). Their data indicate G decreasing from 2 x 10^{-10} m s^{-1} to 4 x 10^{-11} m s^{-1} with increasing undercooling, with the highest values pertaining to heterogeneous nucleation overgrowth rim. An opposite trend has been observed in this study on Etna samples, although the estimated values of G are overall similar (average growth rate from 6 x 10^{-11} m s^{-1} to 1.3 x 10^{-10} m s^{-1}). Similar values (G=7.1 x 10^{-11} m s^{-1}) were also inferred by Armienti et al., (1994) for plagioclase on lavas collected at different times during the 1991-1993 Mt Etna eruption. Despite their similar composition Stromboli experiments from this study always show slightly greater G values (from 2.5 x 10^{-10} m s^{-1} to 3 x 10^{-10} m s^{-1}). Moreover, Armienti et al. (2007) provide even lower values for Stromboli natural magmas. In fact, they found from CSD analysis of historical eruptions a plagioclase net growth rate of 2 x 10^{-13} m s^{-1} resulting from a balance of growth (10^{-12} m s^{-1}) and resorption episodes on crystals larger than 60 μm (deep-seated storage).

The nucleation and growth rates obtained in this study pertain to homogeneous microlite (<100 μm) nucleation at constant temperature under flow conditions. The experiments were run on anhydrous basaltic magmas at atmospheric pressure therefore the results could be applied to a near surface ascending and degassing magma. Gas exsolution and gas separation can have profound effects on the phase equilibria of magmas, because rather small amount of water dissolved in magmas can reduce their *liquidus* temperature by hundreds of degrees (Sparks, 2003). Conversely, degassing of magma can cause spontaneous crystallization, as the magma becomes strongly undercooled.

In a study on the kinetics of plagioclase from Etna at 60MPa, under conditions close to water saturation and NNO buffered oxygen fugacity, Simakin and Salova (2004) found that the plagioclase occurs at T=1170±5°C. These authors estimated G for plagioclase to be ~1.5 x 10^{-7} m s^{-1} at ΔT of 10-15°C and suggested that such high value for G should control CSD for crystal sizes smaller than 0.05 cm, when crystallization is coupled with degassing during magma ascent to the surface. Orlando (2008) results in static conditions indicate that next to the surface, when magma is degassed, at high oxygen fugacity for plagioclase is ~ 3-4 orders of magnitude lower than that obtained by Simakin and Sakova (2004) at similar undercooling. In this framework, our data indicate that the effect of deformation during crystallization (especially for the deformation rates applied to Stromboli material) also play a fundamental role in determining microlite crystallization and hence changing the physical properties of ascending magmas.

7.5. Conclusions

A crystallization kinetics study has been experimentally conducted on samples from Stromboli and Etna volcanic systems. The experiments were carried out in air and at 1 atm, under stirring conditions, at different undercooling (ΔT), with respect to the plagioclase phase, varying from 24 to 45°C for Stromboli and from 21 to 72°C for Etna. The main difference between the sets of experiments (Stromboli and Etna) is the initial applied strain rate applied ($\dot{\gamma}_i$=4.26 s^{-1} for Stromboli and $\dot{\gamma}_i$=0.53 s^{-1} for Etna). Post-run plagioclase crystal contents are between ϕ=0.11-0.23 for Stromboli and between ϕ=0.06-0.18 for Etna with increasing undercooling. .

The difference in the initial deformation rate produces different kinetics of the crystallization process. We suggest that the higher deformation rates applied on Stromboli samples favor high nucleation density even at lower undercooling. At these conditions, the crystallization may be facilitated by the lower degrees of undercooling and higher atomic diffusion in the (low viscosity) melt. This behavior allows, within the experimental time, the achievement of an equilibrium crystal content. Conversely, for Etna the occurrence of a slow, diffusion-limited growth, create limits the number of crystal nucleated in the experimental time-scale, to a low- non equilibrium amount.

Crystal Size Distribution (CSD) of the experimental plagioclase crystals are always characterized by a log-linear decrease of population density as a function of crystal size. With increasing degree of undercooling a systematic increase of the steepness of the curves has been observed for both datasets. The CSD parameter (slopes and intercept) are linearly correlated with the overall crystal content of the sample. However, given the difference of the crystal content vs. undercooling

behavior for the two datasets, two different linear correlation have been found for Stromboli and Etna, relating the CSD parameters to the degree of undercooling.

One experiment conducted on Etna showed evidence of textural coarsening, for all the others a size-independent growth rate can be assumed. In the framework of the CSD theory average value of G and average J were obtained. Stromboli data always show higher values of both G and J with respect to Etna data. Stromboli growth rates G are not simply correlated with undercooling, however they display a relative small variation ranging between 2.5-3 $x10^{-8}$ m/s. On the other hand, a slight increase of G can be observed for Etna with decreasing temperature, from 0.6 x 10^{-8} to 1.3 x 10^{-8} m/s. Nucleation rates J always continuously increase with undercooling from 1.3 x 10^{7} to 8.72 x 10^{7} m^{-3} s^{-1} for Stromboli. As for Etna, nucleation rate assumes an extremely low value of 9.2 x 10^{4} m^{-3} s^{-1} at the highest undercooling experiment ($\Delta T=20°C$), confirming that the crystallization process in this experiment is growth-dominated and that possible effects of textural coarsening occur. With increasing undercooling the nucleation rates increase continuously to values more comparable (yet lower) with those obtained on experiments on Stromboli material (up to 2.9 x 10^{7} m^{-3} s^{-1}). Data obtained for G and J in this study are consistent with those obtained in literature, both from natural samples and from experimental studies. G and J data obtained in this work can be applied to natural volcanic system to infer residence times in magma chambers and magma ascent velocities. This work underline also the need and the importance to consider the deformation rates in the variation of the crystallization kinetics.

8. Conclusions

As a step towards the characterization of the rheological properties of natural magmatic mixtures a detailed experimental investigation on natural sample derived from Italian Volcanic systems (Stromboli, Etna and Phlegrean Fields) has been performed.

Viscosity measurements were conducted on basaltic melts from Stromboli and Etna during their crystallization. At the investigated *subliquidus* temperatures (1131°C<T<1187°C), a strong increase in viscosity due the presence of crystals (ϕ=0.06-0.27) was observed. At T > 1175°C and ϕ up to 0.12-0.14 both studied compositions behave as Newtonian, while with decreasing temperature, the increase in crystal content leads to the onset of a weak shear thinning behavior (n=0.9). A strong departure from the well-known (strain-rate independent) Einstein-Roscoe equation and from the strain-rate dependent model developed by Costa et al. (2009) has been observed. The origin of this departure is related primarily to the effect of elongated plagioclase in increasing crystal interactions at low ϕ. Detailed textural analyses allowed to develop for the first time on natural liquids a parameterization of the multiphase rheology, which takes into account the crystal shape, crystal size distribution of the suspension and the deformation regime. The results were applied to a synthetic suspension HPG8Na20 containing a variable amount of almost spherical corundum particles with known textural features at T=1000-1100 °C.

Multiphase rheology of natural vesicles- and crystal- bearing magmas from Monte Nuovo have been investigated by uniaxial deformation experiments in the T range 600°C-800°C and strain rates between 10^{-7} and 10^{-4} s^{-1}. Brittle behavior of the magma has been observed at T<600°C and strain rates of 10^{-5} s^{-1} and at T=800°C for the higher applied strain rate (10^{-4} s^{-1}). All other experiments were performed in the viscous regime and Monte Nuovo magma showed always a non-Newtonian shear thinning behavior. Effective viscosity in the range of 10^{10}-10^{13} were calculated by the no slip model by Gent (1960). Fitting of experimental data using the Herschel-Bulkley model revealed that at the studied condition, no yield stress was present and yielded a parametrization of the flow behavior in terms of consistency *K* and flow index *n*. The relative viscosities indicated a dependence from experimental temperature and applied strain rate. Higher relative viscosities (up to 2.1 $\log_{10}$ units) were observed with increasing temperature and decreasing strain rates. Negative relative viscosities were observed at T=640°C, when the melt approaches the glass transition temperature (Giordano et al., 2005). To derive the net effect of vesicles on the rheology of Monte Nuovo magmas, the relative viscosity was further normalized to the relative viscosity obtained by

Caricchi et al. (2008) on the same sample composition and no porosity. Normalization revealed that the presence of vesicles has a major influence on the rheology of magmas and can lead to a decrease of the viscosity of more than two orders of magnitude.

Viscosity measurements have been performed on basaltic melts from Etna at low oxygen fugacity conditions and T between 1150°C-1300°C. Reducing conditions yield a slight decrease in viscosity compared to the expected viscosity versus temperature relationship at fO_2 = air (Giordano and Dingwell 2003). Moreover, another effect of lowering the oxygen fugacity conditions is the decrease of *liquidus* temperature of the melt which leads to none or minor crystallization compared to experiments conducted at fO2=air. The results of two experiments conducted at two different oxidation state at T=1300°C (Fe3+/ΣFe = 0.18 and 0.76, respectively) indicated that the viscosity decrease observed as an inverse function of fO2, is smaller than what observed by many authors on simplified iron-bearing silicate melts. We suggest that this behavior is linked to the competition in natural systems between Fe^{3+} and Al^{3+} for the tetrahedric structural sites. Being Al favored in tetrahedrical coordination, part of Fe^{3+} is forced to behave as network-modifier also at high fugacity condition, thus the depolymerization of the melt when the reduction Fe^{3+}- Fe^{2+} takes place is limited. Our data seem to be consistent with those obtained by Bouhifd et al. (2004) on basalts, confirming that the effect of oxidation state on viscosity is more pronounced at lower than at higher temperatures and for Al-free synthetic liquids rather than for natural melts.

Rheological measurements conducted on basaltic melts from Stromboli and Etna at *subliquidus* conditions (see above) were also used to investigate the effect of the deformation rate ($\dot{\gamma}_i$=4.26 s^{-1} for Stromboli and $\dot{\gamma}_i$=0.53 s^{-1} for Etna) on the crystallization kinetics of plagioclase at different degree of undercooling (ΔT), varying from 24 to 45°C for Stromboli and from 21 to 72°C for Etna. Post-run plagioclase crystal contents are between ϕ=0.11-0.23 for Stromboli and between ϕ=0.06-0.18 for Etna with increasing undercooling. Different kinetics of the crystallization process has been observed. Higher deformation rates seem to play a fundamental role in favoring the achievement of phase equilibria in a short time-scale. Crystal Size Distribution (CSD) of the experimental plagioclase crystals are always characterized by a log-linear decrease of population density as a function of crystal size. With increasing degree of undercooling a systematic increase of the steepness of the curves has been observed for both datasets. The CSD parameter of all samples (slopes and intercept) are linearly correlated with the overall crystal content. However, given the difference of the crystal content vs. undercooling behavior for the two datasets, two different linear correlation have been found for Stromboli and Etna, relating the CSD parameters to the degree of

undercooling. In the framework of the CSD theory average value of G and average J were obtained. Stromboli data always show higher values of both G and J with respect to Etna data. Stromboli growth rates G are quite stable with increasing undercooling, however they display a relative small variation ranging between 2.5-3 $x10^{-8}$ m/s. A slight increase of G can be observed for Etna with decreasing temperature, from 0.6 x 10^{-8} to 1.3 x 10^{-8} m/s. Nucleation rates J always continuously increase with undercooling from 1.3 x 10^{7} to 8.72 x 10^{7} m^{-3} s^{-1} for Stromboli and for Etna (9.2 x 10^{4} m^{-3} s^{-1} - 2.9 x 10^{7} m^{-3} s^{-1}). However, the lowest value of J for Etna is relative to a sample in which evidence of textural coarsening have been observed and hence it represents a minimum value. Data obtained for G and J in this study are comparable with those obtained in literature, both from natural samples and from experimental studies. Data from this study can be applied to natural volcanic system to take into account the effect of deformation rate on the variation of crystallization kinetics. G and J data obtained in this work can be applied to natural volcanic system to infer residence times in magma chambers and magma ascent velocities. This work underline also the need and the importance to consider the deformation rates in the variation of the crystallization kinetics.

9. References

Ardia, P., Giordano, D., and Schmidt, M. W., 2008. A model for the viscosity of rhyolite as a function of H_2O-content and pressure: A calibration based on centrifuge piston cylinder experiments. *Geochimica Et Cosmochimica Acta* **72**, 6103-6123.

Armienti P., Clocchiatti R., D'Orazio M., Innocenti F., Petrini R., Pompilio M. Tonarini S., and Villari L., 1994. The long-standing 1991-1993 Mount Etna eruption: petrography and geochemistry of lavas. *Acta Vulcanologica* **4**, 15-28.

Armienti, P., Francalanci, L., and Landi, P., 2007. Textural effects of steady state behaviour of the Stromboli feeding system. *Journal of Volcanology and Geothermal Research* **160**, 86-98.

Barberi, F., Rosi M. and Sodi A., 1993. Volcanic hazard assessment at Stromboli based on eview of historical data. *Acta Vulcanologica*, **3**, 173-187.

Batchelor, G.K., 1970. The stress system in a suspension of force-free particles. *J. Fluid Mech.* **41**, 470– 545.

Beall, G.H., Rittler, H.L., 1976. Basalt glass ceramics. *Bull. Am. Ceram. Soc.* **55**, 579-582.

Bird, R.B., Dai, G.C., and Yarusso, B.J., 1982. The Rheology and Flow of Viscoplastic Materials *Rev. Chem. Eng*. **1**, 1-70.

Bouhifd, M. A., Richet, P., Besson, P., Roskosz, M., and Ingrin, J., 2004. Redox state, microstructure and viscosity of a partially crystallized basalt melt. *Earth and Planetary Science Letters* **218**, 31-44.

Bird, R. B.,Armstrong, R. C. and Hassager, O., 1987. *Dynamics of polymeric liquids. Vol. 1. Fluid Mechanics.* Wiley and Sons, New York, NY.

Bruckner, R. and Deubener, J., 1997. Description and interpretation of the two phase flow behaviour of melts with suspended crystals. *Journal of Non-Crystalline Solids* **209**, 283-291.

Burkhart L.E., Hoyt R.C., Oolman T., 1980. Control of particle size distribution and agglomeration in continuous precipitations. In: Kuczynski GC (ed) Sintering processes. Plenum, New York, pp 23–38.

Calvari, S., Coltelli, M., Neri, M., Pompilio, M., and Scrivano, V., 1994. The 1991-1993 Etna eruption: chronology and lava flow-field evolution. *Acta Vulcanologica* **4**, 1-14.

Caricchi, L., Burlini, L., Ulmer, P., Gerya, T., Vassalli, M., and Papale, P., 2007. Non-Newtonian rheology of crystal-bearing magmas and implications for magma ascent dynamics. *Earth and Planetary Science Letters* **264**, 402-419.

Caricchi, L., Giordano, D., Burlini, L., Ulmer, P., and Romano, C., 2008. Rheological properties of magma from the 1538 eruption of Monte Nuovo (Phlegrean Fields, Italy): An experimental study. *Chemical Geology* **256**, 158-171.

Cashman, K.V., 1990. Textural constraints on the kinetics of crystallization of igneous rocks. In J. Nicholls & J.K. Russell, eds., Modern Methods of Igneous Petrology: Understanding Magmatic Processes. Washington DC: Mineralogical Society of America, pp. 259–314.

Cashman, K.V., 1993. Relationship between plagioclase crystallisation and cooling rate in basaltic melts. *Contributions to Mineralogy and Petrology*, **113**, 126–42.

Cashman, K. V. and Marsh, B. D., 1988. Crystal size distribution (CSD) in rocks and the kinetics and dynamics of crystallization II: Makaopuhi lava lake. *Contributions to Mineralogy and Petrology* **99**, 292-305.

Champallier, R., Bystricky, M., and Arbaret, L., 2008. Experimental investigation of magma rheology at 300 MPa: From pure hydrous melt to 76 vol.% of crystals. *Earth and Planetary Science Letters* **267**, 571-583.

Chester D.K., Duncan A.M., Guest J.E. and Kilburn C.R.J., 1985. Mount Etna. The anatomy of a volcano. Chapman and Hall London: 1-404.

Chong, J. S., Christiansen, E. B., and Baer, A. D., 1971. Rheology of concentrated suspensions. *Journal of Applied Polymer Science* **15**, 2007-2021.

Clocchiatti, R., Schiano, P., Ottolini, L., and Bottazzi, P., 1998. Earlier alkaline and transitional magmatic pulsation of Mt Etna volcano. *Earth and Planetary Science Letters* **163**, 399-407.

Condomines, M., Tanguy, J. C., Kieffer, G., and Allègre, C. J., 1982. Magmatic evolution of a volcano studied by 230Th-238U disequilibrium and trace elements systematics: The Etna case. *Geochimica et Cosmochimica Acta* **46**, 1397-1416.

Cooney,T., Sharma, S.K., Urmos, J.P., 1987. Structure of glasses along the join forsteritefayalite and tephroite-fayalite (abstract). *EOS*, **68**, 436.

Cordonnier, B., Hess, K. U., Lavallee, Y., and Dingwell, D. B., 2009. Rheological properties of dome lavas: Case study of Unzen volcano. *Earth and Planetary Science Letters* **279**, 263-272.

Costa, A., 2005. Viscosity of high crystal content melts: dependence on solid fraction. *Geophysical Research Letters* **32**, 5 pp.

Costa, A., Melnik, O., Vedeneeva E., 2007. Thermal effects during magma ascent in conduits. *J. Geophys. Res.* **112**, B12205.

Costa, A., Caricchi, L., and Bagdassarov, N., 2009. A model for the rheology of particle-bearing suspensions and partially molten rocks. *Geochemistry Geophysics Geosystems* **10**.

Coussot, P. and Ancey, A., 1999. Rheophysical classification of concentrated suspensions and granular pastes. *Physical Review E* **59**, 4445-4457.

Cristini, V., Macosko, C.W., Jansseune, T., 2002. A note on the transient stress calculation via numerical simulations. *J. Non- Newton. Fluid Mech.* **105**, 177– 187.

Cukierman, M. and Uhlmann, D. R., 1974. Effects of Iron Oxidation State on Viscosity, Lunar Composition 15555. *J. Geophys. Res.* **79**, 1594-1598.

D'Orazio M., Tonarini S., Innocenti F., Pompilio M., 1997. Northern Valle del Bove volcanic succession (Mt. Etna, Sicily): petrography, geochemistry and Sr-Nd isotope data. *Acta Vulcanologica* **9**, 73-86.

D'Oriano, C., Poggianti, E., Bertagnini, A., Cioni, R., Landi, P., Polacci, M., Rosi, M., 2005. Changes in eruptive style during the AD 1538 Monte Nuovo eruption (Phlegrean Fields, Italy): the role of syn-eruptive crystallization. *Bulletin of Volcanology* **67** (7), 601–621.

de Bruijn, H., 1951. General discussion. *Discuss Faraday Soc.* **11**, 86–86.

Deines P., Nafziger, R.H., Ulmer, G.C., and Woermann, E., 1974. Temperature-oxygen fugacity tables for selected gasmixtures in the system C-H-O at one atmosphere total pressure. Pennsylvania State University, College of Earth and Mineral Sciences, *Bulletin of the experimental station*, **88**, 129.

Deubener, J. and Bruckner, R., 1997. Influence of nucleation and crystallisation on the rheological properties of lithium disilicate melt. *Journal of Non-Crystalline Solids* **209**, 96-111.

DiVito, M., Lirer, L., Mastrolorenzo, G., Rolandi, G., 1987. The 1538 Monte Nuovo eruption (Campi Flegrei, Italy). *Bulletin Of Volcanology* **49**, 608–615.

Dingwell, D.B., 1986. Viscosity-temperature relationships in the system $Na_2Si_2O_5$-$Na_4Al_2O_5$. *Geochim. Cosmochim. Acta* **50**, 1261-1265.

Dingwell, D.B., 1989a. Shear viscosities of ferrosilicate liquids. *Am. Mineral.* **74**, 1038-1044.

Dingwell, D.B., 1989b. Effect of fluorine on the viscosity of dipside liquid. *Am. Mineral.* **74**, 333-338.

Dingwell, D.B., 1991. Redox viscometry of some Fe-bearing silicate liquids. *Am. Mineral*. **76**, 1560-1562.

Dingwell, D. B., 1996. Volcanic dilemma: Flow or blow? *Science* **273**, 1054-1055.

Dingwell, D.B., 2006. Transport properties of magmas: diffusion and rheology. *Elements* **2**, 281-286.

Dingwell, D. B. and Virgo, D., 1987. The effect of oxidation state on the viscosity of melts in the system Na_2O-FeO-Fe_2O_3-SiO_2. *Geochimica et Cosmochimica Acta*, 195-205.

Dingwell, D.B., and Virgo, D., 1988. Viscosity-oxidation state relationship for hedenbergitic melt. *Carnegie Institution of Washinglon Year Book*, **87**, 48-53.

Dingwell, D. B., Knoche, R., Webb, S. L., and Pichavant, M., 1992. The effect of B_2O_3 on the viscosity of haplogranitic liquids. *American Mineralogist* **77**, 457-461.

Dingwell, D.B., Bagdassarov, N.S., Bussod, G.Y., and Webb, S.L., 1993. Magma rheology. In R.W. Luth, Ed., Experiments at high pressure and applications to the Earth's mantle. *Mineralogical Association of Canada, Short Course Handbook*, **21**, 131–196.

Dingwell, D. B., Romano, C., and Hess, K. U., 1996. The effect of water on the viscosity of a haplogranitic melt under P-T-X conditions relevant to silicic volcanism. *Contributions to Mineralogy and Petrology* **124**, 19-28.

Doi, M. and Edwards, S. F., 1978. Dynamics of rod-like macromolecules in concentrated-solution .1. *Journal of the Chemical Society-Faraday Transactions Ii* **74**, 560-570.

Donev, A., Cisse, I., Sachs, D., Variano, E., Stillinger, F. H., Connelly, R., Torquato, S., and Chaikin, P. M., 2004. Improving the density of jammed disordered packings using ellipsoids. *Science* **303**, 990-993.

Dowty, E., 1980. Crystal growth and nucleation theory and the numerical simulation of igneous crystallization. In R. B. Hargraves, ed., Physics of Magmatic Processes. Princeton: Princeton University Press.

Eberl, D. D., Drits, V. A. & Srodon, J., 1998. Deducing growth mechanisms for minerals from the shapes of crystal size distributions. American Journal of Science, **298**, 499–533.

Einstein, A., 1906. Eine neue Bestimmung der Molekul-dimensionen. *Ann. Phys.* **19**, 289-306.

Farris, R.J., 1968. Prediction of the viscosity of multimodal suspensions from unimodal viscosity data. *Trans. Soc. Rheol.* **12**, 281-301.

Fiquet, G., Richet, P., Montagnac, G. 1999. High-temperature thermal expansion of lime, periclase, corundum and spinel. *Physics and Chemistry of Minerals* **27**, 103-111.

Fornaciai, A., Landi, P., and Armienti, P., 2009. Dissolution/crystallization kinetics recorded in the 2002-2003 lavas of Stromboli (Italy). *Bulletin of Volcanology* **71**, 631-641.

Francalanci, L., Tommasini, S., Conticelli, S., and Davies, G. R., 1999. Sr isotope evidence for short magma residence time for the 20th century activity at Stromboli volcano, Italy. *Earth and Planetary Science Letters* **167**, 61-69.

Francalanci, L., Tommasini, S., and Conticelli, S., 2004. The volcanic activity of Stromboli in the 1906-1998 AD period: mineralogical, geochemical and isotope data relevant to the understanding of the plumbing system. *Journal of Volcanology and Geothermal Research* **131**, 179-211.

Francalanci, L., Davies, G. R., Lustenhouwer, W., Tommasini, S., Mason, P. R. D., and Conticelli, S., 2005. Intra-grain Sr isotope evidence for crystal recycling and multiple magma reservoirs in the recent activity of Stromboli volcano, southern Italy. *Journal of Petrology* **46**, 1997-2021.

Francalanci L., Bertagnini A., Métrich N., Renzulli A., Vannucci R., Landi P., Del Moro S., Menna M., Petrone C.M., Nardini I., 2008. Mineralogical, geochemical and isotopic characteristics of the ejecta from the 5 April 2003 paroxysm at Stromboli, Italy: inferences on the pre-eruptive magma dynamics. In: S. Calvari, S. Inguaggiato, G. Puglisi, M. Ripepe, M. Rosi (edts). The Stromboli volcano: an integrated study of the 2002-2003 eruption, pp. 331-345, Washington DC.

Gaillard, F., Scaillet, B., Pichavant, M., and Bény, J.-M., 2001. The effect of water and fO_2 on the ferric-ferrous ratio of silicic melts. *Chemical Geology* **174**, 255-273.

Gay, E., P. Nelson, and W. Armstrong, 1969. Flow properties of suspensions with high solids concentration, AIChE J. **15**, 815–822.

Gent, A. N., 1960. Theory of the parallel plate viscometer. *British Journal of Applied Physics*, **85**.

Ghiorso, M. S. & Sack, R. O., 1995. Chemical mass-transfer in magmatic processes. 4. A revised and internally consistent thermodynamic model for the interpolation and extrapolation of liquid-solid equilibria in magmatic systems at elevatedtemperatures and pressures. Contributions to Mineralogy and Petrology, **119**, 197–212.

Gillot P.Y., Kieffer G. and Romano R., 1994. The evolution of Mount Etna in the light of potassium-argon dating. *Acta Vulcanologica* **5**, 81-87.

Giordano, D. and Dingwell, D. B., 2003. Non-Arrhenian multicomponent melt viscosity: a model. *Earth and Planetary Science Letters* **208**, 337-349.

Giordano, D., Romano, C., Papale, P., and Dingwell, D. B., 2004. The viscosity of trachytes, and comparison with basalts, phonolites, and rhyolites. *Chemical Geology* **213**, 49-61.

Giordano, D., Nichols, A.R.L., Dingwell, D.B., 2005. Glass transition temperatures of natural hydrous melts: a relationship with shear viscosity and implications for the welding process. *J. Volc. Geotherm. Res.* **142**, 105-118.

Giordano, D., Mangiacapra, A., Potuzak, M., Russell, J. K., Romano, C., Dingwell, D. B., and Di Muro, A., 2006. An expanded non-Arrhenian model for silicate melt viscosity: A treatment for metaluminous, peraluminous and peralkaline liquids. *Chemical Geology* **229**, 42-56.

Giordano, D., Russell, J. K., and Dingwell, D. B., 2008. Viscosity of magmatic liquids: A model. *Earth and Planetary Science Letters* **271**, 123-134.

Giordano, D., Ardia, P., Romano, C., Dingwell, D. B., Di Muro, A., Schmidt, M. W., Mangiacapra, A., and Hess, K.-U., 2009. The rheological evolution of alkaline Vesuvius

magmas and comparison with alkaline series from the Phlegrean Fields, Etna, Stromboli and Teide. *Geochimica et Cosmochimica Acta* **73**, 6613-6630.

Giordano, D., Polacci, M., Papale, P., and Caricchi, L., 2010. Rheological control on the dynamics of explosive activity in the 2000 summit eruption of Mt. Etna. *Solid Earth* **1**, 61-69.

Gonnermann, H.M., Manga, M., 2005. Flow banding in obsidian: A record of evolving textural heterogeneity during magma deformation. *Earth and Planetary Science Letters* **236**, 135-147.

Guth, E. and Gold, O., 1938. On the hydrodynamical theory of the viscosity of suspensions. *Phys. Rev*. **53**, 322-322.

Herschel, W. H. and Bulkley, R., 1926. Konsistenzmessungen von Gummi-Benzollösungen. *Kolloid Z.* **39**, 291-300.

Hess, K. U., Dingwell, D. B., and Webb, S. L., 1995. The influence of excess alkalis on the viscosity of a haplogranitic melt. *American Mineralogist* **80**, 297-304.

Hess, K.U., Dingwell, D.B., 1996. Viscosities of hydrous leucogranitic melts: A non-Arrhenian model. *Am. Mineral*. **81**, 1297-1300.

Hess, K. U., Dingwell, D. B., and Rossler, E., 1996. Parametrization of viscosity-temperature relations of aluminosilicate melts. *Chemical Geology* **128**, 155-163.

Hess K.U., Helo C, Potuzak M. & Dingwell D.B., 2006. Advanced dilatometric method to characterise the rheological behaviour of multiphase liquids. EMPG XI – Bristol.

Higgins, M. D., 1994. Numerical modeling of crystal shapes in thin-sections estimation of crystal habit and true size. *American Mineralogist* **79**, 113-119.

Higgins, M.D., 2002. A crystal size-distribution study of the Kiglapait layered mafic intrusion, Labrador, Canada: evidence for textural coarsening. Contrib Mineral Petrol **144**(3): 314–330

Higgins, M. D., 2006. Use of appropriate diagrams to determine if crystal size distributions (CSD) are dominantly semi-logarithmic, lognormal or fractal (scale invariant). Journal of Volcanology and Geothermal Research.

Hinch, E.J., Acrivos, A., 1980. Long slender drops in a simple shear flow. *J. Fluid Mech.* **98**, 305–328.

Holtz, F., Behrens, H., Dingwell, D. B., and Taylor, R. P., 1992. Water solubility in aluminosilicate melts of haplogranite composition at 2 kbar. *Chemical Geology* **96**, 289-302.

Hoover, S. R., Cashman, K. V., and Manga, M., 2001. The yield strength of subliquidus basalts - experimental results. *Journal of Volcanology and Geothermal Research* **107**, 1-18.

Hu, Y.T., Lips, A., 2003. Transient and steady state three-dimensional drop shapes and dimensions under planar extensional flow. *J. Rheol.* **47**, 349–369.

Hui, H. J. and Zhang, Y. X., 2007. Toward a general viscosity equation for natural anhydrous and hydrous silicate melts. *Geochimica et Cosmochimica Acta* **71**, 403-416.

Ishibashi, H., 2009. Non-Newtonian behavior of plagioclase-bearing basaltic magma: Subliquidus viscosity measurement of the 1707 basalt of Fuji volcano, Japan. *Journal of Volcanology and Geothermal Research* **181**, 78-88.

Ishibashi, H. and Sato, H., 2007. Viscosity measurements of subliquidus magmas: Alkali olivine basalt from the Higashi-Matsuura district, Southwest Japan. *Journal of Volcanology and Geothermal Research* **160**, 223-238.

Jackson W. E., Waychunas G. A., Brown G. E. Jr., Mustre de Leon J., Conradson S., Comber J.-M., 1993. High-temperature XAS study of Fe2SiO4: Evidence for reduced coordination of ferrous iron in the liquid. *Science* **262**, 229–233.

Jeffery, G. B., 1922. The motion of ellipsoidal particles immersed in a viscous fluid. *Proceedings of the Royal Society of London A* **102**, 161-179.

Jeffrey, D. J. and Acrivos, A., 1976. The rheological properties of suspensions of rigid particles. *AIChE Journal|AIChE Journal* **23**, 417-32.

Kansal, A. R., Torquato, S., and Stillinger, F. H., 2002. Computer generation of dense polydisperse sphere packings. *Journal of Chemical Physics* **117**, 8212-8218.

Kirkpatrick R. J., 1981: Kinetic of crystallization of igneous rocks in kinetics of Geochemical Processes. Min Soc Amer. Vol. **8** (ed. A Lasaga and R.Kirkpatrick), pag. 321 - 397 .

Kitano, T., Kataoka, T., and Shirota, T., 1981. An empirical equation of the relative viscosity of polymer melts filled with various inorganic fillers. *Rheologica Acta* **20**, 207-209.

Klein, L.C., Fasano, B.V., Wu, J.M., 1983. Viscous flow behavior of four iron-containing silicates with alumina, effects of composition and oxidation condition, *J. Geophys. Res.* **88,** A880-A886.

Knoche, R., Dingwell, D. B., and Webb, S. L., 1995. Melt densities for leucogranites and granitic pegmatites: Partial molar volumes for SiO_2, Al_2O_3, Na_2O, K_2O, Li_2O, Rb_2O, Cs_2O, MgO, CaO, SrO, BaO, B_2O_3, P_2O_5, F_2O^{-1}, TiO_2, Nb_2O_5, Ta_2O_5, and WO_3. *Geochimica et Cosmochimica Acta* **59**, 4645-4652.

Kouchi, A., Tsuchiyama, A., and Sunagawa, I., 1986. Effect of stirring on crystallization kinetics of basalt: texture and element partitioning. *Contributions to Mineralogy and Petrology* **93**, 429-438.

Kress, V. C. and Carmichael, I. S. E., 1988. Stoichiometry of the iron oxidation reaction in silicate melts. *American Mineralogist* **73**, 1267-1274.

Krieger, I. M., 1972. Rheology of monodisperse latices. *Advances in Colloid and Interface Science* **3**, 111-136.

Kreiger, I.M. and Maron S.H., 1954. Direct determination of the flow curves of non-Newtonian fluids. III. Standardized treatment of viscometric data. *J. Appl. Phys.* **25**, 72–75.

Krieger, I. M. and Dougherty, T. J., 1959. A Mechanism for Non-Newtonian Flow in Suspensions of Rigid Spheres. *Journal of Rheology* **3**, 137-152.

Kushiro, I., 1975. On the nature of silicate melt and its significance in magma genesis; regularities in the shift of the liquidus boundaries involving olivine, pyroxene, and silica minerals. *American Journal of Science* **275**, 411-431.

Jansseune, T., Vinckier, I., Moldernaers, P., Mewis, J., 2001. Transient stresses in immiscible polymer blends during startup flows. *J. Non-Newton. Fluid Mech.* **99**, 167– 181.

Jackson, N.E., Tucker, C.L., 2003. A model for large deformation of an ellipsoidal droplet with interfacial tension. *J. Rheol.* **47**, 659–682.

Landi, P., Metrich, N., Bertagnini, A., and Rosi, M., 2004. Dynamics of magma mixing and degassing recorded in plagioclase at Stromboli (Aeolian Archipelago, Italy). *Contributions to Mineralogy and Petrology* **147**, 213-227.

Landi, P., Francalanci, L., Pompilio, M., Rosi, M., Corsaro, R. A., Petrone, C. M., Nardini, I., and Miraglia, L., 2006. The December 2002 July 2003 effusive event at Stromboli volcano, Italy: Insights into the shallow plumbing system by petrochemical studies. *Journal of Volcanology and Geothermal Research* **155**, 263-284.

Landi, P., Metrich, N., Bertagnini, A., and Rosi, M., 2008. Recycling and "re-hydration" of degassed magma inducing transient dissolution/crystallization events at Stromboli (Italy). *Journal of Volcanology and Geothermal Research* **174**, 325-336.

Landi, P., Corsaro, R. A., Francalanci, L., Civetta, L., Miraglia, L., Pompilio, M., and Tesoro, R., 2009. Magma dynamics during the 2007 Stromboli eruption (Aeolian Islands, Italy): Mineralogical, geochemical and isotopic data. *Journal of Volcanology and Geothermal Research* **182**, 255-268.

Lange, R. L. and Carmichael, I. S. E., 1987. Densities of Na_2O-K_2O-CaO-MgO-FeO-Fe_2O_3-Al_2O_3-TiO_2-SiO_2 liquids: New measurements and derived partial molar properties. *Geochimica et Cosmochimica Acta* **53**, 2195-2204.

Lasaga, A. C., 1998. Kinetic Theory in the Earth Sciences. Princeton NJ: Princeton University Press.

Lavallée, Y., Hess, K.U., Cordonnier, B.,Dingwell, D.B., 2007. Non-Newtonian rheological law for highly crystalline dome lavas. *Geology* **35**, 843-846.

Lavallée, Y., Meredith, P. G., Dingwell, D. B., Hess, K. U., Wassermann, J., Cordonnier, B.,

Gerik, A., and Kruhl, J. H., 2008. Seismogenic lavas and explosive eruption forecasting. *Nature* **453**, 507-510.

Le Bas, M. J. L., Maitre, R. W. L., Streckeisen, A., Zanettin, B., and Rocks, I. S. o. t. S. o. I., 1986. A Chemical Classification of Volcanic Rocks Based on the Total Alkali-Silica Diagram. *Journal of Petrology* **27**, 745-750.

Lejeune, A. M. and Richet, P., 1995. Rheology of crystal-bearing silicate melts - An experimental study at high viscosities. *Journal of Geophysical Research-Solid Earth* **100**, 4215-4229.

Liebske, C., Behrens, H., Holtz, F., and Lange, R. A., 2003. The influence of pressure and composition on the viscosity of andesitic melts. *Geochimica Et Cosmochimica Acta* **67**, 473-485.

Liebske, C., Schmickler, B., Terasaki, H., Poe, B. T., Suzuki, A., Funakoshi, K., Ando, R., and Rubie, D. C., 2005. Viscosity of peridotite liquid up to 13 GPa: Implications for magma ocean viscosities. *Earth and Planetary Science Letters* **240**, 589-604.

Llewellin, E. W., Mader, H. M., and Wilson, S. D. R., 2002a. The rheology of a bubbly liquid. *Proceedings of the Royal Society of London Series a-Mathematical Physical and Engineering Sciences* **458**, 987-1016.

Llewellin, E.W., Mader, H.M., Wilson, S.D.R., 2002b. The constitutive equation and flow dynamics of bubbly magmas. *Geophys. Res. Lett.* **29** (Art. No. 2170).

Llewellin, E. W. and Manga, A., 2005. Bubble suspension rheology and implications for conduit flow. *Journal of Volcanology and Geothermal Research* **143**, 205-217.

Loewenberg, M., Hinch, E.J., 1996. Numerical simulation of a concentrated emulsion in shear flow. *J. Fluid Mech.* **321**, 395–419.

Maaloe, S., Tumyr, O. & James, D., 1989. Population density and zoning of olivine phenocrysts in tholeiites from Kauai, Hawaii. Contributions to Mineralogy and Petrology, **101**, 176–86.

Maffettone, P.L., Minale, M., 1998. Equation of change of ellipsoidal drops in viscous flow. *J. Non-Newton. Fluid Mech.* **78**, 227–241.

Manga, M., Loewenberg, M., 2001. Viscosity of magmas containing highly deformable bubbles. *J. Volcanol. Geotherm. Res.* **105**, 19–24.

Manga, M., Castro, J., Cashman, K., Loewenberg, M., 1998. Rheology of bubble-bearing magmas. *J. Volcanol. Geotherm. Res.* **87**, 15– 28.

Maron, S. H. and Pierce, P. E., 1956. Application of ree-eyring generalized flow theory to suspensions of spherical particles. *Journal of Colloid Science* **11**, 80-95.

Marsh, B. D., 1981. On the crystallinity, probability of occurrence, and rheology of lava and magma. *Contributions to Mineralogy and Petrology* **78**, 85-98.

Marsh, B. D., 1988. Crystal size distribution (CSD) in rocks and the kinetics and dynamics of crystallization. *Contributions to Mineralogy and Petrology* **99**, 277-291.

Marsh, B. D., 1998. On the interpretation of crystal size distributions in magmatic systems. *Journal of Petrology* **39**, 553-599.

Marsh, B. D., 2007. Crystallization of silicate magmas deciphered using crystal size distributions. *J. Am. Ceram. Soc.* **90**, 746-757.

Marti, I., Hofler, O., Fischer, P., and Windhab, E. J., 2005. Rheology of concentrated suspensions containing mixtures of spheres and fibres. *Rheologica Acta* **44**, 502-512.

Metrich, N., Bertagnini, A., Landi, P., and Rosi, M., 2001. Crystallization driven by decompression and water loss at Stromboli volcano (Aeolian Islands, Italy). *Journal of Petrology* **42**, 1471-1490.

Metrich, N., Bertagnini, A., Landi, P., Rosi, M., and Belhadj, O., 2005. Triggering mechanism at the origin of paroxysms at Stromboli (Aeolian Archipelago, Italy): The 5 April 2003 eruption. *Geophysical Research Letters* **32**.

Moretti R., 2005. Polymerisation, basicity, oxidation state and their role in ionic modelling of silicate mets. *Annals of Geophysics*, **48**, 4/5, 583-608.

Mueller, S., Llewellin, E. W., and Mader, H. M., 2010. The rheology of suspensions of solid particles. *Proceedings of the Royal Society a-Mathematical Physical and Engineering Sciences* **466**, 1201-1228.

Mungall, J.E., Bagdassarov, N.S., Romano, C., Dingwell, D.B., 1996. Numerical modeling of stress generation and microfracturing of vesicle walls in glassy rocks. *Journal of Volcanology and Geothermal Research* **73**, 33-46.

Mysen, B.O., 1988. Structure and properties of Silicate Melts. Elsevier, Amsterdam, 354 pp.

Mysen, B.O. and Richet, P., 2005. Silicate Glasses and Melts - Properties and Structure. pp. 544, Elsevier, Amsterdam.

Mysen, B.O, Ryerson, F.J., Virgo, D., 1980. The influence of TiO_2 on structure and derivative properties of silicate melts. *Am. Mineral.* **65**, 1150-1165.

Mysen, B. O., Virgo, D., and Seifert, F. A., 1985. Relationships between properties and structure of aluminosilicate melts. *American Mineralogist* **70**, 88-105.

Navrotsky, A., Hon, R., Weill, D. F., and Henry, D. J., 1980. Thermochemistry of glasses and liquids in the systems $CaMgSi_2O_6$-$CaAl_2Si_2O_8$-$NaAlSi_3O_8$, SiO_2-$CaAl_2Si_2O_8$-$NaAlSi_3O_8$ and SiO_2-Al_2O_3-CaO-Na_2O. *Geochimica et Cosmochimica Acta* **44**, 1409-1423.

Oldroyd, J.G., 1953. The elastic and viscous properties of emulsions and suspensions. *Proc. R. Soc. A* **218**, 122– 132.

Oosterbroek, M., Mellema, J., 1981. Linear viscoelasticity in emulsions: I. The effect of an interfacial film on the dynamic viscosity of nondilute emulsions. *J. Colloid Interface Sci.* **8**, 14– 26.

Orlando, A., D'Orazio, M., Armienti, P., Borrini, D., 2008. Experimental determination of plagioclase and clinopyroxene crystal growth rates in an anhydrous trachybasalt from Mt Etna (Italy). *Eur. J. Mineral.*, **20,** 653-664.

Pabst, W., Gregorova, E., and Berthold, C., 2006. Particle shape and suspension rheology of short-fiber systems. *Journal of the European Ceramic Society* **26**, 149-160.

Papale, P., 1999. Strain-induced magma fragmentation in explosive eruptions. *Nature* **397**, 425-428.

Paterson, M. S. and Olgaard, D. L., 2000. Rock deformation tests to large shear strains in torsion. *Journal of Structural Geology* **22**, 1341-1358.

Peccerillo, A. and Taylor, S. R., 1976. Geochemistry of eocene calc-alkaline volcanic rocks from the Kastamonu area, Northern Turkey. *Contributions to Mineralogy and Petrology* **58**, 63-81.

Peccerillo, A. e Perugini, D., 2003. Introduzione alla Petrografia ottica. Morlacchi Editore.

Petford, N., 2009. Which effective viscosity? *Mineralogical Magazine* **73**, 167-191.

Pinkerton, H. and Stevenson, R. J., 1992. Methods of determining the rheological properties of magmas at sub-liquidus temperatures. *Journal of Volcanology and Geothermal Research* **53**, 47-66.

Pinkerton, H. and Norton, G., 1995. Rheological properties of basaltic lavas at sub-liquidus temperatures: laboratory and field measurements on lavas from Mount Etna. *Journal of Volcanology and Geothermal Research* **68**, 307-323.

Piochi, M., Mastrolorenzo, G., Pappalardo, L., 2005. Magma ascent and eruptive processes from textural and compositional features of Monte Nuovo pyroclastic products, Campi Flegrei, Italy. *Bulletin of Volcanology* **67** (7), 663–678.

Pocklington, H.C., 1940. Rough measurement of high viscosities. *Proceedings of the Cambridge Philosophical Society* **36**, 507-508.

Pupier, E., Duchene, S., Toplis, M.J., 2008. Experimental quantification of plagioclase crystal size distribution during cooling of a basaltic liquid. *Contrib. Mineral. Petrol.* **155**, 555-570.

Quane, S. L., Russell, J. K., and Kennedy, L. A., 2004. A low-load, high-temperature deformation apparatus for volcanological studies. *American Mineralogist* **89**, 873-877.

Randolph, A. D. & Larson, M. A., 1971. Theory of Particulate Processes. New York: Academic Press.

Reuss, A., 1929. Berechnung der Fließgrenze von Mischkristallen auf Grund der Plastizitätsbedingung für Einkristalle. *Z. Angew. Math. Mech.* **9**, 49-58.

Richet, P., 1984. Viscosity and configurational entropy of silicate melts. *Geochimica et Cosmochimica Acta* **48**, 471-483.

Richet, P., Lejeune, A. M., Holtz, F., and Roux, J., 1996. Water and the viscosity of andesite melts. *Chemical Geology* **128**, 185-197.

Riebling, E.F., 1964. Structure of magnesium aluminosilicate liquids at 1700 °C. *Can. J. Chemistry* **42**, 2811-2821.

Riebling, E.F., 1966. Structure of sodium aluminosilicate melts containing at least 50 mole % SiO_2 at 1500°. *C. J. Chem. Phys*. **44**, 2857-2865.

Rintoul, M.D. & Torquato, S., 1996. Computer simulations of dense hard-sphere systems. *J. Chem. Phys.* **105**, 9258-9265.

Robert, G., Russell, J. K., and Giordano, D., 2008a. Rheology of porous volcanic materials: High-temperature experimentation under controlled water pressure. *Chemical Geology* **256**, 216-230.

Robert, G., Russell, J. K., Giordano, D., and Romano, C., 2008b. High-temperature deformation of volcanic materials in the presence of water. *American Mineralogist* **93**, 74-80.

Robie R. A., Hemingway B. S., and Fisher J. R., 1979. Thermodynamic properties of minerals and related substances at 298.5 K and 1 bar (10^5 Pascals pressure and at higher temperatures), 456 pp.

Rogers, P.S., Williamson, J. 1969. The nucleation of crystalline phases in silicate glasses containing iron oxides. *Glass Technol.* **10**, 128-133.

Romano, C., Mungall, J.E., Sharp, T., Dingwell, D.B., 1996. Tensile strength of hydrous vesicular glasses: An experimental study. *American Mineralogist* **81**, 1148-1154.

Romano, C., Giordano, D., Papale, P., Mincione, V., Dingwell, D. B., and Rosi, M., 2003. The dry and hydrous viscosities of alkaline melts from Vesuvius and Phlegrean Fields. *Chemical Geology* **202**, 23-38.

Roscoe, R., 1952. The viscosity of suspensions of rigid spheres. *British Journal of Applied Physics* **3**, 269-367.

Rosi, M., Bertagnini, A., and Landi, P., 2000. Onset of the persistent activity at Stromboli Volcano (Italy). *Bulletin of Volcanology* **62**, 294-300.

Rosi, M., Landi, P., Polacci, M., Di Muro, A., and Zandomeneghi, D., 2004. Role of conduit shear on ascent of the crystal-rich magma feeding the 800-year B.P. Plinian eruption of Quilotoa Volcano (Ecuador). *Bulletin of Volcanology* **66**, 307-321.

Rossin, R., Bersain, J., Urbain, G., 1964. Etude de la viscosite de laitiers liquids appurtenant au systeme ternaire: SiO_2-Al_2O_3-CaO. *Revue Hautes temperatures Refractoires* **1**, 159-170.

Russell, J. K., Giordano, D., and Dingwell, D. B., 2003. High-temperature limits on viscosity of non-Arrhenian silicate melts. *American Mineralogist* **88**, 1390-1394.

Rust, A.C., Manga, M., Cashman, K.V., 2003. Determining flow type, shear rate and shear stress in magmas from bubble shapes and orientations. *J. Volcanol. Geotherm. Res.* **122**, 111–132.

Rust, A.C., Manga, M., 2002. Effects of bubble deformation on the viscosity of dilute suspensions. *J. Non-Newton. Fluid Mech.* **104**, 53– 63.

Rutgers, I. R., 1962a. Relative viscosity and concentration. *Rheologica Acta* **2**, 305-348.

Rutgers, I. R., 1962b. Relative viscosity of suspensions of rigid spheres in Newtonian liquids. *Rheologica Acta* **2**.

Rybacki, E., Dresen, G., 2004. Deformation mechanism maps for feldspar rocks. *Tectonophysics* **382** (3–4), 173–187.

Ryerson, F. J. and Hess, P. C., 1980. The role of P2O5 in silicate melts. *Geochimica et Cosmochimica Acta* **44**, 611-624.

Ryerson, F. J., Weed, H. C., and Piwinskii, A. J., 1988. Rheology of subliquidus magmas 1. Picritic compositions. *Journal of Geophysical Research-Solid Earth and Planets* **93**, 3421-3436.

Saar, M. O., Manga, M., Cashman, K. V., and Fremouw, S., 2001. Numerical models of the onset of yield strength in crystal-melt suspensions. *Earth and Planetary Science Letters* **187**, 367-379.

Sato, H., 2005. Viscosity measurement of subliquidus magmas: 1707 basalt of Fuji volcano. *Journal of Mineralogical and Petrological Sciences* **100**, 133-142.

Scarfe, C.M., Mysen , B.O., Virgo, D., 1987. Pressure dependence of the viscosity of silicate melts. In: Magmatic processes: Physicochemical Principles. *Geochem. Soc. Spec. Pub.* **1**, 59-67.

Scott, T. and Kohlstedt, D. L., 2006. The effect of large melt fraction on the deformation behavior of peridotite. *Earth and Planetary Science Letters* **246**, 177-187.

Shannon, R. D., 1976. Revised effective ionic radii and systematic studies of interatomic distances in halides and chalcogenides. *Acta Crystallogr.* **A32**, 751-767.

Shaw, H. R., 1965. Comments on viscosity, crystal settling, and convection in granitic magmas. *Am J Sci* **263**, 120-152.

Shaw, H. R., 1969. Rheology of Basalt in the Melting Range. *J. Petrology* **10**, 510-535.

Shaw, H. R., 1972. Viscosities of magmatic silicate liquids - Empirical method of prediction. *American Journal of Science* **272**, 870-&.

Simakin, A. G., Salova, T.P., 2004. Plagioclase crystallization from a Hawaiitic melt in experiments and in volcanic conduit. *Petrology,* **12**, 82-92.

Seki, K., Oeters, F., 1984. Viscosity measurements on liquid slags in the system CaO-FeO-Fe_2O_3-SiO_2. *Trans. Iron Steel Inst. Jap.* **24**, 445-454.

Sparks, R. S. J., 2003. Dynamics of magma degassing (in Volcanic degassing). *Geological Society Special Publications*, **213**, 5-22.

Spera, F.J., Stein, D.J., 2000. Comment on "Rheology of bubble bearing magmas" by Lejeune et al.. *Earth Planet. Sci. Lett.* 175, 327– 331.

Spera F.J., Borgia A., Strimple J., 1988. Rheology of melts and magmatic suspensions 1. Design and calibration of concentric cylinder viscometer with application to rhyolite magma, *Journal of Geophysical Research* **93**, 273–10,294.

Stebbins, J. F., Carmichael, I. S. E., and Weill, D. E., 1983. The high temperature liquid and glass heat contents and the heats of fusion of diopside, albite, sanidine and nepheline. *American Mineralogist* **68**, 717-730.

Stein, D.J., Spera, F.J., 1992. Rheology and microstructure of magmatic emulsions: theory and experiments. *J. Volcanol. Geotherm. Res.* **49**, 157–174.

Stevenson, R. J., Bagdassarov, N. S., Dingwell, D. B., and Romano, C., 1998. The influence of trace amounts of water on the viscosity of rhyolites. *Bulletin of Volcanology* **60**, 89-97.

Stickel, J. J. and Powell, R. L., 2005. Fluid mechanics and rheology of dense suspensions. *Annual Review of Fluid Mechanics* **37**, 129-149.

Tanguy, J.-C., Condomines, M., and Kieffer, G., 1997. Evolution of the Mount Etna magma: Constraints on the present feeding system and eruptive mechanism. *Journal of Volcanology and Geothermal Research* **75**, 221-250.

Taylor, G.I., 1934. The formation of emulsions in definable fields of flow. *Proc. R. Soc. A* **146**, 501– 523.

Thomas, D. G., 1965. Transport characteristics of suspension: VIII. A note on the viscosity of Newtonian suspensions of uniform spherical particles. *Journal of Colloid Science* **20**, 267-277.

Tobolsky, A.V. and Taylor, R.B., 1963. Viscoelastic properties of a simple organic glass. *J.Phys.Chemistry* **67**, 2439-2442.

Toguri, J.M., Kaiura, G.H., Marchant, G., 1976. The viscosity of molten FeO-Fe_2O_3-SiO_2 system. In *Extraction Metallurgy of Copper. I. Physical Chemistry of Copper Smelting*, 259-273.

Metall. Soc. Of AIME, New York.

Tsuchiyama A., 1983. Crystallization kinetics in the system CaMg-Si2O6-CaAl2SiO8: the delay in nucleation of diopside and anorthite. Am Mineral 68:687698.

Tucker, C.L., Moldenaers, P., 2002. Microstructural evolution in polymer blends. *Annu. Rev. Fluid Mech.* **34**, 177–210.

Tuffen, H., Dingwell, D.B., Pinkerton, H., 2003. Repeated fracture and healing of silicic magma generate flow banding and earthquakes? *Geology* **31** (12), 1089–1092.

Uhlmann DR, Klein LC, Handwerker CA, 1977. Crystallization kinetics, viscous flow, and thermal history of lunar breccias 67975. Proc Lunar Sci Conf 8th, pp 206-2078

Urbain, G., Bottinga, Y., and Richet, P., 1982. Viscosity of liquid silica, silicates and alumino-silicates. *Geochimica et Cosmochimica Acta* **46**, 1061-1072.

Van der Werff, J. C. and de Kruif, C. G., 1989. Hard-sphere Colloidal Dispersions: The Scaling of Rheological Properties with Particle Size, Volume Fraction, and Shear Rate. *Journal of Rheology* **33**, 421-454.

Vetere, F., Behrens, H., Holtz, F., and Neuville, D. R., 2006. Viscosity of andesitic melts - new experimental data and a revised calculation model. *Chemical Geology* **228**, 233-245.

Vetere, F., Behrens, H., Misiti, V., Ventura, G., Holtz, F., De Rosa, R., and Deubener, J., 2007. The viscosity of shoshonitic melts (Vulcanello Peninsula, Aeolian Islands, Italy): Insight on the magma ascent in dikes. *Chemical Geology* **245**, 89-102.

Vetere, F., Behrens, H., Schuessler, J. A., Holtz, F., Misiti, V., and Borchers, L., 2008. Viscosity of andesite melts and its implication for magma mixing prior to Unzen 1991-1995 eruption. *Journal of Volcanology and Geothermal Research* **175**, 208-217.

Virgo, D. and Mysen, B., 1985. The structural state of iron in oxidized vs. reduced glasses at 1 atm: A ^{57}Fe Mössbauer study. *Physics and Chemistry of Minerals* **12**, 65-76.

Voigt, W., 1928. *Lehrbuch der Kristallphysik*, Leipzig, Germany.

Voorhees, P. W., 1992. Ostwald ripening of two-phase mixtures. Annual Review of Materials Science, **22**, 197–215.

Waychunas, G. A., Apted, M. J., and Brown, G. E., 1983. X-ray K-edge absorption spectra of Fe minerals and model compounds: Near-edge structure. *Physics and Chemistry of Minerals* **10**, 1-9.

Webb, S. L. and Dingwell, D. B., 1990. The onset of Non-Newtonian rheology of silicate melts – A fiber elongation study. *Phys. Chem. Minerals* **17**, 125-132.

Whittington, A., Richet, P., and Holtz, F., 2000. Water and the viscosity of depolymerized aluminosilicate melts. *Geochimica Et Cosmochimica Acta* **64**, 3725-3736.

Whittington, A., Richet, P., Linard, Y., and Holtz, F., 2001. The viscosity of hydrous phonolites and trachytes. *Chemical Geology* **174**, 209-223.

Wilke, M., Partzsch, G.M., Bernhardt, R., Lattard, D., 2005. Determination of the iron oxidation state in basaltic glasses using XANES at the K-edge. *Chemical Geology* **220** (1–2), 143–161.

Williamson, J., Tipple, A.J., Rogers, P.S., 1968. Influence of iron oxides on kinetics of crystal growth in CaO-MgO-Al_2O_3-SiO_2 glasses, *J. Iron Steel. Inst.* **206,** 898-903.

Wilson, A.D., 1960. The micro-determination of ferrous iron in silicate melts by a volumetric and a colorimetric method. *Analyst*, **85**, 823-827.

Wu, Y., Zinchenko, A.Z., Davis, R.H., 2002. Ellipsoidal model for deformable drops and application to nonNewtonian emulsion flow. *J. Non-Newton. Fluid Mech.* **102**, 281–298.

Yu, W., Bousmina, M., 2003. Ellipsoidal model for droplet deformation in emulsions. *J. Rheol.* **47**, 1011 –1039.

Zieg M.J., Marsh B.D., 2002. Crystal size distributions and scaling laws in the quantification of igneous textures. J Petrol **43**(1) : 85–101.

Zieg M.J., Lofgren G.E., 2006. An experimental investigation of texture evolution during continuous cooling. J Volcanol Geotherm Re **154**(1–2) : 74–88.